

# **Colloidal crystallization in bulk, gravity and spherical confinement**

---

Tonnishtha Dasgupta

**Cover:** A binary icosahedral supraparticle spontaneously formed in computer simulations of hard-sphere-like particles under spherical confinement.

**Invitation bookmark:** Photonic Laves phase self-assembly on a patterned template *via* sedimentation.

PhD thesis, Utrecht University, the Netherlands, March 2019.

ISBN: 978-90-393-7102-2

Printed by: ProefschriftMaken || [www.proefschriftmaken.nl](http://www.proefschriftmaken.nl)

A digital version of this thesis is available at <https://colloid.nl/publications/theses/>

# **Colloidal crystallization in bulk, gravity and spherical confinement**

---

## **Colloïdale kristallisatie in bulk, zwaartekracht en in een bolvormige ruimte**

(met een samenvatting in het Nederlands)

### **Proefschrift**

ter verkrijging van de graad van doctor aan de Universiteit Utrecht op gezag van de rector magnificus, prof. dr. H.R.B.M. Kummeling, ingevolge het besluit van het college voor promoties in het openbaar te verdedigen op woensdag 6 maart 2019 des middags te 2.30 uur

door

**Tonnishtha Dasgupta**

geboren op 25 september 1988 te Kolkata, India

**Promotor:** Prof. dr. ir. M. Dijkstra

This work is part of the Industrial Partnership Programme (IPP) *Computational Sciences for Energy Research* (13CSER025) of the Netherlands Organisation for Scientific Research (NWO). This research programme is co-financed by Shell Global Solutions International B.V.

# Contents

<b>1</b>	<b>Introduction</b>	<b>1</b>
1.1	Hard spheres: Entropy and free volume	2
1.2	Photonic crystals: Research interest	4
1.3	Computer simulations	6
1.3.1	Monte Carlo methods	6
1.3.2	Calculating phase coexistence: Common tangent construction	8
1.4	Scope of this thesis	11
<b>2</b>	<b>Growth of defect-free colloidal hard-sphere crystals using colloidal epitaxy</b>	<b>13</b>
2.1	Introduction	14
2.2	Simulation methods	16
2.2.1	Systems studied	16
2.2.2	Order parameters	17
2.3	Results and Discussion	19
2.3.1	Sedimentation on the fcc (100) template	19
2.3.2	Comparison with the flat wall, fcc (111) and fcc (110) templates	24
2.3.3	Effect of lattice spacing of the fcc (100) template	28
2.3.4	Effect of initial volume fraction	29
2.4	Conclusions	31
2.5	Acknowledgements	32
<b>3</b>	<b>Towards a colloidal Laves phase from binary hard-sphere mixtures <i>via</i> sedimentation</b>	<b>33</b>
3.1	Introduction	34
3.2	Methodology	36
3.2.1	Bulk phase behaviour of binary hard-sphere systems	36
3.2.2	Accounting for gravity	37
3.2.3	Event-Driven Brownian Dynamics simulations	38
3.3	Results and Discussion	39
3.3.1	Bulk phase diagram for $q = 0.85$	39
3.3.2	Stacking diagram for $q = 0.85$	40
3.3.3	Bulk phase diagram for $q = 0.82$	42
3.3.4	Stacking diagram for $q = 0.82$	44
3.3.5	Event-Driven Brownian Dynamics	47
3.4	Conclusions	52

<b>4</b>	<b>Stabilizing the Hexagonal Close Packed Structure of Hard Spheres with Polymers: Phase diagram, Structure, and Dynamics</b>	<b>55</b>
4.1	Introduction	56
4.2	Model and Methods	58
4.2.1	Configurational Bias Monte Carlo Method	59
4.2.2	Transition Matrix Monte Carlo method	59
4.3	Results	60
4.3.1	Motivation: Thermodynamics of a freely-jointed polymer in a rigid colloidal framework	60
4.3.2	Polymer adsorption as a function of colloid packing fraction	61
4.3.3	Phase behaviour	64
4.3.4	Structure and dynamics	66
4.4	Discussion and Conclusions	71
4.5	Outlook: Stabilizing the MgCu <sub>2</sub> Laves phase	73
4.6	Acknowledgements	74
<b>5</b>	<b>The role of attractions in the crystallization of nanoparticles under spherical confinement</b>	<b>75</b>
5.1	Introduction	76
5.2	Crystallization of attractive nanoparticles in spherical confinement	77
5.2.1	Experimental findings	77
5.2.2	Model and EDBD simulations	77
5.2.3	Role of attractions in the crystallization kinetic pathways	80
5.2.4	Structures obtained for different system sizes	84
5.3	Summary	87
5.4	Acknowledgements	88
<b>6</b>	<b>Spontaneous nucleation of binary Laves phases in nearly hard spheres</b>	<b>89</b>
6.1	Introduction	90
6.2	Model	93
6.3	Bulk phase diagram	93
6.3.1	Free-energy calculations	93
6.3.2	Phase behaviour	95
6.4	Spontaneous nucleation	106
6.4.1	Order parameters	106
6.4.2	Nucleation	108
6.4.3	Nucleation at constant density	108
6.4.4	Nucleation at constant pressure	109
6.5	Hard sphere equivalence: Isomorphs	115
6.6	Nucleation barrier, $k_B T / \varepsilon = 0.2$	126
6.7	Summary and conclusions	130
6.8	Acknowledgements	132

<b>7 Binary icosahedral quasicrystals of hard-sphere-like colloids in spherical confinement</b>	<b>133</b>
7.1 Introduction	134
7.2 Results and Discussion	136
7.2.1 Recap: Laves phases in Bulk	136
7.2.2 Effect of spherical confinement	136
7.2.3 Nucleation and growth	144
7.2.4 Implications for photonic crystal research	146
7.3 Conclusions and outlook	148
7.4 Acknowledgements	149
<b>References</b>	<b>151</b>
<b>Summary</b>	<b>165</b>
<b>Samenvatting</b>	<b>169</b>
<b>Acknowledgements</b>	<b>173</b>
<b>List of publications</b>	<b>177</b>
<b>Oral and poster presentations</b>	<b>178</b>
<b>About the author</b>	<b>179</b>



# 1

---

## Introduction

---

In this Chapter we lay out at a general level, the ideas, challenges and the motivation behind this thesis.

## 1.1 Hard spheres: Entropy and free volume

This thesis discusses physical phenomena in relation to hard spheres, in particular, crystallization from a disordered fluid phase. In the case of hard-sphere interactions, temperature does not factor in and therefore the phase behaviour is only dependent on the volume fraction. Crystallization of hard spheres, a phase transition from a disordered to an ordered phase, is entropy-driven. From thermodynamics, we know that for a system of a fixed number of particles, constant volume and temperature  $T$ , a phase transition can only take place if the Helmholtz free energy  $F = E - TS$  is lowered. Therefore, for *athermal* systems such as hard spheres, where the potential energy  $E$  falls out, a spontaneous phase transition can only result from an increase in entropy  $S$ . Entropy  $S$  is defined by

$$S = k_B \ln \Omega \quad (1.1)$$

where  $k_B$  is the Boltzmann constant and  $\Omega$  is the number of microscopic states accessible to the system at that thermodynamic state point. The common, and often misunderstood, interpretation of Eq. 1.1 is that  $\Omega$ , the number of accessible microstates, is a measure of the ‘*disorder*’ of a system. The misinterpretation is not in the term disorder, rather the intuitive way that people think of order and disorder: crystals are assumed to be *ordered* and fluids are considered to be *disordered*. At first, it may seem counterintuitive that at high densities a hard-sphere system can increase its entropy by going from a disordered fluid phase to an ordered crystal phase. At low densities, the fluid phase has a high entropy as the number of distinct configurations is large. However, at high densities, although the entropy corresponding to the number of distinct configurations decreases, the overall entropy increases because the *free volume* per particle (volume within which the centre of a hard sphere can move without changing other sphere positions) is larger in the crystalline phase than in the fluid phase, which is directly tied to expression 1.1. The first-order freezing transition of hard spheres was predicted by Kirkwood in the early 1950s [1], but the acceptance of an entropy-driven ordering transition was met with scepticism until computer simulations on hard spheres by Alder and Wainwright [2], and by Wood and Jacobson [3] provided support for such a phase transition. Thereafter, the acceptance of the concept of entropy-driven freezing came slowly [4].

At infinite pressures, entropy is maximized for the densest packing. Here, the volume fraction tends to the close-packed limit, and the distance between the surfaces of spheres becomes 0. In this limit, the system becomes formally equivalent to a system of hard dodecahedra which *do not rotate* [5]. In this way, Alder *et al.* [6] could simulate the close-packed limit directly. Estimation of the maximum volume fraction of close-packed hard spheres has an interesting mathematical history. In his 1611 paper entitled *Six-cornered snowflake*, Johannes Kepler *conjectured* that the maximum packing of equal-sized hard spheres corresponds to a volume fraction of  $\frac{\pi}{3\sqrt{2}}$  ( $\sim 0.74$ ) for any arrangement of such spheres, either regular or irregular. This, as we know, is the volume fraction of the face-centered-cubic (FCC) and hexagonal-close-packed (HCP) structures which are regular crystalline lattices, and also for a random stacking of hexagonally close-packed planes (rHCP) which are aperiodic in the direction of the stacking. Kepler’s studies were incited by the renowned mathematician and astronomer Thomas Harriot, who was asked by the famous explorer Sir Walter Raleigh what the most efficient stacking is of cannonballs on the deck of his ship. However Kepler could not provide a proof of his conjecture, and it took nearly two centuries until Carl Friedrich Gauss proved that Kepler’s conjecture is true for

spheres are arranged on a regular lattice. This implied that any conjecture which disproved the Kepler conjecture would have to be an irregular one, which is understandably very difficult. The volume fraction of maximum random close packing (RCP) in 3D is reported to lie between 0.6 [7] and 0.68 [8] depending on the method employed. A century later, the Kepler conjecture formed part of Hilbert's 18<sup>th</sup> problem which addresses packings in 3D Euclidean space. In the 1950s, Fejes Tóth provided a strategy for proving the Kepler conjecture at the same time suggesting that computers were required [9]. A breakthrough in proving the conjecture was established in 1998 by Ferguson and Hales but it took more than 7 years to publish the proof due to difficulties in verifying each step by an incredibly large group of referees. This proof without complete certification was finally published in 2006 [10]. In 2003, at the *Joint Math Meetings*, Hales announced a project to give a formal proof of Kepler's conjecture - the project was called *Flyspeck*, an expansion of the acronym FPK which stands for the Formal Proof of the Kepler conjecture. Finally, the official published proof of the Flyspeck project was published as recently as 2017 [11].

**Hard spheres as model colloids** The hard-sphere model was initially devised to model an idealistic atomic liquid by modelling the short-range harshly repulsive forces by an infinitely steep potential. Later, Pusey, van Megen, Vrij and others pioneered experimental colloidal systems, such as polymethyl-methacrylate (PMMA) and silica particles coated with polymers, which can be approximately modelled by the hard-sphere potential [12, 13]. Colloidal suspensions, important in industrial products such as paints, food, pharmaceutical products etc., consist of particles of sizes ranging from a few nanometers to a few micrometers, dispersed in a fluid medium. Colloidal systems are known to form ordered structures which are analogous to atomic and molecular structures, earning them the name "big atoms" [14]. Therefore they may serve as model systems for condensed matter physics for studying physical phenomena such as crystallization, freezing, demixing and gelation. The length scales of colloidal systems are comparable to the wavelength of light and therefore light-scattering studies may be performed on these systems for studying both structure - such as the Bragg reflection of visible light by colloidal crystals - and dynamics, such as the structural relaxation of colloidal systems over long timescales (of the order of seconds). For example, a crystalline colloidal sample can be destabilised into a metastable fluid just by shaking up as colloidal solids are mechanically weak, and the recrystallization spans from minutes, hours to days therefore allowing studies of the crystallization process and the metastable liquid structure. Expounding a bit on the mechanical 'weakness' through an example, a jar of salt crystals would be unaffected if we shook it, but a colloidal crystal would break apart under such treatment. This difference is based on  $\sim 10^{12}$  difference in mechanical properties such as the elastic constants, which govern the strength of a crystal.

**Binary hard-sphere mixtures** A lot of the discussion in this thesis centers around the crystallization of binary hard-sphere (or hard-sphere-like) mixtures. The entropy of mixing of a binary mixture of large ( $L$ ) and small ( $S$ ) species with a large species fraction  $x_L = N_L/(N_L + N_S)$ , and  $N_L(N_S)$  the number of large (small) particles, can be obtained trivially from the partition function

$$s_{id}(x_L) = -k_B [x_L \ln x_L + (1 - x_L) \ln(1 - x_L)] \quad (1.2)$$

Formation of a *binary* crystal from a binary hard-sphere mixture can be seen in terms of an increase in free volume in the ordered phase, similar to one-component crystals as discussed above. However, in binary crystals, where the two components/species occupy different sublattices of the crystalline lattice, there is also an additional loss of entropy of mixing on crys-

tallization. Nevertheless, binary crystals of icosahedral  $LS_{13}$  (atomic analog  $NaZn_{13}$ ) [15–17],  $LS_2$  (atomic analog  $AlB_2$ ) and cubic  $LS_{13}$  [18–20],  $LS$  (atomic analog  $NaCl$ ) [21] and  $LS_2$  (atomic analog  $MgZn_2$ ,  $MgNi_2$ ) [22–24] structures have been found in experiments on mixtures of soft repulsive and nearly hard-sphere colloids of dissimilar diameters. Free-energy calculations from simulations of binary hard-sphere mixtures provide a range of diameter ratios ( $q$ ) for which these binary (hard-sphere) crystals are thermodynamically stable at high enough densities in the thermodynamic phase diagram -  $NaCl$  ( $0.414 \leq q \leq 0.45$ ) [25],  $AlB_2$  ( $0.425 \leq q \leq 0.6$ ) [26],  $NaZn_{13}$  ( $0.485 \leq q \leq 0.625$ ) [26],  $MgZn_2/MgCu_2/MgNi_2$  ( $0.76 \leq q \leq 0.84$ ) [27, 28]. However, binary crystals nucleate from a (repulsive) binary fluid mixture at much higher densities as compared to binary crystals that are formed by attractive interactions, which poses significant challenges for spontaneous nucleation (despite thermodynamic predictions), such as slow dynamics and glassy behaviour.

Another interesting discussion in binary hard-sphere mixtures, although it is not the main focus of this thesis, is the question of phase separation in the fluid phase. Monodisperse hard spheres do not show fluid-fluid demixing because there is no source for attraction between the spheres. In view of Eq.1.2, even though it is an approximation, phase separation in binary hard-sphere fluid mixtures is possible if there is an entropy *increase* on demixing, driven by excluded volume interactions. The discussion here is in the context of “additive” mixtures *i.e.*  $\sigma_{LS} = (\sigma_L + \sigma_S)/2$ . Theoretically, there are conflicting predictions on this demixing. Lebowitz and Rowlinson [29] found, using the Percus-Yevick (P-Y) closure in integral equation theory generalized for a multi-component mixture [30], that binary mixtures of hard spheres uniformly mix in all proportions in a fluid mixture for all densities and all diameter ratios. In contrast, Hansen and Biben [31], using the Rogers-Young closure, found in dense fluid mixtures that for  $q < 0.2$ , phase separation is obtained when the partial volume fractions of the two species become comparable. However, both theories are approximate, and the contrasting findings demonstrate the dependence on how well the theory captures the mixture equation of state. Subsequently, Dijkstra *et al.* [32] indeed found in computer simulations of highly asymmetric binary hard spheres  $q = 0.033, 0.05$  and  $0.1$ , a fluid-fluid phase separation but *metastable* with respect to a broad fluid-solid transition. There are strong connections between such (asymmetric) binary hard-sphere mixtures and colloid (big sphere)- nonadsorbing polymer (linear chains of small sphere monomers) mixtures. We discuss later in this thesis, the phase behaviour of such a colloid-polymer mixture.

## 1.2 Photonic crystals: Research interest

Photonic crystals, and their significance, are best described by a direct analogy to semiconductor crystals in which positive and negative charges are either alternately positioned on a lattice or the positive charges are dispersed in a sea of electrons. The arrangement of charges produces an electric potential difference. In this charge arrangement, the energies of individual electrons start to overlap, forming a continuous band of allowed energy states, resulting in a state where the highest completely occupied energy state (top of the valence band) is separated from the first subsequent empty energy state (bottom of the conduction band) by a region of energy states that the electrons in the solid cannot occupy. This region is termed an electronic band gap. Photonic band gap materials or photonic crystals show a *photonic band gap* arising from periodically

varying dielectric contrasts in the material. The so-called photonic band gap (PBG) represents the forbidden energy range where photons can not be transmitted through the material. Just like semiconductors are adaptable, *i.e.* their conductivity can be modulated by doping with impurities or gating with electric fields, photonic crystals can manipulate light and stand to revolutionise the field of photonics just as semiconductor transistors revolutionised the field of electronics.

Photonic crystals can either be direct or inverse structures. The direct structure would have a high dielectric constant material in a medium with a low dielectric constant, and vice-versa for the inverse structure. To take an example, if holes are drilled into the dielectric material in a periodic lattice, with a lattice constant on the order of the wavelength of the visible spectrum, light entering the material would scatter off the material-medium interface and the complex pattern of interfering beams would lead to a cancellation of a band of wavelengths in all directions, resulting in the prevention of propagation of this band of light frequencies in the crystal. In the context of this thesis, we are specifically interested in *colloidal* photonic crystals, which due to the size of the building blocks, display a band gap in the visible and infrared range of light frequencies. However, the most significant challenge is that photonic crystals are difficult to fabricate. Let us take a look at a few well known structures which show a photonic band gap. The field gained momentum with the coincident pioneering works of Yablonovitch [33] and John [34], where they showed the theoretical realization of a PBG. Most structures with a complete photonic band gap are either a diamond or an FCC structure or variations of them. As widely known, the FCC structure is significant because it is the thermodynamically stable crystal phase for hard spheres and as such it can be assembled experimentally and computationally from monodisperse hard spheres. However, it does not show a complete photonic band gap. This is because at two symmetry points in the Brillouin zone, there is degeneracy between the valence and conduction bands which closes up the band gap. However, Yablonovitch showed that this symmetry induced degeneracy is lifted by using nonspherical atoms in the FCC microstructure [35]. Yablonovite, as this structure is called, shows a photonic band gap at visible frequencies. In another study, Vlasov *et al.* spontaneously self-assembled colloidal microspheres onto an fcc lattice, infiltrated semiconductor material into the template and then removed the template giving an inverted opal structure which still follows the fcc lattice geometry but now has a clear photonic band gap [36]. The band gap displayed by an (inverted) FCC structure is narrow, and therefore susceptible to defects. The clear champions in colloidal photonic crystals are the diamond [37] and pyrochlore [38] structures, as they display wide photonic band gaps for low refractive index contrasts. However, unlike the FCC structure, these are low-coordination structures, and therefore difficult to obtain from colloidal crystallization as they have a low volume fraction and are therefore mechanically unstable. An intriguing solution to the conundrum of a low volume fraction presents itself in form of the binary  $\text{MgCu}_2$  Laves phase (LP) crystal structure, whose large species and small species sublattices are the diamond and pyrochlore structures respectively. The Laves phases refer to structures whose atomic analogs are  $\text{MgZn}_2$ ,  $\text{MgCu}_2$  and  $\text{MgNi}_2$ . Interestingly, the  $\text{MgZn}_2$  LP is thermodynamically stable at certain diameter ratios for a simple binary hard-sphere mixture and the  $\text{MgCu}_2$  LP has only marginally higher free-energy ( $O(10^{-3}k_B T)$  per particle) than its LP counterpart. Furthermore, it has been shown that the  $\text{MgCu}_2$  LP can be grown selectively with templating approaches [27] in such mixtures, or even if the  $\text{MgZn}_2$  LP is formed (as it has the lowest free energy), a synchroshear mechanism may be employed to transform it into the  $\text{MgCu}_2$  LP structure [39]. The challenge

for the moment is the spontaneous self-assembly of the binary Laves phases from a binary hard-sphere fluid mixture, for which the difficulties were already briefly discussed in Section 1.1. Parts of this thesis attempts to address some aspects of self-assembly of the Laves phases.

## 1.3 Computer simulations

As our work is based on computer simulations of hard sphere or hard-sphere-like systems, We would like to begin by briefly acknowledging some female scientists who were instrumental in early scientific literature on hard-sphere systems, whose names are less publicly known. In relation to colloidal crystallization, the full name regarding the famous Kirkwood statistical mechanical theory of freezing in hard spheres is actually the Kirkwood-*Monroe* theory of freezing. Elizabeth Monroe was the co-author of John Kirkwood on the 1941 paper [40], where they presented an integral equation for calculating the radial density distribution based on the local free energy at that radial coordinate. For certain parameters, the density distribution obtained was observed to be periodic, indicating a crystalline phase. Moving from theory to computer simulations, Arianna Rosenbluth and Augusta Teller were major contributors towards the development of the Metropolis algorithm. Augusta Teller wrote the initial version of the code and Arianna Rosenbluth wrote the final code for the published implementation of the widely used Markov chain Monte Carlo algorithm for early computers in order to compute equilibrium properties of statistical-mechanical systems [41]. Arianna Rosenbluth and Augusta Teller were authors, together with their husbands Marshall Rosenbluth and Edward Teller along with Nicholas Metropolis, on the highly cited 1953 paper [41] wherein Monte Carlo integration was performed over configuration space to calculate the equation of state for rigid disks, and in a later paper, for three-dimensional hard spheres [42]. Continuing on phase transition in hard-sphere systems, Berni Alder and Tom Wainwright wrote some of the earliest papers establishing molecular dynamics simulations as a time-evolution based alternative scheme to Monte Carlo simulations [2]. However, even though Alder, Wainwright, and physicists in other research institutes, knew what calculations they wanted the computers of the time to perform, none of them were able to translate them into a language that the computer could decipher. For this reason research centers which were working on computer simulations to solve statistical-mechanical problems, such as Livermore (Alder/Wainwright) and Los Alamos (Wood/Jacobson [3]), started hiring programmers specialised in machine language, many of whom were women with advanced degrees in mathematics, to do the job [43]. One such programmer working with Berni Alder was Mary Ann Mansigh Karlsen [44], who programmed the algorithms underlying the scientific papers published by the Alder group for over twenty years (her name became quite a fixed feature in the acknowledgement sections of his articles).

Now we discuss some of the simulation techniques used, with a main focus on Monte Carlo methods and phase diagram construction.

### 1.3.1 Monte Carlo methods

Monte Carlo simulations are performed to sample configurational phase space, weighted with a Boltzmann factor, in order to calculate the equilibrium properties of a system. In this thesis, we

use Monte Carlo simulations in various ensembles depending on the equilibrium properties we wish to calculate. For illustration, we discuss here the  $NVT$  ensemble.

In statistical mechanics, we study systems that are described by a *Hamiltonian*  $H$  which represents the total energy of the system. In the  $NVT$  ensemble, the number of particles  $N$ , volume  $V$  and temperature  $T$  are kept fixed. The temperature  $T$  is kept fixed by bringing the system in contact with a heat bath, which acts as a source or sink of energy, and with which the system can constantly exchange energy. In this way, the temperature is kept fixed to the temperature of the reservoir  $T$ . The partition function of this system is given by

$$Z = \frac{1}{N!h^{3N}} \int d\mathbf{r}^N d\mathbf{p}^N \exp(-\beta H(\mathbf{r}^N, \mathbf{p}^N)), \quad (1.3)$$

where  $\mathbf{r}^N$  and  $\mathbf{p}^N$  are the coordinates and momenta of the  $N$  particles,  $\beta = 1/k_B T$  with  $k_B$  the Boltzmann constant and  $h$  is the Planck constant. The average value of a measurable equilibrium property  $A$  can be obtained from

$$\langle A \rangle = \frac{\int d\mathbf{r}^N d\mathbf{p}^N A(\mathbf{r}^N, \mathbf{p}^N) \exp(-\beta H(\mathbf{r}^N, \mathbf{p}^N))}{\int d\mathbf{r}^N d\mathbf{p}^N \exp(-\beta H(\mathbf{r}^N, \mathbf{p}^N))}. \quad (1.4)$$

If property  $A$  depends only on particle coordinates, Eq. 1.4 simplifies to

$$\langle A \rangle = \frac{\int d\mathbf{r}^N A(\mathbf{r}^N) \exp(-\beta U(\mathbf{r}^N))}{\int d\mathbf{r}^N \exp(-\beta U(\mathbf{r}^N))}, \quad (1.5)$$

where  $U(\mathbf{r}^N)$  is the potential energy. As the direct evaluation of the integrals in Eq. 1.5 is mostly impossible due to the large number of configurations that need to be sampled,  $\langle A \rangle$  is determined using what is commonly referred to as the Metropolis algorithm [41].

The Metropolis algorithm utilises the fact that Eq.1.5 is equivalent to an average of  $A(\mathbf{r}^N)$  weighted according to the corresponding Boltzmann weight  $\exp(-\beta U(\mathbf{r}^N))$  of a configuration, thereby avoiding the computationally impossible sampling of all possible states. The Metropolis method corresponds in essence to an *importance sampling* of the configurations which contribute the most to the evaluation of Eq.1.5

$$\langle A \rangle = \frac{1}{M} \sum_{i=1}^M A(\mathbf{r}_i^N), \quad (1.6)$$

where  $i = 1, M$  denote configurations sampled according to the Boltzmann distribution.

However, if the weighted sampling just involved accepting or rejecting states with the Boltzmann probability, it would hardly be any better than simply selecting states at random, which is where the *Markov process* comes in for generating the right distribution of random states according to the Boltzmann probability distribution. The Markov process is based on the conditions that the probability to transition from state  $\mu$  to state  $\mu'$  should (i) not change over time and (ii) depend only on the states  $\mu$  and  $\mu'$  without any knowledge of the other states that the system has gone through. The system traverses a Markov chain of states based on the condition that, in equilibrium, the average number of accepted trial moves leaving *any* state  $\mu$  to state  $\mu'$  should be equal to the average number of accepted trial moves from state  $\mu'$  to *any* state  $\mu$ . This is called the *balance* condition [45]. However, it is convenient to impose a much

stricter condition on the algorithm - the *detailed balance* condition - where in equilibrium, the average number of accepted trial moves from state  $\mu$  to state  $\mu'$  is equal to the average number of accepted trial moves from state  $\mu'$  to state  $\mu$ :

$$p(\mu)P(\mu \rightarrow \mu')w_{\mu \rightarrow \mu'} = p(\mu')P(\mu' \rightarrow \mu)w_{\mu' \rightarrow \mu}, \quad (1.7)$$

where  $p(\mu)$  is the Boltzmann weight associated with state  $\mu$ ,  $P(\mu \rightarrow \mu')$  is the probability of performing a trial move from  $\mu$  to  $\mu'$ , and  $w_{\mu \rightarrow \mu'}$  is the probability of accepting the move from  $\mu$  to  $\mu'$ . The transition probabilities must also satisfy the constraint  $\sum_{\mu} P(\mu \rightarrow \mu') = 1$ .

In the original Metropolis scheme [41],  $P(\mu \rightarrow \mu')$  is chosen to be symmetric *i.e.*  $P(\mu \rightarrow \mu') = P(\mu' \rightarrow \mu)$ , for example a random displacement of a randomly selected particle. As the Boltzmann probability for the system to be in state  $\mu$  is proportional to  $\exp(-\beta U_{\mu})$ , the transition from state  $\mu$  to  $\mu'$  is accepted with a probability

$$\frac{w_{\mu \rightarrow \mu'}}{w_{\mu' \rightarrow \mu}} = \exp\left(-\beta(U_{\mu'} - U_{\mu})\right). \quad (1.8)$$

The Markov Chain Monte Carlo method can also be used to determine ensemble averages in other ensembles, and the acceptance probabilities change accordingly. Let us take for example the *NPT* ensemble, where the number of particles  $N$ , pressure  $P$  and temperature  $T$  are kept fixed. The configurations in the Markov chain in the *NPT* ensemble are generated through trial changes in particle displacements (as for the *NVT* ensemble) as well as changes in the volume  $V$ . Here, the transition from state  $\mu$  to  $\mu'$  is accepted with a probability  $\exp\left(-\beta(U_{\mu'} - U_{\mu}) + \beta P(V_{\mu'} - V_{\mu}) - N \ln(V_{\mu'}/V_{\mu})\right)$ .

An excellent and comprehensive description of Monte Carlo simulations in statistical physics can be found in [46], [47] and [48].

### 1.3.2 Calculating phase coexistence: Common tangent construction

We start this section by remarking that the method to calculate (Helmholtz) free energies is described in detail in various chapters of this thesis, according to the systems under investigation. In this section, we briefly describe how to construct thermodynamic phase diagrams once we have calculated the relevant free energies. We first describe the computation of phase coexistence for a single component system. Two phases  $\alpha$  and  $\gamma$  are said to be in thermodynamic equilibrium with each other if the temperature  $T$ , pressure  $P$  and chemical potential  $\mu$  in both phases are equal

$$\begin{aligned} T^{\alpha} &= T^{\gamma} \\ P^{\alpha} &= P^{\gamma} \\ \mu^{\alpha} &= \mu^{\gamma} \end{aligned} \quad (1.9)$$

The thermodynamic properties of the coexisting phases can be calculated from the above equalities, but the mathematical construct for applying these criteria varies depending on the statistical-mechanical ensemble. In the *NPT* ensemble, the chemical potential  $\mu$  is simply the Gibbs free

energy per particle  $\mu = G/N$  with  $G = F + PV$  the Gibbs free energy,  $F$  the Helmholtz free energy,  $V$  the volume and  $N$  the number of particles. Once  $G$  has been calculated at fixed  $P$  and  $T$ , the chemical potential  $\mu$  can be obtained trivially, and the pressure at which the chemical potentials in the two phases  $\alpha$  and  $\gamma$  are equal is the coexistence pressure, and the densities of the coexisting phases can be obtained from the corresponding equations of state. In the  $NVT$  ensemble, the chemical potential and pressure are defined as  $\mu = \left. \frac{\partial F}{\partial N} \right|_{V,T} = \left. \frac{\partial f}{\partial \rho} \right|_T$  and  $P = -\left. \frac{\partial F}{\partial V} \right|_{N,T} = -f + \rho \left( \left. \frac{\partial f}{\partial \rho} \right) \right|_T$ , respectively, where  $f = F/V$  denotes the free-energy density and  $\rho = N/V$  the density. The chemical potential can be obtained directly from the slope of the free-energy density versus density curve, and hence, the chemical potential equality in Eq. 1.9 yields a *common tangent* to these curves for both phases. Combining the equality of the chemical potential with the equal pressure condition at fixed  $T$  in Eq. 1.9 yields the so-called common tangent construction

$$\mu^\alpha = \mu^\gamma = \frac{f^\alpha - f^\gamma}{\rho^\alpha - \rho^\gamma} \quad (1.10)$$

Additionally, if there are multiple phase coexistences, the lowest lying tangent represents the stable coexistence. Fig. 1.1 illustrates some example stable and metastable phase coexistences. **Binary mixtures.** In case of binary mixtures of species 1 and species 2, phases  $\alpha$  and  $\gamma$  are in thermodynamic equilibrium if

$$\begin{aligned} T^\alpha &= T^\gamma \\ P^\alpha &= P^\gamma \\ \mu_1^\alpha &= \mu_1^\gamma \\ \mu_2^\alpha &= \mu_2^\gamma \end{aligned} \quad (1.11)$$

In the  $N_1N_2PT$  ensemble, the chemical potential of species 1 and 2 read

$$\begin{aligned} \mu_1(N_1, N_2, P, T) &= \left. \frac{\partial G}{\partial N_1} \right|_{N_2, P, T} = g(x) + (1-x) \left( \left. \frac{\partial g}{\partial x} \right) \right|_{N, P, T} \\ \mu_2(N_1, N_2, P, T) &= \left. \frac{\partial G}{\partial N_2} \right|_{N_1, P, T} = g(x) - x \left( \left. \frac{\partial g}{\partial x} \right) \right|_{N, P, T} \end{aligned} \quad (1.12)$$

respectively, with  $g = G/N$  and  $x = N_1/(N_1 + N_2)$  where  $N_1$  and  $N_2$  are the number of particles of species 1 and species 2 respectively, and  $N = N_1 + N_2$ . Equating the chemical potentials of both species in the two phases (Eq. 1.11) at fixed  $P$  and  $T$ , we obtain a common tangent on the composition  $x$  – Gibbs free energy per particle  $g$  plane

$$\left. \frac{\partial g}{\partial x} \right|_{x^\alpha} = \left. \frac{\partial g}{\partial x} \right|_{x^\gamma} = \frac{g^\alpha - g^\gamma}{x^\alpha - x^\gamma} \quad (1.13)$$

An illustration of the common tangent for a binary mixture on the  $g(x)$ – $x$  plane is shown in Fig. 1.2. The chemical potentials  $\mu_1$  and  $\mu_2$  of species 1 and 2 at coexistence, respectively, can be obtained directly from the y-intercepts of the common tangent, as seen from Eq. 1.12.

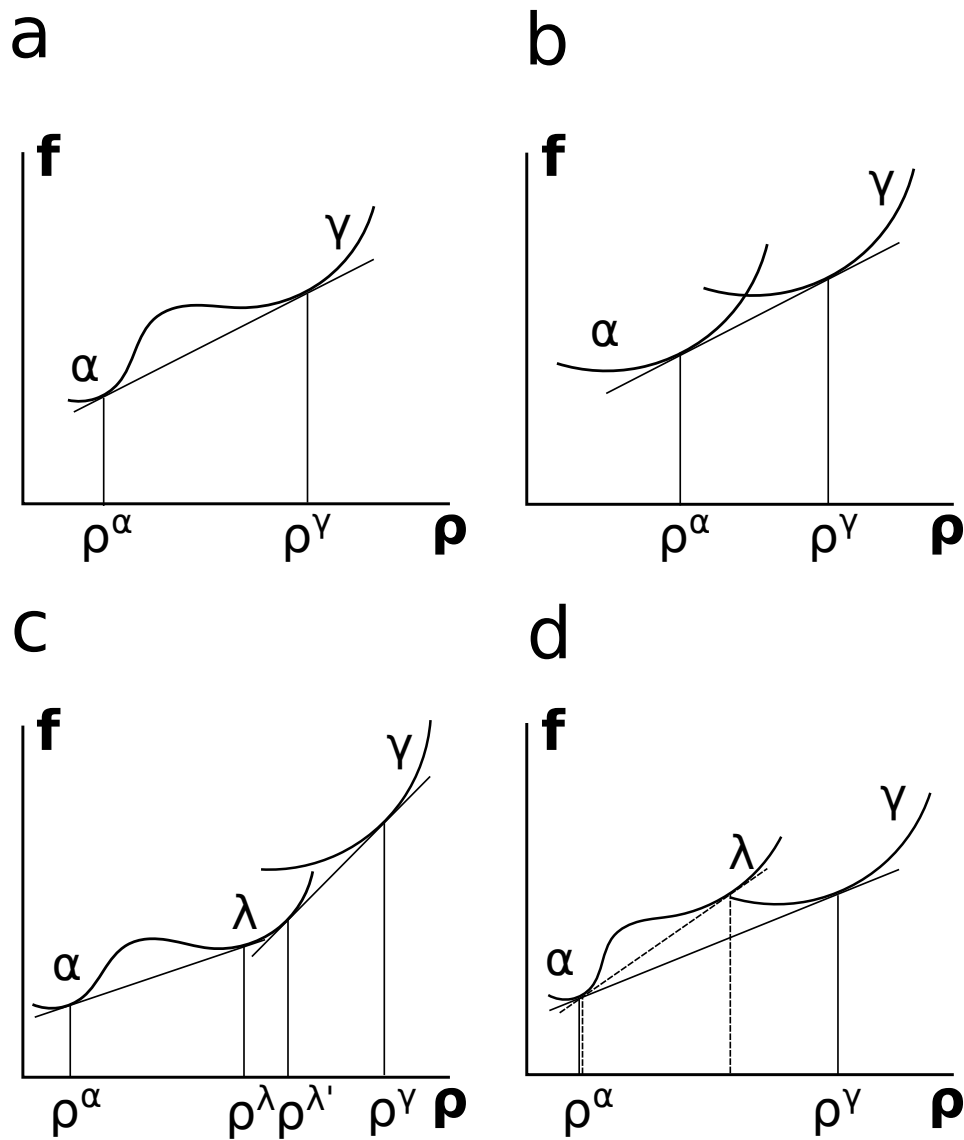


**Figure 1.1:** Schematic illustrations of common tangent construction on the Helmholtz free energy per volume  $F/V$  – density  $\rho$  plane depicting phase coexistence of phases  $\alpha$ ,  $\gamma$  and  $\lambda$  in a single-component system, and the relative stability of multiple phase coexistence regions. (a) A symmetry-unbroken coexistence (for example, low-density fluid – high-density fluid or an *isostructural* solid – solid coexistence), (b) a symmetry-broken phase coexistence (such as a fluid – solid coexistence), (c) a stable symmetry-unbroken coexistence at lower densities between phases  $\alpha$  and  $\lambda$  and a stable symmetry-broken phase coexistence at higher densities between phases  $\lambda$  and  $\gamma$ , (d) a *metastable* symmetry-unbroken coexistence between phases  $\alpha$  and  $\lambda$  (shown by a dashed common tangent) and a stable symmetry-broken coexistence between phases  $\alpha$  and  $\gamma$  (the common tangent is a solid line). The coexistence densities for the stable phase coexistences are marked.

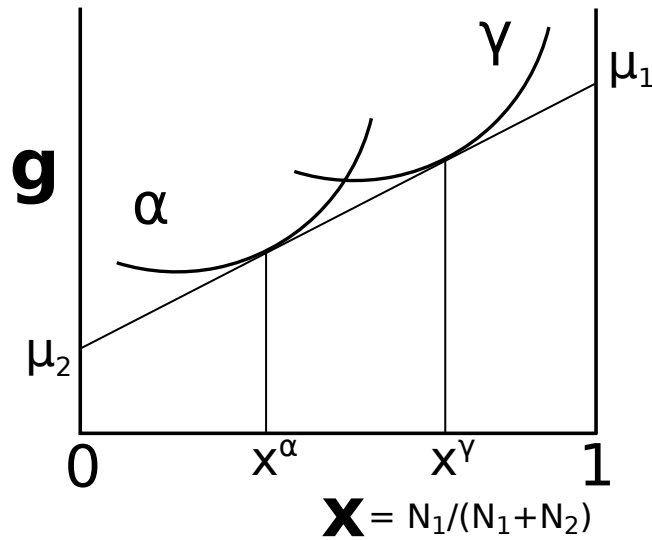


**Figure 1.2:** Schematic illustration of a common tangent construction on the Gibbs free-energy per particle  $g$  – composition  $x$  plane, depicting the symmetry-broken coexistence between phase  $\alpha$  and  $\gamma$ , for a *binary* mixture of species 1 and 2.  $x$  is the number fraction of species 1. The species chemical potentials  $\mu_1$  and  $\mu_2$  at coexistence are obtained from the y-intercepts (see Eq. 1.12). For  $x < x^\alpha$  the  $\alpha$  phase is stable,  $x > x^\gamma$  the  $\gamma$  phase is stable, for  $x^\alpha < x < x^\gamma$  there is coexistence between phase  $\alpha$  and  $\gamma$ .

## 1.4 Scope of this thesis

The objective of this thesis is to study the phase behaviour and crystallization dynamics of hard-sphere or hard-sphere-like colloids, (i) in bulk, (ii) in a gravitational field, and (iii) under spherical confinement, particularly in the context of developing colloidal crystals for photonic applications. Here, we use the term ‘bulk’ to describe an unconfined system with no external fields acting upon it. The chapters in this thesis are organised as follows.

We start off in Chapter 2 by investigating the templated growth of colloidal FCC crystals in a gravitational field. We show how nearly defect-free FCC crystals of monodisperse hard spheres can be obtained by choosing the appropriate template and sedimentation conditions. In Chapter 3, we investigate the self-assembly of the *photonic* colloidal  $\text{MgCu}_2$  Laves phase from a sedimenting binary hard-sphere mixture. In particular, we study the sedimentation phase behaviour by constructing so-called *phase stacking diagrams*, and investigate crystallization based on thermodynamic predictions using event-driven Brownian dynamics simulations. In Chapter 4, we study the phase behaviour of a binary mixture of colloidal hard spheres and freely-jointed polymer chains of hard monomer beads, using Monte Carlo simulations. The objective is to stabilize the hexagonal close packed (HCP) crystal over its free-energetically degenerate counterpart, the FCC crystal, by making use of the different void distributions in the two crystals. In Chapter 5, we investigate the role of attractions in the crystallization kinetic pathways of so-called supraparticles (particles made from particles), in direct comparison with that of hard-sphere supraparticles. Our findings emphasize the importance of accounting for attractions in nanoparticle self-assembly. In Chapter 6, we report the spontaneous nucleation of binary Laves phases (LPs) by using a purely-repulsive binary mixture. We discuss the phase behaviour, LP structure, nucleation barrier, and the kinetic glass transition for these mixtures. We also show

how our soft repulsive system is a good approximation for hard spheres from the presence of isomorphic curves on the thermodynamic phase diagram. Along these curves, the structure and dynamics, in reduced units, of thermodynamic state points are invariant, signifying an effectively one-dimensional phase diagram, a feature reminiscent of hard spheres. In Chapter 7 we show, in collaboration with experiments, how the same binary mixture, which forms Laves phases in bulk, under spherical confinement *homogeneously* nucleates into a binary icosahedral quasicrystalline structure.

The work presented in this thesis is aimed at extending our understanding of crystallization of hard-sphere-like colloidal particles, and how this can be exploited to fabricate photonic band gap materials.

---

## **Growth of defect-free colloidal hard-sphere crystals using colloidal epitaxy**

---

Using event-driven Brownian Dynamics simulations we investigate the epitaxial growth of hard-sphere crystals with a face-centered-cubic (fcc) crystal structure on the three densest cross-sectional planes of the fcc structure: i) fcc (100) ii) fcc (111) and iii) fcc (110). We observe that for high settling velocities, large fcc crystals with very few extended defects, grow on the fcc (100) template. Our results show good agreement with the experiments of Jensen *et al.*, [49], who observed such large fcc crystals upon centrifugation on an fcc (100) template. We also compare the quality of the fcc crystal formed on the fcc (111) and fcc (110) templates with that of the fcc (100) template and conclude that the latter yields the best crystal. We also briefly discuss the dynamical behaviour of stacking faults that occur in the sediments.

## 2.1 Introduction

Template assisted sedimentation, more commonly known as colloidal epitaxy is a simple and robust approach to grow single crystals of colloidal particles, a key component of next generation optoelectronic devices [50]. The ability to study the structure and dynamics of such systems in real space using confocal microscopy lends valuable information to understand the growth and defect dynamics at the atomic scale in growth of atomic semiconductor materials [51–53]. For the above stated reasons sedimentation of colloidal hard-sphere fluids has been extensively investigated by both experiments and simulations. As is well known, the hard-sphere model captures several equilibrium and non-equilibrium phenomena of condensed matter systems. Computer simulations established that the stable crystal phase of hard spheres exhibits the face-centered cubic (fcc) structure [54–56]. However, this structure is only slightly more stable than the hexagonal close-packed (hcp) crystal structure with a free-energy difference on the order of  $10^{-3}k_B T$  per particle at the melting transition point ( $k_B$  is Boltzmann’s constant and  $T$  the temperature). This small free-energy difference leads to the formation of the random-hexagonal-close-packed (rhcp) structure instead of a perfect single fcc crystal. Even though an rhcp structure restructures into the fcc crystal over long periods of time [57–59], methods to rapidly grow large colloidal crystals are highly desirable. Fabricating large defect-free single crystals, which are technologically significant, has posed severe challenges even in the simple case of hard spheres. A complete understanding of the sedimentation behaviour of hard sphere like systems would further provide clues on how to selectively grow a chosen crystal structure from a set of competing structures with similar values of free energy.

Here we briefly discuss a few experimental studies on sedimentation of such colloidal hard spheres on flat walls. Experimental realisations of the hard-sphere model are achieved by index matching a suspension of colloidal particles [12, 60]. The key factors that affect the quality of the crystalline sediment are i) the initial volume fraction  $\eta_i$  of the suspension, and ii) Péclet number  $Pe = mg\sigma/k_B T$ , where  $g$  is the gravitational acceleration,  $\sigma$  the particle diameter and  $m$  the buoyant mass of the particles. Typically in experiments,  $\eta_i$  is kept low to ensure that crystal growth is nucleated and directed by the wall. Hoogenboom *et al.* experimentally studied the sedimentation of hard-sphere-like silica colloids on a flat wall [61, 62]. For sufficiently low  $\eta_i$ , [61], they observed the formation of a predominant fcc crystal. They showed that the sedimentation flux given by  $J = \eta_i Pe$  is the key variable that determines the fraction of fcc stacked layers in the sediment. In the regime of very low particle flux, the crystallizing layers have sufficient time to equilibrate and the fraction of fcc stacked layers is large, whereas predominantly randomly stacked hexagonal layers are found if  $J$  is high [55, 61, 63, 64]. In density matched hard-sphere suspensions or under microgravity conditions [65, 66], typically the rhcp structure is observed. Therefore the predominant presence of fcc domains in the slowly grown samples of the sediment is surprising. As noted earlier, the difference in free energies between the fcc and hcp structures is very small, however fcc is the stable structure. Pronk and Frenkel [57] calculated the fcc-hcp interfacial free energy and used it to estimate the time that it takes to form a pure fcc crystal from the randomly stacked phase. They estimated that the healing of stacking faults in micrometer sized hard-sphere crystallites occurs on the time scale of days. The slow growth rates together with the slightly low free energy of the fcc structure might have tipped the balance towards fcc in the experiments of Hoogenboom *et al.* [61]. It is also possible that in the presence of a gravity field the fcc structure is more stable than in bulk,

or that the dynamic pathways of crystallization under gravity could lead predominantly to the formation of fcc domains. Another explanation for this observation was provided by Hillhorst *et al.* [67]. Using confocal microscopy, they showed that these fcc domains often contained slanted stacking faults, which are two subsequent hcp stacked layers that run along the  $(\bar{1}11)$ ,  $(1\bar{1}1)$ , or  $(11\bar{1})$  planes. They speculated that these faults direct the formation of the fcc crystal domains.

Using computer simulations, Marechal *et al.* [68] studied the crystallization dynamics of hard spheres sedimenting on a flat wall. Note that in these simulations and in our work, the role of the solvent is taken into account through the Brownian noise, and hydrodynamic effects are not treated rigorously. Nevertheless, their simulations showed that slow sedimentation favours the growth of fcc crystals over rhcp crystals, for low initial volume fractions, similar to the experimental findings of Hoogenboom *et al.* [61]. Furthermore they showed that quality of the formed fcc crystal depends on the combined effect of initial volume fraction and Péclet number just as shown by Hoogenboom *et al.* A good quality fcc crystal is a single crystal which is not divided into different crystalline domains and contains very few defects. They attributed the formation of predominantly fcc-like domains to the free-energy difference between fcc and hcp and not to the slanted stacking faults found in the fcc regions.

The introduction of patterned templates in place of a flat wall, together with a slow deposition rate has been shown to direct layer by layer growth of the crystal with very few defects [49, 69–73]. The template can often drastically reduce the metastability of the crystallizing fluid [74]. One of the first noteworthy studies on colloidal epitaxy is that of van Blaaderen *et al.* [69]. They demonstrated experimentally that under slow sedimentation, templates can be used to effectively grow large defect-free crystals and control the lattice spacing and orientation of the resulting crystals. They also found that sedimenting hard spheres on an isotropically deformed hcp (1100) template resulted in the epitaxial growth of a perfect hcp crystal [72, 73].

In the case of flat walls, slow sedimentation rates are preferred to avoid amorphization of the sediment [75], but how the scenario changes when the crystal is grown epitaxially remained unexplored until recently. Jensen *et al.* looked at the sedimentation of hard-sphere-like fluids for a wide range of sedimentation velocities on flat walls, fcc (100), fcc (111) and the fcc (110) template [49]. They showed that large defect-free fcc colloidal crystals can be grown by centrifuging at surprisingly high speeds of up to 3000g onto a (100) oriented fcc (square) template. These findings are particularly attractive as they describe a way to rapidly grow fcc crystals with only a few extended defects, as large time scales of slow sedimentation are undesirable. Their findings also raise interesting questions on the growth mechanism and the dynamics of defects, if any, that occur in crystals grown at very large sedimentation velocities. They observed that this was unique to the fcc (100) template and noted that the absence of stacking degeneracy might be the cause.

Motivated by these experiments, we present in this Chapter a computer simulation study of the crystallization dynamics of hard-sphere fluids under an applied gravitational field in the presence of three different crystalline templates. Using a series of order parameters as described by Marechal *et al.* [68], we characterise the sediment and identify optimal conditions for the growth of large defect-free fcc crystals. This Chapter is organised as follows. In Section 2.2, we describe the simulation methods, including the event-driven Brownian Dynamics (EDBD) simulations and the order parameters that we use. We present our results in Section 4.3. We first discuss our simulation results for an fcc (100) template, which gives by far the best quality

fcc crystals even at high sedimentation velocities. We then discuss sedimentation on different templates and end with some conclusions in Section 2.4.

## 2.2 Simulation methods

### 2.2.1 Systems studied

We use EDBD simulations [76, 77] in the  $NVT$  ensemble to simulate a system of  $N$  hard spheres with diameter  $\sigma$  in a volume  $V$  subject to a gravitational field. The method consists of computing a sequence of collision events that involves only two particles at any instant. During the simulation stochastic adjustments of the particle velocities are periodically made at an interval of  $\Delta t$  according to

$$\mathbf{v}_f(t = s\Delta t) = \alpha_t \mathbf{v}_0(t) + \beta_t \mathbf{v}_R(t), \quad (2.1)$$

where  $\mathbf{v}_0(t)$  ( $\mathbf{v}_f(t)$ ) is the velocity of the particle before (after) the stochastic adjustment or thermalization,  $s$  is an integer,  $\mathbf{v}_R(t)$  a 3D Gaussian variable with mean 0 and variance  $k_B T/m$  with  $m$  the mass of the particle,  $k_B$  the Boltzmann constant, and  $T$  the temperature. We set  $\alpha_t = 1/\sqrt{2}$  with a probability  $\nu \Delta t$  and 1 otherwise. We set  $\beta_t = \sqrt{1 - \alpha_t^2}$  in order to keep the temperature constant. Following Ref. [68], we set  $\nu = 10\tau_{MD}^{-1}$  and  $\Delta t = 0.01 \tau_{MD}$  in all our simulations, where  $\tau_{MD} = \sqrt{m/k_B T} \sigma$  is the time unit of an event-driven MD simulation. The details of the EDBD simulations are elaborately described in Refs. [68, 77].

The spheres are confined between a template (or a smooth wall) at  $z = 0$  and another smooth wall at  $z = H$ . The height  $H$  of the column is chosen such that the density of the colloids at the top of the sedimentation column is almost negligible when sedimentation-diffusion equilibrium is reached. The template particles are not fixed but carry a reduced weight 1000 times that of the sedimenting particles. Therefore their positions remain unaltered and the structure of the template remains fixed during the course of the simulation. We perform simulations for a system size of  $N = 100,000$  particles with the cross-sectional area of the simulation box fixed at  $\simeq 50\sigma \times 50\sigma$ . The simulation box is periodic in the  $x$  and  $y$  directions. The gravitational field is oriented along the  $z$ -direction, and the colloids experience an external potential  $\phi(z) = mgz$  with  $g$  the gravitational acceleration and  $z$  the vertical coordinate of the colloid. The parameter that describes the effect of the gravity field on the particles is the ‘‘gravitational length’’ given as  $l_g = k_B T/mg$ . It is a measure of the length scale over which the effect of gravity manifests [78]. Another dimensionless parameter of interest is the gravitational Péclet number,  $Pe = mg\sigma/k_B T$ . As we keep  $\sigma$  fixed in our simulations, a change in the value of  $Pe$  changes the gravitational length.

In this work we simulate sedimentation on three different templates for  $Pe = 0.5, 1, 2, 3, 4, 5$  and  $10$ . The higher the Péclet number, the faster is the sedimentation and the shorter the time available for the particles to rearrange and equilibrate. As already mentioned in the introduction, another relevant parameter for sedimentation is the initial volume fraction  $\eta_i$  of the suspension. We perform simulations with an initial volume fractions  $\eta_i = 0.01, 0.02$  and  $0.104$ . The figures that we present below correspond to simulations using an initial volume fraction  $\eta_i = 0.02$ , unless otherwise stated. The initial configurations of our simulations are homogeneous fluid phases of non-overlapping hard spheres which fill the entire sedimentation column.

## 2.2.2 Order parameters

In this section we briefly describe the order parameters, as described by Marechal *et al.* [68], that we use to identify the differently arranged fcc and hcp structures in the sediment. The fcc and hcp crystal structures differ from each other by the stacking sequence of the hexagonal layers formed by the particles. To determine if a particle is solid-like we estimate its local symmetry by using bond orientational order parameters. The un-normalised 3D bond order parameter for particle  $i$  is defined as

$$q_{l,m}^{(u)}(i) = \frac{1}{N_{nb}(i)} \sum_{j=1}^{N_{nb}(i)} Y_{l,m}(\theta_{i,j}, \phi_{i,j}), \quad (2.2)$$

where  $N_{nb}(i)$  denotes the number of neighbours of particle  $i$ ,  $\theta_{i,j}$  and  $\phi_{i,j}$  are the polar and azimuthal angles, respectively, of the center-of-mass distance vector  $\mathbf{r}_{ij} = \mathbf{r}_j - \mathbf{r}_i$  with  $\mathbf{r}_i$  the position of particle  $i$ .  $Y_{l,m}(\theta, \phi)$  are the spherical harmonics for  $m$  ranging from  $[-l, l]$ . The summation runs over all neighbouring particles  $j$ , which we define as the particles that lie within a center-of-mass distance of  $1.3\sigma$  with respect to  $i$ . The normalised bond order parameter is defined as

$$q_{l,m}(i) = \frac{q_{l,m}^{(u)}(i)}{\left(\sum_{m=-l}^l |q_{l,m}^{(u)}(i)|^2\right)^{1/2}}. \quad (2.3)$$

A neighbour  $j$  of particle  $i$  forms a solid-like bond with  $i$  if  $d_l(i, j) > d_c$  with

$$d_l(i, j) = \sum_{m=-l}^l q_{l,m}(i) q_{l,m}^*(j). \quad (2.4)$$

Solid-like or crystalline particles are defined as particles for which the number of solid-like bonds  $n_{con}(i)$  is greater than a critical value  $n_c$  [79]. The symmetry index in the above equations is chosen as  $l = 6$ . Following Marechal *et al.* [68] we set the cut-off values defined above as  $n_c = 4$  and  $d_c = 0.7$ .

Upon identifying solid-like particles we then identify its crystal structure. The fcc (111) and hcp crystals are composed of stacked hexagonal layers. Therefore we use two-dimensional bond order parameters to quantify the hexagonal symmetry of the layers. For a particle  $i$ , this is given by

$$\psi_m^S(i) = \frac{1}{N_s(i)} \sum_{j=1}^{N_s(i)} \exp(mi\phi_{ij}), \quad (2.5)$$

where the sum over  $j$  runs over the  $N_s(i)$  neighbours in environment  $S$  of particle  $i$  and  $\phi_{ij}$  denotes the angle between the projection of  $\mathbf{r}_{ij}$  on the  $x - y$  plane and the  $x$ -axis. The  $x - y$  plane is defined as the plane parallel to the template (perpendicular to gravity). Because of the in-plane hexagonal order of these two crystals, we chose the symmetry index to be  $m = 6$ .

The difference between the fcc (111) and hcp crystal structures is the stacking sequence of hexagonal layers. While fcc (111) shows ABC..ABC stacking of layers, the stacking sequence in an hcp structure is ABA..BAB. Thus, after confirming the hexagonal symmetry of the layers, the next step is to calculate a ‘‘stacking parameter’’  $\alpha$  that distinguishes the two different kinds

**Table 2.1:** Bond order parameters and corresponding threshold values for identifying fcc and hcp structures

Type of structure	Conditions on particle $i$
Crystalline	$n_{con}(i) > 4$
fcc (100)	$n_{con}(i) > 4, \psi_6^0(i) < 0.7, \psi_4(i) > 0.5$
fcc (111)	$n_{con}(i) > 4, \psi_6^0(i) > 0.7, \psi_6^{surr}(i) > 0.5, \alpha(i) > 0.5$
hcp	$n_{con}(i) > 4, \psi_6^0(i) > 0.7, \psi_6^{surr}(i) > 0.5, \alpha(i) < 0.5$

of stacking. To determine the stacking parameter  $\alpha_i$  for a given particle  $i$ , we look at three different environments of a particle  $i$ .

The environment  $S = 1$  corresponds to the neighbours  $j$  in the layer above particle  $i$  as defined by  $0.55\sigma < (z_j - z_i) < 1.2\sigma$  and  $r_{ij} = |\mathbf{r}_{ij}| \leq 0.95\sigma$ . The environment  $S = -1$  comprises of particles that are the neighbours  $j$  in the layer below particle  $i$  for which  $-1.2\sigma < (z_j - z_i) < -0.55\sigma$  and  $r_{ij} \leq 0.95\sigma$ , and for environment  $S = 0$  the neighbours lie in the same layer defined by  $|z_j - z_i| < 0.5\sigma$  and  $r_{ij} \leq 1.3\sigma$ . The environment of a solid-like particle  $i$  is hexagonally ordered in the same layer if  $|\psi_6^0(i)| > 0.7$ . The stacking can only be defined if the layer above and below particle  $i$  are also hexagonally ordered and are part of the same crystalline domain: i.e.  $\psi_6^{surr}(i) \equiv |\psi_6^1(i) + \psi_6^{-1}(i)| > 0.5$ .

Once the hexagonal order of the domain is ascertained, the stacking can be determined using the trigonal bond order parameter, which for a perfect fcc is  $\psi_3^{fcc}(i) = \frac{1}{2}|\psi_3^1(i) - \psi_3^{-1}(i)| = 1$ , while for a perfect hcp,  $\psi_3^{hcp}(i) = \frac{1}{2}|\psi_3^1(i) + \psi_3^{-1}(i)| = 1$ . The stacking parameter  $\alpha$  is then defined as the fraction of fcc stacked particles i.e.  $\alpha = \psi_3^{fcc} / (\psi_3^{fcc} + \psi_3^{hcp})$ . Note that when the averaged value of  $\alpha$  over all hexagonally ordered particles is 0.5, it signifies perfectly random packing.

The other crystal structure that we characterise in this work is the cubic fcc (100). In this case the layers that are stacked parallel to the  $x - y$  plane exhibit square symmetry. Therefore to characterise the order within each layer in the  $z$ -direction, we compute the two dimensional bond order parameter  $\psi_4^0(i)$  given by equation 2.5 with the symmetry index  $m = 4$ .

We list the bond order parameters that we used and the respective threshold values to distinguish the various crystal structures in Table 2.1. Particles which are crystalline in nature and are not identified as fcc (100), fcc (111) and hcp crystal structures also appear in the sediment as discussed in Section III. These are observed to either belong to a stacking fault or some other crystal structure which has not been analysed in this study. Such particles are termed as defects in the subsequent sections, and coloured in lilac. In addition, to assess the quality of a crystalline sediment we estimate the fraction of fcc particles  $\phi_{fcc} = N_{fcc}/N_{cr}$  with  $N_{fcc}$  being the number of particles that are fcc-like and  $N_{cr}$  being the number of particles that are identified as solid-like.

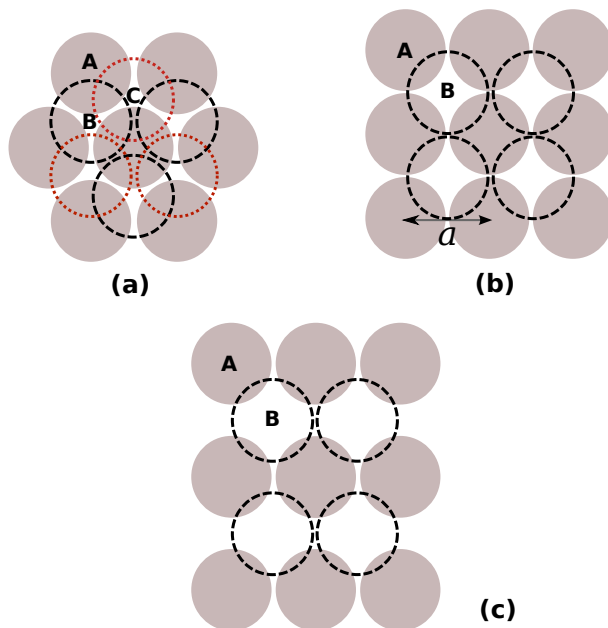


**Figure 2.1:** Stacking degeneracy on different fcc templates. (a) Hexagonal fcc (111) template, (b) Square fcc (100) template, (c) fcc (110) template. “A” (drawn as filled circles) represents the first layer of particles. “B” and “C”, shown as black and red dashed hollow circles, respectively, in (a), are the two degenerate stacking positions for the second layer of particles. For (b) and (c), “B” shown as black dashed circles represents the second layer of particles on top of layer A.  $a$  is the lattice spacing of the square template.

## 2.3 Results and Discussion

As mentioned in the introduction we study the epitaxial growth of the hard-sphere fcc crystal on three different templates. The (100), (111) and (110) cross-sectional planes of the fcc structure are the obvious choices for simple patterning because they represent the three densest cross-sectional planes of the fcc crystal. The hexagonal template in Fig. 2.1(a) is the densest possible packing of particles on the template and is the (111) cross-section of the fcc crystal. There are two ways in which the next layer of spheres can sit on this pattern (labelled as B and C in Fig. 2.1(a)), both of which are energetically degenerate. Therefore the stacking sequence of the hexagonal layers is likely to be random. The fcc (110) template shown in Fig. 2.1(c) does not show this stacking degeneracy but is the least dense of all three templates. Being the closest packed template which does not show stacking degeneracy, the square fcc (100) template in Fig. 2.1(b) is therefore the most promising template for growing large fcc crystals.

### 2.3.1 Sedimentation on the fcc (100) template

Therefore we first present the results on sedimentation of hard spheres on the (100) plane of a close-packed fcc crystal, for varying Péclet numbers ( $Pe$ ) and initial volume fraction ( $\eta_i$ ). First, we show visualizations of the final configurations of the sediment for (i)  $\eta_i = 0.02$ ,  $Pe = 2$  (Fig. 2.2(a)) and (ii)  $\eta_i = 0.02$ ,  $Pe = 10$  (Fig. 2.2(d)). The time taken for the sediment to crystallize and equilibrate is inversely related to the Péclet number. The snapshots of the final

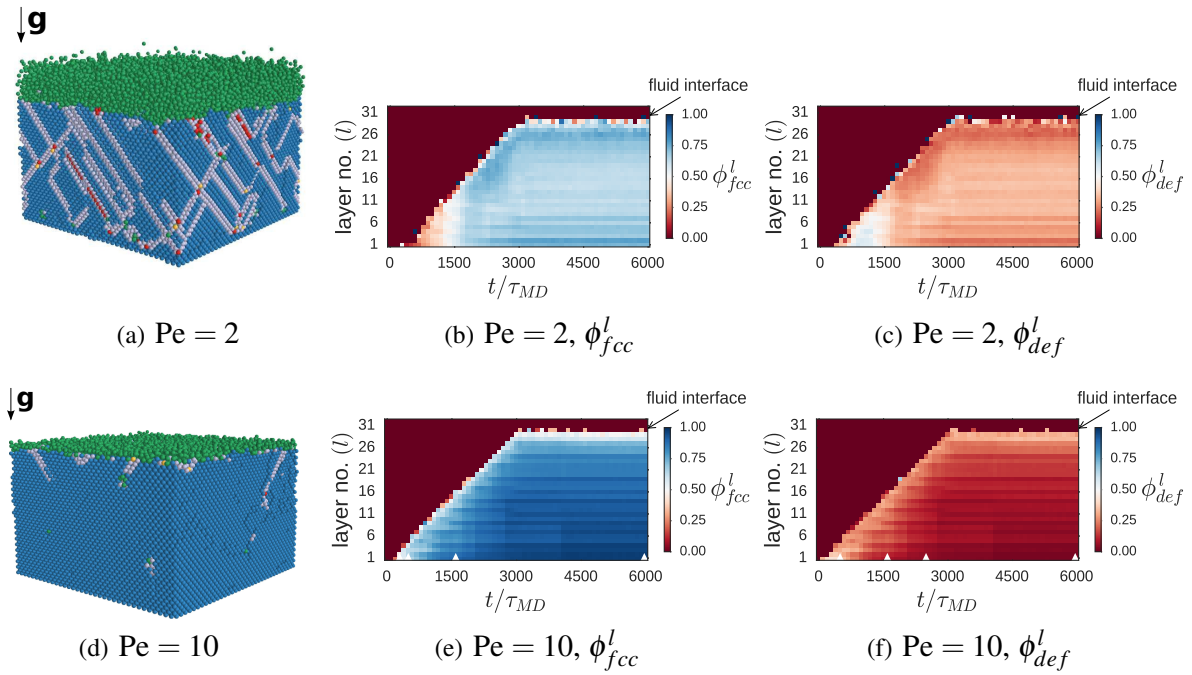


**Figure 2.2:** (a) and (d) Side view of the final configurations at  $t/\tau_{MD} = 6000$  of hard spheres sedimenting on an fcc (100) template with lattice spacing  $a = 1.004\sigma$  for  $Pe = 2$  and 10, respectively. The spheres in the snapshots are coloured as follows: red fcc (111), yellow hcp, blue fcc (100), lilac stacking fault or another crystal structure, green disordered. (b) and (e) Fraction of fcc particles  $\phi_{fcc}^l$  as denoted by the colour bar, calculated over the total number of crystalline particles in each layer, showing the crystallization of each layer with time. (c) and (f) Fraction of particles belonging to a fault/defect  $\phi_{def}^l$  as denoted by the colour bar, calculated over the total number of crystalline particles in each layer, plotted for each layer over time. The dark red region to the left of the four plots represents absence of crystalline particles in the layer i.e. a fluid layer. The initial packing fraction  $\eta_i = 0.02$ .

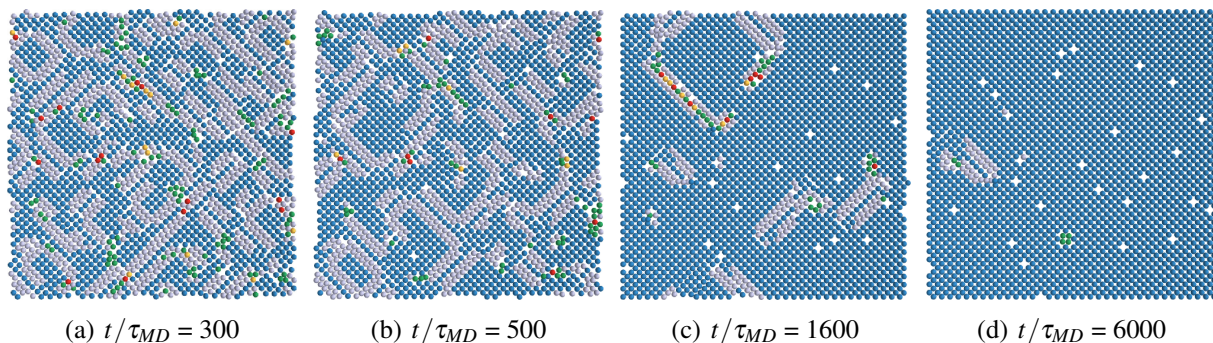


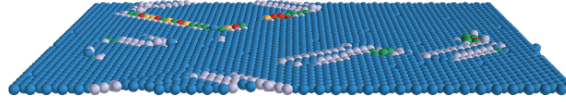
**Figure 2.3:** Typical configurations of the top view of the first layer of the crystalline sediment for different times as labeled for hard spheres sedimenting on a close-packed fcc (100) template at  $Pe = 10$ . The colour code is the same as in Fig. 2.2.

configurations presented in Figs. 2.2, 2.6 and 2.8 are taken at a time which is well after  $\phi_{fcc}$  has equilibrated with respect to simulation time. The colour of a particle in Fig. 2.2 indicates if it belongs to an fcc or an hcp crystalline domain, based on the criteria listed in section II. Lilac-coloured particles in the snapshots indicate defects and we observe from the snapshots (Figs. 2.2(a) and 2.2(d)) that the crystalline sediment is less defective for higher settling speeds i.e. higher  $Pe$ . This observation, which agrees very well with experiments [49], is surprising because at high  $Pe$  there is less time available to the particles to equilibrate. At the growth front, the particles of the layer that crystallizes appear to precisely sit on the holes (possible lattice positions) left by the previous layer of particles even under rapid sedimentation.

Next we take a closer look at the dynamics of the sedimentation process. In Figs. 2.2(b), (c), (e), and (f), we show the time evolution of each layer of the sediment for both  $Pe = 2$  and  $Pe = 10$ . The horizontal axis denotes the time scale  $t/\tau_{MD}$  and the vertical axis indicates a layer  $l$  of the sediment. We colour the plots according to the values of  $\phi_{fcc}^l$  or  $\phi_{def}^l$ , which we define as follows.  $\phi_{fcc}^l(l, t/\tau_{MD})$  is the fraction of similarly oriented fcc particles over the total number of crystalline particles in each layer of the sediment. Similarly,  $\phi_{def}^l(l, t/\tau_{MD})$  denotes the number of solid-like particles that are neither strictly fcc- or hcp-like divided by the total number of crystalline particles in each layer. One can read the evolution of the crystallinity of a layer in time from such a plot by following the horizontal time axis for that layer. Similarly, one may also examine the crystalline nature of the entire sediment at a fixed instant of time by following the positive vertical axis from the bottom of the sediment to the top.

Based on Figs. 2.2(b) and (e), we make the following observations. The dark red regions to the top left of the plots correspond to disordered or fluid-like particles in the sediment. We clearly observe that the dark red region at the top shrinks with time as progressively more layers crystallize in the sediment. A deep blue region indicates a high fraction of fcc particles. Clearly, the crystal grown at  $Pe = 10$  has a much higher fcc composition than the one for  $Pe = 2$ . The fraction of fcc in each layer increases as we go down the sediment for  $Pe = 10$ .

Moreover from Figs. 2.2(c) and (f), we observe that the sediment for  $Pe = 10$  has far fewer defects than the one for  $Pe = 2$ . The nearly uniform light red colour in Fig. 2.2(c) across the layers for the  $Pe = 2$  case indicates the presence of a number of extended defects across layers, which do not anneal out in the simulation times studied. In contrast in Fig. 2.2(f), the deepening

(a)  $t/\tau_{MD} = 1600$ , side view, cropped(b)  $t/\tau_{MD} = 1600$ , tilted side view

**Figure 2.4:** Side view (a) and tilted side view (b) of layer 1 at  $t/\tau_{MD} = 1600$  to show more clearly the stacking faults. The colour code is the same as in Fig. 2.2.

red colour (indicating a decrease in  $\phi_{def}^l$ ) from the top to the bottom layer for  $Pe = 10$  represents few extended defects and progressively fewer stacking faults as we go down the sediment. If we follow the evolution of each layer in time, we can observe that there are further rearrangements of defects in the layers to form similarly oriented fcc particles.

For the  $Pe = 10$  case, from the very beginning, the layers crystallize rapidly into fcc particles, with the result that in a short amount of time a high fraction of fcc particles is formed. The crystalline sediment shows a linear growth front in time indicating that crystallization proceeds in a layer-wise manner. As earlier described by Heni *et al.*, [80] the mechanism behind the layer-by-layer growth of a crystal on a patterned template [62, 64, 81–83] originates from the fact that the crystallised  $(n - 1)^{th}$  layer serves as a template for the  $n^{th}$  layer leading to its subsequent crystallisation. As the settling particles crystallize in a layer, some particles are stacked a little differently, at slightly higher positions than their neighbours in that layer. This may lead to a local stacking fault.

Next we discuss the birth of these local stacking faults in the crystallizing layers and how they behave over time. In Figs. 2.3(a)-(d) we present different snapshots in time of the first layer that is formed on top of the template for Péclet number  $Pe = 10$ . In the initial stages of crystallization, we observe numerous stacking faults as coloured in lilac in Fig. 2.3. The stacking faults are formed when a crystalline domain, in which the particles are four-fold hollow-site stacked, is next to a domain where the particles are bridge-site stacked on the template. A hollow-site refers to a hole left by the particles of a layer and is therefore a lattice site for a particle in the next layer to sit. For a square template, the hollow-sites would have four-fold symmetry. A hollow-site stacked particle is therefore a perfectly stacked particle as regards to forming a perfect fcc crystal. A bridge-site is located anywhere on the line connecting two in-plane particles (lattice sites) of a layer. Therefore, bridge-site stacked particles have to be slightly out of plane with respect to the particles in a layer but not exactly in the layer above. The bridge-site stacked particles are therefore at a higher height than the hollow-site stacked particles as shown in Figs. 2.4(a) and (b). In the course of the sedimentation, the bridge-site stacked particles will be pushed towards the hollow-site positions by the weight of the particles that settle upon these particles, in order to minimise the gravitational potential energy. Here it

is important to note that in case of flat walls, typically slow sedimentation rates are preferred to grow good crystals because there is more equilibration time available for particles to diffuse in-plane and therefore for defects to rearrange [75]. However, for the close-packed fcc (100) template at high  $Pe$  ( $= 10$ ), there is negligible time for in-plane diffusion of particles and the annealing of defects in the layer is mainly governed by the gravitational pressure acting on the particles from the layers above. In this way the stacking faults anneal out fairly quickly, hereby leaving behind point vacancies in the crystalline layers. These point vacancies appear to be very persistent as they are in-plane with the layer and hard to anneal out when the next crystalline layer is already formed. It is worth noting that the confocal images of the crystalline layers in the colloidal crystals grown by centrifugation onto a (100) template at  $3000g$  also show numerous point vacancies, which is remarkably consistent with our observations here [49]. The simulation time that corresponds to the images in Figs. 2.3(a)-(d) are marked in Fig. 2.2(e) and (f) by white triangles. We also looked at the evolution of layers 4 and 10 (not shown here) in our sediment and the behaviour of the stacking faults is qualitatively similar with the dynamics of those in the first layer. As expected, there are more faults in the tenth layer which is higher up in the sediment because the lower the pressure these defects feel from the layers above, the more difficult it is for these defects to rearrange. To illustrate this, we plot in Fig. 5 the fraction of crystalline defects  $\phi_{def}^l$  in a layer  $l$  as a function of the gravitational pressure ( $\beta P \sigma^3(l)$ ) on that layer for a well-equilibrated sediment at  $t/\tau_{MD} = 6000$ . We determine  $\beta P \sigma^3(l)$  by integrating the density profile of the hard spheres along the sedimentation column [84]. We clearly observe that  $\phi_{def}^l$  decreases monotonically with increasing pressure.

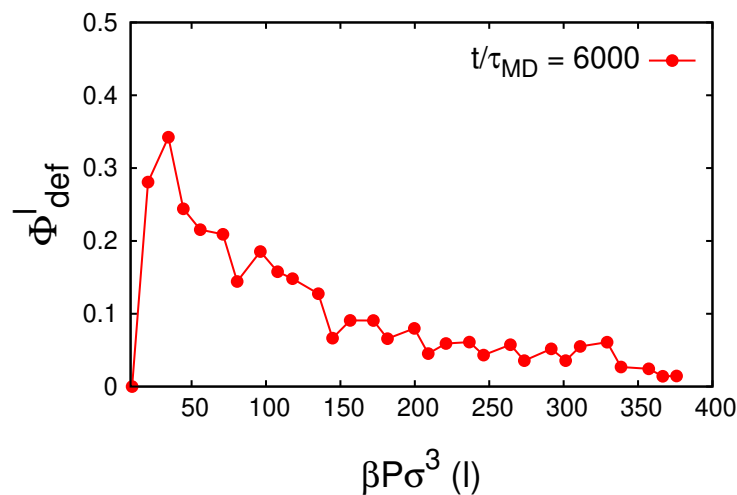


**Figure 2.5:** The fraction of crystalline defects  $\phi_{def}^l$  in each layer  $l$  as a function of the gravitational pressure at that layer for a well-equilibrated sediment at  $t/\tau_{MD} = 6000$  on a  $1.004\sigma$  fcc (100) template and  $Pe = 10$ .

Our results for the fcc (100) template show very good agreement with Jensen *et al.* [49] who obtained single fcc crystals up to the top of the sediment by applying fields between  $15g$  to  $3000g$  *via* centrifugation. These single crystals are not broken up into smaller crystallites and contain few extended defects. Our simulation results also show that for the fcc (100) template, the higher the Péclet number i.e. the faster the particles settle, the less defective the crystal (compare Figs. 2.2(a) and (d)). This is surprising as it contrasts the results of sedimentation

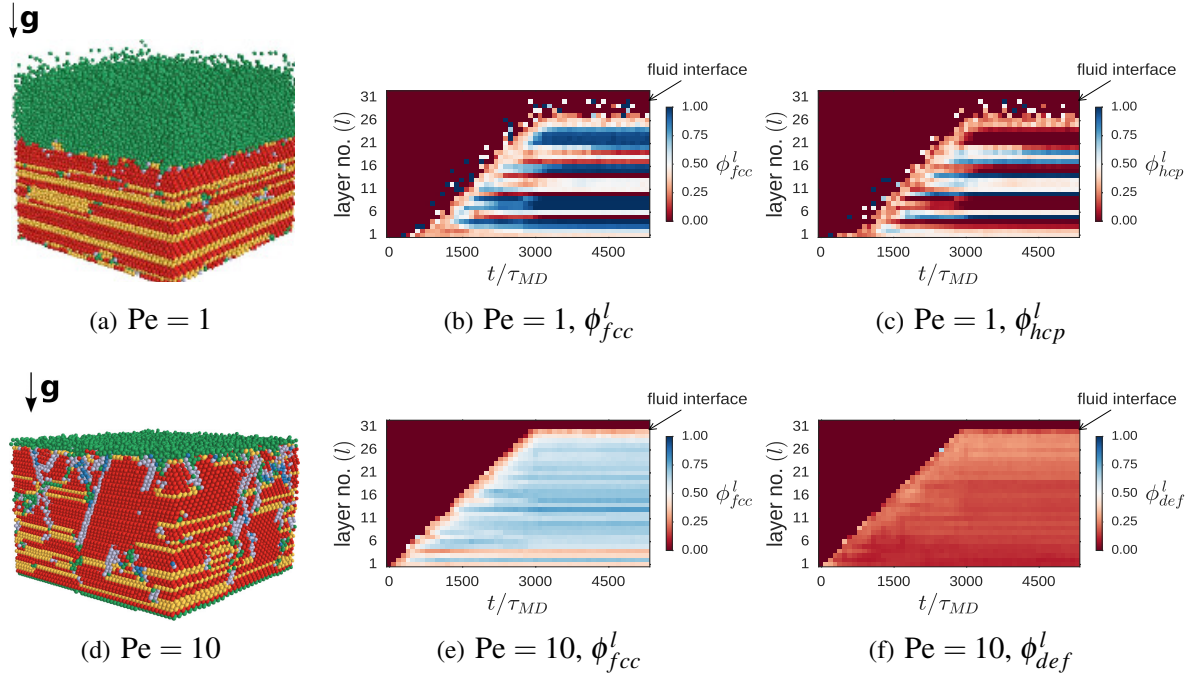


**Figure 2.6:** (a) and (d) Side view of the final configurations at  $t/\tau_{MD} = 5300$  of hard spheres sedimenting on an fcc (111) template with lattice spacing  $a = 1.004\sigma$  for  $Pe = 1$  and 10 as labeled. The colour code is the same as that in Fig. 2.2. (b) and (e) Fraction of fcc particles  $\phi_{fcc}^l$  represented by a colourbar showing the fcc-crystallization of each layer with time. (c) Fraction of hcp particles  $\phi_{hcp}^l$  represented by a colourbar showing the hcp-crystallization of each layer with time. (f) Fraction of particles belonging to a fault/defect  $\phi_{def}^l$  as indicated by a colourbar, for  $Pe = 10$ , plotted for each layer over time. The metrics of (b) and (c) are intentionally chosen differently from (e) and (f) to demonstrate random stacking of hexagonal layers at low  $Pe$ . The dark red region to the left of the four plots discussed above represents absence of crystalline particles in the layer, i.e. a fluid layer. The initial packing fraction  $\eta_i = 0.02$ .

on a flat wall, where predominantly fcc-stacked crystals are observed only at sufficiently slow sedimentation rates [61, 68], and where disorder sets in at high  $Pe$ .

### 2.3.2 Comparison with the flat wall, fcc (111) and fcc (110) templates

Next we investigate the structure of the crystalline sediment using different cross-sectional planes of the close-packed fcc crystal as a template i.e. the (i) fcc (111), (ii) fcc (110) crystal planes as well as a (iii) flat wall for comparison.

The hexagonal fcc (111) template is the densest plane of the fcc crystal and one can expect that this might help direct the settling particles to the right lattice positions. However for this template, there are two lattice sites on which the next layer of particles can sit as shown in Fig. 2.1(a) giving rise to stacking degeneracy. We focus first on slow sedimentation rates, or the near-equilibrium growth regime ( $Pe = 1$ ), where the crystallizing particles get sufficient time to rearrange within the crystallizing layer to form a hexagonal layer with little or no defects. As mentioned earlier in the introduction, stacking degeneracy for this template must result in a random stacking of hexagonal layers (rhcp) and this is what we observe. In Fig. 2.6(a) we show

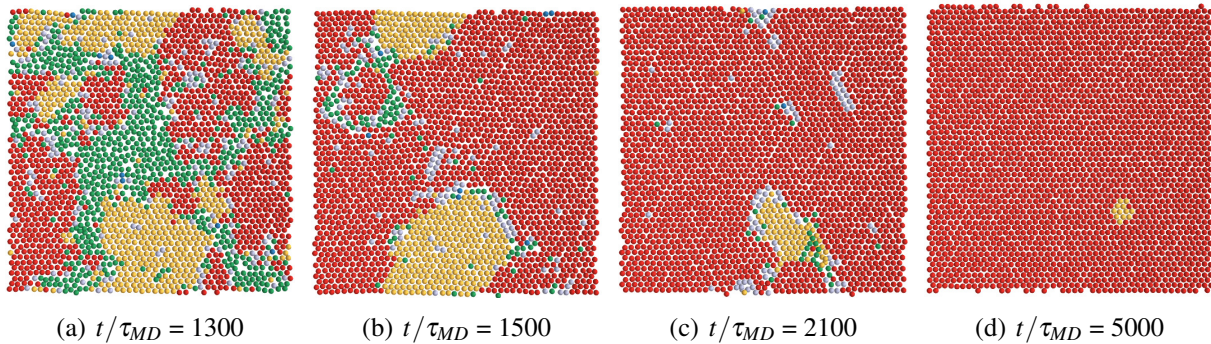


**Figure 2.7:** Typical configurations of the top view of the fourth layer of the crystalline sediment for different times as labeled for hard spheres sedimenting on a close-packed fcc (111) template at  $Pe = 1$ . The colour code is the same as in Fig. 2.2.

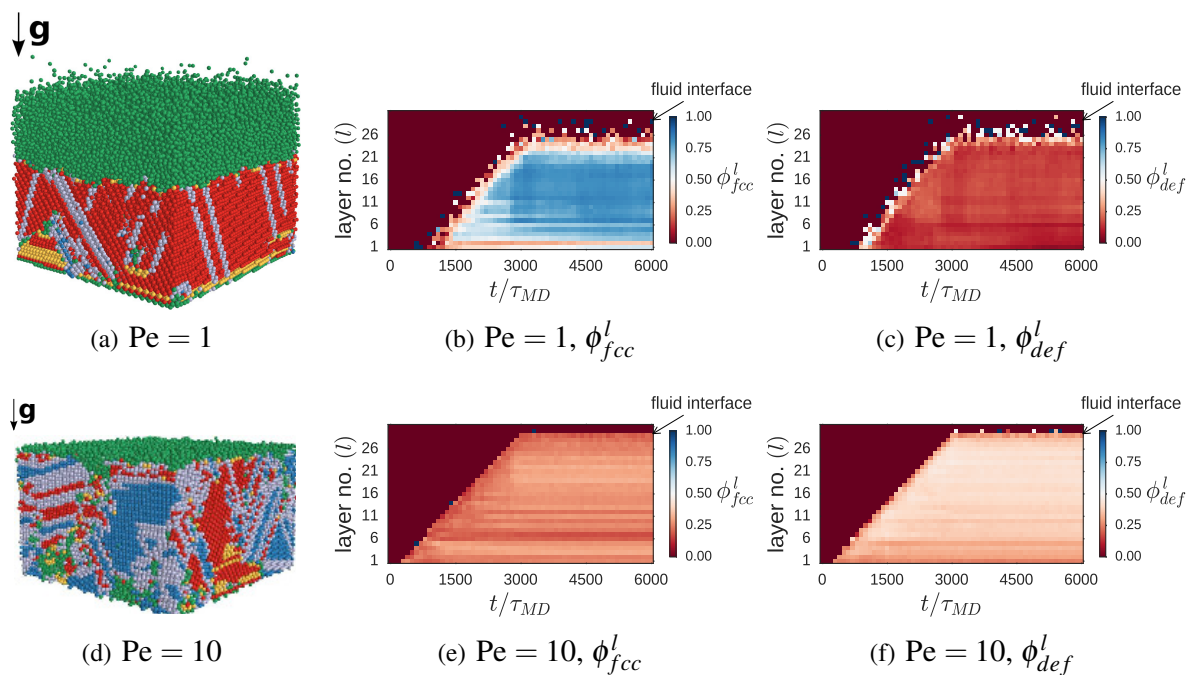


**Figure 2.8:** (a) and (d) Side view of the final configurations at  $t/\tau_{MD} = 6000$  of hard spheres sedimenting on an fcc (110) template with lattice spacing  $a = 1.004\sigma$  for  $Pe = 1$  and  $10$  as labeled. The colour code is the same as that in Fig. 2.2. (b) and (e) Fraction of fcc particles  $\phi_{fcc}^l$  represented by a colourbar showing the crystallization of each layer with time. (c) and (f) Fraction of particles  $\phi_{def}^l$ , again indicated by a colourbar, belonging to a fault/defect plotted for each layer over time. The dark red region to the left of the four plots discussed above represents absence of crystalline particles in the layer, i.e. a fluid layer. The initial packing fraction  $\eta_i = 0.02$ .

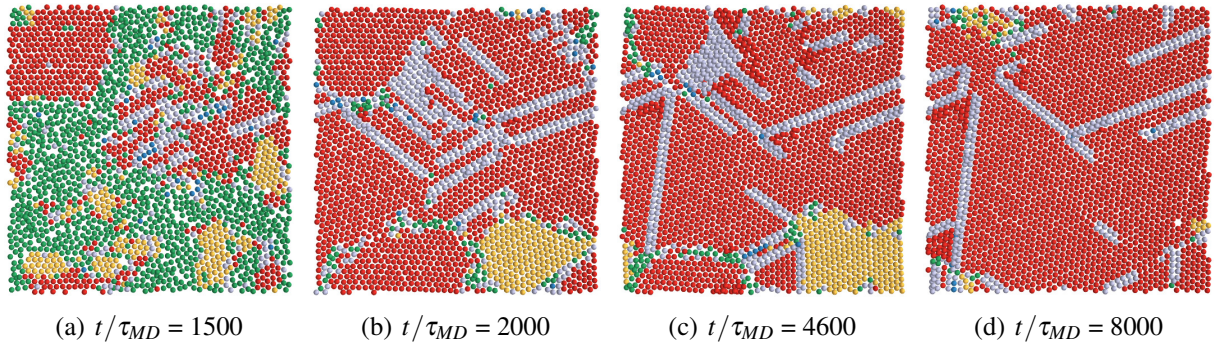


**Figure 2.9:** Typical configurations of the top view of the fourth layer of the crystalline sediment for different times as labeled for hard spheres sedimenting on a close-packed fcc (110) template at  $Pe = 1$ . The colour code is the same as in Fig. 2.2.

a snapshot of the sediment in the long time limit. Our observation is similar to experimental studies where it was observed that under microgravity conditions, the rhcp structure is formed [65].

A more quantitative description of the dynamics is shown in Figs. 2.6(b) and (c). Note that in these graphs, the colour bars represent the overall fraction of fcc ( $\phi_{fcc}^l$ ) and hcp ( $\phi_{hcp}^l$ ) particles in each layer, respectively. The colours in the two figures are complementary i.e. for the deep blue layer in Fig. 2.6(b) we see a corresponding deep red layer in Fig. 2.6(c) and vice-versa, showing that each layer is either fcc- or hcp-stacked. We also observe in certain layers that a smaller crystalline domain merges into and aligns itself with the largest growing planar 2D domain. This is shown in Figure 2.7. The deepening of colour in time for certain layers in Figs. 2.6(b) and (c) are indicative of this process. Eventually this results in a fully hcp- or fcc-stacked layer. From Fig. 2.6(b), it is evident that the quality of the fcc crystal is quite poor.

As discussed earlier, fcc and hcp crystals have a free-energy difference of the order of  $10^{-3}k_B T$  per particle in favour of fcc. In addition to the free-energy argument, Pronk *et al.* calculated the interfacial free energy between fcc and hcp to be very low  $\simeq 26 \pm 6.10^{-5}k_B T / \sigma^2$ , which favours the formation of a single fcc crystal [57]. Therefore we can expect the randomly stacked crystal to evolve into the fcc crystal over long periods of time [58, 59]. We do not see this transformation within the simulation times that we studied and expect it to occur at much longer time scales in the presence of a gravitational field than in bulk.

Next we present results on crystal growth at higher sedimentation speeds, i.e.  $Pe = 10$  in Figs. 2.6 (d)-(f). Looking at the snapshot it is clear that the number of slanted stacking faults observed is very high. A slanted stacking fault is formed when two differently stacked domains grow on a horizontal hexagonal layer [85], resulting in a line defect. Hilhorst *et al.* [67] argued that the persistence of these line defects across layers and the stacking of subsequent layers of particles leads to two fcc-stacked crystallites which are displaced from each other by a hcp-stacked layer of particles, and results in a planar defect. When such a planar defect shifts perpendicular to the defect-plane so that the gap on either side of the defect closes, a slanted stacking fault forms. A more detailed description of these defects can be found in the works of Hilhorst *et al.* and Marechal *et al.* [68]. The nature of the sediment is still primarily fcc-like (Fig. 2.6(e)). We do not observe the formation of the rhcp structure in this case, and we

therefore plot  $\phi_{def}^l$  in Fig. 2.6(f) instead of  $\phi_{hcp}^l$  as we did for  $Pe = 1$ . The increased number of slanted stacking faults are apparent from the lighter red shade of Fig. 2.6(f). In the limit of high  $Pe$ , the fcc (100) template clearly gives a much better crystal than the fcc (111) (compare Figs. 2.2(e) and 2.6(e)).

Next we move on to the flat wall case. We do not show any of our results for sedimentation on flat walls and only discuss a few observations we made by comparing it to the sedimentation on the fcc (111) template presented above. The interfacial tension between a featureless smooth wall and the fcc (111) hexagonal plane is the lowest among all fcc orientations [86]. Therefore, when hard spheres sediment on a flat wall the layer formed at the wall is of a hexagonal symmetry. We observe from our simulation snapshots, taken at time intervals of  $t/\tau_{MD} = 100$ , that the first two layers crystallize simultaneously and once they form, the ensuing crystallization occurs at the growth front is layer-wise [64, 84, 87]. This is then in principle equivalent to sedimentation on the fcc (111) template and therefore it is interesting to observe how these two cases compare in the low  $Pe$  regime. Our simulations of sedimentation on the flat wall showed a random stacking of hexagonal layers, as observed with the fcc (111) template, at  $Pe = 0.5$  with a higher fraction of fcc particles. At  $Pe = 1$  we did not observe a random stacking but a primarily fcc-like sediment, in agreement with Marechal *et al.* In addition to Ref. [68] where only a low  $Pe$  was investigated, we looked at a range of  $Pe$  for the flat wall case and observe that the fraction of fcc particles  $\phi_{fcc}$  steadily decreases with increasing  $Pe$  from  $\phi_{fcc} \simeq 0.7$  at  $Pe = 1$  to  $\simeq 0.5$  at  $Pe = 10$ . At higher  $Pe$  for the flat wall case we see disorder setting in from the bottom layers and propagating to the top.

Interestingly for high  $Pe$ , unlike the flat wall, the fcc (111) template appears to restrict the onset of a crystalline to disordered transition in the bottom layers as a result of which the fraction of the orientationally aligned fcc remains largely constant at  $\phi_{fcc} \simeq 0.7$  for the entire range of  $Pe$  investigated.

We round off the template comparison with a look at sedimentation on the least dense of all the three templates i.e. the fcc (110) template, for a low and high Péclet number,  $Pe = 1$  and 10, respectively. The corresponding snapshots of our EDBD simulations are shown in Figs. 2.8(a) and (d). From Fig. 2.8(b), we observe that at low  $Pe = 1$ , the crystalline sediment is fcc-like with  $\phi_{fcc} \simeq 0.75$ . However, a large number of stacking faults are already seen to appear in the sediment, plotted as defects in Fig. 2.8(c). However, it is important to note here that the particles form the (111)-oriented fcc, which is of a different orientation than that of the (110) template. This is highly surprising as the sedimenting particles seem to completely ignore the (110) template. van Blaaderen *et al.* [69] and Jensen *et al.* [49] both reported that at low  $Pe$ , a crystalline sediment can grow on an fcc (110) template, but they did not study the quality or orientation of the crystal. Similar to the rearrangements of smaller domains observed in the sediment on the fcc (111) template as discussed above, certain layers in this crystalline sediment also show the annealing out of smaller hcp domains into larger fcc domains as shown in Fig.2.9. However the realignment process takes longer, presumably due to the presence of extended slanted stacking faults in the sediment.

When sedimentation is faster, i.e at  $Pe = 10$ , we observe that (i) disorder sets in at the bottom of the sediment because the template is not sufficiently close-packed to constrain the particles to a layer and (ii) the bottom-most layers are composed of both fcc (100) and (111) like particles, with no clear preference for either. The presence of fcc (100) is likely because it has a lower density mismatch with the template in comparison to fcc (111). Jensen *et al.* [49] also discussed

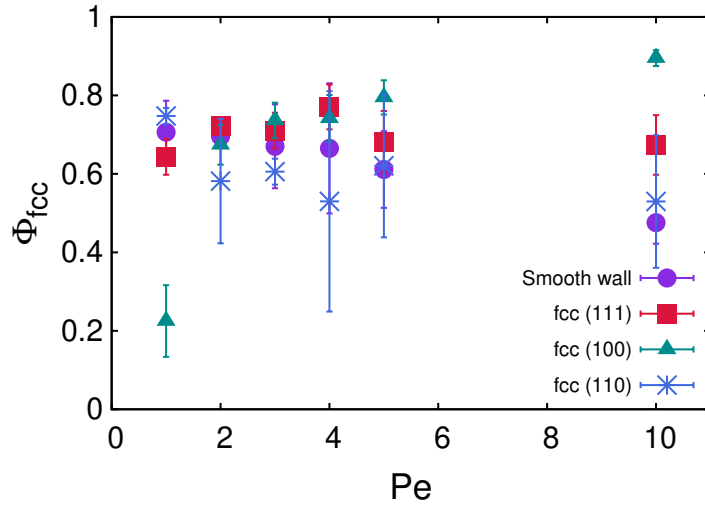


**Figure 2.10:** Fraction of fcc particles  $\phi_{fcc}$  in the crystalline sediment as obtained from simulations of sedimenting hard spheres on a smooth wall, an fcc (111), fcc (100), and an fcc(110) template and varying Péclet numbers. The values are averaged over three independent simulations. All simulations are performed for templates with a lattice spacing  $a = 1.004\sigma$  and initial packing fraction  $\eta_i = 0.02$ .

high speed centrifugation on the fcc (110) template. They reported that for high sedimentation flux (short time for equilibration and diffusion of particles in-plane), the fcc (110) template is not dense enough to sufficiently constrain the incoming particles in-plane therefore resulting in an eventually crystalline to amorphous cross-over. From our simulations, we also observe, commensurate with their findings, a local onset of disorder at high Pe. We observe from the plot shown in Fig. 2.8(f) that the sediment is highly defective with approximately 50% defects from the fifth layer upwards. There are distorted crystalline domains making up this defective crystal when there is rapid sedimentation on the fcc (110) template. These domains are not strictly parallel to the template and are coloured in lilac in Figure 2.8(d). We calculated the 3D bond orientational order parameters for these domains and found that they are fcc-like in nature.

To summarise our findings, we estimated the crystallinity of the final sediment for all the cases discussed above by calculating  $\phi_{fcc}$ , defined as the fraction of similarly oriented fcc particles over the crystalline particles in the whole sediment. A quantitative comparison of the flat wall and the three templates is shown in Fig. 2.10 from which it is apparent that the best fcc crystals with  $\phi_{fcc} \simeq 90\%$  are found for the fcc (100) template at high Péclet numbers (Pe = 10). This metric has been averaged over three independent simulation runs. The dependence of  $\phi_{fcc}$  on Pe is most evident for the fcc (100) template where the percentage of fcc increases with sedimentation rate, and the flat wall for which the reverse trend is observed i.e. the lower Pe, the better the fcc crystal.

### 2.3.3 Effect of lattice spacing of the fcc (100) template

Having established the fcc (100) template as the best template for forming large fcc crystals, we study the effect of lattice spacing of this template on the sediment formed. All the results presented in sections III.A and III.B correspond to a lattice spacing of  $a = 1.004\sigma$ . van Blaaderen *et al.* [69] experimented with different lattice spacings of the square template and

observed that larger spacings lead to a higher number of defects, thus affecting the quality of the crystal significantly [69]. Therefore we simulate sedimentation on a fcc (100) template with a lattice spacing  $a = 1.1\sigma$  which corresponds roughly to the density of the bulk crystal at co-existence. The first layer that forms on this template has also square symmetry. The effect of the template is prominent in that the lattice spacing of this layer is also  $1.1\sigma$ . Therefore there is no density mismatch between the template and the crystal formed. The particles in each layer sit on the holes left by the previous layer similar to the close-packed  $a = 1.004\sigma$  case. However there are numerous defects in the layer because of the lower density. This is true for the subsequent layers, which do not rearrange over time. In the case of the close-packed template, the weight of the sediment causes the layer defects to anneal out. In the case of the less dense template ( $a = 1.1\sigma$ ) this effect is counteracted by the fact that the bridge-site (defect) particles span across the entire cross-sectional area and form a network of closed connected circuits, and thus adversely affecting the layer to restructure. Therefore we see the drop in the overall fraction of fcc particles ( $\phi_{fcc}$ ) in the final crystal. In Fig. 2.11, we plot the fraction of fcc particles  $\phi_{fcc}$  as a function of Péclet number for a fcc (100) template with lattice spacing  $a = 1.004\sigma$  and  $a = 1.1\sigma$ . While we find for the template with  $a = 1.1\sigma$  that  $\phi_{fcc}$  is largest at low Péclet number i.e.  $Pe = 1$ , the opposite trend is observed for the close-packed template, which gives the highest  $\phi_{fcc}$  for high Péclet number. We explored further the source of lattice mismatch by calculating the pressure at the bottom and the bulk density of an fcc crystal at this pressure. The pressure at the bottom of the sample ( $z = 0$ ) is given by the weight of the sediment per unit area [84]

$$\beta P(z = 0)\sigma^3 = g^* \rho_A^*$$

with  $\rho_A^* = N\sigma^2/A$  and  $g^* = mg\sigma/k_B T$ . In our simulations, the cross-sectional area of the column is  $A \simeq 50\sigma \times 50\sigma$  and the number of particles is  $N = 100000$ . With these parameters,  $\beta P(z = 0)\sigma^3 \simeq 400$  for  $Pe=10$ . We determined the density of the fcc crystal at this pressure using the Speedy equation of state, corresponding to a volume fraction and lattice spacing of 0.732 and  $1.0036\sigma$ , respectively. This may explain the superior quality of the fcc crystals formed on the  $1.004\sigma$  fcc (100) template at  $Pe = 10$ . Similarly, for  $Pe = 1$ , we find  $\beta P(z = 0)\sigma^3 \simeq 40$ . The fcc crystal at this pressure corresponds to a lattice spacing of  $\simeq 1.05\sigma$  (and volume fraction of 0.634), which differs significantly from that of the template. This may explain the poor quality of the fcc crystal. It would be interesting to look at several values of the lattice spacing and identify if the optimal value of  $a$ , which yields the best sediment for a given  $Pe$ , is the one with the least mismatch. In the case of the template with the wider lattice spacing,  $\phi_{fcc} \simeq 0.70$  remains rather constant as a function of  $Pe$ , whereas the close-packed template shows a steady increase of  $\phi_{fcc}$  from  $\sim 0.5$  at  $Pe = 1$  to  $\sim 0.9$  for  $Pe = 10$ . To summarise, the best fcc crystal is obtained by sedimentation on a close-packed square template at  $Pe = 10$ .

### 2.3.4 Effect of initial volume fraction

Finally, we investigate the dependence of the overall fraction of fcc particles  $\phi_{fcc}$  on the initial volume fraction  $\eta_i$  in the case of sedimentation on a close-packed fcc (100) template. Hooenboom *et al.* showed from experiments and Marechal *et al.* [68] by simulations that the fraction of fcc particles  $\phi_{fcc}$  in a sediment deposited on a smooth wall depends strongly on the dimensionless sedimentation flux  $J = \eta_i \times Pe$ , which sets the time available for the particles to crystallize at the growth front. The dimensionless sedimentation flux was also used by Jensen

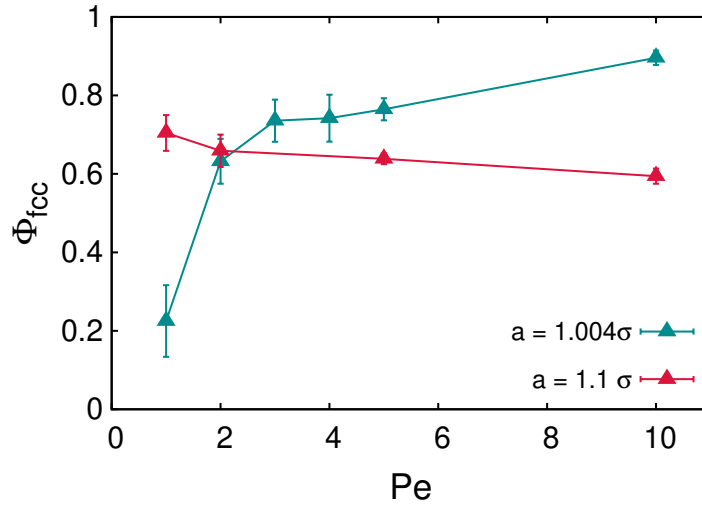


**Figure 2.11:** Fraction of fcc particles  $\phi_{fcc} = N_{fcc}/N_{cr}$  in the crystalline sediment of hard spheres settling on a square fcc (100) template with lattice spacing  $a = 1.004\sigma$  and  $1.1\sigma$  as a function of Péclet number  $Pe$ . The values are averaged over three independent simulations. The lines are guides to the eye. The initial packing fraction  $\eta_i = 0.02$ .

*et al.* [49] to characterise their sedimentation experiments on different templates and further compare their results on the flat wall with Hoogenboom *et al.* [61] and Davis *et al.* [75]. In Fig. 2.12, we plot the overall fraction of fcc particles ( $\phi_{fcc}$ ) of a crystalline sediment on a square fcc (100) template as a function of  $Pe$  for three different initial volume fractions,  $\eta_i = 0.01, 0.02$ , and  $0.104$ . We find a strong dependence of  $\phi_{fcc}$  on  $Pe$  at least for  $\eta_i \leq 0.1$ . In the inset of Figure 2.12, we plot  $\phi_{fcc}$  as a function of the dimensionless sedimentation flux  $J$ , which clearly shows no collapse of the data for varying  $\eta_i$ . This is different from the case of a flat wall as Marechal *et al.* [68] observed a collapse of the average stacking parameter for different values of  $Pe$  and  $\eta_i$  but the same value of  $J$  (sedimentation flux). In contrast, on the fcc (100) template for  $Pe > 1$ , the fcc crystal quality shows a strong dependence on  $Pe$  but not on  $\eta_i$ . For the case,  $Pe = 1$ , we do see an effect of increased packing fraction, indicating that at very slow sedimentation rates, a higher initial packing fraction results in a higher  $\phi_{fcc}$ .

The reason for the different dependencies can be the mechanistic differences in the way that the faults in the two crystals rearrange. In the case of the fcc (100) template, the defects are forced to anneal out by the weight of the sediment on top, and this effect is more pronounced at higher  $Pe$ . The hard spheres that Marechal *et al.* studied were sedimented on a smooth wall at low  $Pe$ , i.e the near-equilibrium regime [68]. In this case, planar defects that shift perpendicular to the plane merge with each other and form slanted stacking faults across layers. Therefore the quality of crystal formed is determined by the time available for the layer at the growth front to restructure such that these planar defects can rearrange, and not propagate to form 3D crystal grain boundaries. The time available for this restructuring is set by the value of flux  $J$ , and this may explain the collapse of the curves shown in a similar plot to the inset of Fig. 2.12 for the smooth wall case [68]. In addition, we observe for the fcc (100) template that for  $Pe = 1$ , the quality of the crystal improves drastically upon increasing the initial packing fraction such that the stacking faults, as observed in the initial stages of the crystalline sediment, anneal out. In

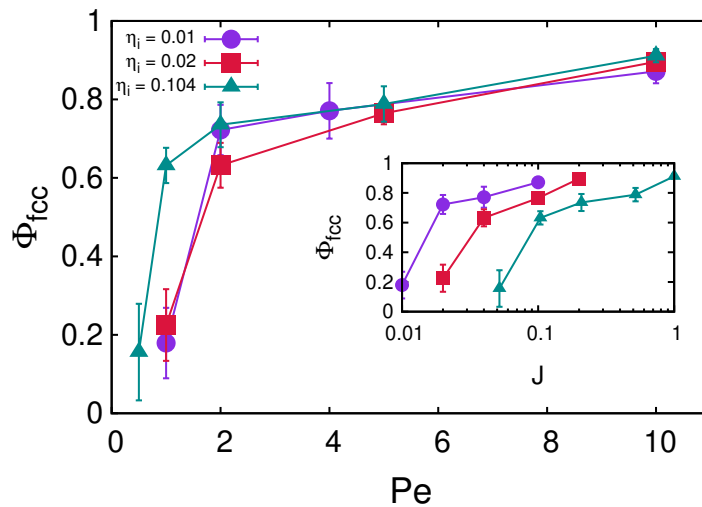


**Figure 2.12:** Fraction of fcc particles  $\phi_{fcc} = N_{fcc}/N_{cr}$  in the crystalline sediment of hard spheres settling on the (100) plane of a close-packed fcc crystal as a function of Péclet number  $Pe$  for varying initial volume fractions  $\eta_i$  as labeled. The values are averaged over three independent simulations. The lines are guides to the eye. The inset shows  $\phi_{fcc}$  as a function of  $J = \eta_i \times Pe$ .

summary, we do not see a strong dependence of the fcc crystal quality on the initial volume fraction for the square fcc (100) template for  $Pe \geq 2$ .

## 2.4 Conclusions

To summarise, we used event-driven Brownian Dynamics simulations to study the crystallization dynamics of hard-sphere colloids sedimenting on three different templates, the (100), (111) and (110) cross-sectional planes of the fcc crystal. We make the following observations.

1. Crystalline sediments grown on the fcc(100) template exhibited the fcc structure with very few defects (see Figs. 2.2(a) and (d)). The fraction of similarly oriented fcc particles ( $\phi_{fcc}$ ) increases with settling velocity and is as high as  $\simeq 90\%$  for high settling velocities  $Pe = 10$ . This surprising observation is in excellent agreement with the experimental work of Jensen *et al.* [49]. As noted by the authors the primary reason for this observation is the absence of stacking degeneracy for the fcc (100) template.
2. While the quality of crystalline sediment formed on a smooth flat wall is determined by the sedimentation flux, which is a combination of the Péclet number and the initial volume fraction, for the fcc(100) case the Péclet number ( $Pe$ ) alone determines the quality of the sediment.
3. We also studied the effect of initial volume fraction  $\eta_i$  for the fcc (100) template with lattice spacing  $a = 1.004\sigma$ . For  $Pe > 1$ , we do not observe a significant effect of the initial packing fraction  $\eta_i$  on the quality of the sediment. However, at very slow sedimentation rates ( $Pe = 1$ ), the quality of the crystal improves with the initial packing fraction  $\eta_i$ .

4. When we compare the crystal formed from sedimentation on two different lattice spacings ( $1.004\sigma$  and  $1.1\sigma$ ) of the fcc (100) template, we observe that for lower  $Pe$ , a better quality of fcc crystal is formed for the  $1.1\sigma$  template, whereas for higher  $Pe$  the close-packed or  $1.004\sigma$  template is clearly superior.
5. We also looked at the fcc (111) template which is the densest one and observed that at low  $Pe$ , the layers in the crystalline sediment are randomly “fcc- or hcp-stacked” with only a very few stacking faults. As evidenced by previous simulation and experimental studies, a randomly stacked crystal should eventually rearrange into an fcc crystal over long periods of time [57–59], however our simulations are not long enough to make this observation. Sedimentation at high  $Pe$  on the fcc (111) template still results in an fcc-like sediment but with several stacking faults.
6. The third template, fcc (110), also gives an fcc-like sediment but with an (111) orientation, which is of a different orientation than that of the (100) template. The template appears to play no role in directing the orientation of the growing crystal. Already at low  $Pe$ , several slanted stacking faults are seen in the sediment. Upon increasing the settling velocity ( $Pe$ ), disorder sets in rapidly.

In summary we conclude that the best fcc crystals are found in the case of sedimentation on a close-packed fcc (100) template at high  $Pe$ , and on an fcc (111) template at low  $Pe$ . Our simulations treat the solvent effects *via* the Brownian noise. It would be interesting to simulate these systems with methods that treat hydrodynamic effects in a rigorous manner. It would also be interesting to look at template assisted sedimentation of binary hard-sphere mixtures and we plan to work on these issues in the future.

## 2.5 Acknowledgements

I would like to thank John Edison for providing his EDMD code at the initial stage of the project, and many useful discussions during the writing of the manuscript on this project. I gratefully acknowledge Wiebke Albrecht, Chris Kennedy and Douglas Hayden for critical reading of the Chapter.

---

## **Towards a colloidal Laves phase from binary hard-sphere mixtures *via* sedimentation**

---

Colloidal photonic crystals, which show a complete band gap in the visible region, have numerous applications in fibre optics, energy storage and conversion, and optical wave guides. Intriguingly, two of the best examples of photonic crystals, the diamond and pyrochlore structure, can be self-assembled into the colloidal  $\text{MgCu}_2$  Laves phase crystal from a simple binary hard-sphere mixture. For these colloidal length scales thermal and gravitational energies are often comparable and therefore it is worthwhile to study the sedimentation phase behaviour of these systems. For a multicomponent system this is possible through a theoretical construct known as a phase stacking diagram, which constitutes a set of all possible stacking sequences of phases in a sedimentation column, and uses as input the bulk phase diagram of the system in the chemical potential plane. We performed free-energy calculations to determine the stable phases for binary hard-sphere systems with different diameter ratios, using Monte Carlo simulations and analytical equations of state available in literature, and subsequently calculated the corresponding phase stacking diagrams. We also discuss observations from event-driven Brownian Dynamics simulations in relation to our theoretical stacking diagrams.

### 3.1 Introduction

Colloidal particles can serve as physical models for atomic systems in that they can crystallize into periodic, ordered phases which are analogous to atomic crystals. The best known example of this, first reported by simulations [2] and followed up later by experiments [12], is the formation of the face-centered-cubic (fcc) crystal phase, which crystallizes from a colloidal hard-sphere fluid. As the length and time scales of colloidal systems are easier to study experimentally than their atomic counterparts, these systems can provide valuable fundamental insights into physical processes such as crystallization and phase transitions [88, 89].

A significant application of colloidal particles is to serve as building blocks for photonic crystals. Photonic crystals can control the propagation of light by virtue of their periodically varying refractive index or dielectric contrast. With lattice constants of the same order as the wavelength of light, these materials show a photonic band gap for certain light frequencies. Photonic bandgap materials have a broad range of applications such as optical wave guides [90], sensors [91] and in energy storage [92] / conversion [93] among others. A complete photonic bandgap may be shown by a three-dimensional photonic crystal which prevents the propagation of specific wavelengths of light in all directions. With colloids as building blocks, photonic crystals can open up a band gap in the visible range of frequencies [94], depending on their refractive index, packing geometry and density. In particular, the diamond [95] and pyrochlore [38] structures have been known to open up a wide photonic band gap even at low refractive indices, thereby making their photonic properties robust to defects [36]. However, the colloidal diamond and pyrochlore crystals are open structures with a low packing fraction rendering them entropically unfavourable and mechanically unstable for colloidal crystallization. This problem may be circumvented by the fact that these two structures make up the large (Mg) and small (Cu) species sublattices of the colloidal  $\text{MgCu}_2$  Laves phase, respectively, which is not a low coordination structure. The Laves phase (LP) structures which have a stoichiometry of  $LS_2$  ( $L$  = large species,  $S$  = small species), were first found in intermetallic compounds:  $\text{MgCu}_2$ ,  $\text{MgZn}_2$  and  $\text{MgNi}_2$  [96]. The  $\text{MgZn}_2$  LP is the thermodynamically stable binary crystal phase for binary hard-sphere mixtures of diameter ratios in the range 0.76 to 0.84, but the photonic  $\text{MgCu}_2$  LP as has only a marginally higher free energy  $\sim 10^{-3}k_B T$  per particle at freezing [27, 28]. The three LP structures may be considered to be thermodynamically degenerate owing to this small free-energy difference, and one would expect to obtain a random stacking of the LP structures on spontaneous crystallization, similarly to the rHCP structures (which can be seen as a mixture of fcc and hcp crystals) obtained from monodisperse hard-sphere-like particles [55, 61, 97]. However, the  $\text{MgCu}_2$  LP may be selected for growth by templating [27], and by removing the particles on one of its sublattices (for example by burning or dissolution) the photonic open structures may subsequently be retrieved.

In order for the  $\text{MgCu}_2$  LP to possess an optical band gap for its sublattices, the spheres must be on the colloidal length scale, which corresponds to a regime where the thermal and gravitational energies of the particles are comparable. Therefore it is important to account for gravity while studying the self-assembly of colloidal LP structures. The competition between thermal and gravitational forces leads to a sedimentation-diffusion equilibrium, which we study in this work. For a one-component colloidal system under gravity, it is fairly straightforward to obtain information about the bulk thermodynamics of the system from its sedimentation behaviour [78, 98]. For this, one simply needs to calculate the height-dependent density profile

and invert it to calculate the osmotic pressure at every point along the sedimentation column. In this way, a single experiment/simulation can yield the entire equation of state, i.e. the pressure as a function of density. However, for systems with more than one component, correlating bulk thermodynamics to the sedimentation-diffusion equilibria is not trivial. In this case, the bulk phase diagram (in the absence of gravity) is converted to an alternate phase space which accounts for gravity. This constructed phase space is referred to as a phase stacking diagram, or simply, a stacking diagram [99, 100].

A stacking diagram (SD) is a set of all possible stacking sequences of phases found in a sedimentation column. A stacking sequence indicates the phases observed sequentially from the bottom to the top of a sedimentation column. The theory for calculating a SD takes as input a bulk phase diagram calculated in the chemical potential plane. The method to convert this into a stacking diagram involves a Legendre transformation to an alternative plane [99]. SDs can be used to predict various unexpected phenomena in sedimenting systems. For example, “floating phases” were observed in colloid-polymer mixtures, where a floating colloid-rich liquid slab was sandwiched between two polymer-rich colloidal gas slabs [101], and “floating hexagonal crystal phases” have been reported in simulations of colloidal spheres with a soft corona [102]. A reentrant percolating network in a patchy colloidal mixture was both predicted and observed in simulations [103]. In another example, a floating nematic phase suspended on an isotropic phase was observed in an experimental system of colloidal platelets and spheres [104]. This observation was backed up by a stacking diagram which showed floating phases in certain stacking sequences. This demonstrates the power of this simple but predictive theory in bridging the gap between theory and experiments and asserts the importance of constructing SDs.

In a recent work, the  $\text{MgCu}_2$  LP was reported to have the lowest free energy out of the three LPs for a hard sphere-hard tetramer mixture [105], and its free-energy difference with the  $\text{MgZn}_2$  LP structure was calculated to be an order of magnitude higher ( $O(10^{-2}k_B T)$  per particle) with respect to the binary hard-sphere system. The tetramer building blocks were based on the idea that the pyrochlore structure can be grouped into tetrahedral clusters of spheres. Following a similar logic of building blocks, an experimental system of DNA-coated spheres and preassembled tetrahedral clusters was used in a recent work to obtain the  $\text{MgCu}_2$  LP [106]. However, this system used DNA-mediated short-ranged attractions between the unlike species to promote self-assembly and the  $\text{MgCu}_2$  LP was not observed for tetrahedral clusters made of non-overlapping adjacent spheres. As hard-sphere colloids are notably experimentally realizable and the tunability of their length scales is well within control to suit various photonic applications, it is worthwhile to study the sedimentation phase behaviour of this system.

In this Chapter, we study the sedimentation-diffusion equilibria of binary colloidal hard-sphere mixtures, where the spheres interact only through hard-core interactions, by constructing stacking diagrams. Our objective is to design a self-assembly route, *via* sedimentation, for the colloidal  $\text{MgCu}_2$  LP, as it is a precursor for photonic band-gap structures. We calculate SDs for a diameter ratio of 0.85, for which the LPs are not stable, and 0.82, which shows an entrant stable LP. We first calculate the bulk phase diagrams in the pressure-composition (most common), packing fraction (experimentally significant) and chemical potential (required for constructing SDs) representations. We note that these phase diagrams have already been reported but solely in the pressure-composition and packing fraction representation [27, 28]. In order to construct the stacking diagrams, we need to obtain the bulk phase diagrams in the chemical potential plane. We therefore repeat these calculations in order to determine the phase

diagrams in the chemical potential plane. This Chapter is organised as follows. In Section 3.2, we describe how to go from a thermodynamic bulk phase diagram to an alternative phase space (phase stacking diagram) which includes gravity in the description, and briefly describe event-driven Brownian Dynamics (EDBD) simulations that we later use to simulate specific state points in the constructed SDs. In Section 3.3.1-3.3.4, we present the bulk phase diagrams and the corresponding stacking diagrams for two BHS size ratios, one of which features a stable Laves phase, which show the different stacking sequences of phases in a gravitational field, for a range of gravitational lengths, bulk compositions and bulk concentrations. In Section 3.3.5 we show event-driven Brownian Dynamics simulations for selected state points in the SD corresponding to a size ratio of 0.82 and discuss the sedimentation behaviour observed in relation to our theoretical predictions.

## 3.2 Methodology

### 3.2.1 Bulk phase behaviour of binary hard-sphere systems

The first step towards studying the sedimentation-diffusion equilibrium of a binary mixture of large hard spheres with diameter  $\sigma_L$  and small hard spheres with diameter  $\sigma_S$  is to ascertain the bulk thermodynamics of the system, i.e., the phase behaviour in the absence of gravity. Therefore we first calculate the bulk phase diagram for a specific diameter ratio  $q = \sigma_S/\sigma_L$ , which describes the coexistence between different phases for this system. Coexistence between phase  $\alpha$  and  $\beta$  is calculated using the mechanical equilibrium condition,  $P^\alpha = P^\beta$ , with  $P$  the pressure, and employing the chemical or diffusive equilibrium condition for both the large and small species,  $\mu_L^\alpha = \mu_L^\beta$  and  $\mu_S^\alpha = \mu_S^\beta$ , respectively, with  $\mu_L(\mu_S)$  the chemical potential of the large (small) species. The chemical potential equivalence criteria dictate that we construct common tangents on the Gibbs free energy  $G$  - composition  $x$  plane at a fixed pressure  $P$ . Here, we define  $x_S = N_S/N$  with  $N = N_S + N_L$  and  $N_S(N_L)$  the number of small (large) hard spheres. From this technique, we can directly obtain the coexistence species compositions at each pressure and calculate other coexistence properties on the packing fraction ( $\eta_L = \pi\sigma_L^3 N_L/6V - \eta_S = \pi\sigma_S^3 N_S/6V$ ) representation with  $V$  the volume of the system, or on the chemical potential ( $\mu_L - \mu_S$ ) plane. In order to obtain the Gibbs free energy  $G = F + PV$ , we first calculate the Helmholtz free energies  $F$  of the different fluid and solid phases. The phases that we consider are the binary fluid, two face-centered-cubic (fcc) crystals formed of purely large or small hard-sphere species, and the MgZn<sub>2</sub> LP, and ignore hereby the substitutional solid solutions of the crystal phases. We remark here that the phase diagram calculated with the MgCu<sub>2</sub> LP is fairly identical owing to the minute free-energy difference between the two LP structures as mentioned earlier, and coincident equations of state. We employ analytical expressions from literature for the Helmholtz free energy of a binary hard-sphere fluid [107]. We obtain the equations of state for the LPs from Monte Carlo simulations in the  $NPT$  ensemble, and employ the Speedy equation of state [108] for the fcc phases.

In order to obtain the Helmholtz free energy as a function of density  $\rho = N/V$ , we integrate the equation of state from a reference density  $\rho_0$

$$\frac{\beta F(\rho)}{N} = \frac{\beta F(\rho_0)}{N} + \int_{\rho_0}^{\rho} d\rho' \frac{\beta P(\rho')}{\rho'^2}, \quad (3.1)$$

where  $\beta = 1/k_B T$ ,  $k_B$  denotes the Boltzmann constant, and  $T$  the temperature. The Helmholtz free energy  $F(\rho_0)$  of the crystal phases at a reference density  $\rho_0$  is calculated using the Frenkel-Ladd method in Monte Carlo simulations in the  $NVT$  ensemble, which involves an Einstein integration of a system of non-interacting particles that are connected to the lattice positions of an ideal crystal phase *via* harmonic springs

$$\beta U_\lambda(\mathbf{r}^N) = \beta U(\mathbf{r}^N) + \lambda \sum_{i=1}^N (\mathbf{r}_i - \mathbf{r}_{0,i})^2 / \sigma_L^2. \quad (3.2)$$

Here  $U(\mathbf{r}^N)$  is the potential energy of the system due to the hard-sphere interactions,  $\mathbf{r}_{0,i}$  denotes the ideal lattice position of particle  $i$  in the crystal of interest, and  $\lambda$  is a dimensionless coupling parameter, which goes from 0, corresponding to the interacting system of interest for which we want to compute the free energy, to  $\lambda_{max}$ , which corresponds to an Einstein crystal, where the spring constant is chosen sufficiently large that the particles do not interact with each other.

The Helmholtz free energy is obtained from [109, 110]

$$\begin{aligned} \frac{\beta F(N, V, T)}{N} &= \frac{\beta U(\mathbf{r}_0^N)}{N} + \frac{3(N-1)}{2N} \ln \left( \frac{\Lambda^2 \lambda_{max}}{\pi \sigma_L^2} \right) \\ &+ \frac{1}{N} \ln \left( \frac{N \Lambda^3}{V} \right) - \frac{3}{2N} \ln(N) \\ &- \frac{1}{N} \int_{\ln c}^{\ln(\lambda_{max}+c)} (\lambda + c) \left\langle \sum_{i=1}^N \frac{(\mathbf{r}_i - \mathbf{r}_{0,i})^2}{\sigma_L^2} \right\rangle_\lambda^{CM} d[\ln(\lambda + c)], \end{aligned} \quad (3.3)$$

where  $U_\lambda(\mathbf{r}_0^N)$  is the potential energy when all particles are at their ideal lattice positions,  $\Lambda$  is the thermal wavelength,  $\langle \dots \rangle_\lambda^{CM}$  denotes that the ensemble average is sampled for a solid with a fixed center of mass using the Boltzmann factor  $\exp(-\beta U_\lambda)$ , and

$$c = \frac{1}{\left\langle \sum_{i=1}^N (\mathbf{r}_i - \mathbf{r}_{0,i})^2 / \sigma_L^2 \right\rangle_0^{CM}}. \quad (3.4)$$

The integral is calculated numerically using a 20-point Gauss-Legendre quadrature.

### 3.2.2 Accounting for gravity

Once we have ascertained the bulk thermodynamics, we study this binary system sedimenting under gravity. To this end, we construct a stacking diagram, which is the set of all possible sequences of phases stacked in a sedimentation column.

The theory behind the construction of a stacking diagram [99] is based on the chemical potentials of the two species. Once gravity is “switched on”, a non-trivial density and composition profile is obtained along the direction of gravity  $z$  of the sedimentation column. We define a local chemical potential  $\mu_i(z)$  of species  $i$ , which varies linearly with height  $z$  along the sedimentation column

$$\mu_i(z) = \mu_i^0 - m_i g z \quad (3.5)$$

where  $\mu_i^0$  is the chemical potential of species  $i$  in the absence of gravity,  $m_i$  is the buoyant mass of particle species  $i$ , and  $g$  is the gravitational acceleration. Eliminating the  $z$ -dependence, we obtain a linear relation between the local chemical potentials of the large ( $\mu_L$ ) and small spheres ( $\mu_S$ ).

$$\mu_S(\mu_L) = a + s\mu_L, \quad (3.6)$$

where the slope  $s$  of the sedimentation path is given by the ratio of the buoyant masses

$$s = \frac{m_S}{m_L}, \quad (3.7)$$

and  $a$  denotes the composition variable, which is a function of the initial composition and concentration of the system [99, 111]

$$a = \mu_S^0 - s\mu_L^0. \quad (3.8)$$

For low Péclet numbers, i.e., in the case of slowly varying inhomogeneities, we assume that the local density approximation (LDA) is valid. This approximation implies that the local chemical potential  $\mu_i(z)$  of species  $i$  is equal to the chemical potential  $\mu_i$  of a corresponding equilibrium bulk reservoir. The significance of the LDA is that the correlation between gravitational variable  $s$  and composition variable  $a$  now appears as a straight line (Eq. 3.6) on the bulk phase diagram in the plane of chemical potentials  $\mu_L - \mu_S$ . This straight line is called a “sedimentation path” and the set of all such paths constitutes a stacking diagram. The point at which a sedimentation path intersects with a bulk binodal represents a phase transition. Therefore, each sedimentation path corresponds to a specific stacking sequence of phases in the corresponding stacking diagram.

### 3.2.3 Event-Driven Brownian Dynamics simulations

Once we have mapped out the stacking diagrams of a binary mixture of hard spheres, we perform event-driven Brownian Dynamics (EDBD) simulations [68, 77] at selected state points for such a mixture sedimenting under gravity on a hard wall. We carry out simulations on a binary system of  $N$  hard-sphere colloids with a diameter ratio  $q = 0.82$  in a volume  $V$  in the  $NVT$  ensemble. The gravitational field is directed along the  $z$ -axis and each colloid  $i$  is subjected to an external potential  $U(z_i) = m_i g z_i$  where  $g$  is the acceleration due to gravity,  $m_i$  is the buoyant mass of particle  $i$ , and  $z_i$  is the vertical coordinate of colloid  $i$ . Two hard walls are placed at  $z = 0$  and  $z = H - \sigma_L$ . The simulation method considers particle collisions (with the wall and each other) as discrete events and progresses through a sequence of collision time intervals to the nearest event calculated through the Newtonian equations of motion. During the simulation, particle velocities are stochastically and periodically adjusted at a regular interval of  $\Delta t$  to account for the Brownian “kicks” from the surrounding solvent

$$\mathbf{v}(t + \Delta t) = \alpha_t \mathbf{v}(t) + \beta_t \mathbf{v}_R(t), \quad (3.9)$$

where  $\mathbf{v}(t + \Delta t)$ ,  $\mathbf{v}(t)$  are the particle velocities before and after the Brownian adjustment,  $\mathbf{v}_R(t)$  is a variable calculated from a 3D Gaussian distribution with mean 0 and variance  $k_B T / m_i$ . We set  $\alpha_t = 1/\sqrt{2}$  with a probability  $\nu \Delta t$  and 1 otherwise. We employ  $\beta_t = \sqrt{1 - \alpha_t^2}$  in order to keep the temperature constant. Following Ref. [112], we set  $\nu = 10\tau_{MD}^{-1}$  and  $\Delta t = 0.01 \tau_{MD}$  in all our simulations and use  $\tau_{MD} = \sqrt{m_L/k_B T} \sigma$  as the time unit of our event-driven MD

simulations. The details of the EBD simulations are elaborately described in Refs. [68] and [112].

The parameter that describes the effect of gravity on sedimenting colloids is the gravitational length given as  $l_g^i = k_B T / m_i g$ , which corresponds to the height difference over which the gravitational energy of colloid  $i$  is comparable to the thermal energy [78]. The dimensionless parameter of interest is the gravitational Péclet number which is given by  $Pe_i = \sigma_i / l_g^i$ . In this work, we show simulation results for a binary mixture of hard spheres with a diameter ratio  $q = 0.82$ , and three different gravitational length ratios  $(l_g^L / l_g^S) = 0.4, 0.68$  and  $1.0$ , corresponding to specific points in the stacking diagram.

### 3.3 Results and Discussion

We first calculate the bulk phase diagrams for two diameter ratios,  $q = 0.85$ , for which the Laves phase is not stable, and  $q = 0.82$ , for which the phase diagram shows the stable LP, as shown in Refs. [27, 28]. Subsequently, we determine the bulk phase diagrams in the large-sphere chemical potential  $\mu_L$  – small-sphere chemical potential  $\mu_S$  representation in order to determine the stacking diagrams of these systems that represent the different phase stacking sequences in a sedimentation-diffusion equilibrium. We will first present our results for  $q = 0.85$  and, subsequently, we will describe our findings for  $q = 0.82$ .

#### 3.3.1 Bulk phase diagram for $q = 0.85$

Using the method described in Section 3.2.1, we calculate the bulk phase diagram for  $q = 0.85$ . In Fig. 3.1, we present the bulk phase diagram in the pressure  $\beta P \sigma_L^3$  – composition  $x_S$  representation, where  $x_S$  refers to the number fraction of small spheres. We observe three thermodynamically stable phases, the pure fcc of large spheres ( $fcc_L$ ), pure fcc of small spheres ( $fcc_S$ ), and the binary fluid mixture. The phase diagram exhibits a fluid– $fcc_L$ , a fluid– $fcc_S$ , and a  $fcc_S$ – $fcc_L$  coexistence region. The Laves phase is unstable at all pressures. At pressures  $\beta P \sigma_L^3 \leq 11.5$ , the fluid phase is stable. In the range  $11.5 \leq \beta P \sigma_L^3 \leq 24.65$ , we observe two coexistence regimes. For composition  $x_S > 0.7$ , the fcc of small spheres ( $fcc_S$ ) coexists with the fluid phase and for  $x_S < 0.7$ , coexistence is found between the fcc of large spheres ( $fcc_L$ ) and the fluid phase. Interestingly, at pressures  $\beta P \sigma_L^3 \geq 24.65$ , we observe that the binary system demixes into two pure component fcc phases, which is to be expected as the phase-separated fcc phase yields the best packing for a binary mixture at this diameter ratio. A triple point between the three phases is observed at  $\beta P \sigma_L^3 = 24.65$ , at which all the three phases are in thermodynamic equilibrium. For experimentalists, a more appealing representation of the phase diagram is the plane of packing fractions of the individual species. We therefore also present the phase diagram in an  $\eta_L - \eta_S$  representation. This is shown in Fig. 3.2. Interestingly one can observe that the triple point, which is a point in the  $\beta P \sigma_L^3 - x_S$  plane where three coexistence binodals meet, appears as a triangular region in the  $\eta_L - \eta_S$  plane.

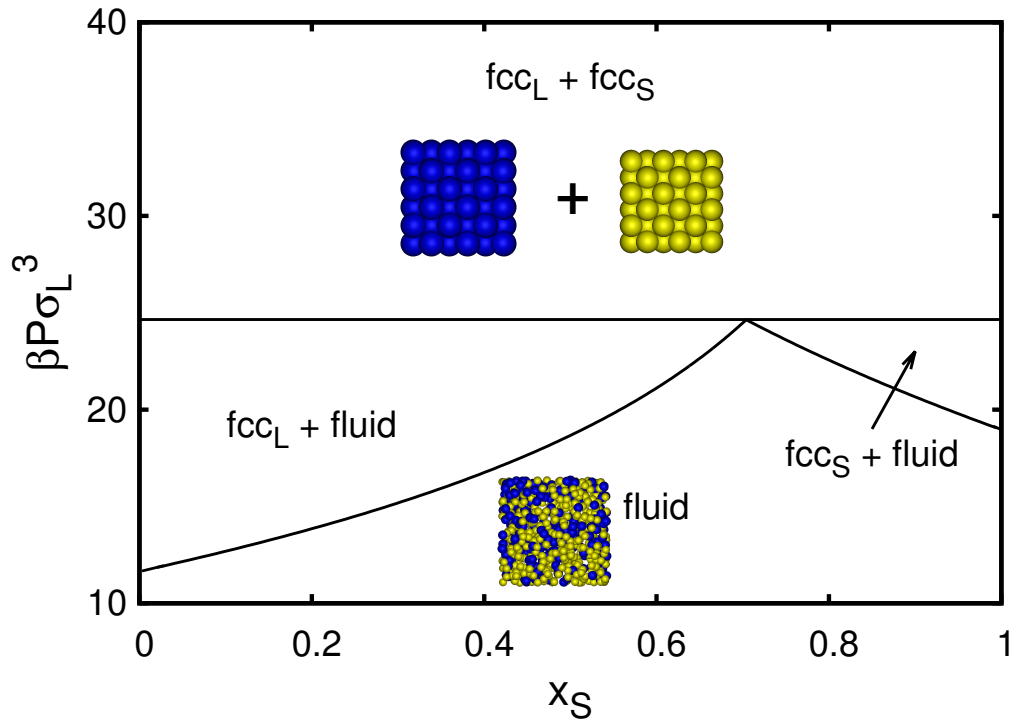


**Figure 3.1:** Bulk phase diagram of a binary mixture of hard spheres with a diameter ratio  $q = 0.85$  in the pressure  $\beta P \sigma_L^3$  – composition  $x_S$  representation.

### 3.3.2 Stacking diagram for $q = 0.85$

In the previous subsection, we calculated the bulk phase diagram of a binary hard-sphere mixture with a diameter ratio of  $q = 0.85$ . We now consider this system in a gravitational field. Following the formulation described in section 3.2.2, we calculate the corresponding stacking diagram to describe the sedimentation-diffusion equilibria of this system. To calculate the stacking diagram, we first convert Fig. 3.1 to the chemical potential ( $\mu_L - \mu_S$ ) plane as shown in Fig. 3.3. Subsequently, the bulk phase diagram in the chemical potential plane can be converted to a stacking diagram in the  $a - s$  plane, which describes the different stacking sequences that can be observed in a sedimentation-diffusion equilibrium. The sedimentation paths, as described by  $a = \mu_S - s\mu_L$ , are drawn as coloured dashed lines in the  $\mu_L - \mu_S$  phase diagram in Fig. 3.3. Each of these sedimentation paths corresponds to a unique stacking sequence and a unique point in the stacking diagram as shown in Fig. 3.4. Each region in the stacking diagram represents a collection of points with identical stacking sequences and the colour of these regions corresponds to the colour of the sedimentation paths drawn in the phase diagram in the chemical potential plane (Fig. 3.3). It is important to mention here that these sedimentation paths are considered infinite, therefore a pure component crystal will always be present at the

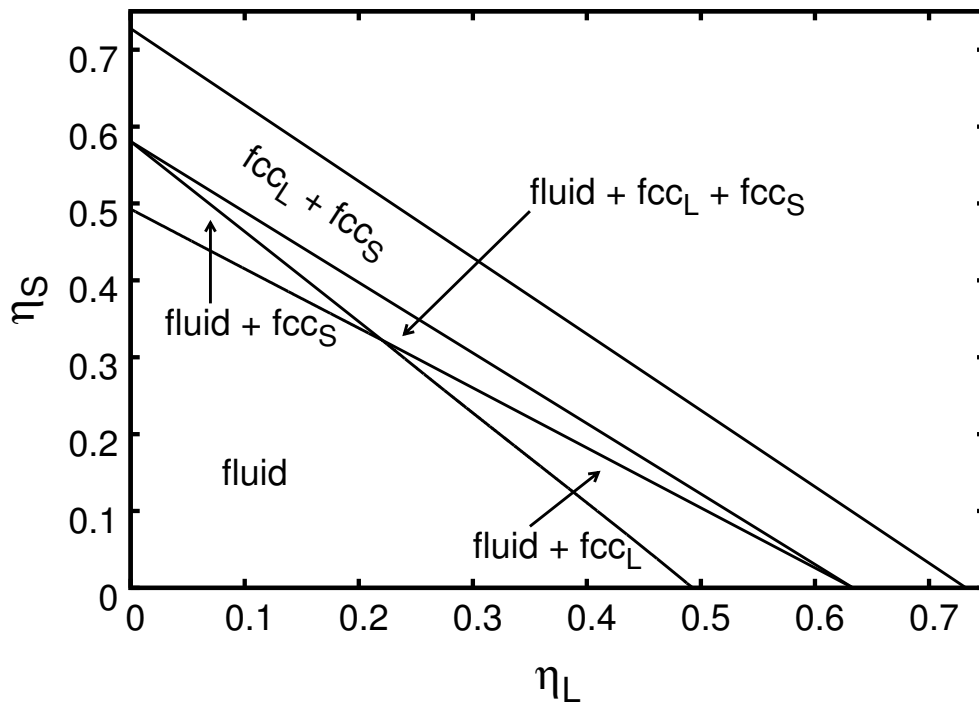


**Figure 3.2:** Bulk phase diagram of a binary mixture of hard spheres with a diameter ratio  $q = 0.85$  in the large-sphere packing fraction  $\eta_L$  – small-sphere packing fraction  $\eta_S$  representation.

bottom. In case we consider sedimentation paths that are bounded by a pressure at the bottom and at the top of the sample cell, the stacking diagram will be much richer [113].

The stacking diagram as shown in Fig. 3.4 is divided into different regions which are delimited from each other through the following boundaries or features.

1. **Sedimentation binodal:** This is the locus of all sedimentation paths which are tangential to a bulk binodal. In this case, we have three bulk binodals, a fluid– $\text{fcc}_L$ , fluid– $\text{fcc}_S$ , and  $\text{fcc}_S$ – $\text{fcc}_L$  binodal, and therefore three corresponding sedimentation binodals.
2. **Terminal lines:** These lines represent sedimentation paths passing through any terminal point of a binodal. A terminal point may be a critical point, a triple point or indeed any point at which a binodal terminates. There is one triple point observed in the bulk phase diagram for this system - where the solid  $\text{fcc}_L$  phase, solid  $\text{fcc}_S$  phase and the binary fluid phase coexist. This triple point translates into a terminal line in the stacking diagram.
3. **Asymptotic terminal lines:** The difference between terminal lines and asymptotic terminal lines is that the former appears when a binodal ends at finite chemical potentials and the latter corresponds to infinite chemical potentials of one or both of the species. For example, when the phase transition involves a pure component phase, the chemical potential of the absent species becomes  $-\infty$ . Therefore the  $\text{fcc}_S$ –fluid binodal tends to a horizontal asymptote in the  $\mu_S$ – $\mu_L$  plane as the chemical potential of the absent large sphere species  $\mu_L \rightarrow -\infty$ . We remind the reader that the parameter  $s$  represents the slope of the tangent to the bulk binodal (Eq. 3.6) which in the above case corresponds to  $s \rightarrow 0$ .

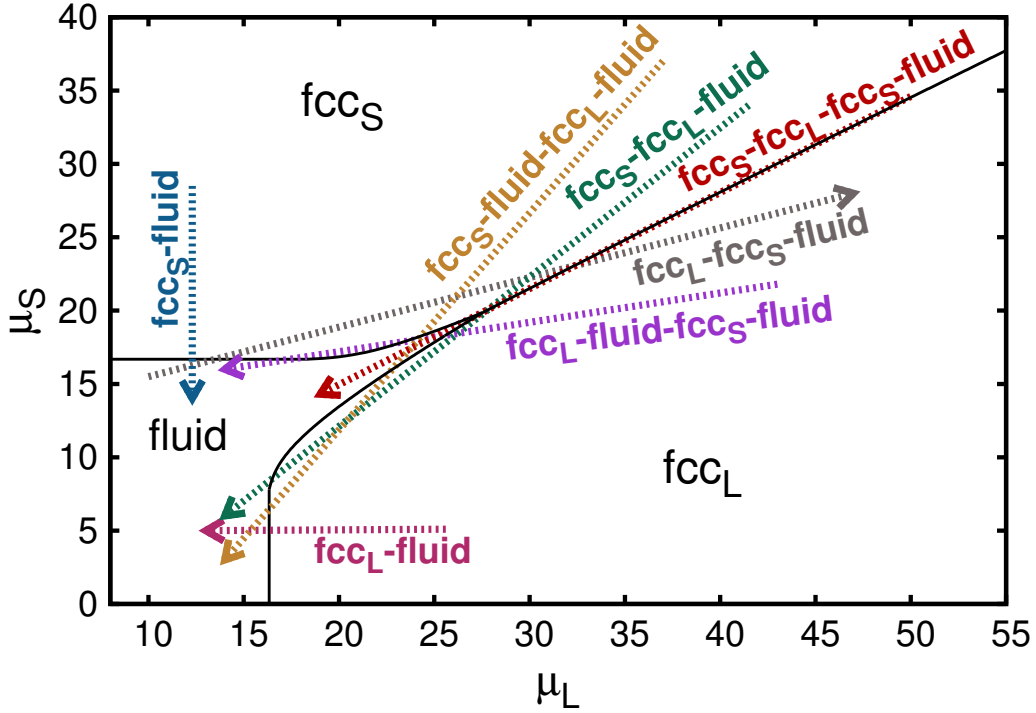


**Figure 3.3:** Bulk phase diagram of a binary mixture of hard spheres with a diameter ratio  $q = 0.85$  in the chemical potential of large spheres  $\mu_L$  – chemical potential of small spheres  $\mu_S$  representation. The solid lines represent the bulk binodals - each point on a binodal represents two phases in equilibrium with each other. The phase transition to the pure fcc of small and large spheres are shown by the horizontal and vertical asymptotic extensions of the respective binodals. The coloured dashed lines represent typical sedimentation paths.

Therefore all sedimentation paths parallel to the horizontal asymptote on the  $\mu_S$ - $\mu_L$  plane yield a vertical line at  $s = 0$  in the corresponding stacking diagram as shown in Fig. 3.4. Similarly, a binodal that involves the pure phase of small spheres corresponds to a vertical asymptote in the  $\mu_S$ - $\mu_L$  plane as the chemical potential  $\mu_S \rightarrow -\infty$ , and hence  $s = -\infty$ . The vertical line  $s = -\infty$  for  $\forall a$  is clearly beyond the scale of Fig. 3.4. In the limit of infinite pressure,  $P \rightarrow \infty$ , the binary mixture demixes into a pure large-sphere close-packed fcc phase with  $\mu_L \rightarrow \infty$  and a pure small-sphere close-packed fcc phase with  $\mu_S \rightarrow \infty$ . However, as can be seen from Fig. 3.3, the slope of this asymptote in the  $\mu_L - \mu_S$  representation approaches a constant corresponding to a vertical line at  $s \simeq 0.65$  in the SD of Fig. 3.4.

### 3.3.3 Bulk phase diagram for $q = 0.82$

Next, we map out the phase diagram for a binary hard-sphere mixture with a slightly smaller diameter ratio, i.e.,  $q = 0.82$  instead of  $q = 0.85$ . We present the resulting phase diagram in the  $\beta P \sigma_L^3 - x_S$  representation in Fig. 3.5, which shows regions where there is a stable LP. In particular, we observe a large  $\text{fcc}_L$ -Laves phase coexistence region for a composition  $x_S < 0.667$  as well as an  $\text{fcc}_S$ -Laves phase coexistence region for  $x > 0.667$  in the pressure range

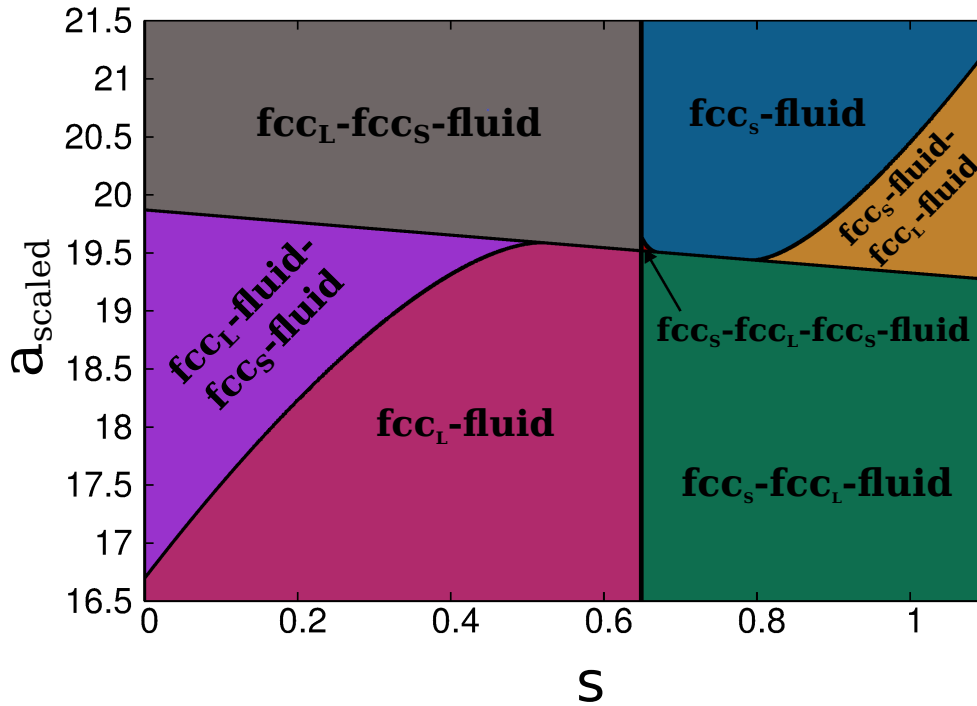


**Figure 3.4:** The stacking diagram for a binary mixture of hard spheres with a diameter ratio  $q = 0.85$ . The coloured regions represent the different stacking sequences of phases observed in a sedimentation column. The regions correspond to the similarly coloured sedimentation paths shown in Fig. 3.3. For visualisation purposes, the  $a$  axis was linearly scaled with respect to  $s$  by a constant  $c$ . The new scaled  $a_{scaled} = a - c \times s$  where  $c = -27$ .

$23.08 \leq \beta P \sigma_L^3 \leq 56.5$ , which lies in between the fluid– $fcc_L$ , fluid– $fcc_S$ , and the  $fcc_L$ – $fcc_S$  phase coexistence regions. Similar to  $q = 0.85$ , we find a stable fluid phase for  $\beta P \sigma_L^3 \leq 11.5$  as expected as this transition point is solely determined by a system of pure hard spheres at  $x_S = 0$ . For a pressure range  $11.5 \leq \beta P \sigma_L^3 \leq 23.08$ , we observe phase coexistence between a fluid and an fcc phase of only large spheres for  $x_S < 0.6608$ . Correspondingly, for  $21.25 \leq \beta P \sigma_L^3 \leq 24.35$  and  $x_S > 0.835$ , the fluid phase coexists with an fcc phase of small spheres. Additionally, there is a coexistence region between a LP and the fluid phase with a composition  $0.667 < x_S < 0.835$  for  $23.0783 \leq \beta P \sigma_L^3 \leq 24.35$ , as well as an extremely narrow coexistence region between a LP and fluid phase with  $0.6608 < x_S < 0.667$  for  $23.0783 \leq \beta P \sigma_L^3 \leq 23.0796$ . The inset of Fig. 3.5 shows a zoom in of this part of the phase diagram. The latter coexistence region was missed in Ref. [28]. At pressures  $\beta P \sigma_L^3 \geq 56.35$ , we observe complete demixing of the two species into two pure fcc phases,  $fcc_L$  and  $fcc_S$ , since this corresponds to the best packing with a packing fraction of  $\eta_L = \eta_S \simeq 0.74$  at infinite pressures. It is worth noting that a LP with a maximum packing fraction of  $\eta \simeq 0.71$  is not the best-packed *binary* crystal structures at  $q = 0.82$  as the  $\alpha IrV$ ,  $\gamma CuTi$ ,  $AuTe_2$ , and  $Ag_2Se$  phases have a higher maximum packing fraction than either one of the LPs, but lower than the close-packed fcc phase [27, 28, 114]. Thus, for finite pressures, the stable crystal structures are not determined by maximum packing, but Gibbs free-energy calculations are required to determine the stable crystal phases.

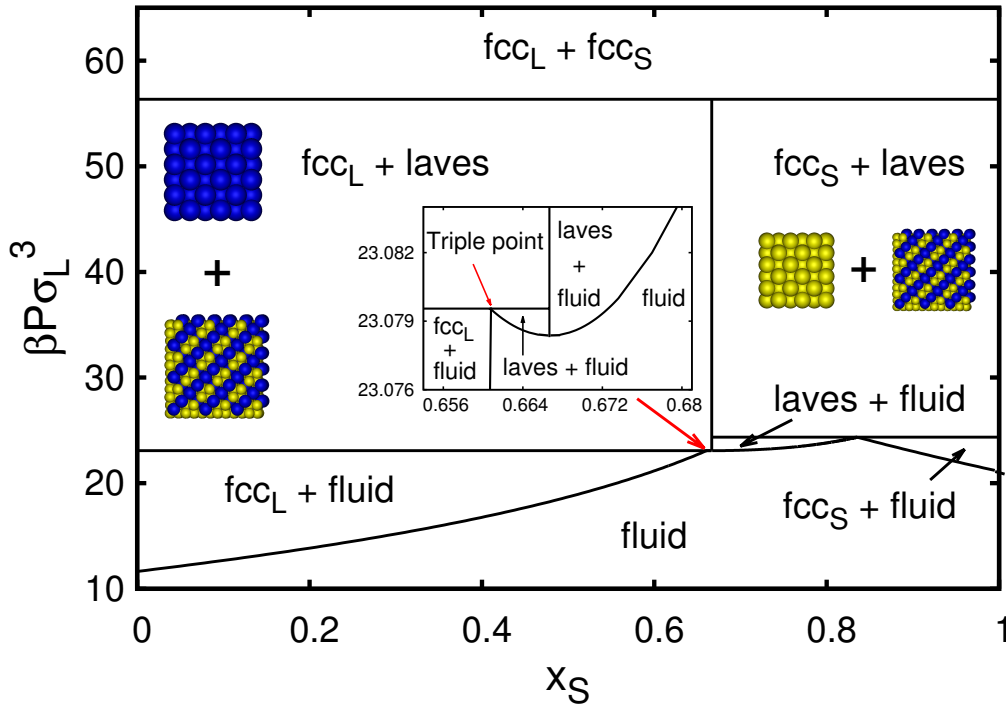


**Figure 3.5:** Bulk phase diagram of a binary hard-sphere mixture with diameter ratio  $q = 0.82$  in the pressure  $\beta P \sigma_L^3$  – composition  $x_S$  representation. The inset shows a zoom-in of the Laves–fcc<sub>L</sub>–fluid triple point.

To summarise, the addition of the stable LP in the phase diagram of  $q = 0.82$  in comparison to that of  $q = 0.85$  results in three additional two-phase coexistence regions, i.e., Laves–fluid, fcc<sub>L</sub>–Laves, and fcc<sub>S</sub>–Laves phase coexistences, as well as three triple points representing in turn either a Laves–fcc<sub>L</sub>–fcc<sub>S</sub>, Laves–fcc<sub>S</sub>–fluid, or Laves–fcc<sub>L</sub>–fluid three-phase coexistence. For completeness, we also present the phase diagram in the  $\eta_L - \eta_S$  plane in Fig. 3.6 to facilitate comparison with experiments. The three triple points that are seen in Fig. 3.5 show up as triangular regions in Fig. 3.6.

### 3.3.4 Stacking diagram for $q = 0.82$

The appearance of an extra phase in the bulk phase diagram leads to a considerably more complicated stacking diagram. In order to determine the stacking diagram, we first convert the bulk phase diagram to the chemical potential  $\mu_S - \mu_L$  plane as shown in Fig. 3.7. We present the stacking diagram in the  $a - s$  representation in Fig. 3.8). The stacking diagram is divided into different regions that are delimited from each other through the following boundaries or features.

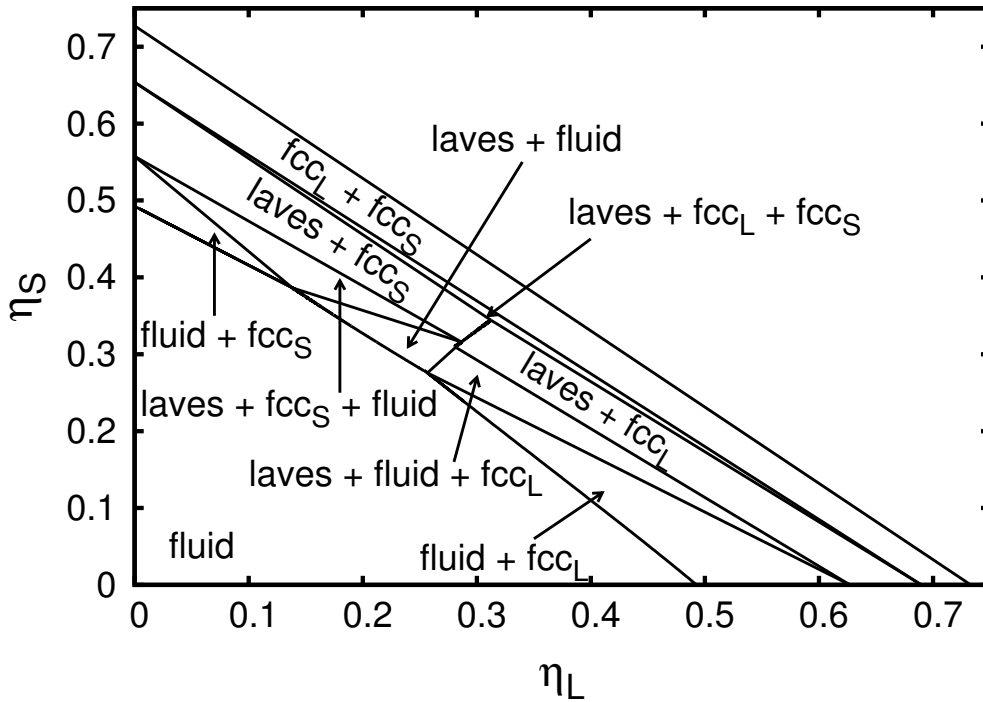


**Figure 3.6:** Bulk phase diagram of a binary mixture of hard spheres with a diameter ratio  $q = 0.82$  in the large-sphere packing fraction  $\eta_L$  – small-sphere packing fraction  $\eta_S$  representation.

1. **Sedimentation binodal:** In this case, we have six bulk binodals corresponding to the six two-phase regions as shown in Fig. 3.5 and 3.7, and as discussed above. The six bulk binodals translate into six sedimentation binodals in the stacking diagram in Fig. 3.8.
2. **Terminal lines:** We have three terminal points of a binodal in the bulk phase diagram of this system:
  - A triple point with Laves– $\text{fcc}_L$ – $\text{fcc}_S$  phase coexistence.
  - A triple point with Laves– $\text{fcc}_S$ –fluid phase coexistence.
  - A triple point with Laves– $\text{fcc}_L$ –fluid phase coexistence.

The three terminal points appear as three terminal lines in the stacking diagram.

3. **Asymptotic terminal lines:** Similar to the  $q = 0.85$  case, there are two binodals that involve a pure-component phase in the bulk phase diagram. These correspond to vertical asymptotic terminal lines at  $s = 0$  in the case that the pure phase consists of large spheres and at  $s = -\infty$  if the pure phase contains only small spheres. The latter does not appear in the stacking diagram as it is beyond the scale of Fig. 3.8. For infinite pressures, the binary mixture demixes into two pure fcc phases with a finite slope of this asymptote in the  $\mu_L - \mu_S$  representation corresponding to a vertical line at  $s \simeq 0.57$  in the SD of Fig. 3.8.

We note that the stacking diagram in Fig. 3.8 includes a region of negative  $s$ , which signifies that one species sediments while the other floats upward due to a negative buoyant mass. In this

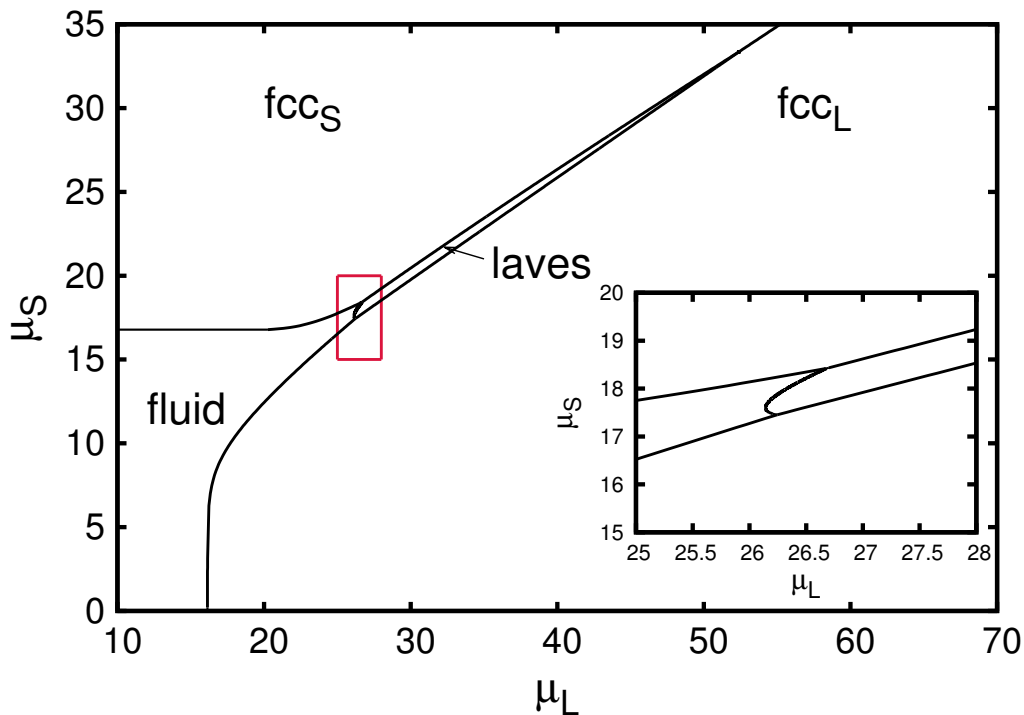


**Figure 3.7:** Bulk phase diagram of a binary mixture of hard spheres with a diameter ratio  $q = 0.82$  in the chemical potential of large spheres  $\mu_L$  – chemical potential of small spheres  $\mu_S$  representation. The solid lines represent the bulk binodals. The phase transition to the pure fcc of small and large spheres are shown by the horizontal and vertical asymptotic extensions of the respective binodals. The inset shows a zoom-in of the two triple points.

work, we assume that the large spheres always sediment signifying that its buoyant mass  $m_L$  is always positive. If the identity of the settling species for the case of negative  $s$  is reversed, then the phases in the stacking sequences in this region are simply reversed. Fig. 3.8 is primarily divided into four broad regions with respect to the value of gravitational variable  $s$ .

1.  $s < 0$ : As mentioned above, a negative  $s$  implies that the large spheres sediment while the small spheres cream up. As a result the large species crystallize at the bottom of the column and the small spheres crystallize towards the top as their density and chemical potential increase in the direction opposite to gravity. At intermediate heights, the system forms a binary fluid phase, which should crystallize to form LPs at sufficiently high chemical potentials, i.e., sufficiently high  $a$ .
2.  $0 < s < 0.57$ : Both species sediment in this regime. However the mass of the large species is higher and hence the large spheres sediment faster. As expected, at sufficiently high bulk chemical potentials (i.e. high concentrations), the large species crystallizes and forms an fcc phase at the base of the column. For low values of  $a$ , the  $\text{fcc}_L$  crystal phase is followed by the fluid phase whereas for higher  $a$  values, crystalline phases such as the Laves or  $\text{fcc}_S$  phases can form.
3.  $0.57 < s < 1$ : This region may seem counterintuitive as the pure component phase formed at the bottom of the sedimentation column is that of the small species, whereas the large

species is still the heavier species. However, the bulk chemical potentials,  $\mu_S^0$  and  $\mu_L^0$ , are chosen such that it corresponds to the  $\text{fcc}_S$  phase at the bottom of the column.

4.  $s > 1$  In this region, the smaller species is heavier and consequently, an  $\text{fcc}_S$  forms at the bottom of the column.

### 3.3.5 Event-Driven Brownian Dynamics

In order to verify our theoretical predictions, we perform simulations at specific state points in the stacking diagram of Fig. 3.8. We perform EDBD simulations using the method as described in Section 3.2.3 on a binary mixture of 100000 hard spheres with a diameter ratio  $q = 0.82$  and number fraction  $x_S = 0.667$ . The cross-sectional area of the simulation box is  $\simeq 50\sigma_L \times 50\sigma_L$ . We set the gravitational length of the large spheres  $l_g^L$  to unity and test the gravitational length ratios  $s = l_g^L/l_g^S = 0.4, 0.68$  and  $1.0$ . We assume that for these gravitational lengths the sedimentation is slow enough that the local density approximation is valid. We set the composition variable  $a$  as defined in Eq. 3.8 by calculating the chemical potentials  $\mu_L^0$  and  $\mu_S^0$  in a bulk mixture without gravity using the Widom particle insertion method [115], for the overall mixture composition and overall packing fraction of the sedimentation box as used in our simulations. The simulation state points  $(s, a)$  are marked with purple crosses in Fig. 3.8.

We first discuss our results for  $s = 0.4$  and  $s = 1.0$  (marked in Fig. 3.8(a)). The initial packing fraction in the column is 0.01. In Fig. 3.9, we present typical configurations of the sedimentation-diffusion equilibria observed. In Figs. 3.9(a) and (b), we colour the larger spheres red and the smaller species green. We clearly observe that the crystal formed at the bottom of the sedimentation column consists predominantly of large spheres at  $s = 0.4$  and of small spheres at  $s = 1.0$ . This is further illustrated by Figs. 3.9(c) and (f) where we have plotted the species density profiles,  $\rho_L(z)$  and  $\rho_S(z)$ , as a function of height  $z$ . The density profiles show discrete peaks at  $z \leq 10\sigma_L$  which indicates layering. To analyze the crystallinity of the sediment, we use the  $q_6$  bond order parameter [68, 116] to determine whether a particle is solid-like or fluid-like. In Figs. 3.9(d) and (e), we colour the solid-like particles with a darker shade than the fluid-like particles, which shows that the sediment at the bottom of the sample is crystalline. Then, using a 2D bond order analysis on the layers of the sediment [112] we identify that the crystalline sediment for  $s = 0.4$  is a predominantly fcc-like crystal of large spheres in magenta with a few hexagonal-close-packed(hcp)-stacked particles coloured in yellow (Fig. 3.9(g)), and an fcc crystal of small spheres with again a few hcp-stacked particles for  $s = 1.0$  (Fig. 3.9(h)). The SD as presented in Fig. 3.8 shows that the fcc crystal formed at the bottom of the sedimentation column consists of large spheres,  $\text{fcc}_L$ , for  $s < 0.57$ , and of small spheres,  $\text{fcc}_S$ , for  $s > 0.57$ . Hence, our simulations are in excellent agreement with the theoretical predictions for  $q = 0.82$ . Interestingly, for  $s = 1.0$ , which signifies that both species sediment at the same rate, the smaller species forms an fcc crystal at the bottom of the column.

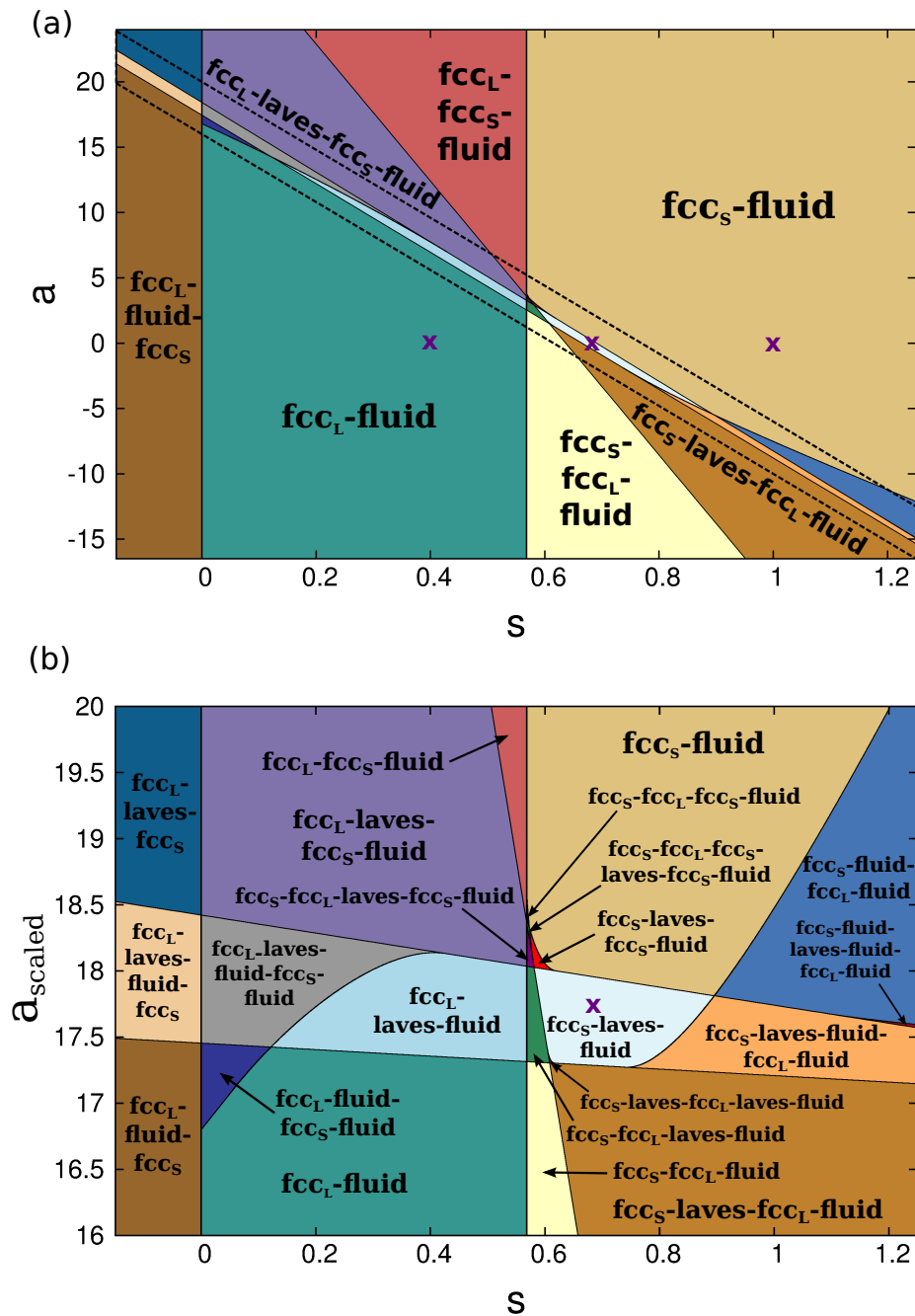


**Figure 3.8:** (a) The stacking diagram for a binary mixture of hard spheres with a diameter ratio  $q = 0.82$ . The coloured regions represent the different stacking sequences of phases observed in a sedimentation column. (b) Zoom-in of a rich section of the stacking diagram marked by a black dashed line in (a), where the  $a$  axis was linearly scaled with respect to  $s$  by a constant  $c$  for visualisation purposes. The new scaled  $a_{scaled} = a - c \times s$  where  $c = -26$ . The purple crosses denote state points for EDBD simulations.

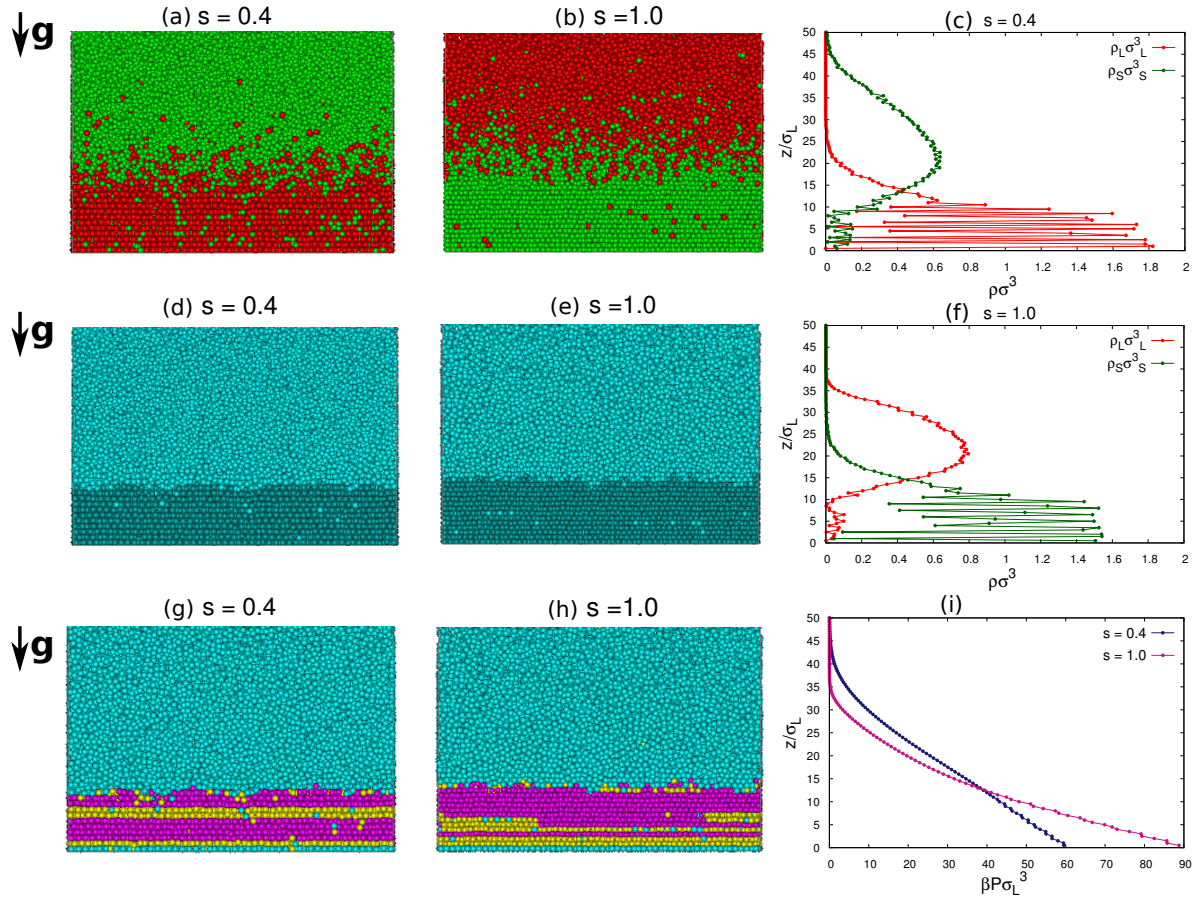


**Figure 3.9:** Typical configurations of a sedimentation-diffusion equilibrium as obtained from EDBD simulations of a binary mixture of hard spheres with a diameter ratio  $q = 0.82$  and a gravitational length ratio  $s = l_g^L/l_g^S = 0.4$  (left) and 1.0 (right) with  $l_g^L = 1$  at  $t/\tau_{MD} = 50000$ . The state points of these simulations are shown as purple crosses in Fig. 3.8. (a),(b) The particles are coloured according to their size. Red denotes the large spheres and green represents the small spheres. (d),(e) The particles are coloured according to a  $q_6$  bond order parameter analysis to distinguish the solid-like particles from the fluid-like particles. The solid-like particles are denoted by a darker shade of cyan than the fluid-like particles. (g),(h) The particles are coloured according to the crystal type. Magenta denotes fcc-stacked particles, yellow denotes hcp-stacked particles, cyan denotes the fluid-like particles. (c),(f) Density profiles  $\rho_{L/S}(z)$  of the two species as a function of the height  $z$ . (i) Pressure  $\beta P(z)\sigma_L^3$  as a function of  $z$ .

Additionally, we calculate the pressure along the column by integrating the density profile along the direction of gravity. Fig. 3.9(i) shows the pressure profile in the column from which we find that the pressure  $\beta P(z=0)\sigma_L^3 \approx 60$  for  $s = 0.4$  and  $\approx 90$  for  $s = 1.0$ . The pressure at the bottom of the column  $\beta P(z=0)\sigma_L^3$ , where the gravitational potential equals 0, directly relates to the bulk phase diagram of Fig. 3.5. These values for the pressure correspond to the  $\text{fcc}_L$ – $\text{fcc}_S$  coexistence region in Fig. 3.5, and one might naively expect to find a phase-separated fcc phase at the bottom of the sediment. However, from Fig. 3.7 it becomes evident that the crystal at this specific pressure value at the bottom of the sediment corresponds most probably to one of the pure fcc phases since only one unique combination  $(\mu_L(x_S, P, T), \mu_S(x_S, P, T))$  corresponds to a point exactly on the binodal.

As the fcc phases crystallize in accordance with our theoretical predictions, we next attempt to self-assemble the  $\text{MgCu}_2$  LP structure. This is a significant challenge when one considers that the spontaneous self-assembly of LP structures has never been observed in ‘brute force’ simulations of binary hard-sphere mixtures, even in the absence of a gravitational field. We perform simulations as before on a binary hard-sphere mixture for the following simulation parameters:  $q = 0.82$ ,  $x_S = 0.667$ ,  $s = l_g^L/l_g^S = 0.68$ . The initial overall packing fraction of the column is 0.1. This simulation state point is shown in Fig. 3.8 as a purple cross representing a specific point  $(s, a) = (0.68, 0.0537)$ . The expected stacking sequence for this state point from bottom to top of the sedimentation column is  $\text{fcc}_S$ –Laves–fluid. We suspect that the formation of a binary crystal phase on top of a single-component fcc phase may be hampered by kinetic constraints. For example, the particles may get arrested in the holes of the fcc phase and may not have sufficient time to equilibrate to the desired LP structure. Additionally there may be energetic constraints as the formation of an interface between two crystal phases may be energetically unfavourable. Therefore we truncate the stacking sequence and set the pressure to a lower value  $\beta P(z=0)\sigma_L^3 \simeq 30$  such that the phase at the bottom of the column corresponds to the Laves phase. Also keeping in mind that the interfacial tension between the smooth wall and the hexagonal geometry is the lowest among known geometries [86], it is probable that the first layer in contact with the wall attempts to partially order into hexagonal order as the composition in the layer would be  $x_S > 0.667$ . In order to eliminate this possibility, but more importantly, to selectively form the  $\text{MgCu}_2$  LP structure, we template the bottom wall with the (110) cross-sectional plane of the  $\text{MgCu}_2$  LP crystal in accordance with the study by Hynninen *et al.* [27]. The density that we choose for our template needs to be high enough to (i) restrain the incoming particles in-plane [49, 112] and (ii) minimize substitutional ordering of species. However it should not be so high that there is a density mismatch between the first crystalline layer and the template [112] at  $\beta P(z=0)\sigma_L^3 \simeq 30$ . Keeping these factors in mind the packing fraction of the  $\text{MgCu}_2$  (110) template (shown in Figs. 3.10(a)-(c)) that we use is 0.656. In Fig. 3.10(d) we show the first layer of particles that sediment on the template. If we look closely at this layer, and zoom-in to the section enclosed within the black box (shown in Fig. 3.10(e)), we observe that the particles sit at the lattice positions in direct comparison with the template below. Interestingly, we observe that the first layer displays the characteristic ‘‘six-bead’’ ordering of the small species which is also typical of the  $\text{MgCu}_2$  (110) template (Fig. 3.10(f)). We have highlighted these ‘‘six-bead’’ sequences formed by the small species by black lines. For exact comparison, we first draw these connecting black lines on the template, reproduce them unaltered in scale and orientation on Fig. 3.10(e), and subsequently shift them so that they approximately run through the center of the first layer particles. As a result of this, some order

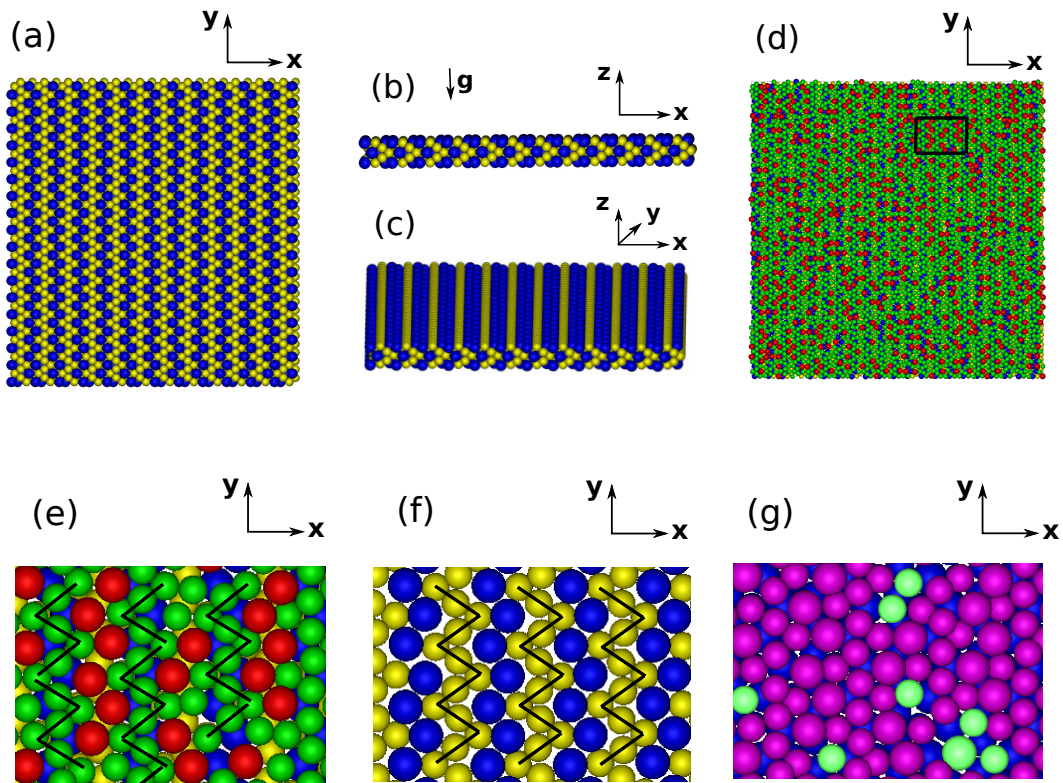


**Figure 3.10:** Typical configuration of the first layer of a binary mixture of hard spheres with a diameter ratio  $q = 0.82$  sedimenting on a  $\text{MgCu}_2$  (110) template as obtained from EDBD simulations using a gravitational length ratio  $s = l_g^L/l_g^S = 0.68$  with  $l_g^L = 1$  at  $t/\tau_{MD} = 45000$ . (a),(b),(c) Blue and yellow denote the large and small hard spheres of the template, respectively. (d),(e) Red denotes the large spheres and green represent the small spheres of the sedimenting mixture. (f) shows the ordering of the two species on the template. Black lines are used to highlight the patterning/ordering. (g) To indicate the substitutional ordering, the on-lattice species are coloured in purple and the substitutionally ordered species are highlighted in fluorescent green.

mismatches (*i.e.* tips of the black lines do not meet) are evident in the first layer. On closer inspection, these mismatches appear when there is substitutional ordering in the local environment. Substitutional ordering refers to spheres that sit at lattice positions irrespective of their identity, *i.e.*, a small sphere may be positioned on a large sphere lattice location and vice versa. Also worth noting is that these six-bead small species arrangements stack on the larger species of the template, which is also commensurate with how the two species stack on a perfect  $\text{MgCu}_2$  (110) template. This kind of stacking is particularly interesting when one considers that there are no interactions between the species and that the two species are very comparable in size ( $q = 0.82$ ). We depict substitutional ordering in Fig. 3.10(g) by colouring the particles that sit at the right lattice positions in purple and those that are positioned at the wrong lattice positions in fluorescent green. From this figure, it is also clear that substitutional defects also result in an increase in the number of defects in their local environments, which hampers the formation of the  $\text{MgCu}_2$  LP. We therefore suspect that short-ranged repulsive or attractive potentials may be required to better direct the (templated) self-assembly. We surmise that attractive interactions

between unlike species [106] and/or repulsive interactions between like species may assist the ordering of the  $\text{MgCu}_2$  LP during the sedimentation. We leave this for a future study.

### 3.4 Conclusions

To summarise, we have studied the sedimentation behaviour of a binary mixture of hard spheres with a size ratio  $q$  for which there is a stable LP in the thermodynamic bulk phase diagram. We first construct the stacking diagram (SD) that describes the possible stacking sequences of stable phases in a sedimentation-diffusion equilibrium using the bulk phase diagram of the system in the chemical potential plane as input. We discuss in detail the features of the SD which delimit the regions representing unique phase stacking sequences, in relation to the corresponding bulk phase diagram. Specifically, we calculate the SD for  $q = 0.85$  for which there is no stable LP, and for  $q = 0.82$  for which there is a thermodynamically stable LP in a certain pressure range. We observe that the SD increases considerably in complexity with the entry of an extra stable phase in the bulk phase diagram. More specifically, the SD for  $q = 0.85$  shows 7 unique stacking sequences in Fig. 3.4, whereas the SD for  $q = 0.82$  shows 18 (+2, not shown) stacking sequences in Fig. 3.8. We also observe for both size ratios  $q$  stacking sequences that contain floating crystalline phases.

We then select specific state points in the SD for  $q = 0.82$ , and employ event-driven Brownian Dynamics (EDBD) simulations to investigate the sedimentation behaviour for a binary hard-sphere mixture in relation to our theoretical predictions. The first two simulation state points that we select for the purposes of comparison are (the ratio of buoyant masses  $s$ , the composition variable  $a$ ) =  $(0.4, 0.033)$  and  $(s, a) = (1.0, -0.025)$ , in order to observe the reversal of the fcc phase that forms at the bottom of the sedimentation column. Our EDBD simulations indeed demonstrate that the large spheres crystallize at the bottom of the sediment into an  $\text{fcc}_L$  phase for  $s = 0.4$ , whereas the smaller spheres form the  $\text{fcc}_S$  phase at the bottom of the column for  $s = 1$  in agreement with our stacking diagram.

As the “reversal” of the single-component fcc phase agrees with our theoretical predictions, we then attempt to self-assemble the  $\text{MgCu}_2$  LP using EDBD simulations. For this purpose, we template the bottom of the sedimentation column with the (110) plane of a  $\text{MgCu}_2$  crystal [27]. We select the simulation parameters from a third state point in our SD which corresponds to the  $\text{fcc}_S$ -Laves-fluid phase stacking sequence from bottom to top in a sediment-diffusion equilibrium. In order to bypass the kinetic and energetic constraints in the formation of a binary crystal on top of a single-component fcc phase, we truncate the sedimentation path by setting the maximum pressure to  $\beta P(z=0)\sigma_L^3 \simeq 30$  so that the pressure at the bottom of the sediment corresponds to the  $\text{MgCu}_2$  LP. A closer inspection of the first layer that sediments on the template reveals the characteristic “six-bead” sequences of small spheres that are predominantly stacked on top of the large species in the template. This is particularly interesting if one considers that there is no energetic interactions between the two species and the stacking arrangement is driven by entropy alone. Furthermore, the first layer of particles also displays substitutional ordering of species on the template i.e. spheres are positioned at lattice positions of the template irrespective of their identity. The occurrence of such a “substitutional defect” is seen to lead to an increase in local defects. From an entropic point of view, we expect that the  $\text{MgCu}_2$  LP possesses a finite equilibrium concentration of substitutional defects. We leave

the explicit calculations of the free energy as a function of the equilibrium defect concentration for future investigations. The presence of substitutional defects hinders further growth of the  $\text{MgCu}_2$  structure. We postulate that short-ranged repulsive or attractive interactions may be required to direct the self-assembly of the  $\text{MgCu}_2$  LP on the template. This will be studied in more detail in our next study.

## **Acknowledgements**

I thank Rik Koster and Somil Gupta for useful discussions on templating. John Edison, Harini Pattabhiraman and Guido Avvisati are sincerely thanked for useful discussions. I gratefully acknowledge Chris Kennedy and Douglas Hayden for critical reading of this Chapter.



---

## **Stabilizing the Hexagonal Close Packed Structure of Hard Spheres with Polymers: Phase diagram, Structure, and Dynamics**

---

We study the phase behaviour of a binary mixture of colloidal hard spheres and freely-jointed chains of beads using Monte Carlo simulations. Recently Panagiotopoulos and coworkers predicted that the hexagonal close packed (HCP) structure of hard spheres can be stabilized in such a mixture due to the interplay between polymer and the void structure in the crystal phase [117]. Their predictions were based on estimates of the free-energy penalty for adding a single hard polymer chain in the HCP and the competing face centered cubic (FCC) phase. Here we calculate the phase diagram using free-energy calculations of the full binary mixture and find a broad fluid-solid coexistence region and a metastable gas-liquid coexistence region. For the colloid-monomer size ratio considered in this work, we find that the HCP phase is only stable in a small window at relatively high polymer reservoir packing fractions, where the coexisting HCP phase is nearly close packed. Additionally we investigate the structure and dynamic behaviour of these mixtures.

## 4.1 Introduction

Colloidal self-assembly is a promising and viable approach to fabricate new designer materials. Recent advancements in colloid chemistry have enabled the synthesis of a wide variety of building blocks, with immense control over the size, shape and functionality. This has opened the possibilities to fabricate via self-assembly, a vast variety of hierarchical structures. Very often the targeted structure cannot be accessed due to kinetic traps or due to competing crystal morphologies, which differ very little in free energy. It is the latter problem we deal with in this work. A well-known example of this problem is the crystallization of colloidal particles that are hard-sphere-like. It is well-established that the stable crystal structure of hard spheres is the face centered cubic (FCC) structure [54, 118]. The hexagonal close packed (HCP) structure, which differs from the FCC structure only by the stacking order of the hexagonal planes of spheres, costs an extra free energy of  $O(10^{-3}k_B T)$  per particle. This minute free-energy difference between the two competing structures results in crystallization of the hard-sphere fluid into a random hexagonal close packed (rHCP) phase of which the stacking sequence is random [55, 57, 61, 65]. Binary mixtures of hard spheres with a diameter ratio of  $\simeq 0.8$  show a similar behaviour, where three different crystalline structures, the so-called binary Laves phases  $\text{MgCu}_2$ ,  $\text{MgZn}_2$ , and  $\text{MgNi}_2$ , differ very little in free energy [28]. The  $\text{MgCu}_2$  structure can be used to fabricate photonic crystals with a bandgap in the visible region [27] and therefore a strategy to selectively stabilize this structure is of technological importance.

One approach to target a certain polymorph from its competing structures is to tune the interactions between the colloids in a suitable manner. Significant efforts have been undertaken in the last decade to devise strategies to tune colloidal interactions; some examples are the addition of polymer depletants [119] and tuning of salt concentration in systems of charged colloids. Recently, Mahynski *et al* [117] have shown via computer simulations that in a system of colloids which can exhibit more than one competing crystalline structure, addition of non-adsorbing polymers with a carefully chosen architecture can stabilize one polymorph over all the others. This observation has served as the motivation for our work in this paper. Using computer simulations, Mahynski *et al.* showed that the free-energy penalty incurred to add a freely-jointed chain of hard beads to the FCC and HCP crystal of hard spheres, which are kept at the same packing fraction, differed significantly beyond a certain chain length of  $M$  beads. The polymers exhibited a clear preference to reside in the void space of one crystal polymorph over the other. Mahynski *et al* attributed the observed preference, to the difference in distribution of void spaces between the two competing (FCC/HCP) polymorphs in the hard-sphere system.

While at a fixed colloid packing fraction both HCP and FCC structures possess the same amount of total void space, their distribution in space or connectivity, which places constraints on the possible conformations adopted by the polymer, is very different. Note that by void space we do not refer to vacancies on the crystal lattice, but just the free volume available to the polymer, which is as large as 26% in a close-packed hard-sphere crystal since the maximum colloid packing fraction is  $\eta_{cp} \simeq 0.74$ . The shape of the voids in a hard-sphere crystal can be described by polyhedra [117]. In both the FCC and the HCP structure the void space consists of one octahedral void (OV) and two tetrahedral voids (TV) per particle. The free volume of an OV, as given by the size of the largest inscribed sphere, is about 6 times larger than a TV. Furthermore, for both the FCC and HCP structure, the void arrangement is the same in the plane of the hexagonal layers, i.e., OVs only share faces with TVs. However, the crucial

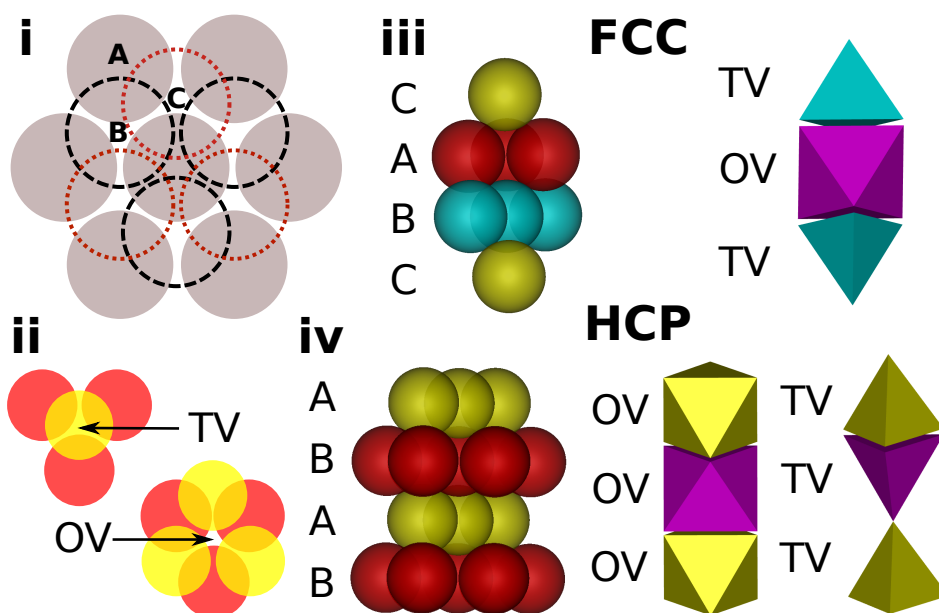


**Figure 4.1:** (i) Schematic of the stacking of hexagonal layers found in an FCC lattice shown from a top view, for which the stacking sequence follows  $..ABCABC..$ . For an HCP lattice, the stacking sequence follows  $..ABAB..$  (ii) Schematic of an octahedral void (OV) and a tetrahedral void (TV). (iii) Side view of the stacking of the hexagonal layers, and void distribution in a perfect FCC structure. Two OVs do not share a face in the FCC structure, the connection between two neighbouring OVs is interrupted by a TV. (iv) Side view of the stacking of the hexagonal layers, and void distribution in a perfect HCP structure. There are two kinds of void connectivities observed, and here two adjacent OVs indeed share a common face.

difference between FCC and HCP lies in the connectivity of the OVs and TVs in the direction perpendicular to the hexagonal layers. In the FCC lattice, each unit cell has a octahedral void (OV) in the middle capped by smaller tetrahedral voids (TV), and hence the larger OVs in the FCC structure are all isolated from each other. On the other hand in the HCP structure, the OVs are stacked on top of each other and share faces, whereas TVs are likewise stacked and share either a face or a vertex in the direction perpendicular to the hexagonal planes. An illustration of the void connectivity in the FCC and HCP structures is shown in Fig. 4.1.

Therefore a hard-bead chain which requires more free space than provided by a single OV void, prefers the HCP structure where neighbouring OVs are easily accessible, as they are merely stacked on top of each other. In the FCC structure the same polymer chain has to incur a higher free-energy penalty as it has to find its way through a much narrower TV. Hence Mahynski *et al* predicted that a system of colloids and polymer depletants should display a stable HCP crystal phase under certain conditions. In this work we affirm their predictions by computing the phase diagram of a binary mixture of hard spheres and freely-jointed chains of hard beads as depletants.

This Chapter is organised as follows. In Section 4.2 we describe our model of a colloid-polymer mixture and the techniques we use to calculate the phase diagram. In Section 4.3 we present our results on the phase behaviour and structure of the model. Finally we discuss the

relevance of our studies to experimental studies on colloid-polymer mixtures and summarise our conclusions in Section 4.4.

## 4.2 Model and Methods

We consider a binary mixture consisting of hard spheres with size  $\sigma_c$  and freely-jointed hard bead chains. The chains, which model linear homopolymers, are composed of  $M$  monomer beads of size  $\sigma_m$ . The bond length between bonded monomers is constrained to a distance of  $\lambda \sigma_m$ . All non-bonded interactions of the system are assumed to be hard-sphere-like and set by the no-overlap condition.

$$U(r_{ij}) = \begin{cases} \infty & r_{ij} < \sigma_{ij} \\ 0 & \text{otherwise} \end{cases} \quad (4.1)$$

Here  $r_{ij}$  and  $\sigma_{ij}$  denote the radial center-of-mass distance and mean diameter between a pair of spheres or beads,  $i$  and  $j$ . The bonded interactions between the beads read

$$U_{bond}(r_{ij}) = \begin{cases} \infty & r_{ij} < \sigma_m \\ 0 & \sigma_m \leq r_{ij} \leq \lambda \sigma_m \\ \infty & r_{ij} > \lambda \sigma_m \end{cases} \quad (4.2)$$

In this work, we fix the diameter ratio of the monomer beads and colloids to  $q = \sigma_m/\sigma_c = 1/7$ , and set  $\lambda = 1.1$ . We investigate polymer chain lengths equal to  $M = 10$  and  $M = 14$  beads and compare the colloid-polymer phase diagrams. Our methodology to compute the phase diagram directly follows the work of Dijkstra and Evans [32, 120]. To compute the phase diagram it is convenient to study the system in the fixed  $\{N_c, z_p, V, T\}$  ensemble. Here  $N_c$  denotes the number of colloids,  $z_p = \exp[\beta \mu_p]/\Lambda_p^3$  is the fugacity of the hard bead chains,  $\mu_p$  the chemical potential of the bead chains,  $T$  is the temperature,  $\beta = 1/k_B T$ ,  $\Lambda_p$  the thermal wavelength of the polymer, and  $V$  is the volume. The exact free energy of the system in this ensemble  $F(N_c, z_p, V, T)$ , is given by the following identity.

$$\begin{aligned} \beta F(N_c, z_p, V) &= \beta F(N_c, z_p = 0, V) + \int_0^{z_p} \left( \frac{\partial \beta F(N_c, z'_p, V)}{\partial z'_p} \right) dz'_p \\ &= \beta F(N_c, z_p = 0, V) - \int_0^{z_p} \frac{\langle N_p \rangle_{z'_p}}{z'_p} dz'_p \end{aligned} \quad (4.3)$$

The first term of the right hand side is just the Helmholtz free energy of a pure system of  $N_c$  colloidal hard spheres in volume  $V$ . We use the Carnahan-Starling free-energy expression for the fluid phase, while for the solid phase we use the Frenkel-Ladd method to obtain accurate estimates of the free energies of FCC and HCP crystal phases of system size  $N_c = 108$  spheres. The second term is the excess contribution that arises due to the presence of hard-bead chains in the system, where  $\langle N_p \rangle$  is the average number of polymers present in a system with  $N_c$  colloids in equilibrium with a polymer reservoir fixed at fugacity  $z_p$ . The ‘‘adsorption’’ of polymer chains onto a system of  $N_c$  colloids in a volume  $V$  can be measured directly in a Monte Carlo

simulation, where the polymer is treated grand canonically. Subsequently, we estimate the densities of the coexisting phases at a given  $z_p$  by performing common tangent construction on the resulting  $\beta F(\eta_c, z_p)/V$  vs  $\eta_c$  data. Here  $\eta_c$  is the colloid packing fraction. More details can be found in the Appendix of Ref. [32].

### 4.2.1 Configurational Bias Monte Carlo Method

As stated in the previous section, to compute the Helmholtz free energy  $\beta F(N_c, z_p, V)$ , we measure the “polymer adsorption”  $\langle N_p \rangle$  onto a system of  $N_c$  colloids in volume  $V$  from a Monte Carlo simulation at fixed polymer fugacity  $z_p$ . In simulations of chain molecules the biggest bottleneck lies in generating trial configurations that are likely to be accepted. A vast majority of the trial configurations result in overlaps with other chain molecules or colloids. One strategy to overcome this issue is to bias the generation of trial configurations. The bias can then be accounted for by modifying the Monte Carlo acceptance factors suitably. The configurational bias Monte Carlo (CBMC) method uses the Rosenbluth scheme to generate trial configurations. In this method, we grow the polymer chain bead by bead. In order to add a bead, we generate first a fixed number of trial positions, say  $k$ , and calculate the associated Boltzmann weight. We choose a certain trial position among the  $k$  options, with a probability proportional to its Boltzmann weight. In this way, we generate trial configurations that are more likely to be accepted. More details on the implementation of this method can be found in the following references [115, 121]. We employ CBMC in our simulations to insert/delete/translate the polymer chains. A single sweep in our simulations consists of the following steps: i) translation moves of all particles in the system, ii) 2000 configurational bias moves which are equally split between polymer translation, insertion and deletion.

The measurement of  $\langle N_p \rangle$  requires a simultaneous canonical averaging of the colloid (big species) configurations. At the chosen colloid-monomer size ratio  $q = 1/7$ , we find that the colloids sample the configuration space efficiently, with just single particle moves. At a few state points we have employed the rejection-free event-chain Monte Carlo [122] algorithm, which helps the colloids to sample the configuration space more efficiently. The adsorption isotherms computed with and without the event chain moves are indiscernible. This indicates that the rate limiting steps for equilibration are the polymer addition/deletion moves.

### 4.2.2 Transition Matrix Monte Carlo method

To obtain an accurate estimate of the adsorption of polymer onto a system of  $N_c$  colloids in volume  $V$  as a function of fugacity  $z_p$ , we employ the Transition Matrix Monte Carlo (TMCMC) method, developed by Fitzgerald and coworkers [123, 124]. In a typical simulation at fixed  $\{N_c, z_p, V, T\}$ , the number of polymers  $N_p$  fluctuates around an equilibrium value. Using TMCMC, we measure the probability of observing a certain number of polymers in the system  $P(N_p)$ . The technique involves performing the same simulation as mentioned above in Section 4.2.1 together with a few bookkeeping steps.

After every insertion ( $N_p \rightarrow N_p + 1$ ) and deletion ( $N_p \rightarrow N_p - 1$ ) in a configurational bias Monte Carlo move for a polymer chain, we update a collection matrix  $C$  in the following fash-

ion.

$$\begin{aligned} C(N_p \rightarrow N_p + \delta N_p) &= C(N_p \rightarrow N_p + \delta N_p) + a(N_p \rightarrow N_p + \delta N_p) \\ C(N_p \rightarrow N_p) &= C(N_p \rightarrow N_p) + 1 - a(N_p \rightarrow N_p + \delta N_p) \end{aligned} \quad (4.4)$$

Here  $a$  is the configurational bias acceptance probability of the proposed move. Note that the collection matrix is updated regardless of the move being accepted or rejected. The dimension of the collection matrix is  $\{3, N_p^{max} + 1\}$ , where  $N_p^{max}$ , is a chosen upper limit of the range we wish to sample. Since we attempt to add or remove a single chain in each configurational bias Monte Carlo move,  $\delta N_p$  is  $\pm 1$ . Periodically during the simulation we use the information obtained via bookkeeping to compute a biasing function  $\Phi(N_p)$ . To compute  $\Phi(N_p)$ , we estimate transition probabilities  $W(N_p \rightarrow N'_p)$  using the data in the collection matrix  $C$ .

$$W(N_p \rightarrow N'_p) = \frac{C(N_p \rightarrow N'_p)}{\sum_{N''_p} C(N_p \rightarrow N''_p)} \quad (4.5)$$

The summation runs over the three possible states of  $N'_p$ , which are  $N_p + 1, N_p - 1$  and  $N_p$ . The Monte Carlo detailed balance expression is then employed to estimate the probability distribution  $P(N_p)$ .

$$P(N_p)W(N_p \rightarrow N'_p) = P(N'_p)W(N'_p \rightarrow N_p) \quad (4.6)$$

The biasing function is given by,  $\Phi(N_p) = -\ln(P(N_p))$  and the proposed polymer addition or removal moves are then accepted or rejected based on a biased acceptance criterion,  $\min\{1, a \exp(\Phi(N_p + \delta N_p) - \Phi(N_p))\}$ . Note that the collection matrix  $C$  is always updated with the unbiased acceptance probabilities. The simulation continues until the biasing function (probability distribution) converges within a preset tolerance. A more detailed description of this method can be found in the work of Errington [123, 125]. The output from a TMMC simulation is the probability of observing a certain number of polymer  $N_p$  in the system at a fixed fugacity  $z_p$ . We use this information to estimate the probability distribution at any other value of fugacity  $z'_p$  using the histogram re-weighting technique [126]. The average number of polymers  $\langle N_p \rangle$  at a fixed fugacity  $z'_p$ , is the first moment of the reweighted distribution  $P(N_p; z'_p)$ .

## 4.3 Results

### 4.3.1 Motivation: Thermodynamics of a freely-jointed polymer in a rigid colloidal framework

In the absence of polymers or for very short polymer chain lengths, hard spheres are experimentally observed to form the rHCP (random hexagonal close-packed) structure [55, 61, 97] on crystallization, although thermodynamics suggests that over longer time scales they may rearrange into the stable FCC structure [57]. However for a polymer chain length which is long enough to span two or more neighbouring voids, the HCP structure is shown to be thermodynamically and kinetically more favourable than the FCC structure [117], purely owing to the difference in the distribution of voids in both structures. In order to study the effect of chain

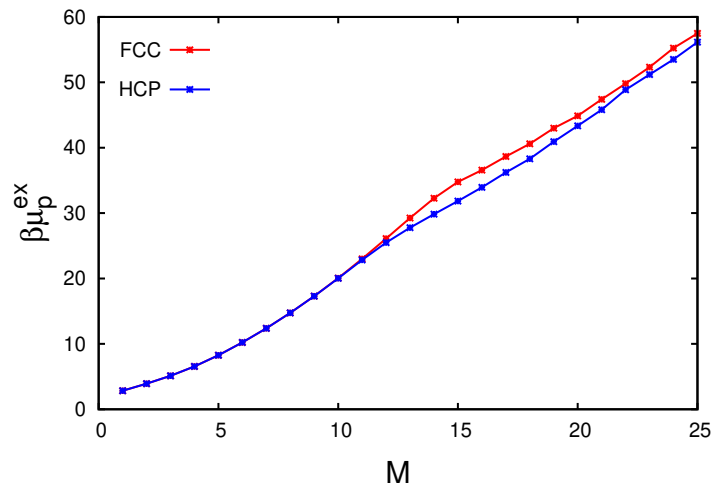


**Figure 4.2:** Excess chemical potential  $\beta\mu_p^{ex}$  difference (free-energy penalty) from inserting a single polymer chain inside the FCC and HCP crystal structures, as a function of the number of monomer hard beads  $M$ .  $\eta_c = 0.707$ . Size ratio  $q$  of monomer bead to hard-sphere colloid =  $1/7$ . Data is averaged over three independent runs.

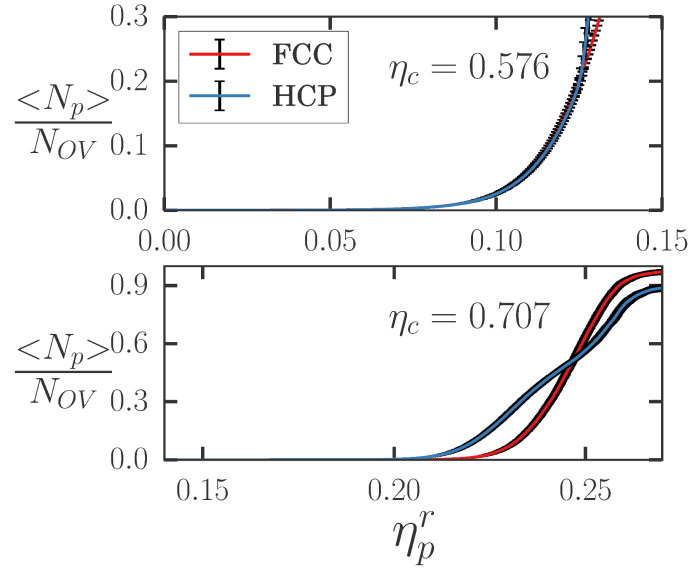
length on the free-energy penalty to insert a single polymer chain inside the FCC and HCP structures, we calculate the excess chemical potential of a polymer chain as a function of the number of monomer beads  $M$  in the colloidal crystal of packing fraction  $\eta_c$ . In Fig. 4.2, we present our results and find a clear difference in free-energy penalty for  $M > 12$  in favour of the HCP polymorph. We therefore compute in this work, phase diagrams of colloidal hard spheres and freely-jointed chains of hard monomer beads for two polymer chain lengths:

1. bead chains of  $M = 10$  monomers, for which the difference in the excess chemical potential (free-energy cost) from inserting a single polymer chain in the colloidal FCC crystal with respect to the HCP crystal is of the order of  $O(10^{-2}k_B T)$ , in favour of HCP. Therefore (i) the polymer chain insertion thermodynamically favours the HCP and (ii) the free-energy difference on insertion is an order of magnitude higher than the free-energy difference between the FCC and HCP phases without polymer ( $O(10^{-3}k_B T)$ ).
2. bead chains of  $M = 14$  monomers, for which the difference in free-energy penalty of inserting a single polymer chain is significantly higher  $\sim 2.44 k_B T$  (Fig. 4.2), in favour of the HCP polymorph.

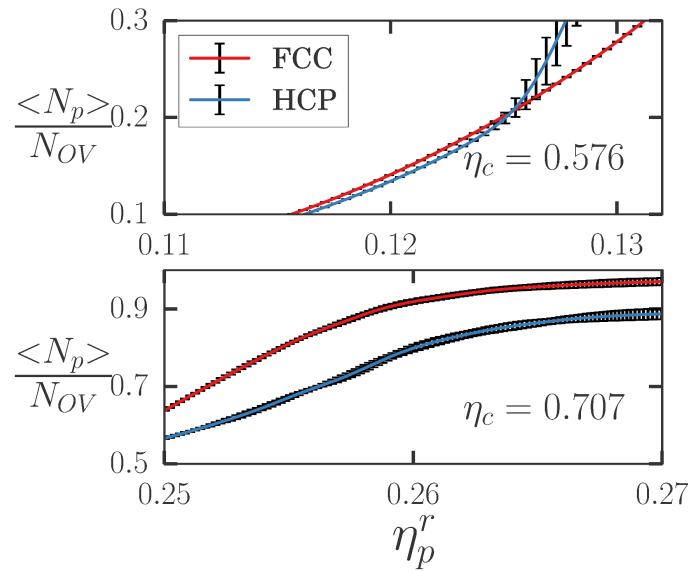
The two phase diagrams, shown later in Section 4.3.3, provide a comparative picture of the relative stability of the FCC and HCP colloidal polymorphs at high polymer depletant concentrations for the two polymer chain lengths mentioned above.

### 4.3.2 Polymer adsorption as a function of colloid packing fraction

In this section, we show the adsorption isotherms for bead chains with  $M = 14$  for a binary mixture of colloidal hard spheres and polymer chains with a diameter ratio of the monomer and colloid of  $q = \sigma_m/\sigma_c = 1/7 \simeq 0.143$ . We choose these specific values of  $M$  and  $q$ , because (i)



(a)



(b)

**Figure 4.3:** a) The average number of adsorbed polymers per octahedral void  $\langle N_p \rangle / N_{OV}$  in the HCP (blue) and FCC (red) polymorphs as a function of the polymer reservoir packing fraction  $\eta_p^r$  at two different colloid packing fractions  $\eta_c = 0.576$  (top) and  $\eta_c = 0.707$  (bottom). The  $\langle N_p \rangle / N_{OV}$  reported in this figure is the mean of  $\langle N_p \rangle / N_{OV}$  computed from five statistically independent runs. The size of the (black vertical) error bars is given by the root mean squared deviation of the five runs with respect to the mean. b) Same as a) with the scales of both axes changed to clearly view the error bars at high  $\eta_p^r$ .

previous studies showed that the free-energy penalty to insert such a polymer greatly favours the HCP structure at sufficiently high colloid packing fraction  $\eta_c$  [117] and (ii) our own calculations (Ref: Section 4.3.1), which support the finding of an appreciably higher free-energy penalty for inserting a polymer chain of this length in the FCC with respect to the HCP structure. It is worth mentioning that the system studied here is composed of hard polymer chains and hard colloids, whereas in Ref. [117] soft repulsive (Weeks-Chandler-Andersen) potentials were employed to model colloid-colloid and colloid-polymer interactions. We choose to use hard interactions for two reasons: (i) the Helmholtz free energy of pure hard spheres is well-known, and (ii) hard interactions are computationally less expensive than soft repulsive interactions. However, we do not expect any qualitative difference in the phase behaviour between the two models. We treat the polymer chains in the grand canonical ensemble, i.e., we fix the polymer fugacity  $z_p$ . We also fix the colloid packing fraction  $\eta_c$ . In simulations, where the colloids are crystalline we fix the number of colloids at  $N_c = 108$ , and choose box-dimensions accordingly. For the fluid phase, we fix the linear dimension of the cubic box as  $L = 30\sigma_m$  and choose  $N_c$ . We measure the average number of polymer chains  $\langle N_p \rangle$  as a function of polymer fugacity  $z_p$  for varying colloid packing fractions  $\eta_c$ .

In Fig. 4.3 we show the adsorption isotherms or the number of polymers adsorbed per octahedral void  $\langle N_p \rangle / N_{OV}$  as a function of the reservoir polymer packing fraction  $\eta_p^r$  at fixed colloid packing fraction  $\eta_c = 0.576$  and  $0.707$ . Here  $\eta_p^r$  is the packing fraction of a reservoir of pure polymers at fugacity  $z_p$ ,  $\langle N_p \rangle$  is the number of polymers adsorbed onto the system, and  $N_{OV}$  is the number of octahedral voids in the system. We determine this conversion by performing Monte Carlo simulations on a pure system of bead chains at fixed polymer fugacity  $z_p$  and measuring the corresponding polymer packing fraction. In figure 4.3 we also show the statistical error bars for the adsorption isotherms of the HCP and FCC structure from five independent runs. For almost the entire range of  $\eta_p^r$ , the size of the error bars are smaller than the symbol size and are negligible. In figure 4.3 b) we zoom into the region where the error bars are the largest. From the top panel of figure 4.3 b) we can see that for  $\eta_c = 0.576$  the error bars become significant, for adsorption in the HCP structure for  $\eta_p^r > 0.125$ . However it should be noted that in this regime phase separation occurs in the simulation box, and therefore we do not use the data for computing free energies. For  $\eta_c = 0.707$  we find that the statistical errors are negligible for  $\eta_p^r < 0.25$  and increases to only a few percent at  $\eta_p^r \simeq 0.27$ .

At colloid packing fraction  $\eta_c = 0.576$  (Fig. 4.3 a) (top) we observe no significant difference in the adsorption isotherms of the FCC and HCP structures for  $\eta_p^r < 0.125$ . The different void distributions in the FCC and HCP structure do not result in a noticeable difference in the polymer adsorption. At this value of  $\eta_c$ , there appears to be plenty of space available for the polymers, and the colloids do not appear to constrain the chain configurations. As noted in the previous paragraph at  $\eta_c = 0.576$ , phase separation was observed in the simulation box for values of  $\eta_p^r > 0.125$ . Hence, there is an upper bound in  $\eta_p^r$  for estimating the free energy  $F(N_c, z_p, V, T)$  at fixed  $\eta_c$ .

At colloid packing fraction  $\eta_c = 0.707$  (Fig. 4.3 a) (bottom) the adsorption isotherms display two interesting features: i) At  $\eta_p^r \simeq 0.225$ , the polymer adsorption in the HCP structure is much higher than for the FCC structure. This can be explained by the fact that the size of the polymer as given by the radius of gyration exceeds the size of the octahedral hole, forcing the polymer to venture to neighbouring voids. Hence, the polymer is forced to explore the smaller tetrahedral voids in the case of the FCC structure, thereby incurring a significant free-energy penalty, while

in the HCP structure, the chains reach into the larger octahedral voids. This is the reason why the polymer adsorption is significantly higher in the HCP than in the FCC phase at low  $\eta_p^r$ . ii) Upon further increasing  $\eta_p^r$ , the polymer adsorption in the FCC structure becomes larger than in the HCP structure. This is because the polymer chains in the FCC structure are predominantly compact, whereas they are stretched out in the HCP phase. This difference in polymer configurations can be appreciated from the typical configurations shown in Figs. 4.5c-4.5e. Consequently, at high  $\eta_p^r$  every octahedral void in the HCP structure is occupied by at least one (part of a) polymer chain. However in the FCC structure the OVs are either occupied by a single chain or left empty. Therefore it becomes easier to insert a chain in one of the empty OVs of the FCC structure, than in a partially filled OV in the HCP structure.

As mentioned earlier in Section 6.2 the average number of polymer chains  $\langle N_p \rangle / N_{OV}$  per octahedral void allows us to calculate the Helmholtz free energy  $F(N_c, z_p, V, T)$ . Our adsorption isotherms together with Eq. 4.3 clearly indicate that there is a region in the phase diagram of this binary mixture of hard spheres and hard polymer chains, where the stable crystal phase is the HCP phase; this is what we intend to establish with free-energy calculations in the next subsection.

### 4.3.3 Phase behaviour

We first compute the phase diagram of a binary mixture of colloidal hard spheres and freely-jointed polymer chains of  $M = 10$  beads, for which polymer chain length the FCC structure incurred a free-energy penalty, as shown in Section 4.3.1, of  $O(10^{-2}k_B T)$  higher than an HCP phase of the same volume fraction, which is an order of magnitude higher than the free-energy difference between the two crystal phases without polymer (in favour of the FCC phase). Using the data as obtained from the adsorption isotherms,  $\langle N_p \rangle$  as a function of  $\eta_p^r$  or  $z_p$ , we calculate  $F(N_c, z_p, V)$  using Eq. 4.3 for the colloidal fluid phase, and the HCP/FCC crystal phases. We employ common tangent constructions at fixed  $z_p$  to determine the phase boundaries. In Fig. 4.4 we plot the phase diagram of the colloid-polymer mixture in the colloid packing fraction  $\eta_c$  vs polymer reservoir packing fraction  $\eta_p^r$  representation. From the phase diagram, it is observable that the stable crystal phase (X) which is in equilibrium with the fluid phase is the FCC phase at all the polymer concentrations studied, and not the HCP phase.

Next, we compute the phase diagram for  $M = 14$  monomer beads. It is worthwhile to note here that the TMMC method was used in the calculation of this phase diagram which gives very accurate estimates of the adsorption of polymer onto a system of  $N_c$  colloids in volume  $V$  as a function of fugacity  $z_p$ . The free-energy cost of inserting a polymer chain of this length is  $2.44 k_B T$  more in the (rigid) FCC structure than in the (rigid) HCP structure of the same volume fraction (Fig. 4.2). The reason for this, as discussed previously, lies in the void distribution in the two crystal structures - whereas in FCC two neighbouring octahedral voids are separated by a tetrahedral void, in HCP two neighbouring octahedral voids share a common face. The phase diagram of this colloid-polymer mixture is shown in Fig. 4.5a. In this representation tie lines that connect the two coexisting phases are horizontal.

There are common features in the phase diagrams for  $M = 10$  (Fig. 4.4) and  $M = 14$  (Fig. 4.5a) beads. At  $\eta_p^r = 0$ , the coexisting densities are simply given by the fluid-solid transition of pure hard spheres. Upon increasing  $\eta_p^r$  ( $\mu_p$ ), an enormous broadening of the fluid-solid transition is observed. Moreover, we also find for both cases a metastable gas-liquid (G+L)

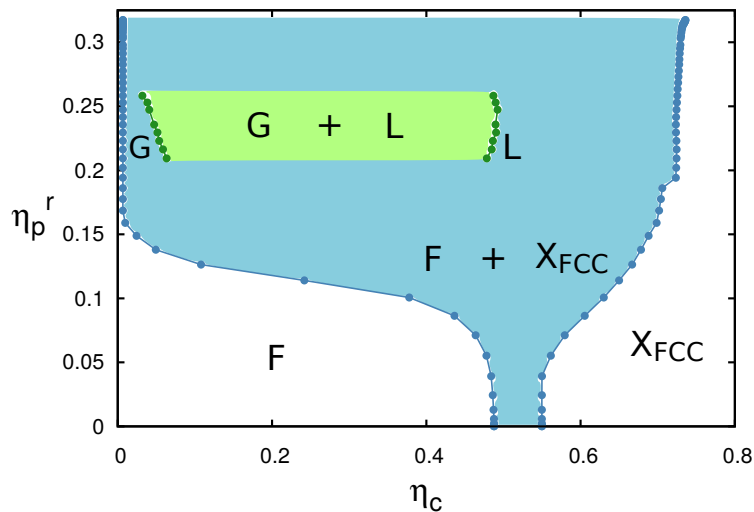


**Figure 4.4:** Phase diagram of a binary mixture of colloidal hard spheres and freely-jointed polymer chains of  $M = 10$  beads and a size ratio  $q = 1/7$  in the polymer reservoir packing fraction  $\eta_p^r$  vs colloid packing fraction  $\eta_c$  representation. The blue symbols represent coexisting colloidal fluid (F) and colloidal crystal states ( $X_{\text{FCC}}$ ) with FCC ordering. The dark green symbols represent coexisting (metastable) colloidal gas (G) and liquid (L) states. The pale blue and pale green represent the two-phase coexistence regions  $F+X_{\text{FCC}}$  and  $G+L$ , respectively, as denoted by the labels.

phase coexistence. This metastable  $G+L$  phase coexistence terminates in a critical point, but we have not been able to accurately locate the critical point due to its metastability. In the limit  $\eta_p^r = 0$ , i.e., pure hard spheres, the stable crystal phase is the FCC phase. As can be seen from Fig. 4.5b and 4.6b the amount of polymer in the coexisting crystal phase is negligible up to about  $\eta_p^r \simeq 0.225$ , and therefore the FCC structure is stable for values of  $\eta_p^r < 0.225$ . However in the phase diagram for  $M = 14$ , upon increasing  $\eta_p^r$  further, the FCC crystal phase becomes metastable with respect to the HCP phase for  $\eta_p^r > 0.225$ . Hence, a two-phase coexistence region between a fluid and an HCP crystal appears in the phase diagram as denoted by the red region in Figs. 4.5a and 4.5b. This HCP-fluid phase coexistence region at high polymer concentrations is absent in the colloid-polymer phase diagram for  $M = 10$  (Fig. 4.4). In Figs. 4.5c-4.5e we show typical configurations of the fluid phase, the metastable FCC crystal phase, and the stable HCP crystal phase. It is interesting to note that Fig. 4.5d shows clearly that the polymer chains in the octahedral voids of the FCC crystal are compact, whereas they are stretched in the HCP phase thereby occupying more than one octahedral void.

It is worthwhile to compare the phase diagram as shown in Fig. 4.5a with the phase diagram of a binary hard-sphere mixture with the same size ratio  $q = 1/7$ . In Ref. [32], phase diagrams are reported for size ratio  $q = 1/10$  and  $q = 1/5$ . We observe that the topology of the phase diagram shows a striking resemblance with the phase diagrams for highly asymmetric binary hard-sphere mixtures, i.e., both phase diagrams show a metastable gas-liquid transition and an enormous widening of the fluid-solid transition at a remarkably similar polymer reservoir

packing fraction, see Figs. 14a and 14b of Ref. [32]. This latter finding is particularly striking as the reservoir packing fraction at which the widening of the fluid-solid transition occurs is similar for both the single-sphere depletant and the polymer depletant, with chain connectivity playing no role. Additionally, the gas-liquid coexistence region shifts to higher values of reservoir polymer concentration with reducing chain length *i.e.*  $\eta_p^r \simeq 0.15$  for  $M = 14$ ,  $\eta_p^r \simeq 0.2$  for  $M = 10$ , and  $\eta_p^r \simeq 0.3$  for  $M = 1$  [32]. In Fig. 4.5b we replot the phase diagram in the  $\eta_p$  vs  $\eta_c$  representation with  $\eta_p$  the actual polymer packing fraction in the coexisting phases. We also show tie lines in Fig. 4.5b as denoted by the slanted dashed lines that connect the two coexisting phases.

The top panel in Fig. 4.6 shows the difference in free energy between the FCC and HCP crystal phases that are in coexistence with a colloidal fluid phase as a function of the packing fraction of the polymer  $\eta_p^r$  in the bulk reservoir. It is clear that for  $\eta_p^r > 0.225$ , the HCP structure is the stable phase, with a free-energy difference becoming more than  $1 k_B T$  per particle. Upon further increasing  $\eta_p^r$ , the free-energy difference begins to fall. The difference in free energy between the colloid-polymer FCC and HCP crystal structure is directly related to the difference in polymer adsorption as expected from Eq. 4.3. In Fig. 4.6 (lower panel) we plot the polymer packing fraction in both the HCP (stable/metastable) and FCC (stable/metastable) crystal phase that are in coexistence with the fluid phase. Both the lower panel in Fig. 4.6 as well as the data shown in Fig. 4.3 (bottom) demonstrate clearly that the polymer adsorption onto the FCC crystal wins over that of the HCP phase at large  $\eta_p^r$ . Based on a stronger polymer adsorption onto the FCC phase, and that the free-energy difference between FCC and HCP decreases at high polymer reservoir packing fractions (see Fig. 4.6 a), it is tempting to speculate that the free-energy difference tends to zero for sufficiently high  $\eta_p^r$ , thereby stabilizing the FCC crystal structure again at very high  $\eta_p^r$ . As simulations are infeasible at high  $\eta_p^r$ , the stability of FCC versus HCP remains as mere speculation at  $\eta_p^r > 0.275$ .

#### 4.3.4 Structure and dynamics

Next we take a closer look at the structure of the polymers in the FCC and HCP polymorphs at a fixed value of the packing fraction of the colloids  $\eta_c = 0.722$ . Using event driven molecular dynamics simulations, we investigate the structure and dynamics of the polymers at fixed  $\{N_c, N_p, V, T\}$ . Note that for  $M = 14$  bead chains, at relatively high polymer adsorption the FCC structure is metastable, and should transform into the HCP structure in the long time limit. However the barrier associated with changing the stacking sequence of the hexagonal planes as well as the fixed shape of the simulation box, allows us to simulate the metastable FCC phase without a spontaneous transformation to the HCP phase. In Fig. 4.7 we plot the probability distribution of the radius of gyration  $R_g$  (in units of monomer size  $\sigma_m$ ) of the polymer chains adsorbed onto the HCP and FCC polymorphs as a function of the polymer packing fraction  $\eta_p$ . From Figs. 4.5d and 4.7a, it is evident that the polymers stay collapsed within the octahedral holes in the FCC polymorph. At low to intermediate polymer packing fractions  $\eta_p$ , the polymers diffuse to the neighbouring octahedral cavity in the FCC crystal phase. This diffusion process occurs via the polymers stretching into a tetrahedral cavity to be able to translocate from one octahedral cavity to another. These jumps are activated as they involve an entropic barrier associated with the entropic penalty the chains incur, as they stretch into a tetrahedral cavity before jumping into the neighbouring octahedral cavity. In Fig. 4.8 we show snapshots

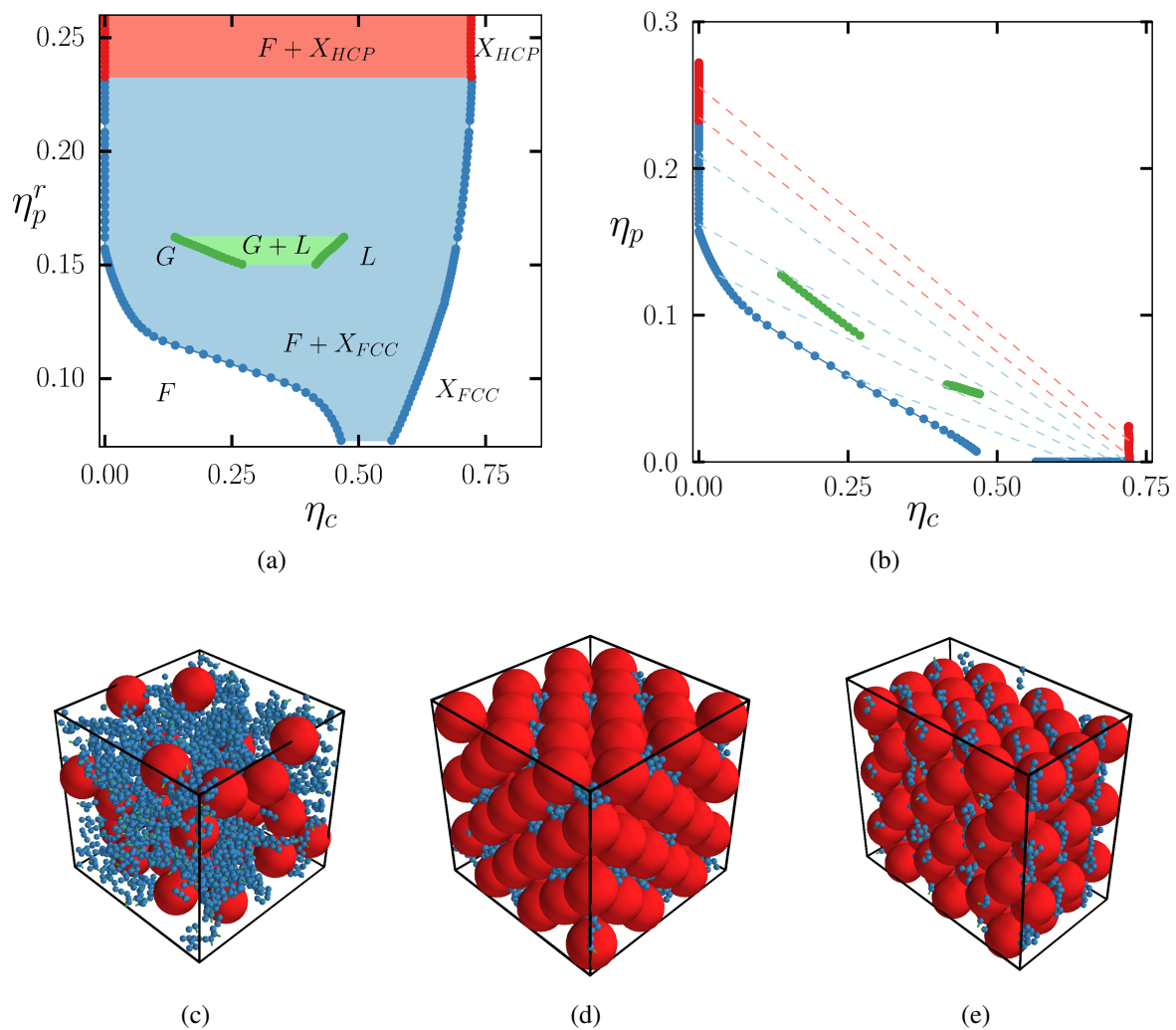


**Figure 4.5:** a. Phase diagram of a binary mixture of colloidal hard spheres and freely-jointed polymer chains of  $M = 14$  beads and a size ratio  $q = 1/7$  in the polymer reservoir packing fraction  $\eta_p^r$  vs colloid packing fraction  $\eta_c$  representation. The blue symbols represent coexisting colloidal fluid (F) and colloidal crystal states ( $X_{FCC}$ ) with FCC ordering. The dark green symbols represent coexisting (metastable) colloidal gas (G) and liquid (L) states. The red symbols denote coexisting colloidal fluid and colloidal crystal states ( $X_{HCP}$ ) with HCP ordering. The pale blue, pale green and pale red regions represent the two-phase coexistence regions  $F+X_{FCC}$ ,  $G+L$ , and  $F+X_{HCP}$ , respectively, as denoted by the labels. b. Phase diagram in the  $\eta_p$  vs  $\eta_c$  representation. The tie-lines (dashed) connect the coexisting phases. Typical configurations of the colloid-polymer mixture representative of c) fluid phase  $N_c = 30$ ,  $\eta_c = 0.20$ ,  $\eta_p^r = 0.096$  d) crystal phase with FCC ordering  $N_c = 108$ ,  $\eta_c = 0.72$ ,  $\eta_p^r = 0.254$  and e) crystal phase with HCP ordering  $N_c = 108$ ,  $\eta_c = 0.72$ ,  $\eta_p^r = 0.254$

from an EDMD simulation which shows a polymer chain (shown in blue) performing an activated jump between two octahedral voids. It might be of interest to investigate the statistics of the translocation times of the hard bead chains between neighbouring cavities, which must be coupled to the vibrations of the colloidal crystal lattice.

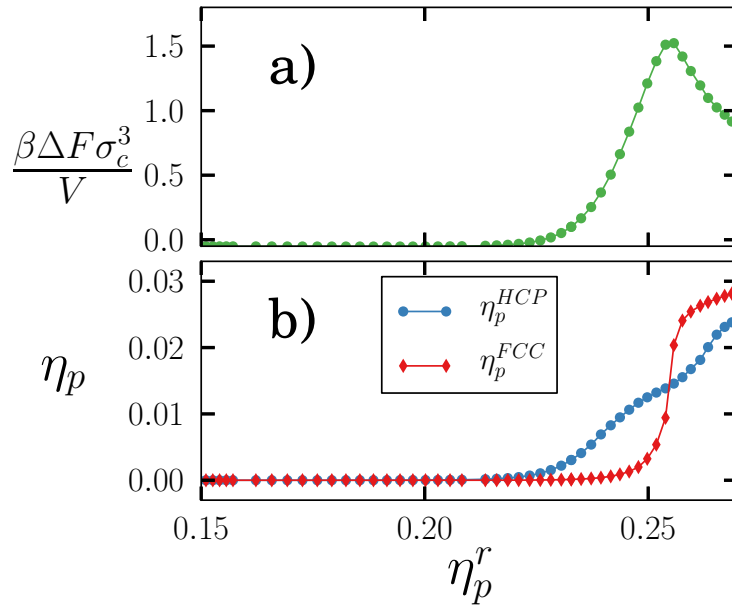


**Figure 4.6:** a) Free-energy difference between the FCC and HCP crystal structure that are in coexistence with the fluid phase,  $\beta(F_{FCC}^{cx} - F_{HCP}^{cx})\sigma_c^3/V$ , as a function of the polymer reservoir packing fraction  $\eta_p^r$ . b) The polymer packing fraction in the FCC (red symbols) and HCP (blue symbols) crystal phase that are in coexistence with the fluid phase vs the polymer reservoir packing fraction  $\eta_p^r$ .

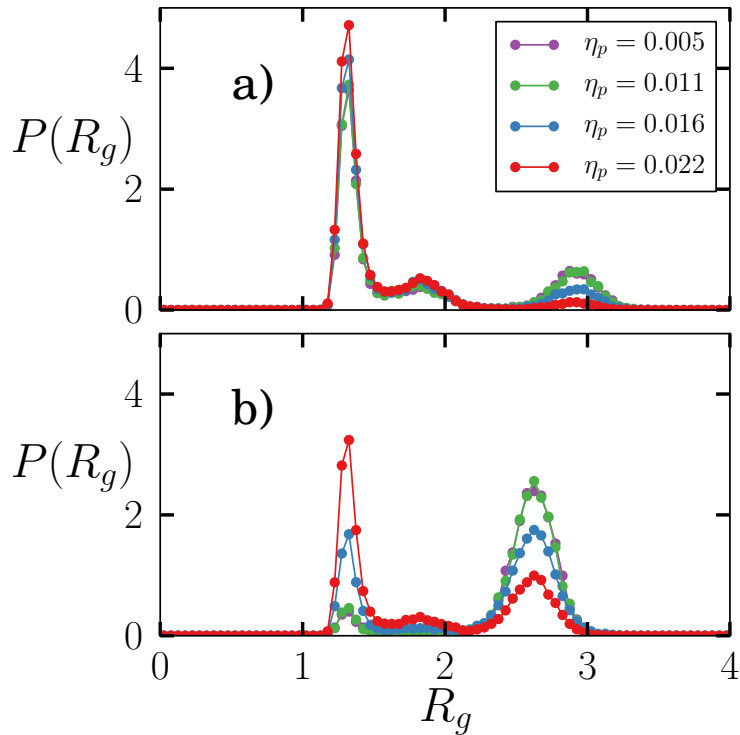


**Figure 4.7:** Probability distribution of the radius of gyration  $P(R_g)$  of the polymer chains with length  $M = 14$  beads for varying polymer packing fraction ( $\eta_p$ ) as indicated in the legend in a) the FCC structure and b) the HCP structure. The packing fraction of the colloid is fixed at  $\eta_c = 0.722$ . The radius of gyration  $R_g$  is expressed in units of monomer size  $\sigma_m$ .

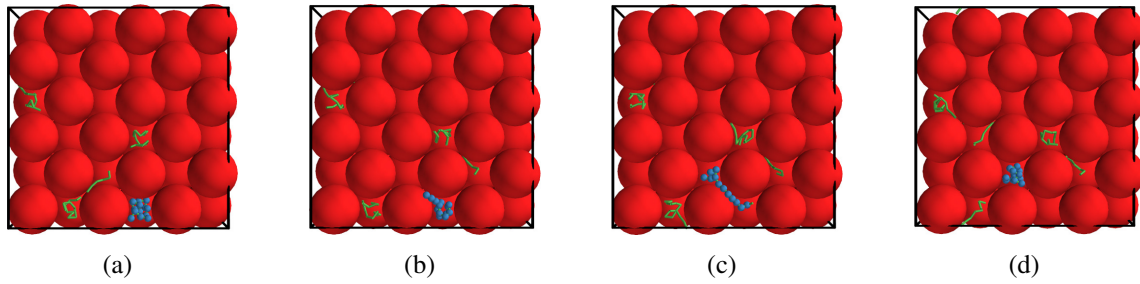


**Figure 4.8:** Snapshots from an event-driven molecular dynamics simulation which show the activated jump of a polymer chain of length  $M = 14$  (shown in blue) from one octahedral void to another in the FCC lattice. The packing fraction of the colloid is fixed at  $\eta_c = 0.722$ .

In the HCP polymorph, the polymer chains are more stretched at low polymer packing fraction and as a consequence the polymers occupy more than one octahedral cavity. However, the polymers do not appear to be freely migrating in the columns formed by the octahedral cavities of the HCP structure. The probability distribution of the radius of gyration as shown in figure 4.7 shows a single peak at  $R_g \simeq 2.7$ . However upon increasing the polymer adsorption  $N_p/N_{OV} \geq 0.5$  or  $\eta_p \geq 0.016$ , effects of crowding set in. This is reflected in the probability distribution of the radius of gyration of the chains which becomes bimodal. The entropy of the system appears to be maximized by the cooperative action of the polymer chains. What happens at these loadings is that a few polymers are in the collapsed state, thereby letting the rest of the chains exist in a stretched state. We now plot the probability distributions of the radius of gyration of polymer chains made up of  $M = 10$  beads (Fig. 4.9) and  $M = 20$  beads (Fig. 4.10) inside the FCC and HCP structures, for a comparison with the  $M = 14$  bead chain dynamics. From the three probability distributions, the size of the octahedral cavity appears to be  $\sim 1-1.5 \sigma_m$ . From the peaks in the distribution curves for the three cases, we make the following observations.

1.  $M = 10$ : From the peak positions in Fig. 4.9 that  $M = 10$  bead chains are short enough to lie bunched up inside one octahedral void in both the FCC and HCP structures and barely show any inter-void translocation.
2.  $M = 14$ : In the HCP polymorph, at low polymer densities, the polymers lie stretched out. For high polymer densities, the chains show a *bimodal* distribution, demonstrating entropy maximization via a cooperative action of polymer chains where some polymers exist in a collapsed state in order to allow others to stretch out.
3.  $M = 20$ : The  $R_g$  peaks positions are  $\sim 3\sigma_m$ , which indicates that the polymer chains are too long to be confined inside one cavity and share neighbouring octahedral voids. In the HCP polymorph (Fig. 4.10b), the shoulder on the distribution curve at low polymer density suggests that the polymers diffuse between adjacent voids in the HCP, visually similar to the (activated) jumps observed for the  $M = 14$  polymer chains in FCC. Such a jump of a  $M = 20$  polymer chain from one octahedral void to a neighbouring octahedral void in the HCP structure is shown in Fig. 4.11a-4.11c. In the FCC polymorph (Fig. 4.10a), the polymer chains lie stretched out between two OV's separated by an intervening TV. The

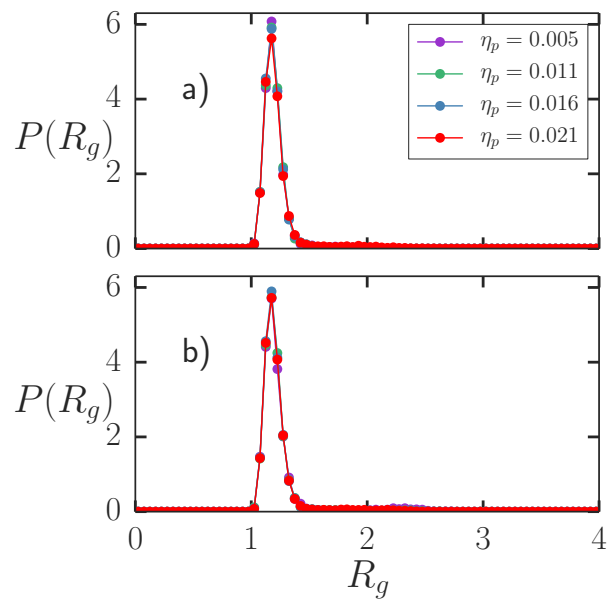


**Figure 4.9:** Probability distribution of the radius of gyration  $P(R_g)$  of the polymer chains with length  $M = 10$  beads for varying polymer packing fraction ( $\eta_p$ ) as indicated in the legend in a) the FCC structure and b) the HCP structure. The packing fraction of the colloid is fixed at  $\eta_c = 0.722$ . The radius of gyration  $R_g$  is expressed in units of monomer size  $\sigma_m$ .

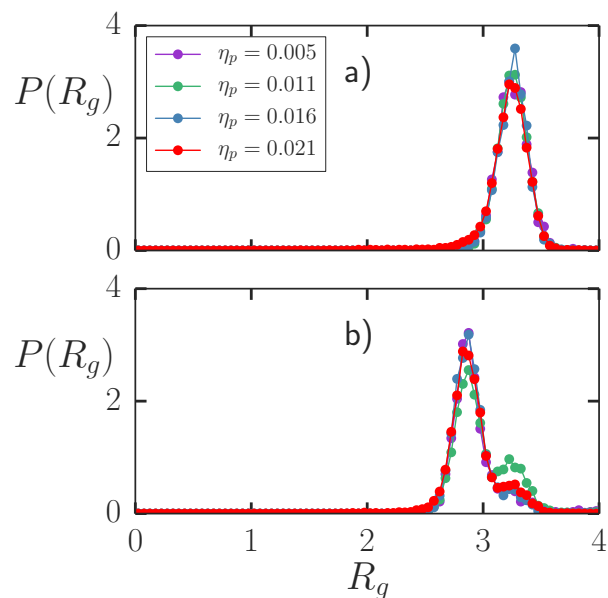


**Figure 4.10:** Probability distribution of the radius of gyration  $P(R_g)$  of the polymer chains with length  $M = 20$  beads for varying polymer packing fraction ( $\eta_p$ ) as indicated in the legend in a) the FCC structure and b) the HCP structure. The packing fraction of the colloid is fixed at  $\eta_c = 0.718$ . The radius of gyration  $R_g$  is expressed in units of monomer size  $\sigma_m$ .

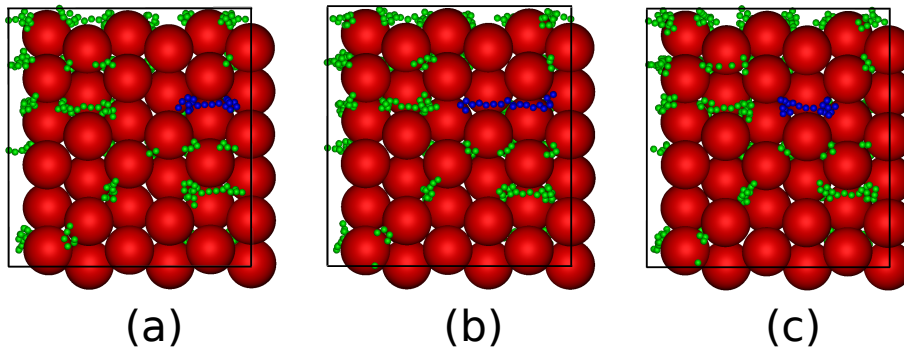


**Figure 4.11:** Snapshots from an event-driven molecular dynamics simulation which shows a polymer chain of length  $M = 20$  jumping from one octahedral void to an adjacent octahedral void in the HCP structure. The ‘jumping’ polymer chain is coloured in blue to distinguish it from the other polymer chains inside the lattice. The polymer packing fraction  $\eta_p = 0.011$  and the packing fraction of the (HCP) colloid is fixed at  $\eta_c = 0.718$ .

polymers in this case do not exhibit an ‘activated jump’ as is observed for the  $M = 14$  case, because in order to execute a whole ‘jump’ to the next OV in line (say  $n + 1$ ), the chain would have to undergo two jumps instead of one. That is, the beads in the  $n - 1$  OV would have to squeeze through the intervening TV between the  $n - 1$  and  $n$  OV-s and similarly the beads in the  $n$  OV would have to stretch out through the intervening TV between the  $n$  and  $n + 1$  OV-s. The combined entropic cost is too high for the polymer chains to diffuse.

## 4.4 Discussion and Conclusions

In conclusion, we have investigated the phase behaviour of a binary mixture of colloid hard spheres with diameter  $\sigma_c$  and freely-jointed bead chains consisting of hard spherical beads with diameter  $\sigma_m$ . We determined the phase diagrams for two chain lengths  $M = 10$  beads and  $M = 14$  beads using free-energy calculations for a fixed monomer-colloid size ratio  $q = \sigma_m/\sigma_c = 1/7$ . We used the configurational bias Monte Carlo (CBMC) method to speed up equilibration of the polymer chains. The transition matrix Monte Carlo (TMMC) method was used in the calculation of the phase diagram for  $M = 14$  beads to determine accurately the adsorption isotherms of the polymer. The phase diagram for  $M = 10$  beads was computed using only the CBMC method. TMMC was not performed for this case due to limited computational resources. Both phase diagrams display a broad fluid-solid two-phase coexistence region and a gas-liquid coexistence region, which is metastable with respect to the broad fluid-solid transition. For  $M = 10$  chain length, we never find the HCP crystal phase to be stable even at high polymer reservoir packing fractions. This phase diagram therefore primarily serves as a comparison for the phase diagram of the binary mixture of colloidal hard spheres and hard bead polymer chains of  $M = 14$  monomer beads.

For  $M = 14$  beads, we find that the FCC crystal structure is stable at low polymer reservoir packing fraction  $\eta_p^r$ , whereas the HCP structure becomes stable for  $\eta_p^r > 0.225$ . The trends observed in polymer adsorption in HCP/FCC structures lead us to speculate that the FCC structure may regain stability at very high values of the polymer reservoir packing fraction  $\eta_p^r$ . We also studied the structure and dynamics of the polymers in the crystal phase. In the FCC structure, the polymers stay collapsed in an octahedral cavity performing activated jumps to neighbouring cavities. It is worth mentioning that a similar behaviour was observed for an interstitial solid solution in a binary hard-sphere mixture with a size ratio of 0.3, which is constructed by filling the octahedral holes of an FCC crystal of large hard spheres with small spheres and where the fraction of octahedral holes filled with small spheres can be tuned from 0 to 1 [127]. In these crystal structures, the small spheres also hop between neighbouring octahedral holes via a tetrahedral hole [127]. In the HCP structure, the polymers are in a stretched state at low polymer packing fraction and they display cooperative behaviour at high polymer packing fraction, resulting in a bimodal distribution of collapsed and stretched polymer configurations.

The chain dynamics for  $M = 10$  and a third case  $M = 20$ , in the HCP polymorph, always show unimodal probability distributions of the polymer radius of gyration, in contrast with the bimodal distribution displayed by  $M = 14$  chains at high polymer densities, thus indicating that the cooperative behaviour described in the previous paragraph is not displayed by polymers of these two other chain lengths.  $M = 10$  polymer chains lie collapsed inside one octahedral cavity while  $M = 20$  chains share two neighbouring octahedral voids.

Coming back to our primary result of the  $M = 14$  polymer-mediated stabilization of the colloidal HCP polymorph over the FCC polymorph, it is worthwhile to explore the possibility to experimentally verify the theoretical predictions regarding the stability of the HCP structure over the FCC structure. Our simulation study shows that for the system parameters that we considered, the HCP structure is stable with respect to the FCC phase for a polymer reservoir packing fraction  $0.225 < \eta_p^r < 0.275$ . The HCP phase, which is dense in colloids and dilute in polymer coexists with a fluid phase, which is very dilute in colloids and rich in polymers (see Fig. 4.5b). The packing fraction of the stable HCP crystal structure  $\eta_c \geq 0.72$ , almost approaches the close-packed density of  $\eta_{cp} \simeq 0.74$ . Typical experimental samples of colloids are polydisperse in size. As noted by Pusey [128] for crystals with high packing fractions, the maximum allowed polydispersity  $\Delta$  is constrained by the expression  $\Delta \simeq (\eta_{cp}/\eta_c)^{1/3} - 1$ . This empirical relation is based on the fact that the particles with sizes corresponding to the tails of the size distribution should still fit onto the crystal lattice without distorting the crystal structure. Using this constraint, we find that the size polydispersity  $\Delta$  should be less than 1% in order to achieve a colloidal crystal with a packing fraction  $\eta_c \simeq 0.72$ , which is highly challenging, but not impossible. Another possible complication might be the size of the polymer as given by its radius of gyration that we considered in our model system, which is approximately on the same order of magnitude as the size of the colloids. Moreover, in a recent series of papers [117, 129, 130] Panagiotopoulos and coworkers have investigated how interactions between the polymers and the colloids impact the stability of the HCP structure over the FCC structure. The colloid-polymer interaction can be characterised by a reduced second virial coefficient  $B_2$ . They showed that for  $B_2 > 0$ , i.e in cases of hard repulsive interactions between the colloids and the polymers the HCP structure can be stabilized. As shown by the authors and described in our work, HCP is favoured as its void space distribution is entropically more favourable to the polymers than FCC. The effect disappears for  $B_2 \simeq 0$ . Interestingly for high negative values of  $B_2$ , i.e for

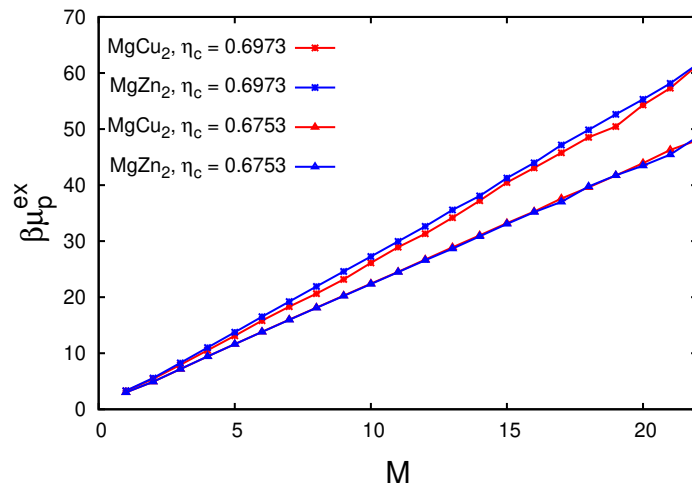


**Figure 4.12:** Excess chemical potential  $\beta\mu_p^{ex}$  difference (free-energy penalty) from inserting a single polymer chain inside the  $\text{MgCu}_2$  and  $\text{MgZn}_2$  Laves phase crystal structures, as a function of the number of monomer beads  $M$ . The results for two colloidal packing fractions  $\eta_c = 0.6753$  and  $0.6973$  are shown. Size ratio  $q$  of monomer bead to hard-sphere colloid =  $1/7$ . The binary colloidal sphere diameter ratio is  $0.82$ . Data is averaged over three independent runs.

attractive colloid-polymer interactions the HCP becomes stable again. Here polymers like to stay collapsed in the small tetrahedral voids, and the presence of face sharing tetrahedral voids in the HCP structure leads it to being more stable than the FCC structure as chain length increases. Another recent work of Mahynski et al shows that complex, open (non-closed packed) crystal morphologies can also be stabilized by suitably designing the architecture of the polymer [131]. In conclusion, it is evident that with a careful fine-tuning of the architecture of the polymer, it is possible to target a particular polymorph among a set of competing structures. We hope that our findings will inspire new experimental studies in this direction.

## 4.5 Outlook: Stabilizing the $\text{MgCu}_2$ Laves phase

As we have already discussed in Chapter 3, the  $\text{MgCu}_2$  Laves phase is of particular interest to us owing to its significance as a champion photonic crystal structure. However, even though the Laves phases (LPs) are thermodynamically stable at high enough pressures for a simple binary hard-sphere mixture of diameter ratio in the range  $0.76$  to  $0.84$ , there are three competing LP crystal structures ( $\text{MgCu}_2/\text{MgZn}_2/\text{MgNi}_2$ ) with a small free-energy difference per particle  $\sim 10^{-3}k_B T$ . Furthermore, the photonic  $\text{MgCu}_2$  LP has the highest free energy among the three with a relative stability order of  $\text{MgZn}_2 > \text{MgNi}_2 > \text{MgCu}_2$ . This is similar to the case of pure hard spheres, where the FCC and HCP crystal phase also have a free-energy difference ( $\sim 10^{-3}k_B T$  per particle). Therefore, just as we discussed in this Chapter, the way that the different void distributions in the FCC and HCP polymorphs can be leveraged to stabilize the HCP phase over the FCC phase in a colloid-polymer mixture, for appropriately chosen polymer chain lengths and polymer concentrations, we surmised that we can perhaps use a similar approach to stabilize one of the Laves phase polymorphs over its free-energetically degenerate

counterparts. Following this train of thought, in a similar treatment as shown in Fig. 4.2, we calculated the excess chemical potential of a polymer chain inserted in the MgZn<sub>2</sub> and MgCu<sub>2</sub> LPs, as a function of the number of monomer beads  $M$ . The MgNi<sub>2</sub> is structurally a combination of the stackings found in the MgZn<sub>2</sub> and MgCu<sub>2</sub> structures and excluded in these calculations. We show the results of our preliminary calculations in Fig. 4.12, for two colloid packing fractions. The monomer to large sphere colloid diameter ratio is again 1/7. The binary (colloid) hard-sphere diameter ratio considered here is 0.82. We observe that while there is no notable difference in the excess chemical potential of the chain in the two LP polymorphs at the lower packing fraction  $\eta_c = 0.6753$ , there is a difference in the free-energy penalty for chain insertion into the two LPs at a high packing fraction  $\eta_c = 0.6973$ . This difference is appreciable for chain length  $M > 7$ , and highest ( $\sim 1.425 k_B T$ ) for  $M = 9$ . However, most encouraging of all, it is the *photonic* MgCu<sub>2</sub> LP which incurs a lower free-energy penalty on insertion of the polymer chain, therefore opening up prospects of stabilizing the MgCu<sub>2</sub> LP over its LP polymorphs in a colloid-polymer mixture consisting of binary colloidal spheres of diameter ratio 0.82 and polymer chains of chain length  $M = 9$ . For a fixed composition (equal to that of the LP), this is effectively again a binary (and not a ternary) mixture. We leave this phase behaviour investigation for a future study.

## 4.6 Acknowledgements

This project was primarily the work of John R. Edison who calculated the phase diagram for the binary mixture of hard sphere colloids and hard bead polymer chains of  $M = 14$  monomer beads, using a combination of CBMC and TMMC simulation methods. The author of this Chapter, who had earlier collaborated on the project with J.R.E., later calculated the phase diagram (using only CBMC simulations) for the polymer chain length  $M = 10$  for a comparative picture with the  $M = 14$  case, and added a comparative study of the chain dynamics for different polymer chain lengths. I sincerely thank John for an excellent collaboration and many useful discussions. I thank Siddharth Paliwal for his help while making a schematic representation of the voids.

---

## The role of attractions in the crystallization of nanoparticles under spherical confinement

---

Despite the broad applicability of nanoparticle self-assembly in spherical confinement, the study of the crystallization mechanism and kinetic pathways has been limited to a few studies so far. The most notable work in this area was performed by de Nijs and Dussi [132], where they reported the entropy-driven formation of icosahedral order in the crystallization of hard-sphere nanoparticles (NPs) under spherical confinement. In this Chapter, we perform event-driven Brownian dynamics simulations to investigate the crystallization kinetics for attractive spheres under spherical confinement, and compare the crystallization mechanism with that of hard spheres. We compare our results with the experimental observations on the self-assembly of nanoparticles by Montanarella *et al.* [133], who observed the formation of colloidal supraparticles with a face-centered-cubic morphology in real-time *in-situ* X-ray measurements. More specifically, they observed homogeneous nucleation at a low volume fraction as opposed to the confinement-induced crystallization at high volume fraction reported in Ref. [132]. We investigate the crystallization kinetic pathways in our simulations, and systematically investigate the role of the attractions between the NPs on crystallization. We find from our simulations, for different attraction strengths, confinement-induced crystallization, homogeneous nucleation, spinodal decomposition of the fluid into crystalline clusters, a two-step kinetic pathway to crystallization *via* a metastable gas-liquid phase separation, and also an arrested percolating gel. Our findings demonstrate the role of attractions in nanoparticle self-assembly.

## 5.1 Introduction

The self-assembly (SA) of colloids into larger periodic structures is a phenomenon commonly observed in nature. Structuring matter by SA with either nanoparticles (NPs) or micron-sized colloids has progressed significantly over the last decades [19, 22, 134–138]. In particular, the ordering of NPs inside drying emulsion droplets into hierarchical supraparticles (SPs), i.e. particles made from particles, has gained prominence recently [132, 135, 139, 140]. This new length scale allows *e.g.* Mie resonances to influence material properties [141], and allows for further hierarchical SA of suprastructures. The significance of SA under spherical confinement is further increased in consideration of the fact that in the last decade it has become possible to study quantitatively in 3D the real space structure of colloidal crystals comprised of NPs [142–144]. Experimentally, the growth of NP superstructures as thin films or two-dimensional sheets has been studied in real time, using *in-situ* X-ray scattering methods in a synchrotron [145–147]. The crystallization kinetics of nanoparticle self-assembly in spherical confinement is relatively less explored. Recently, a significant study on supraparticles of hard spheres under a shrinking spherical confinement, mimicking hard-sphere-like NP SA inside drying emulsion droplets [132], used both experimental and simulation techniques to report the entropy-driven formation of icosahedral colloidal clusters by spherical confinement. The authors reported a confinement-induced crystallization for their hard-sphere nanoparticles.

In this Chapter, we build on the work in Ref. [132], wherein we discuss how the introduction of short-range attractions between the colloidal nanoparticles could directly affect the crystallization kinetics. Depending on the strength of attraction, the crystallization mechanism could switch from being confinement-induced at high volume fractions to homogeneous nucleation at low volume fractions. A further increase in attraction strength could also lead to the arrest of the particles due to long-lived bonds with their neighbours resulting in a percolating gel phase [148]. Physical gels can form when a metastable gas-liquid phase separation is interrupted by kinetic arrest due to an attractive glass transition [149, 150]. In this Chapter, we find that a small difference in the attractions between the NPs can lead to entirely different kinetic pathways in crystallization. We discuss these observations in this Chapter. In Sections 5.2.1 and 5.2.2, we present findings from a collaboration with Montanarella *et al.* [133], who made the first real-time *in-situ* study of colloidal crystallization of (attractive) nanoparticles in spherical confinement. We modeled their NPs (similar to the NPs of Ref. [132]) with an effective pairwise interaction potential, where the two main contributions are the van der Waals interactions originating from the core of the NPs and a steric interaction between the capping ligands. We approximate this potential with a hard-core attractive square-well potential which we use in our event-driven Brownian dynamics (EDBD) simulations to qualitatively corroborate the crystallization mechanism that Montanarella *et al.* proposed from their *in-situ* studies. In Section 5.2.3, we probe the effect of different attraction strengths on the crystallization kinetics. We find four significantly different kinetic pathways, including an arrested state at high attraction strength, which underlines the role of attractions in nanoparticle self-assembly. In Sections 5.2.1–5.2.3, we focus on a single system size of 100,000 NPs in spherical confinement for which face-centered-cubic (FCC)-like clusters, and not icosahedral supraparticles, were found [132]. The main aim here is to investigate the effect of attractions between the NPs on the crystallization pathways. In Section 5.2.4, we present some preliminary results on the different crystal

morphologies that we observed in our simulations on attractive and hard-sphere NPs for varying system sizes.

## 5.2 Crystallization of attractive nanoparticles in spherical confinement

### 5.2.1 Experimental findings

Recently, it was found both in experiments and in simulations that tens of thousands of hard-sphere NPs crystallize into icosahedral clusters under the spherical confinement of a slowly evaporating oil droplet [132]. More recently, a real time *in-situ* study was performed on the crystallization of NPs in spherical confinement [133]. Similar to Ref. [132], NPs were used that consist of an FeO core, a CoFe<sub>2</sub>O<sub>4</sub> shell, and oleate capping ligands, interacting *via* a cyclohexane medium. Using X-ray scattering, Montanarella *et al.* observed a gradual and constant decrease in the droplet size with time, and subsequently NP crystallization in the oil droplets at a volume fraction  $\sim 0.2$ , which is corroborated by the sudden appearance of FCC structure factor peaks. Using computer simulations, we show in this work that crystallization at such a low volume fraction is only possible if attractive interactions between colloidal nanoparticles are taken into account.

### 5.2.2 Model and EDBD simulations

In order to study the effect of attractions on the crystallization pathways of NPs in a slowly evaporating emulsion droplet, we perform event-driven Brownian dynamics simulations of NPs in a slowly shrinking spherical confinement. The effective pair potential  $\beta U_{\text{eff}}(r_{ij}, \sigma_c)$  between two colloidal NPs with diameter  $\sigma_c$  depends predominantly on the van der Waals interactions  $\beta U_{\text{vdw}}(r_{ij}, \sigma_c)$  originating from the NPs [23] and the steric repulsive interaction  $\beta U_{\text{steric}}(r_{ij}, \sigma_c)$  between the capping ligands. The center-of-mass distance between the two NPs, labelled  $i$  and  $j$ , is denoted by  $r_{ij}$ .

The van der Waals interaction  $\beta U_{\text{vdw}}(r_{ij}, \sigma_c)$  between two spherical NPs is given by [22, 151]

$$\beta U_{\text{vdw}}(r_{ij}, \sigma_c) = -\frac{\beta A}{12} \left[ \frac{\sigma_c}{2D_{ij} \left(1 + \frac{D_{ij}}{2\sigma_c}\right)} + \frac{1}{1 + \frac{2D_{ij}}{\sigma_c} + \frac{D_{ij}^2}{\sigma_c^2}} + 2 \ln \left( \frac{2D_{ij} \left(1 + \frac{D_{ij}}{2\sigma_c}\right)}{\sigma_c \left(1 + \frac{2D_{ij}}{\sigma_c} + \frac{D_{ij}^2}{\sigma_c^2}\right)} \right) \right] \quad (5.1)$$

with  $D_{ij} = r_{ij} - \sigma_c$ ,  $A$  the Hamaker constant,  $\beta = 1/k_B T$  the inverse temperature, and  $k_B$  the Boltzmann constant.

We use the Alexander-de Gennes model to describe the steric repulsive interaction between two plates with a densely adsorbed polymer layer in a good solvent [152], and we use the Derjaguin approximation [152] to convert the interaction between two plates to that between two spherical NPs with a high density of capping ligands. The steric repulsive interaction due to the ligands is given by

$$\beta U_{\text{steric}}(r_{ij}, \sigma_c) = \begin{cases} \frac{32\pi\sigma_c L^2}{140s^3} \left[ 28 \left( x_{ij}^{-1/4} - 1 \right) + \frac{20}{11} \left( 1 - x_{ij}^{11/4} \right) + 12 \left( x_{ij} - 1 \right) \right] & \sigma_c < r_{ij} < \sigma_c + 2L \\ 0 & \text{otherwise} \end{cases} \quad (5.2)$$

where  $x_{ij} = D_{ij}/(2L)$ ,  $s$  represents the mean distance between the attachment points of the capping ligands (also referred to as the mean ligand distance), and  $L$  is the thickness of the capping layer. In Fig. 5.1a we plot the effective interaction potential

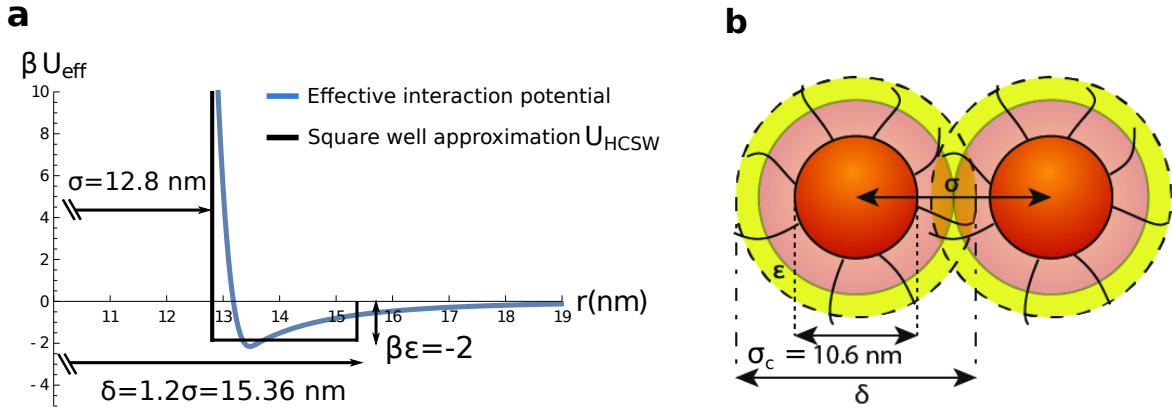


**Figure 5.1:** a) The effective pair potential  $\beta U_{\text{eff}}(r_{ij}, \sigma_c)$  between two spherical FeO/CoFe<sub>2</sub>O<sub>4</sub> core-shell NPs with core diameter  $\sigma_c = 10.6$  nm, along with the hard-core attractive square-well potential  $\beta U_{\text{HCSW}}(r_{ij})$  for comparison, with  $\beta \epsilon = -2$  the strength of attraction,  $\delta = 1.2\sigma$  the range of attraction, and  $\sigma = 12.8$  nm the effective hard-sphere diameter. The NP-NP Hamaker constant  $A$  across a hydrocarbon medium is 2.5 eV, the capping ligand length  $L = 1.5$  nm, mean ligand distance  $s = 0.43$  nm and temperature  $T = 341$  K. b) Model of the system with the relevant length scales labeled.

$$\beta U_{\text{eff}}(r_{ij}, \sigma_c) = \beta U_{\text{vdw}}(r_{ij}, \sigma_c) + \beta U_{\text{steric}}(r_{ij}, \sigma_c)$$

for the FeO/CoFe<sub>2</sub>O<sub>4</sub> NPs. For the NPs used by Montanarella *et al.* in Ref. [133], the NP core-shell diameter  $\sigma_c = 10.6 \pm 0.1$  nm, the NP-NP Hamaker constant  $A$  across a hydrocarbon medium is approximately 2.5 eV [153], the capping ligand length  $L = 1.5$  nm [132], mean ligand distance  $s = 0.43$  nm [23] and temperature  $T = 341$  K. The effective pair potential is repulsive at short distances due to the steric interactions between the ligands and attractive at intermediate distances due to the van der Waals interactions, and approaches zero at sufficiently large distances. In order to speed up equilibration in our event-driven Brownian Dynamics (EDBD) simulations, we approximate this interaction potential with a hard-core attractive square-well potential  $U_{\text{HCSW}}(r_{ij})$

$$\beta U_{\text{HCSW}}(r_{ij}) = \beta U_{\text{HS}}(r_{ij}) + \beta U_{\text{SW}}(r_{ij}), \quad (5.3)$$

where

$$\beta U_{\text{HS}}(r_{ij}) = \begin{cases} \infty, & r_{ij} \leq \sigma \\ 0, & r_{ij} > \sigma, \end{cases}$$

and

$$\beta U_{SW}(r_{ij}) = \begin{cases} \beta \varepsilon, r_{ij} \leq \delta \\ 0, r_{ij} > \delta, \end{cases}$$

with  $\sigma > 0$  the hard-core diameter, and  $\delta > \sigma$  and  $\varepsilon < 0$  the range and strength of the attractive square well, respectively. As shown in Fig. 5.1, the effective pair potential of our core-shell NPs can be approximated by a hard-core attractive square-well potential with an *effective* hard-core diameter  $\sigma = 12.8$  nm, an attraction strength  $\varepsilon = -2 k_B T$  and range of attraction  $\delta = 1.2\sigma = 15.36$  nm as indicated by the dashed lines in Fig. 5.1b.

*EDBD simulations.* In order to mimic the evaporating oil droplets we confine attractive NPs interacting with each other *via* a  $U_{HCSW}$  potential inside a slowly shrinking spherical confinement modelled by a hard spherical wall, shrinking at a constant compression rate  $\gamma = 10^{-3} \sigma / \tau_{MD}$ , where  $\tau_{MD} = \sqrt{m/k_B T} \sigma$  is the time unit of our EDBD simulations, with  $m$  the mass of the particle. The simulation method detects particle collisions (with the spherical wall and each other) as discrete events and calculates an event tree of collision time intervals to each event as calculated through the Newtonian equations of motion. The dynamics evolves through a sequence of (varying) time intervals depending on the nearest event. In order to mimic a colloidal dispersion, particle velocities are stochastically adjusted at a regular interval of  $\Delta t$  to simulate Brownian “kicks” from the surrounding solvent.

$$\mathbf{v}(t + \Delta t) = \alpha_t \mathbf{v}(t) + \beta_t \mathbf{v}_R(t), \quad (5.4)$$

where  $\mathbf{v}(t + \Delta t)$ ,  $\mathbf{v}(t)$  are the particle velocities before and after the Brownian adjustment,  $\mathbf{v}_R(t)$  is a variable calculated from a 3D Gaussian distribution with mean 0 and variance  $k_B T / m$  and we use  $\alpha_t = 1/\sqrt{2}$  with a probability  $v \Delta t$  and 1 otherwise. We set  $\beta_t = \sqrt{1 - \alpha_t^2}$  in order to keep the temperature constant. We set  $v = 10 \tau_{MD}^{-1}$  and  $\Delta t = 0.01 \tau_{MD}$  in all our simulations. We ignore hydrodynamic interactions due to the solvent in our simulations.

In order to determine if a particle is crystalline we investigate its local symmetry using bond orientational order parameters [116]. The (un-normalised) 3D bond order parameter for a particle  $i$  is defined as

$$q_{l,m}(i) = \frac{1}{N_{nb}(i)} \sum_{j=1}^{N_{nb}(i)} Y_{l,m}(\theta_{i,j}, \phi_{i,j}), \quad (5.5)$$

where  $N_{nb}(i)$  represents the number of neighbours of particle  $i$  which we define as the particles that lie within a center-of-mass distance of  $1.2\sigma$  of  $i$ ,  $\theta_{i,j}$  and  $\phi_{i,j}$  are the polar and azimuthal angles, respectively, of the center-of-mass distance vector  $\mathbf{r}_{ij} = \mathbf{r}_j - \mathbf{r}_i$  with  $\mathbf{r}_i$  the position of particle  $i$ .  $Y_{l,m}(\theta, \phi)$  are the spherical harmonics for  $m$  ranging from  $[-l, l]$ . A neighbour  $j$  of particle  $i$  forms a “solid-like” bond with  $i$  if  $d_l(i, j) > d_c$  with

$$d_l(i, j) = \frac{\sum_{m=-l}^l q_{l,m}(i) q_{l,m}^*(j)}{(\sum_{m=-l}^l |q_{l,m}(i)|^2)^{1/2} (\sum_{m=-l}^l |q_{l,m}(j)|^2)^{1/2}}. \quad (5.6)$$

Crystalline particles are defined as particles for which the number of solid-like bonds is greater than a critical value  $n_c$ . The best choice for the symmetry index is  $l = 6$  [68]. We set the cut-off values defined above as  $n_c = 6$  and  $d_c = 0.6$ . In order to further distinguish crystal domains from

one another, we calculate  $d_l(i, j)$  between a crystalline particle with its crystalline neighbours. We contend that two crystalline neighbours belong to the same cluster if  $d_l(i, j) \geq d_c^d$ , where the domain cut-off value  $d_c^d = 0.7$  signifies the degree of order in a similarly oriented crystal domain.

We use the bond order parameters described to identify the crystalline particles in the supraparticles, and therefore we are able to track the onset of crystallization in the droplet as time progresses. As the confinement shrinks with MD time, the volume fraction of the supraparticle,  $\eta = \frac{N\sigma^3}{D_{sph}^3}$  where  $D_{sph}$  is the diameter of the spherical confinement, increases and at  $\eta \sim 0.11$  we observe the formation of multiple crystalline nuclei in the supraparticle. Snapshots of the simulation are shown in Fig. 5.2(a). Upon increasing the volume fraction further, we see that these different nuclei merge to eventually form a single crystal. It is clear from the snapshots that there is no effect of confinement because the crystallization does not start at the wall. The only effect of the spherical confinement is to shape the SP and the appearance of facets/ledges on the surface of the SP (Fig. 5.4). Fig. 5.2(b) highlights a qualitative agreement of simulations with the homogeneous nucleation observed in the experiments as shown in Ref. [133] in that (i) the onset of the crystallization is at a much lower volume fraction ( $\sim 0.11$ ) when compared to hard-sphere NPs ( $\sim 0.5$ ) and (ii) in the attractive NP SP there is homogeneous nucleation while for the hard-sphere NP SP the crystallization proceeds heterogeneously from the spherical confinement (Fig. 5.3). The comparison of crystallization of attractive NPs and hard-sphere NPs is also illustrated in the corresponding thumbnails in the inset of Fig. 5.2(b) which show a cross-section of the attractive and hard-sphere NP SPs after crystallization has set in. The increase in the percentage of crystalline particles is very steep indicating a very rapid crystallization process. In Fig. 5.2(c) we plot (i) the number of particles in the primary crystal domain (left axis) which increases in time until  $\sim 83\%$  of the NPs make up the main crystal, and (ii) the number of crystal nuclei (right axis) which shows a peak during the shrinking process and finally decays to form one main cluster. These two findings corroborate the crystallization mechanism of homogeneous nucleation of multiple nuclei in the case of attractive NPs.

### 5.2.3 Role of attractions in the crystallization kinetic pathways

To summarise, under the spherical confinement of slowly evaporating emulsion droplets, hard-sphere NPs undergo a confinement-induced crystallization which sets in at high volume fractions, whereas homogeneous nucleation was found at low volume fractions for chemically very similar NPs used in Ref. [133], clearly suggesting the presence of attractions. To better understand the different crystallization mechanisms, we plot the effective pairwise interaction potential  $\beta U_{\text{eff}}(r_{ij}, \sigma_c)$  for the FeO/CoFe<sub>2</sub>O<sub>4</sub> core-shell NPs with oleic acid as capping ligands for the systems used in Refs. [132] and [133] in Fig. 5.5. An important difference between these two systems is the overall core-shell NP diameter, which for the system of Ref. [132] is  $\sigma_c = 6.0 \pm 0.3$  nm and for the system of Ref. [133] is  $\sigma_c = 10.6 \pm 0.1$  nm. Fig. 5.5 shows that the attractive interaction decreases with decreasing NP size. We find that NPs used in the present work are attractive, whereas the smaller NPs of Ref. [132] are indeed hard-sphere-like as already anticipated in that work. We now discuss in this subsection how the strength of the attraction between NPs directly affects the crystallization kinetics, by investigating the crystallization for varying attraction strengths.

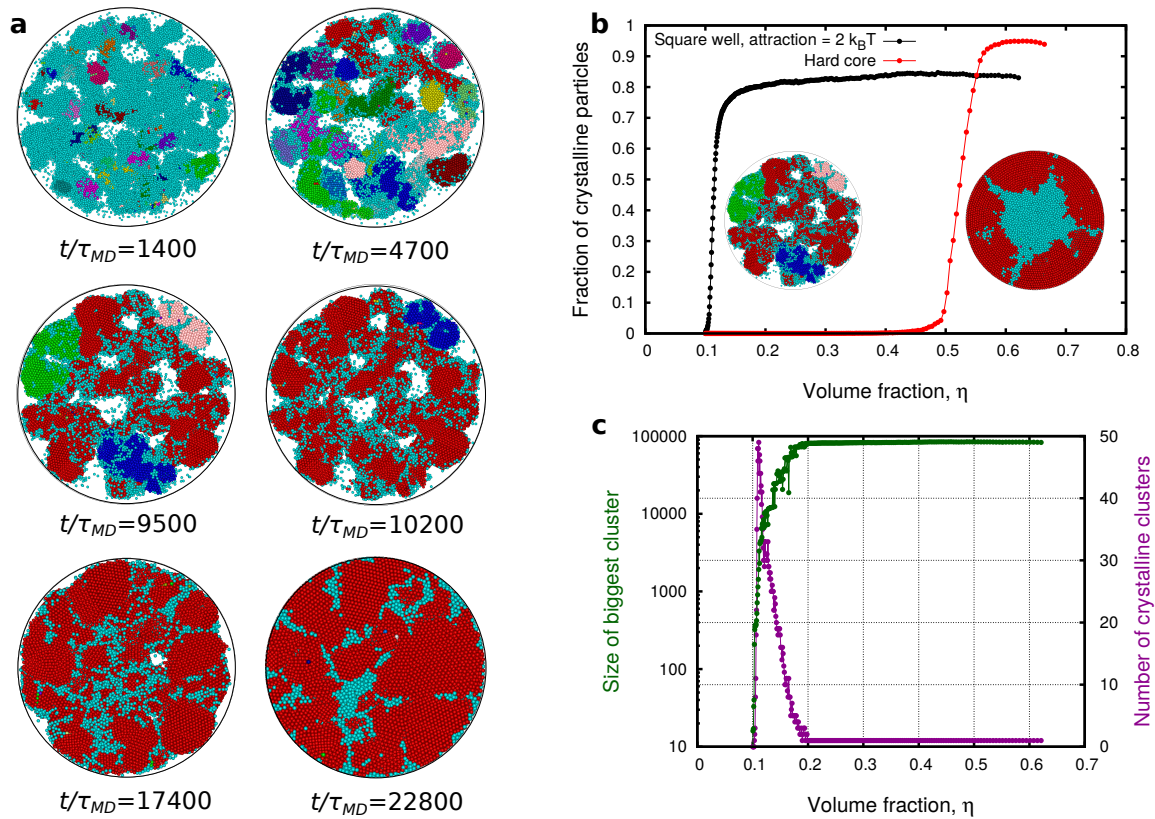


**Figure 5.2:** a) A cross-section (through the center) of the supraparticle comprising attractive NPs with strength of attraction  $\beta\varepsilon = -2$ , at different times ( $t/\tau_{MD}$ ) in a slowly shrinking spherical confinement as obtained from EBD simulations. The crystallization proceeds through *homogeneous nucleation* of multiple crystal nuclei which merge together at long simulation times to form one primary crystalline domain. colours are assigned randomly to distinct nuclei for every time snapshot analyzed (cyan always denotes disordered particles). The crystalline fraction profile is denoted by label A in Fig. 5.6. b) The plot shows the onset of crystallization with respect to volume fraction in an attractive NP system shown in comparison to the crystallization in a hard-sphere NP system. c) The plots show (i) the evolution of the size of the main crystalline domain with volume fraction (time) and, (ii) the number of differently oriented clusters crystallizing with changing volume fraction (time). Eventually there is only one main crystalline domain.

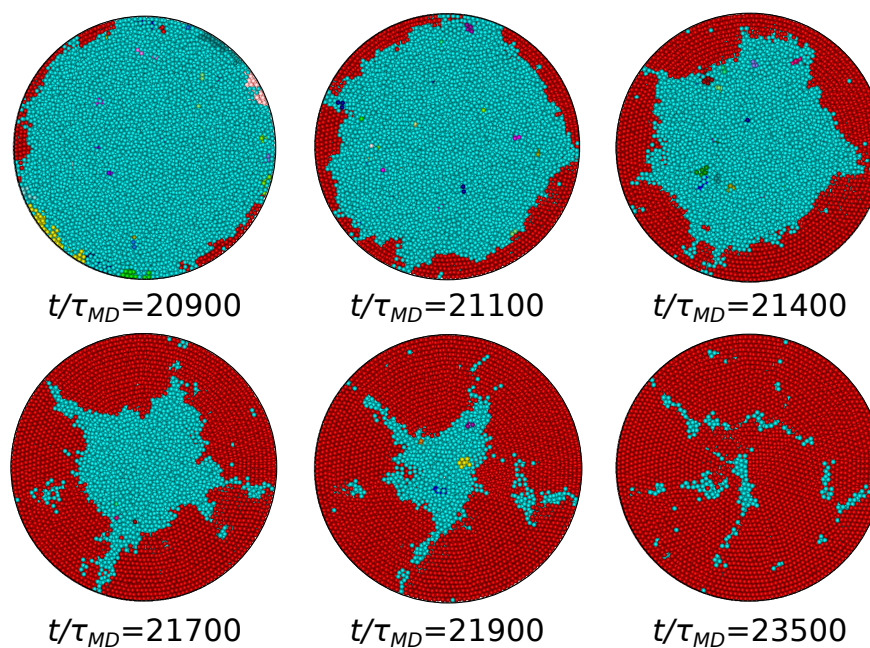


**Figure 5.3:** Typical cross-section views of a supraparticle through the center, from EDBD simulations of hard-sphere NPs, at different times  $t/\tau_{MD}$  in a slowly shrinking spherical confinement. Crystallization proceeds from the confinement. colours are assigned randomly to distinguish different crystalline domains. Fluid-like particles are coloured cyan. The crystalline fraction as a function of volume fraction is denoted by label B in Fig. 5.6.

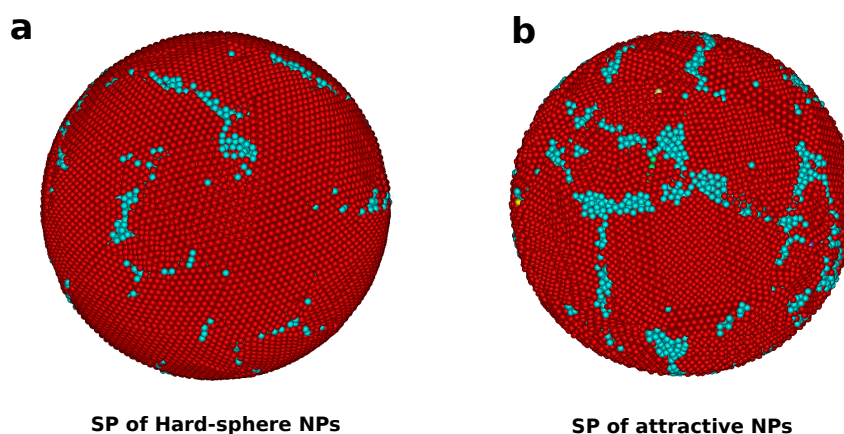


**Figure 5.4:** A look at two supraparticles, one comprised of hard-sphere NPs (left) and the other comprised of hard core soft attractive NPs (right), from the outside - a visual comparison. The hard-sphere NP supraparticle has a smooth outer shell while the attractive NP supraparticle surface shows visible ledges/facets.

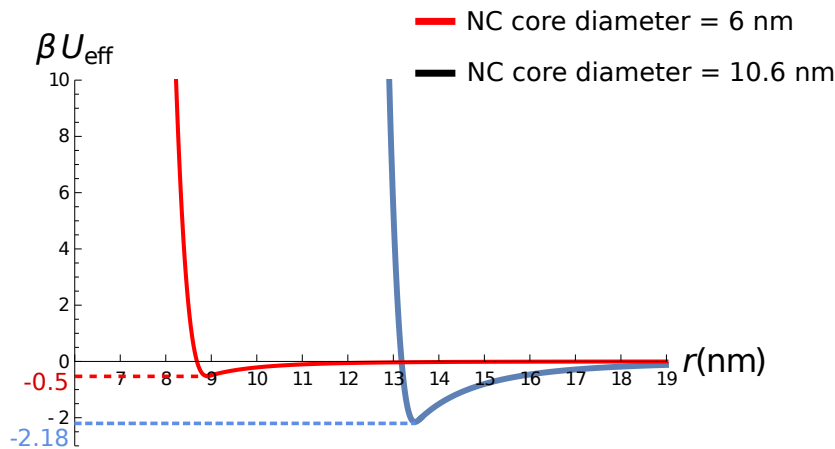


**Figure 5.5:** The effective pair potential between two spherical FeO/CoFe<sub>2</sub>O<sub>4</sub> core-shell NPs for the system employed in Ref. [133] and for a similar system as used in Ref. [132]. The NP core-shell diameters  $\sigma_c$  are 10.6 nm and 6 nm, respectively.

We show in Fig. 5.6 the profile of percentage of crystalline particles as a function of volume fraction of particles in the spherical confinement, for different attraction strengths between the NPs. From Fig. 5.6 we observe that the crystallization kinetics is remarkably sensitive to the attraction strength. In Figs. 5.2, 5.3, 5.7 and 5.8, we show typical snapshots along the time trajectory of the shrinking confinement for the most significant kinetic pathways observed in our simulations, corresponding to the labels A-D in Fig. 5.6. The order of the labels conforms to the order in which the figures appear in this Chapter. (i) Label A corresponds to the simulation snapshots shown in Fig. 5.2(a), depicting the formation of multiple crystalline nuclei in the unstable fluid in a crystallization process similar to that of spinodal decomposition. The crystalline clusters irreversibly merge until the whole structure is crystalline. Subsequently, the shrinking confinement forces the crystalline structure to fill space inside the confinement while maintaining approximately the same crystalline fraction. (ii) Label B depicts the confinement-induced heterogeneous crystallization observed in hard-sphere NPs in a shrinking spherical confinement, which is illustrated in Fig. 5.3. (iii) The kinetic pathway of homogeneous nucleation observed for NPs interacting with a square-well attraction of strength  $\beta\epsilon = -1.8$ , corresponding to label C, is shown in Fig. 5.7. The simulation snapshots show a two-step crystallization: (1) formation of high-density fluid ‘droplets’ in a low-density fluid due to an underlying metastable gas-liquid phase separation, followed by (2) the nucleation of the crystal inside the liquid droplets. The crystalline clusters grow until a local gas-solid phase equilibrium prevails. This process can be explained by the Ostwald rule of stages which states that the transition from one phase to another may evolve *via* metastable states [154]. The observation of such a kinetic pathway proceeding *via* a metastable gas-liquid phase separation was also observed in the crystallization of colloidal particles with depletion-induced short-range attractive interactions with low attraction strength and at low colloid volume fractions [155]. The metastable crystalline clusters survive for a long time due to low diffusion but irreversibly coalesce upon touching, instigated by the shrinking confinement. (iv) The kinetics observed for a slightly higher attraction strength  $\beta\epsilon = -3$  shows the formation of a percolating network. Such an arrested state at low volume

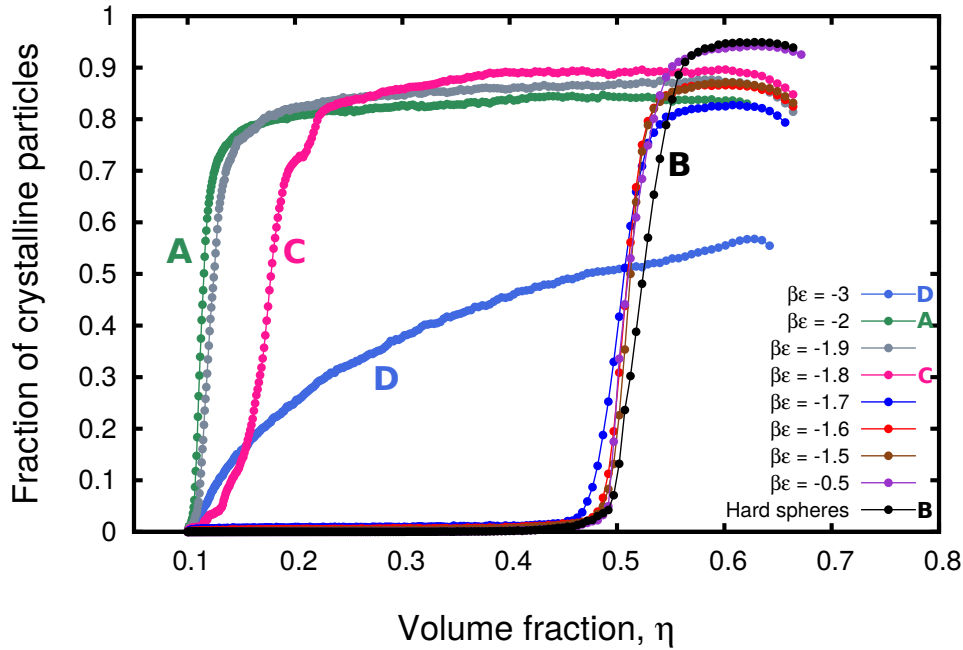


**Figure 5.6:** The fraction of crystalline particles with respect to the total number of particles as a function of volume fraction, as obtained from EDBD simulations of 100,000 attractive spheres with varying attraction strength  $\beta\epsilon$  (as labelled), in a shrinking spherical confinement.

fractions is often called a gel. We remark that the gelation is caused by the onset of an attractive glass transition at this high attraction strength. With the increase in volume fraction resulting from the shrinking confinement, crystalline clusters form inside the gel at long times.

#### 5.2.4 Structures obtained for different system sizes

In Ref. [132], it was shown that by crystallizing hard-sphere NPs under spherical confinement, different clusters were obtained for different system sizes *i.e.* total number of hard spheres ( $N$ ). Specifically, it was found that (i) clusters less than 1000 nanoparticles (NPs) per supraparticle showed the structure of a Mackay icosahedron (ii) the transition from a Mackay icosahedron to an anti-Mackay rhombicosidodecahedron was found to be between 1,000 to 3,000 NPs, (iii) the transition to pure FCC ordering followed a wider range between 25,000 to 90,000 NPs and (iv) clusters of more than 90,000 NPs exhibited solely FCC ordering. In the previous section, we compared the crystallization mechanism of attractive NPs to that observed for hard spheres in Ref. [132]. In this section, we investigate the cluster morphologies for attractive NPs with an attraction strength of  $\beta\epsilon = -1.8$  for varying system sizes in order to obtain a comparative picture with the hard-sphere supraparticles. Here we briefly investigate if the presence of attractions directly affects the crystal morphologies for the system sizes explored in Ref. [132], focusing

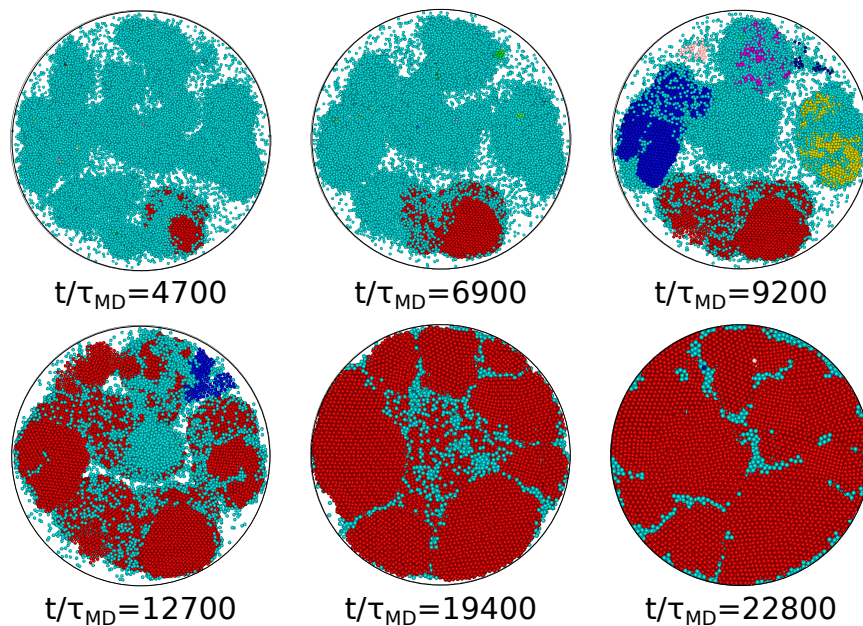


**Figure 5.7:** Typical cross-section views of a supraparticle through the center, from EDBD simulations of attractive NPs with an attraction strength of  $\beta\epsilon = -1.8$ , at different times  $t/\tau_{MD}$  in a slowly shrinking spherical confinement. colours are assigned randomly to distinguish different crystalline domains. Fluid-like particles are coloured cyan. The crystalline fraction as a function of volume fraction is denoted by label C in Fig. 5.6.

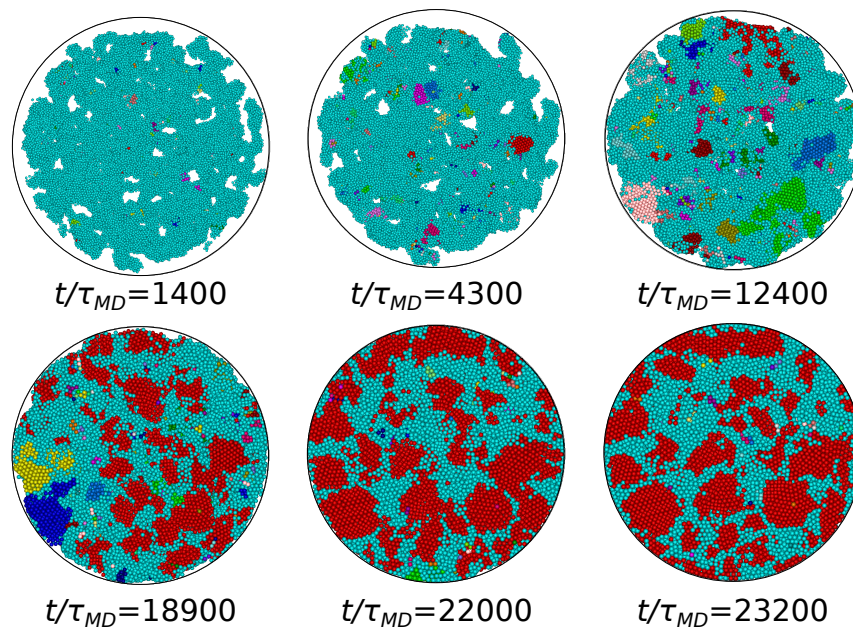


**Figure 5.8:** Typical cross-section views of a supraparticle through the center, from EDBD simulations of attractive NPs with an attraction strength of  $\beta\epsilon = -3$ , at different times  $t/\tau_{MD}$  in a slowly shrinking spherical confinement. colours are assigned randomly to distinguish different crystalline domains. Fluid-like particles are coloured cyan. The crystalline fraction as a function of volume fraction is denoted by label D in Fig. 5.6.

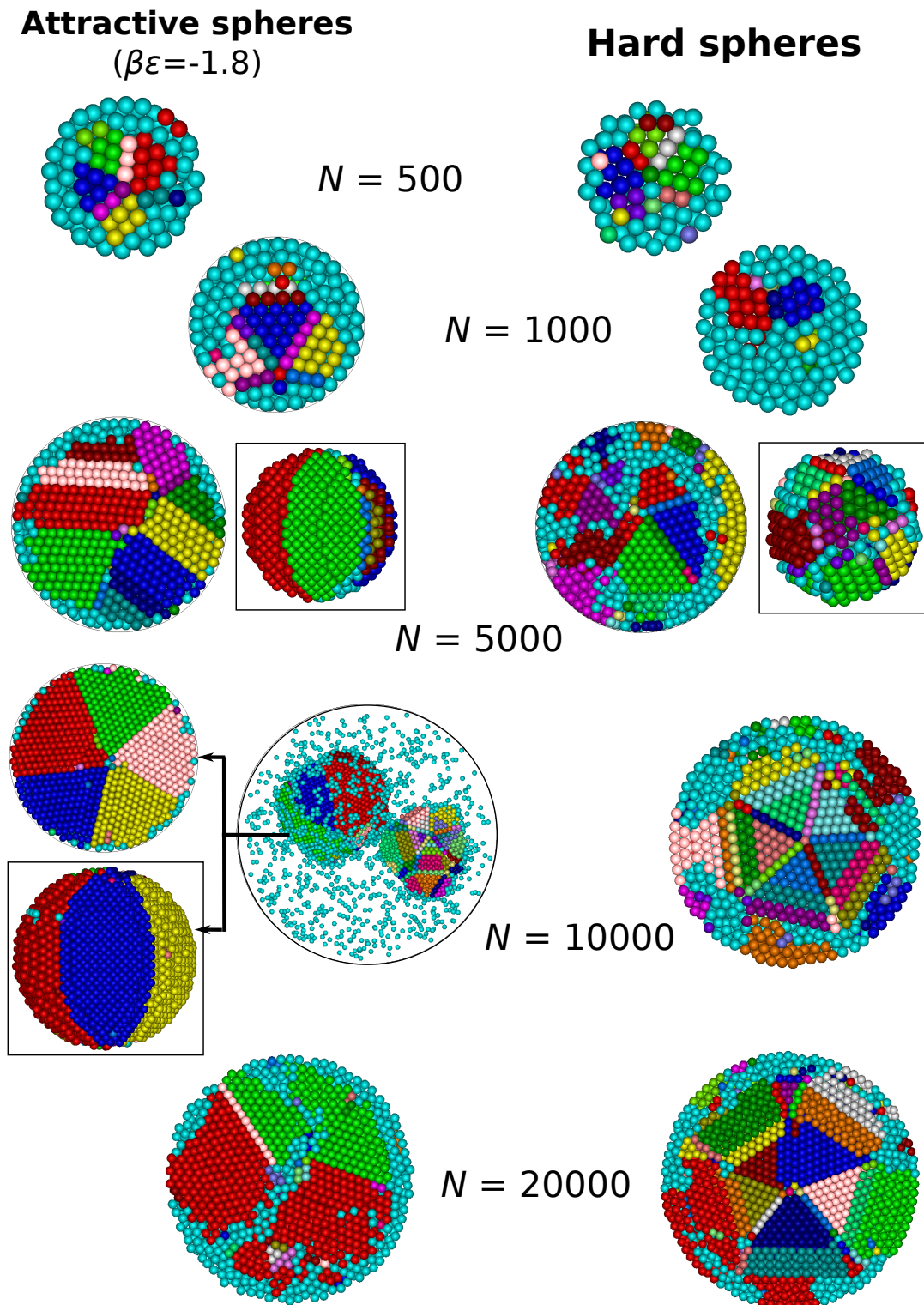


**Figure 5.9:** Typical 3D and cross-section views of a supraparticle showing different crystal morphologies for varying number of particles in spherical confinement, in the case of (i) attractive spheres interacting *via* a square-well potential with an attraction strength  $\beta\varepsilon = -1.8$  (left panel) and (ii) hard spheres (right panel). For  $N = 5000$  hard spheres, the Mackay icosahedron is shown as a 3D view next to the cross-section for  $N = 5000$  hard spheres. “Beach ball” supraparticles are seen for  $N = 5000$  and  $N = 10000$  attractive spheres, while the corresponding hard-sphere supraparticles have an anti-Mackay rhombicosidodecahedron morphology. The 3D views are shown inside boxes.

mainly on the regimes where the Mackay icosahedron and the anti-Mackay rhombicosidodecahedron were observed. We present typical cross-section views of the SPs consisting of NPs interacting with a square-well potential with an attraction strength of  $\beta\epsilon = -1.8$  along with those of SPs consisting of the same number of hard spheres for comparison in Fig. 5.9. A few interesting features are observed. For the smallest system size, we observed that the SPs with both attractive and hard-sphere NPs exhibit icosahedral symmetry. In order to distinguish more clearly the crystalline domains depicting a five-fold symmetry, we use a tighter domain criterion  $d_l(i, j) \geq d_c^d$  with  $d_c^d = 0.9$ . For slightly larger system sizes,  $N = 1,000$ , we see that the five-fold symmetry center (of the icosahedron) is markedly off-center in the case of attractive NPs, as compared to the hard-sphere SP. For even bigger systems  $N = 5,000$ , we observe that the hard-sphere NPs show a Mackay icosahedron in contrast to the attractive NPs, which show a competition of the icosahedral symmetry with randomly stacked multiple FCC crystalline domains. For the largest system sizes  $N = 10,000$  and  $20,000$ , the hard-sphere NPs form an anti-Mackay rhombicosidodecahedron structure in agreement with Ref. [132]. More surprisingly, we observe that the SP consisting of  $N = 10,000$  attractive NPs show five FCC crystalline domains which are forced by the spherical geometry of the confinement to merge at a five-fold pie-point on the north and south poles of the SP, forming a supraparticle which looks like a “beach ball”. Moreover we observe that the cluster consists predominantly of (100) instead of (111) facets. Taking into account the attractive square-well interaction with an attraction range of  $\delta = 1.2\sigma$ , we immediately see that the (100) face, where every particle can form 8 bonds instead of 6 bonds per particle that are formed in the case of the (111) face, is energetically favoured. The crystallization pathway for this case is even more intriguing. At a certain stage of the simulation, we observe two high-density fluid clusters as shown in Fig. 5.9. The smallest cluster exhibits clearly an anti-Mackay rhombicosidodecahedron structure, whereas the larger droplet shows multiple FCC domains. Upon increasing the volume fraction further, the smaller droplet merges into the bigger one, and the final structure at infinite compression is the so-called ‘beach ball’ structure, of which a cross-section and 3D view are shown in Fig. 5.9 as denoted by the black arrows. The SP of 5000 attractive spheres also resembled the ‘beach ball’ cluster but the system size is presumably too small to form a fully developed beach ball. For the largest system size,  $N = 20,000$  attractive NPs, the supraparticle clearly wants to form a single crystal FCC domain but because of finite size effects, forms a *frustrated* FCC structure with multiple FCC domains. In the previous two sections, we already found that SPs consisting of 100,000 attractive spheres form a single crystal FCC.

### 5.3 Summary

In this work, we investigated the kinetic pathways of crystallization (and gelation) for spheres interacting with an attractive square-well interaction with different attraction strengths, in a shrinking (hard) spherical confinement. The square-well interaction is the pair potential that we use to model short-range attractive NPs self-assembling inside a drying emulsion droplet. We briefly summarise here the most significant cases. We observed the formation of an amorphous percolating gel network for the highest attraction strength, *i.e.*  $\beta\epsilon = -3$ , investigated. For a slightly lower attraction  $\beta\epsilon = -2$ , we observe the fast appearance of crystalline clusters in an unstable fluid resembling spinodal decomposition. The crystalline clusters grow out into the

surrounding fluid, and eventually merge to form a percolating spinodal crystalline structure. For a slightly lower attraction strength  $\beta\varepsilon = -1.8$ , we observe a two-step kinetic pathway to a gas-solid phase equilibrium *via* a metastable gas-liquid phase separation where first high-density (liquid) droplets are formed in a low-density fluid, followed by crystal nucleation inside the liquid droplets. The crystalline clusters grow out until an equilibrium is established with the surrounding gas. Eventually, the crystalline clusters eventually irreversibly merge and at high compression, the crystalline fraction observed for this case is slightly higher than the spinodal structure in the previous case. For only a slightly lower attraction strength,  $\beta\varepsilon = -1.7$ , the crystallization mechanism jumps from a homogeneous nucleation at  $\beta\varepsilon = -1.8$  at low volume fractions to a confinement-induced crystallization at high volume fraction, which is the mechanism shown by hard spheres [132], asserting the sensitivity of the nanoparticle self-assembly to attractions between the NPs. For even lower attractions, the crystallization mechanics remains essentially the same, only showing progressively higher crystallinity fractions upon reducing the attractions. In the last section we briefly discuss the effect of attraction ( $\beta\varepsilon = -1.8$ ) on the crystal morphologies formed by the NPs, in direct comparison with hard-sphere NPs. The differences we find are mainly (i) the position of the five-fold symmetry center which is much closer to the surface in the case of attractive spheres at small system sizes, (ii) the destabilization of the icosahedral symmetry for attractive spheres, as opposed to a Mackay icosahedron formed by the hard-sphere NPs for system sizes of  $N = 5,000$ , (iii) the formation of a “beach ball” supraparticle, where five FCC domains meet in a pentagonal symmetry at the north and south poles of a supraparticle, and (iv) a frustrated FCC crystalline SP formed by  $N = 20,000$  attractive NPs, in contrast to the anti-Mackay rhombicosidodecahedron structure for  $N = 10,000$  and  $20,000$  hard-sphere NPs. We leave a more rigorous investigation of the crystal morphologies shown by attractive spheres in spherical confinement for a future study.

## 5.4 Acknowledgements

Some of the results presented in this Chapter are part of a collaboration with Federico Montanarella *et al.*, who performed the experimental work described in this Chapter, under the supervision of Patrick Baesjou, Alfons van Blaaderen and Daniel Vanmaekelbergh. I sincerely thank John Edison whose EDBD code was used in this project. I thank Federico for providing beautiful experimental images, Simone Dussi and Da Wang for useful discussions. Furthermore I am grateful to Bart de Nijs, Simone Dussi and all their co-authors whose beautiful findings of icosahedral order in hard spheres under spherical confinement inspired this work.

---

## Spontaneous nucleation of binary Laves phases in nearly hard spheres

---

Colloidal crystals with a diamond and pyrochlore structure display wide photonic band gaps at low refractive index contrasts. However, these low-coordinated and open structures are difficult to self-assemble from colloids with simple pair interactions. To circumvent these problems, one can self-assemble both structures in a closely-packed  $\text{MgCu}_2$  Laves phase from a binary mixture of colloidal spheres and then selectively remove one of the sublattices. Although Laves phases have been proven to be thermodynamically stable in a binary hard-sphere system, Laves phases have never been observed to spontaneously crystallize in such a fluid mixture in computer simulations. Here we demonstrate, using computer simulations, the spontaneous crystallization of the Laves phase from a binary fluid of nearly hard spheres, and explain why nucleation of the Laves phase has not been observed so far for hard spheres.

## 6.1 Introduction

One area of avid interest in colloidal crystals is centered around the ability of certain crystal structures to display an omnidirectional photonic bandgap in the visible region of the electromagnetic spectrum by virtue of the size of the building blocks. The inverted face-centered-cubic crystal structure is reported to show a complete photonic bandgap but the bandgap is narrow and therefore susceptible to defects [36]. Colloidal crystals that display a wide photonic bandgap at low refractive index contrasts are related to the family of either the diamond or the pyrochlore structure. However, these percolating open lattices with a low coordination number are difficult to self-assemble from colloids with simple pair interactions. One strategy to form open lattices is by employing long-range interactions, such as Coulomb interactions that extend over multiple interparticle spacings [156, 157]. A drawback of this approach is that the range of the potential is set by the Debye screening length of the solvent, and hence the interaction potential is not sufficiently long-ranged for particles with sizes larger than a few hundred nanometers in water and other highly polar solvents. Another approach is to mimic atomic systems such as carbon and silicon, which can form diamond lattices due to the specific directional interactions that favour tetrahedral bonding. Colloidal particles with four tetrahedrally arranged surface patches, which are functionalized with sticky DNA strands, were indeed experimentally realised and may be used to obtain the diamond structure [158]. A more involved procedure was recently adopted, in which gold nanoparticles were trapped inside tetrahedral DNA origami cages, and subsequently these nanocages were self-assembled into the diamond structure using sticky DNA strands at the vertices of the tetrahedral cage [159]. However the lattice spacing is much smaller than the wavelength of light, making it impossible to display an optical photonic bandgap.

To circumvent these problems associated with the self-assembly of low-coordinated structures, one can also follow a completely different route in which both the diamond and pyrochlore structure are self-assembled in a closely-packed  $\text{MgCu}_2$  Laves phase from a binary mixture of colloidal spheres. Subsequently, by selectively removing one of the species, one can obtain either the diamond (Mg, large spheres) or the pyrochlore (Cu, small spheres) structure. Laves phases (LPs) are a class of *binary* crystals with a stoichiometry of  $\text{LS}_2$  ( $L$  = large species,  $S$  = small species), which were first found in intermetallic compounds. The three main structural prototypes of LPs are the hexagonal  $\text{MgZn}_2$ , cubic  $\text{MgCu}_2$  and hexagonal  $\text{MgNi}_2$  structures. Using free-energy calculations in computer simulations, Laves phases has been found to be thermodynamically stable for a binary hard-sphere (BHS) mixture with a diameter ratio  $0.76 \leq q = \sigma_S/\sigma_L \leq 0.84$  [27], but have never been observed to spontaneously crystallize in such a binary fluid mixture in computer simulations. However, recent simulations have shown that on factoring in static or dynamic size polydispersity and by using particle swap Monte Carlo moves, Laves phases may be nucleated from dense hard-sphere fluids [160–162]. Experimentally, Laves phases has been observed in binary nanoparticle suspensions [22, 23], and in submicron-sized spheres interacting *via* a repulsive hard-sphere-like potential [24]. Furthermore, the  $\text{MgCu}_2$  structure is also shown to be stable in a system of preassembled tetrahedral clusters of spheres and single spheres interacting with hard-core potentials [105], and that the self-assembly of the  $\text{MgCu}_2$  has indeed been realised both in simulations and experiments in such a mixture using DNA-mediated interactions between the unlike species [106].

In this Chapter, we investigate the nucleation of Laves phases in a purely repulsive binary mixture in order to obtain a better understanding of why, in spite of thermodynamic favourability, the spontaneous crystallization of Laves phases has never been observed in computer simulations of binary hard spheres. There are many complicating factors that may hamper the nucleation of Laves phases. First of all, as the freezing transition is located at very high densities in the case of repulsive systems, nucleation can only occur when the system is sufficiently dense. In these highly concentrated systems, nucleation is severely hampered by slow dynamics. It is also known that binary mixtures with a diameter ratio in the range of  $q \sim 0.8$ , identical to the range where the Laves phases are stable, are excellent glass-formers. It is for this reason that binary Lennard-Jones and hard-sphere mixtures with diameter ratios exactly in this range are the most popular fruit fly model systems to study glassy behaviour [163]. The slow dynamics due to glassy behaviour in these binary mixtures will obviously also affect the nucleation rates. Secondly, crystallization in fluid mixtures is generally much harder than in one-component systems due to fractionation effects. Phase transformations in binary systems, e.g., spindle-, azeotropic-, eutectic-like phase transitions, involve fractionation when the composition of the crystal phase and the supersaturated phase differ. It is evident that fractionation of the fluid mixture decreases drastically the rate of crystallization, even in the case of a pure crystal or a substitutionally disordered phase [163, 164]. Additionally, the surface tension of the solid-fluid interface increases when the compositions become very different, leading to higher nucleation barriers and lower nucleation rates [165, 166]. Furthermore, nucleation of a *binary* crystal, where the two species are ordered on different sublattices, from a binary fluid mixture will result in a loss of mixing entropy. Hence, the Gibbs free energy for the formation of a binary crystal nucleus is usually higher than that of a substitutionally disordered crystal, making binary crystal nucleation an extremely rare event. This is, perhaps, the main reason that the number of simulation and experimental nucleation studies on binary colloidal crystals is very limited.

Nucleation in one-component systems is well-described by Classical Nucleation Theory (CNT). CNT is based on the ‘capillary approximation’, which describes the free energy to form a cluster of the new phase from the metastable phase by the difference in bulk free energy and a surface free-energy term that is given by that of a planar interface between the two coexisting phases. CNT operates under the assumption that subcritical crystalline clusters are in quasi-equilibrium with the supersaturated fluid phase. Simulation studies on binary hard-sphere mixtures have shown that in the presence of multiple competing crystal structures, the crystal phase that nucleates is the one whose composition is closest to the composition of the fluid phase even when it is metastable [164, 166]. Hence, one can favour the nucleation of the binary crystal by choosing the fluid composition close to that of the desired binary crystal phase. This finding is in agreement with the empirical Ostwald step rule that states that the crystal phase that nucleates from the fluid phase does not have to be the thermodynamically stable one [154]. These observations were rationalized within CNT by Stranski and Totomanov, who postulated that the phase that nucleates is the one that is separated from the fluid phase by the lowest free-energy barrier, which can in principle be a metastable crystal phase [167]. However, Sanz *et al.* reported that kinetics also plays an important role in determining which crystal phase nucleates in the case of competing nucleation pathways [168]. It was shown that in a system of oppositely charged colloids the crystal phase that nucleates is metastable and has, surprisingly, a higher free-energy barrier for nucleation. In this case the disordered face-centered-cubic crystal phase was favoured by non-equilibrium nucleation, and not the stable binary CsCl crystal. These res-

ults greatly challenge the commonly held assumption that the subcritical clusters are always in quasi-equilibrium with the fluid phase [169]. Another simulation study on the homogeneous nucleation of the interstitial solid solution in a binary mixture of hard spheres showed that fractionation during nucleation of the interstitial solid is mainly driven by the nucleation of the large spheres while maintaining chemical or diffusive equilibrium for the smaller spheres throughout the whole system [170]. In conclusion, there is no straightforward generalisation of CNT for multicomponent systems that is thermodynamically consistent and does not lead to unphysical effects. Important unresolved issues are (i) how to define the surface tension for a cluster, which is in quasi-equilibrium with a metastable parent phase with a composition that is very different from those of the coexisting bulk phases, (ii) does the surface tension depend on composition, curvature, and surface effects, and finally (iii) can the capillary approximation be used to describe binary nucleation in systems where fractionation and surface effects are important.

Numerical studies may shed light on these issues, as nucleation can be investigated directly in simulations using various methods such as brute-force molecular dynamics, the umbrella sampling technique, forward-flux sampling, transition path sampling. One of the main difficulties in studying crystal nucleation is, however, that one has to choose an order parameter (or multiple) to be able to distinguish the solid from the fluid phase on a single-particle level. The selection of suitable order parameters relies heavily on intuition, trial and error, and experience. A serious drawback of this pre-selection is that it ignores all other order parameters *a priori*, which may be important for the nucleation kinetics of the target structure. For a one-component system interacting with isotropic potentials the Steinhardt bond order parameters are widely used both in experiments and simulations [58,59]. However, the choice of order parameters is far from trivial in the case of binary crystals, especially if there are three competing crystal structures that are structurally very similar as in the case of the Laves phases. In addition, it is unclear if one can describe the solid-liquid transition with a single order parameter as multiple symmetries may be broken at the transition [60,61]. If the fluid-to-solid transition is driven by fluctuations in two or more order parameters, this may also lead to non-classical pathways such as precursor-mediated crystallization, two-step crystallization, etc.

In this Chapter, we investigate the nucleation of Laves phases in a purely repulsive binary fluid mixture using computer simulations. We systematically study the effect of softness of the pair potential on Laves phase nucleation in order to shed light on why Laves phases have not been observed in a purely hard-sphere system. This Chapter is organised as follows. We describe the model in Section 6.2. In Section 6.3, we describe the technical details of the methods that we use to study the bulk phase behaviour of a binary mixture consisting of large and small spheres that interact with repulsive pair potentials, and we present phase diagrams for varying softness of the pair potential. In Section 6.4, we discuss how we identify crystalline clusters of the Laves phases in the supersaturated fluid phase using bond orientational order parameters, and how we identify the different stackings of crystal planes in the final Laves phase structure. Subsequently, we discuss the observed spontaneous nucleation events at varying thermodynamic state points in the phase diagram. We then investigate the slow dynamics in the supersaturated fluid phase and determine the kinetic glass transition using mode coupling theory. In Section 6.5, we discuss this class of potentials in relation to binary hard spheres under the hidden scale invariance of simple fluids and use the concept of *isomorphs* on the thermodynamic phase diagram to address the question why the spontaneous nucleation of Laves phases has not been observed in binary

mixtures of hard spheres within reasonable time scales. Finally, we calculate the Gibbs free energy for the formation of a crystalline nucleus of a Laves phase from the fluid phase and the interfacial free energy as a function of supersaturation in Section 6.6. We conclude with a summary of our results and a discussion in Section 6.7.

## 6.2 Model

To investigate the effect of softness of the pair potential on the nucleation of the Laves phase, we consider a binary mixture of large ( $L$ ) and small ( $S$ ) spheres interacting with a Weeks-Chandler-Andersen (WCA) potential  $\phi_{\alpha\beta}(r_{ij})$  between species  $\alpha = L, S$  and  $\beta = L, S$  [171]

$$\begin{aligned} \phi_{\alpha\beta}(r_{ij}) &= 4\varepsilon_{\alpha\beta} \left[ \left( \frac{\sigma_{\alpha\beta}}{r_{ij}} \right)^{12} - \left( \frac{\sigma_{\alpha\beta}}{r_{ij}} \right)^6 + \frac{1}{4} \right] & r_{ij} < 2^{1/6}\sigma_{\alpha\beta} \\ &= 0 & r_{ij} \geq 2^{1/6}\sigma_{\alpha\beta}, \end{aligned} \quad (6.1)$$

where  $r_{ij} = |r_i - r_j|$  represents the center-of-mass distance between particles  $i$  and  $j$ ,  $r_i$  the position of particle  $i$ , and  $\varepsilon_{LL} = \varepsilon_{SS} = \varepsilon_{LS} = \varepsilon_{SL} = \varepsilon$  is the interaction strength. We set the diameter (interaction range) ratio  $q = \sigma_S/\sigma_L = 0.78$ , and use  $\sigma_{\alpha\beta} = (\sigma_\alpha + \sigma_\beta)/2$ . The *softness* of the potential can be tuned by changing the reduced temperature  $T^* = k_B T/\varepsilon$  with  $k_B$  Boltzmann's constant and  $T$  the temperature. The WCA potential has been used previously to mimic the hard-sphere potential [172–175] and as such it reduces to the hard-sphere potential in the limit of  $T^* \rightarrow 0$ . The WCA potential has also been successfully used in the self-assembly of the binary  $AB_{13}$  crystal inside a spherical confinement [176]. In this Chapter, we investigate the effect of softness of the pair potential on the phase behaviour of the binary mixture and the nucleation of Laves phases by studying three different reduced temperatures  $T^* = 0.2, 0.1$  and  $0.025$ . In Fig. 6.1, we plot the WCA potential for  $T^* = 0.025$  and  $0.2$  along with the pair potentials of the experimental systems for which Laves phases have been reported in literature, which are nanoparticle suspensions [23], polystyrene latex spheres [177], and more recently, buoyancy matched hard-sphere-like microgel suspensions [24]. Fig. 6.1 shows that the WCA potential at  $T^* = 0.025$ , which is our steepest potential, agrees well with that of the nanoparticle system of Evers *et al.* [23], whereas the WCA potential at  $T^* = 0.2$  agrees reasonably well with that of the microgel particles of Schaertl *et al.* [24]. The pair potential of the polystyrene latex spheres of Hasaka *et al.* [177] is much softer and more long ranged than the WCA pair interactions used in the present study. Previous simulation studies [178, 179] have shown that softness in the interaction potential increases the nucleation rate of spheres. Here we investigate the effect of softness of the pair potential on binary nucleation,

## 6.3 Bulk phase diagram

### 6.3.1 Free-energy calculations

To determine the thermodynamically stable phases in a system and to map out the equilibrium phase diagram, we calculate the free energy of the binary fluid, the  $MgCu_2$ ,  $MgZn_2$ , and  $MgNi_2$

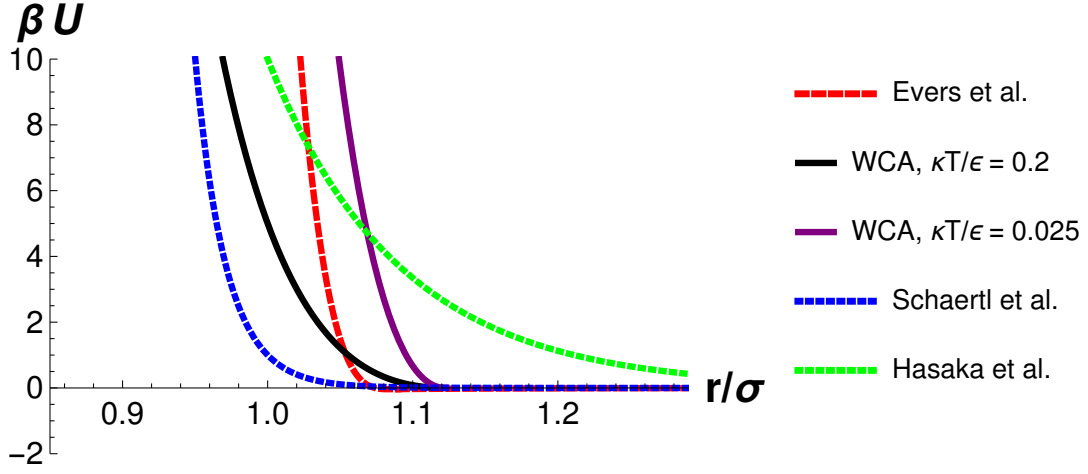


**Figure 6.1:** The WCA potential at  $T^* = k_B T / \epsilon = 0.2$  and  $0.025$  along with the pair potentials of the experimental systems for which the Laves phase has been reported in literature, which are binary nanoparticle suspensions of Evers *et al.* [23], microgel particles of Schaertl *et al.* [24], and polystyrene spheres of Hasaka *et al.* [177].

Laves phases, and the single-component face-centered-cubic (fcc) crystal phases. To this end, we calculate the Helmholtz free energy per particle  $f = F/N$  as a function of density  $\rho$  for all these phases using thermodynamic integration of the equation of state

$$\beta f(\rho) = \beta f(\rho_0) + \int_{\rho_0}^{\rho} d\rho' \frac{\beta P(\rho')}{\rho'^2}, \quad (6.2)$$

where  $\rho = N/V$  is the density with  $N$  the number of particles and  $V$  the volume of the system,  $f(\rho_0)$  denotes the Helmholtz free energy per particle for the reference density  $\rho_0$ ,  $\beta = 1/k_B T$  is the inverse temperature, and  $P$  is the pressure. We calculate the equations of state for the binary fluid and the binary Laves phase (LP) using Monte Carlo simulations in the  $NPT$  ensemble. Isotropic volume change moves are used for the fluid phase and the cubic  $\text{MgCu}_2$  phase, and anisotropic volume change moves are used for the *hexagonal*  $\text{MgZn}_2$  and  $\text{MgNi}_2$  phases. We use the ideal gas as a reference state for the binary fluid phase.

For the solid phases, we employ the Frenkel-Ladd method to calculate the Helmholtz free energy at a reference density  $\rho = N/V$  using Monte Carlo simulations in the canonical ensemble, where we keep the number of particles  $N$ , volume  $V$ , and the temperature  $T$  fixed. In the Frenkel-Ladd method, we start from an Einstein crystal, where the particles are coupled *via* harmonic springs with a dimensionless spring constant  $\lambda$  to the ideal positions of the crystal structure under consideration. We then construct a reversible path from the crystal of interest to the Einstein crystal using the auxiliary potential energy function

$$\beta U_{Ein}(\mathbf{r}^N; \lambda) = \beta U(\mathbf{r}_0^N) + \left(1 - \frac{\lambda}{\lambda_{max}}\right) [\beta U(\mathbf{r}^N) - \beta U(\mathbf{r}_0^N)] + \lambda \sum_{i=1}^N \frac{(\mathbf{r}_i - \mathbf{r}_{0,i})^2}{\sigma_L^2}, \quad (6.3)$$

where  $U(\mathbf{r}^N) = \sum_{i<j}^N \phi(r_{ij})$  is the potential energy of the system due to the interparticle interactions,  $\mathbf{r}_{0,i}$  represents the ideal lattice position of particle  $i$ , and  $\lambda$  is the dimensionless spring

constant, which ranges from 0 to a value  $\lambda_{max}$ . At  $\lambda_{max}$ , the particles are so strongly tied to their respective lattice sites, that the system reduces to an Einstein crystal of non-interacting particles, whereas  $\lambda = 0$  corresponds to the interacting system of interest for which we want to compute the free energy [109, 110]. The Helmholtz free energy of the crystal  $\beta f(\rho)$  can be approximated to that of the Einstein crystal using [180]:

$$\beta f(\rho) = \beta f_{Ein}(\lambda_{max}) - \frac{1}{N} \int_{\lambda=0}^{\lambda_{max}} d\lambda \left\langle \frac{\partial \beta U_{Ein}(\mathbf{r}^N; \lambda)}{\partial \lambda} \right\rangle_{\lambda}^{CM} \quad (6.4)$$

where  $\langle \dots \rangle_{\lambda}^{CM}$  denotes that the ensemble average is sampled for a solid with a fixed center of mass using the Boltzmann factor  $\exp[-\beta U_{Ein}(\mathbf{r}^N; \lambda)]$ , and  $f_{Ein}(\lambda_{max})$  denotes the free energy per particle of an ideal Einstein crystal given by

$$\beta f_{Ein}(\lambda_{max}) = \frac{\beta U(\mathbf{r}_0^N)}{N} + \frac{3(N-1)}{2N} \ln \left( \frac{\lambda_{max}}{\pi} \right) + \frac{1}{N} \ln \left( \frac{N}{V} \Lambda^3 \right) - \frac{3}{2N} \ln(N), \quad (6.5)$$

where  $U(\mathbf{r}_0^N)$  is the potential energy when all particles are at their ideal lattice positions,  $\Lambda$  is the thermal wavelength. We note that it is convenient to rewrite the integral in Eq. 6.4 as

$$\frac{1}{N} \int_{\ln c}^{\ln(\lambda_{max}+c)} (\lambda + c) \left\langle \sum_{i=1}^N \frac{(\mathbf{r}_i - \mathbf{r}_{0,i})^2}{\sigma_L^2} - \frac{1}{\lambda_{max}} [\beta U(\mathbf{r}^N) - \beta U(\mathbf{r}_0^N)] \right\rangle_{\lambda}^{CM} d[\ln(\lambda + c)], \quad (6.6)$$

with

$$c = \frac{1}{\left\langle \sum_{i=1}^N (\mathbf{r}_i - \mathbf{r}_{0,i})^2 / \sigma_L^2 - \frac{1}{\lambda_{max}} [\beta U(\mathbf{r}^N) - \beta U(\mathbf{r}_0^N)] \right\rangle_{\lambda=0}^{CM}}. \quad (6.7)$$

The integral in Eq. 6.6 is calculated numerically using a 40 or 60 point Gauss-Legendre quadrature.

Finally, the phase diagram in the pressure-composition representation can be determined by equating the chemical potential for the large ( $L$ ) and small ( $S$ ) species  $\mu_L^I = \mu_L^{II}$  and  $\mu_S^I = \mu_S^{II}$  as well as the pressure  $P^I = P^{II}$  of the two coexisting phases  $I$  and  $II$ , which is equivalent to a common tangent construction in the  $\beta g - x_L$  plane, where  $g(N, P, x_L, k_B T / \epsilon)$  is the Gibbs free energy per particle  $\beta g = \beta f + \beta P / \rho$  and  $x_L = N_L / N$  denotes the number fraction of large species in the mixture with  $N_{L(S)}$  the number of large (small) particles and  $N$  the total number of particles. We perform common tangent constructions to the Gibbs free energy curves of the binary fluid phase, the two single-component fcc phases, and the *binary* Laves phases. For the binary fluid phase, 50 compositions ranging from  $x_L = 0$  to 1 were sampled in the calculation of the binary phase diagrams.

### 6.3.2 Phase behaviour

We perform full free-energy calculations based on the thermodynamic integration technique as described above, and common tangent constructions to calculate the bulk phase diagrams of a binary WCA mixture with interaction strengths of both species set equal, i.e.  $\epsilon_{LL} = \epsilon_{SS} =$

$\epsilon_{LS} = \epsilon$ , a diameter ratio  $q = \sigma_S/\sigma_L = 0.78$  and  $\sigma_{\alpha\beta} = (\sigma_\alpha + \sigma_\beta)/2$  with  $\alpha, \beta \in L, S$  and  $L$  ( $S$ ) representing the large (small) species. We map out phase diagrams for varying temperatures  $T^* = k_B T/\epsilon = 0.2, 0.1$  and  $0.025$  in order to investigate the effect of softness of the pair potential on the phase behaviour. We plot the WCA pair potential as a function of the center-of-mass distance  $r$  in Fig. 6.2 for the three temperatures. We note that the softness of the pair potential increases upon increasing  $T^*$ , and that the pair potential reduces to the pair potential of hard spheres with a diameter of  $2^{1/6}\sigma$  in the limit of  $T^* \rightarrow 0$ . In Figs. 6.3-6.5, we present the

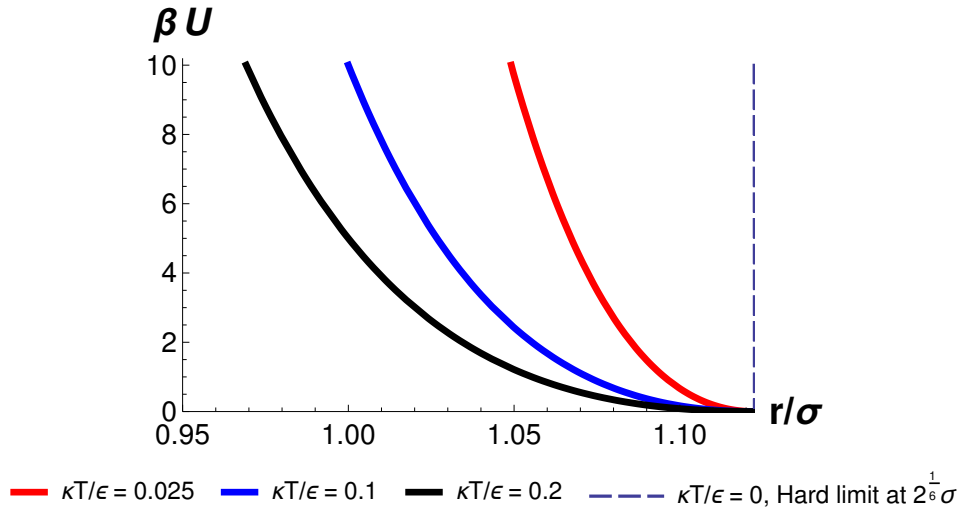


**Figure 6.2:** The WCA potential for three different temperatures  $T^* = k_B T/\epsilon = 0.2, 0.1$  and  $0.025$ . The WCA pair potential reduces to the pair potential of hard spheres with a diameter of  $2^{1/6}\sigma = 1.12\sigma$ , in the limit of  $T^* \rightarrow 0$ .

bulk phase diagrams in the reduced pressure  $\beta P\sigma_L^3$  - number fraction of large species  $x_L$  plane for three temperatures,  $k_B T/\epsilon = 0.2, 0.1$  and  $0.025$ , respectively. The binary phase diagrams yield four stable phases, the two single-component crystalline fcc phases denoted by  $\text{fcc}_L$  and  $\text{fcc}_S$  for the large and small species, respectively, a stable Laves phase, and the binary fluid phase. At low pressures the phase diagram shows a stable fluid phase, whereas at sufficiently high pressure, the system shows fluid- $\text{fcc}_L$ , fluid-Laves, and fluid- $\text{fcc}_S$  phase coexistence regions. Upon increasing the pressure further, the system reveals a Laves- $\text{fcc}_S$  and Laves- $\text{fcc}_L$  coexistence. As the single-component fcc phases are the closest-packed crystal structures, we expect a  $\text{fcc}_L$ - $\text{fcc}_S$  coexistence at even higher pressures as also found for the binary hard-sphere mixtures in Ref. [27, 28]. In addition, we also calculate the phase diagram for a binary mixture of hard spheres with a diameter ratio  $q = 0.78$ . The resulting phase diagram is displayed in Fig. 6.6. The topology of the binary phase diagrams for the WCA mixture and the hard-sphere mixture with diameter ratio 0.78 is very similar as expected. However, a more detailed comparison between the binary phase diagrams for the WCA mixtures (all three temperatures) and the hard-sphere mixture in Figs. 6.3-6.6 shows a phenomenological difference in the Laves-fluid phase coexistence region near  $x_L \simeq 1/3$  as the phase diagrams of the WCA mixtures display two triple points as opposed to one triple points in the hard-sphere case. This implies that for the WCA mixture there is a stable Laves-fluid phase coexistence for a stoichiometric excess of large species ( $x_L > 1/3$ ), that is absent for the binary hard spheres. We note that the phase

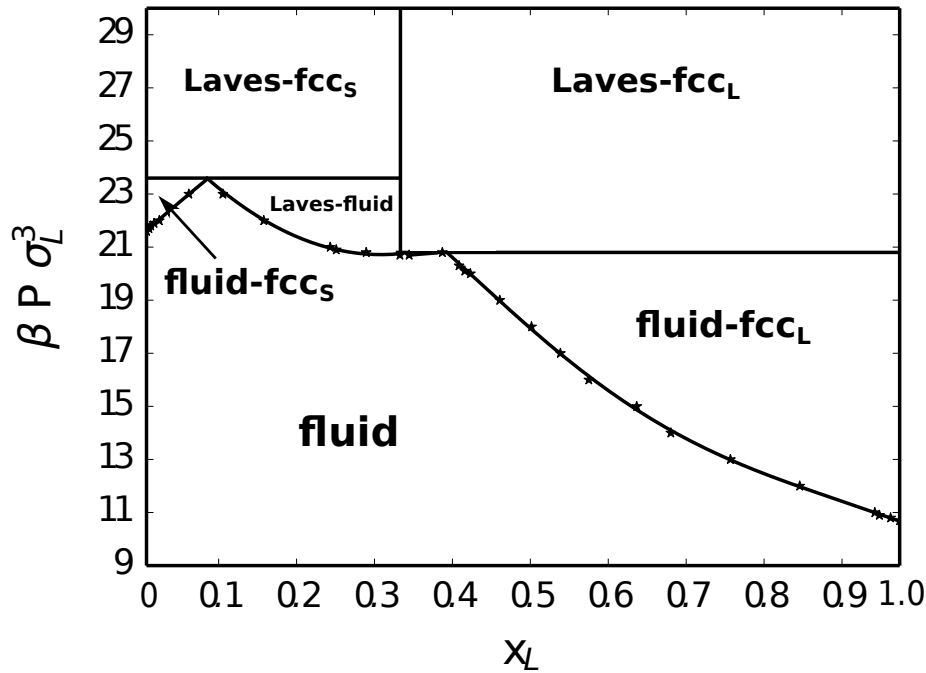


**Figure 6.3:** Phase diagram of a binary mixture of spheres interacting with WCA pair interactions with a diameter ratio  $q = 0.78$  at a reduced temperature  $T^* = k_B T / \varepsilon = 0.2$  in the composition  $x_L = N_L / (N_L + N_S)$ -reduced pressure  $\beta P \sigma_L^3$  plane. Labels “fluid-fcc<sub>L</sub>” and “fluid-fcc<sub>S</sub>” denote coexistence regions between a fcc crystal of large spheres or small spheres and a fluid, “Laves-fluid” denotes a coexistence region between the Laves phase and a fluid, and “Laves-fcc<sub>L</sub>” and “Laves-fcc<sub>S</sub>” denote a coexistence region between the Laves phase and the fcc crystals of large and small spheres, respectively. The label “fluid” represents a stable binary fluid phase.

diagrams display an additional triple point, where the fcc<sub>L</sub>, fcc<sub>S</sub>, and Laves phases coexist, at much higher pressures (not shown here).

We now turn our attention to the stable Laves phase region in the phase diagram. There exist three main types of binary Laves phases as shown in Fig. 6.7, which differ in the way the large-sphere dimers are stacked as viewed along the [110] and [11 $\bar{2}$ 0] projection planes of the cubic and hexagonal structures, respectively. In the cubic MgCu<sub>2</sub> phase the stacking of the large-sphere pairs is “aa-bb-cc”, whereas in the hexagonal MgZn<sub>2</sub> phase the stacking is “aa-bb”. The hexagonal MgNi<sub>2</sub> can be seen as a mixture of MgCu<sub>2</sub> and MgZn<sub>2</sub>, and displays an “aa-bb-cc-bb” stacking, as illustrated in Fig. 6.7. Previous simulation studies have shown that the MgZn<sub>2</sub> phase has the lowest free energy among the three Laves phases for a binary hard-sphere mixture of diameter ratio  $0.76 \leq q \leq 0.84$  [27]. The free-energy difference is very small and is of the order of  $10^{-3} k_B T$  per particle at a volume fraction of  $\eta = 0.6$  and diameter ratio  $q = 0.82$  [28]. Here, we investigate the effect of the softness of the interactions on the stability of the MgZn<sub>2</sub> crystal phase using free-energy calculations. We calculate the Helmholtz free energy for the three Laves phases for a binary mixture of WCA spheres with a diameter ratio of  $q = 0.78$ , at a reduced temperature  $T^* = 0.2$ , and melting density  $\rho \sigma_{av}^3 = 0.953$  with  $\pi \sigma_{av}^3 / 6 = \pi \sigma_L^3 (x_L + (1 - x_L) q^3) / 6$  the “average” particle volume in a binary mixture of

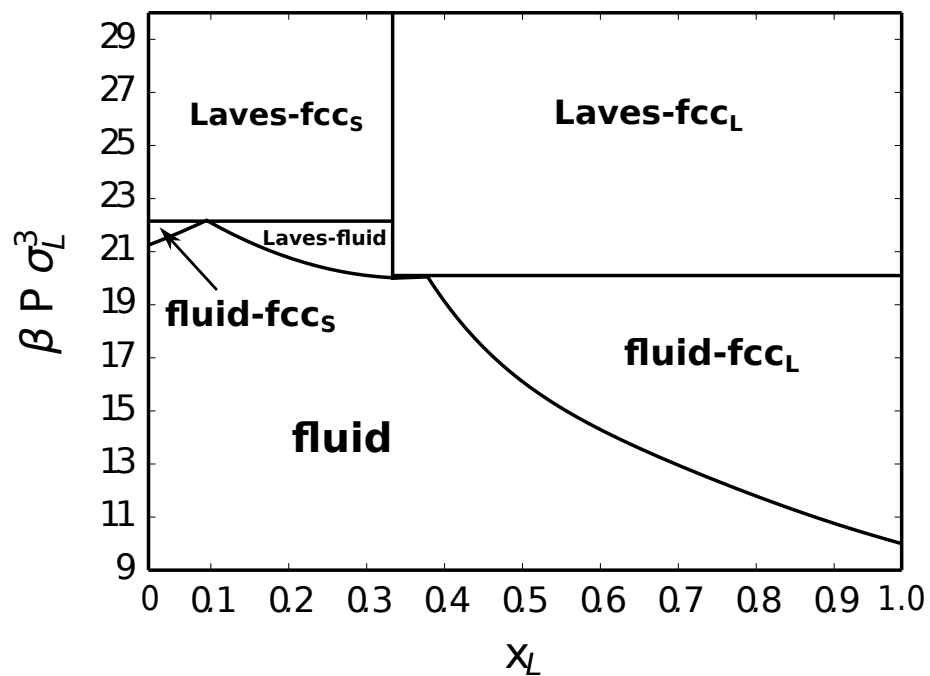


**Figure 6.4:** Phase diagram of a binary mixture of spheres interacting with WCA pair interactions with a diameter ratio  $q = 0.78$  at a reduced temperature  $T^* = k_B T / \varepsilon = 0.1$  in the composition  $x_L = N_L / (N_L + N_S)$ -reduced pressure  $\beta P \sigma_L^3$  plane. The labels are as in Fig. 6.3.

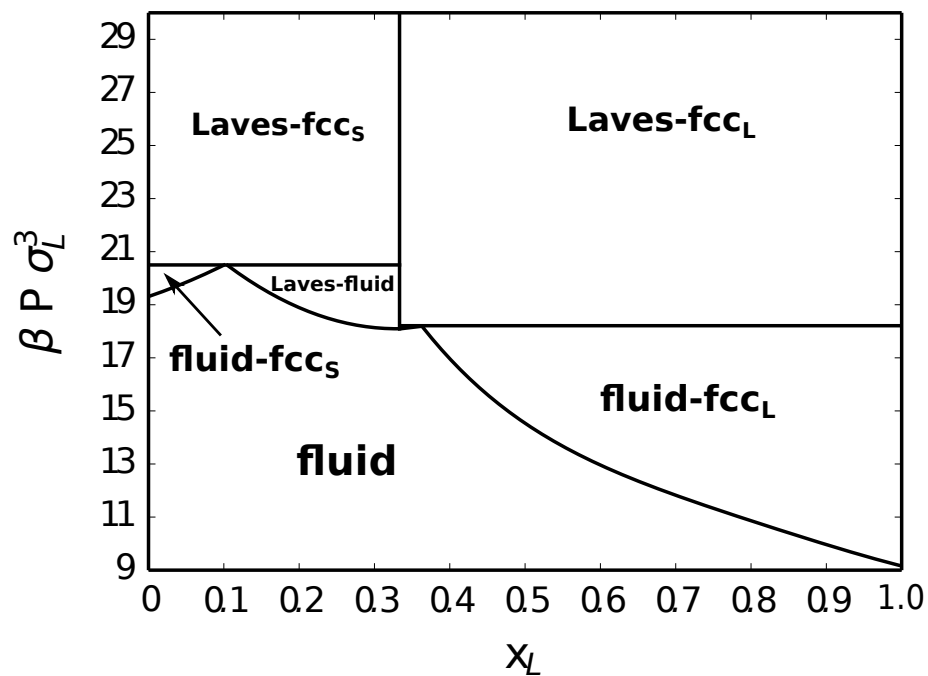


**Figure 6.5:** Phase diagram of a binary mixture of spheres interacting with WCA pair interactions with a diameter ratio  $q = 0.78$  at a reduced temperature  $T^* = k_B T / \varepsilon = 0.025$  in the composition  $x_L = N_L / (N_L + N_S)$ -reduced pressure  $\beta P \sigma_L^3$  plane. The labels are as in Fig. 6.3.

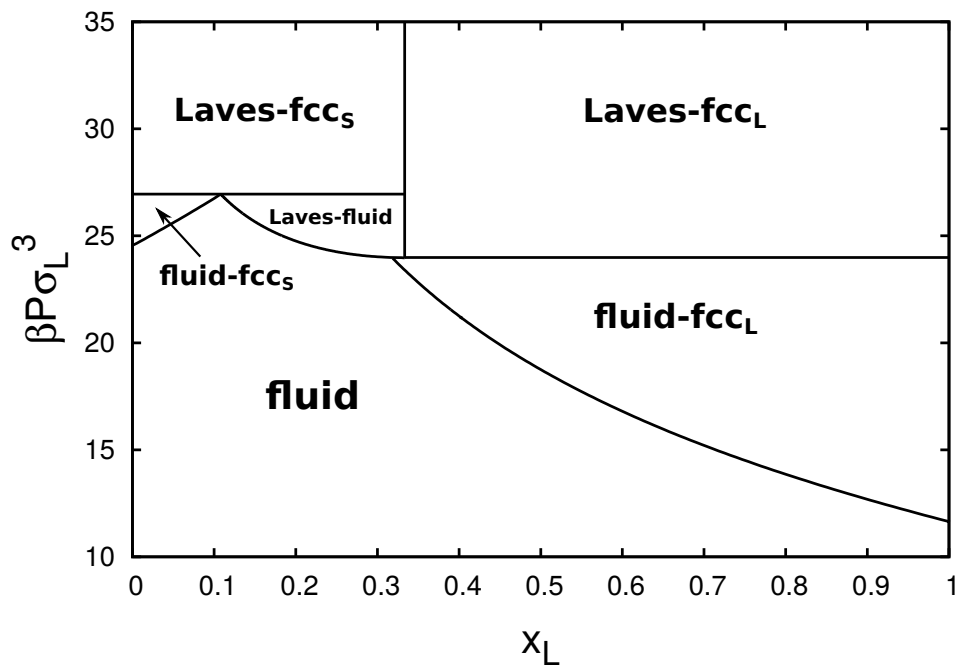


**Figure 6.6:** Phase diagram of a binary mixture of hard spheres with diameter ratio  $q = 0.78$  in the composition  $x_L = N_L/(N_L + N_S)$ -reduced pressure  $\beta P \sigma_L^3$  plane. The labels are as in Fig. 6.3.

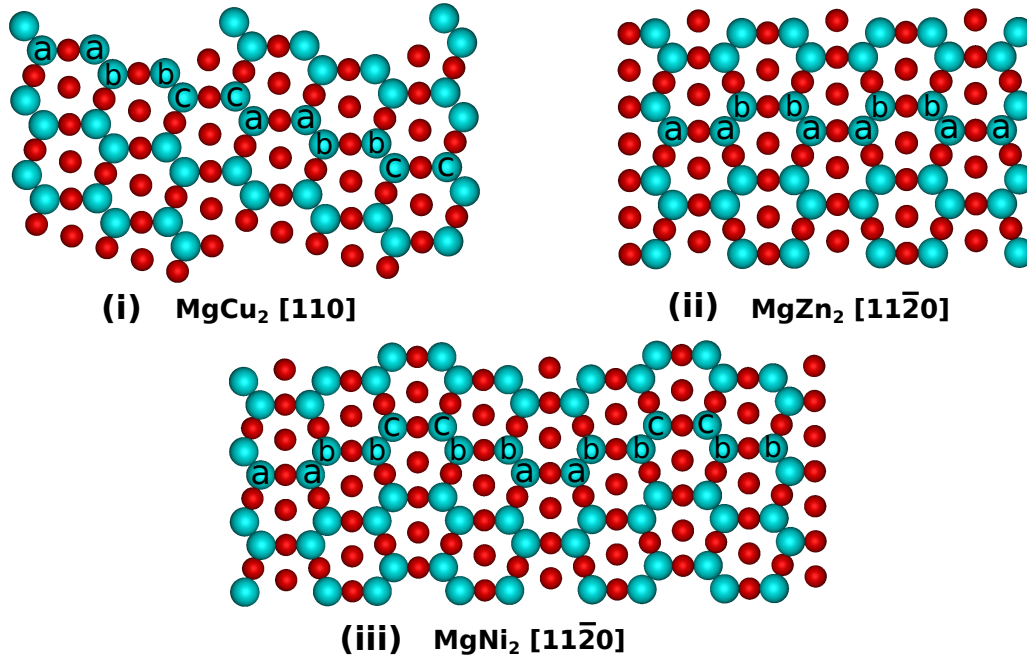


**Figure 6.7:** Structure of the three main types of Laves phases, showing the different stacking sequences of the large-sphere dimers, marked as  $aa$ ,  $bb$  and  $cc$ , when viewed along specific projection planes. The stacking of the large-sphere dimers is (i) “...aa-bb-cc...” for MgCu<sub>2</sub>, (ii) “...aa-bb...” for MgZn<sub>2</sub>, and (iii) “...aa-bb-cc-bb...” for MgNi<sub>2</sub>.

WCA spheres with a diameter ratio  $q$  and composition  $x_L$ , for varying system sizes. The excess Helmholtz free energies  $\beta F_{ex} = \beta F - N_1 \ln(N_1 \Lambda^3 / V) - N_2 \ln(N_2 \Lambda^3 / V) + N$  are listed in Table 6.1. We plot the excess Helmholtz free energy per particle  $F_{ex} / N k_B T + \ln(N) / N$  as a function of  $1/N$  for the three Laves phases, MgCu<sub>2</sub>, MgNi<sub>2</sub>, and MgZn<sub>2</sub>, in Fig. 6.8. We fit the data for  $\beta F_{ex} / N + \ln(N) / N$  as a linear function of  $1/N$  and the intercept at  $1/N = 0$  gives the excess free energy of the infinite bulk system [109]. We again find as in the hard-sphere case that the free-energy difference between the three LPs is of the order of  $10^{-3} k_B T$  per particle, with  $\beta f$  (Cu) = 6.07735,  $\beta f$  (Zn) = 6.07339 and  $\beta f$  (Ni) = 6.07524. In Ref. [24], a MgZn<sub>2</sub> phase was observed at low packing fractions that evolves to more MgCu<sub>2</sub> like at high packing fraction. We therefore also investigate the free-energy difference  $\Delta f(\text{Cu-Zn})$  between the MgCu<sub>2</sub> phase and that of the MgZn<sub>2</sub> as a function of density  $\rho \sigma_{av}^3$ . In the inset of Fig. 6.8, we clearly observe that the free-energy difference reduces with increasing density. Due to this minute free-energy difference, we expect to find a random stacking of LPs in experiments similar to the random-hexagonal-close-packed (rHCP) structure in the case of monodisperse hard spheres, which can be seen as a mixture of fcc and hexagonal-close-packed crystals. We thus conclude that the MgZn<sub>2</sub> LP is the thermodynamically stable phase even for soft repulsive pair potentials up to the degree of softness we have investigated here. We consider, in our calculations, the MgZn<sub>2</sub> LP in the phase diagrams presented in this Chapter.

The aim of this Chapter is to investigate the homogeneous nucleation of Laves phases in a purely repulsive binary fluid mixture. Previous simulation studies showed that the nucleation

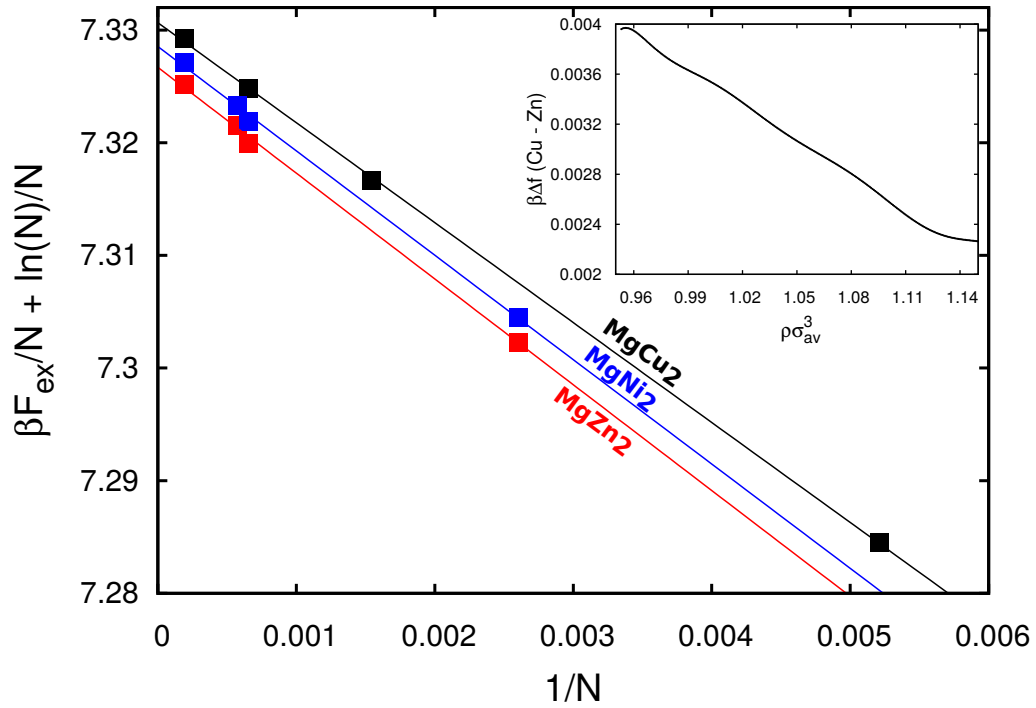


**Figure 6.8:** Finite-size scaling of the excess Helmholtz free energy  $F_{ex}/Nk_B T + \ln(N)/N$  versus  $1/N$  of the three Laves phases MgCu<sub>2</sub>, MgZn<sub>2</sub>, and MgNi<sub>2</sub> of a binary mixture of WCA spheres with a diameter ratio  $q = 0.78$ , at the melting density  $\rho \sigma_{av}^3 = 0.953$  and temperature  $k_B T / \varepsilon = 0.2$ . MgZn<sub>2</sub> is the Laves phase with the lowest free energy. The lines are linear fits to the data points. The inset shows the free-energy difference  $\beta \Delta f$  (Cu-Zn) between MgCu<sub>2</sub> and MgZn<sub>2</sub> Laves phases as a function of density  $\rho$ .

Phase	$N$	$n_{\text{eq}} \times 10^3$	$n_{\text{prod}} \times 10^3$	$\beta F_{\text{ex}}/N$	$\pm$
MgCu <sub>2</sub>	192	100	1000	7.25715	0.00051
MgCu <sub>2</sub>	648	100	1000	7.30665	0.00022
MgCu <sub>2</sub>	1536	100	1000	7.31999	0.00006
MgCu <sub>2</sub>	5184	100	1000	7.32760	0.00006
MgZn <sub>2</sub>	384	100	1000	7.28680	0.00027
MgZn <sub>2</sub>	1536	100	1000	7.31516	0.00002
MgZn <sub>2</sub>	1728	100	1000	7.31722	0.00006
MgZn <sub>2</sub>	5184	100	1000	7.32348	0.00004
MgNi <sub>2</sub>	384	100	1000	7.28900	0.00027
MgNi <sub>2</sub>	1536	100	1000	7.31713	0.00011
MgNi <sub>2</sub>	1728	100	1000	7.31902	0.00003
MgNi <sub>2</sub>	5184	100	1000	7.32545	0.00006

**Table 6.1:** Simulation details for calculating the excess Helmholtz free energies per particle  $\beta F_{\text{ex}}/N$  for different system sizes for a binary mixture of WCA particles with diameter ratio  $\sigma_S/\sigma_L = 0.78$  at the melting density  $\rho\sigma_{\text{av}}^3 = 0.953$ , and dimensionless temperature  $k_B T/\varepsilon = 0.2$ .  $n_{\text{eq}}$  and  $n_{\text{prod}}$  are the number of Monte Carlo cycles in the equilibration and production (sampling) runs, respectively, and the error estimate is given by the standard deviation of three independent simulations.

of a binary crystal, even a metastable one, can be favoured by choosing the composition of the fluid close to that of the desired binary crystal phase [164, 166]. Furthermore, Punnathanam *et al.* showed that the topology of the phase diagram affects the kinetic pathway of crystal nucleation [164]. For example, the phase diagrams for  $k_B T/\varepsilon = 0.2, 0.1$  and  $0.025$  (Figs. 6.3-6.5) show congruent freezing/melting of a stable Laves phase at  $x_L = 1/3$ , *i.e.* a compound solid melts into a fluid of the same composition, whereas the phase diagram of binary hard spheres with diameter ratio  $q = 0.78$  (Fig. 6.6) shows that a stable Laves phase undergoes a peritectic phase transition to a  $\text{fcc}_L$  solid and a fluid phase of composition  $x_L = 0.3187$ . Congruent freezing/melting enables us to study the nucleation of compound solids from a supersaturated fluid phase at the same composition. Hence, in our quest to nucleate Laves phases, we fix the composition of the fluid phase to the stoichiometric composition of the Laves phases, *i.e.*  $x_L = N_L/(N_L + N_S) = 1/3$ , and calculate the freezing and melting densities of the (MgZn<sub>2</sub>) Laves phase and the fluid phase as a function of the temperature  $T^* = k_B T/\varepsilon$ . To this end, we apply common tangent constructions to the Helmholtz free energy density  $\beta f\rho$  as a function of density  $\rho$ . We plot the resulting phase diagrams in the reduced temperature  $k_B T/\varepsilon$  - reduced density  $\rho\sigma_{\text{av}}^3$  plane in Fig. 6.9, and in the reduced pressure  $\beta P\sigma_L^3$  - reduced density  $\rho\sigma_{\text{av}}^3$  plane in Fig. 6.10. Fig. 6.9 shows that the phase transition shifts to lower densities  $\rho\sigma_{\text{av}}^3$  upon decreasing the temperature, which we expect as the spheres become more repulsive as illustrated in Fig. 6.2.

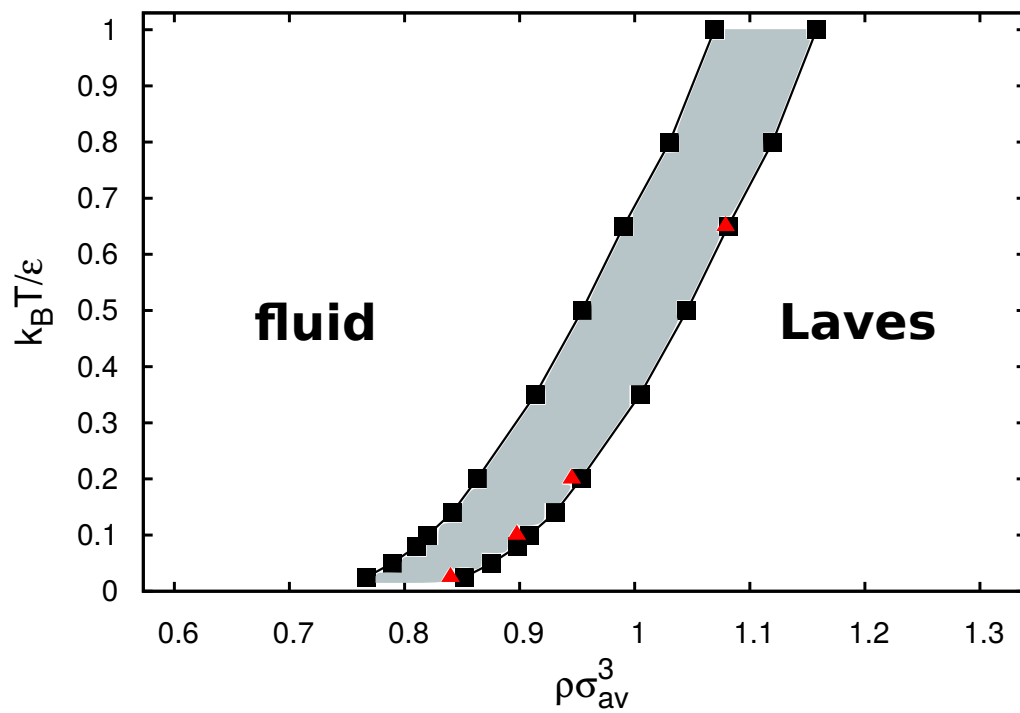


**Figure 6.9:** Fluid-Laves phase coexistence of a binary mixture of WCA spheres with a diameter ratio  $q = 0.78$  at a fixed composition  $x_L = 1/3$  in the reduced temperature  $k_B T / \epsilon$  - reduced density  $\rho \sigma_{av}^3$  plane. The red triangles denote simulation state points at which the spontaneous nucleation of LPs was observed.

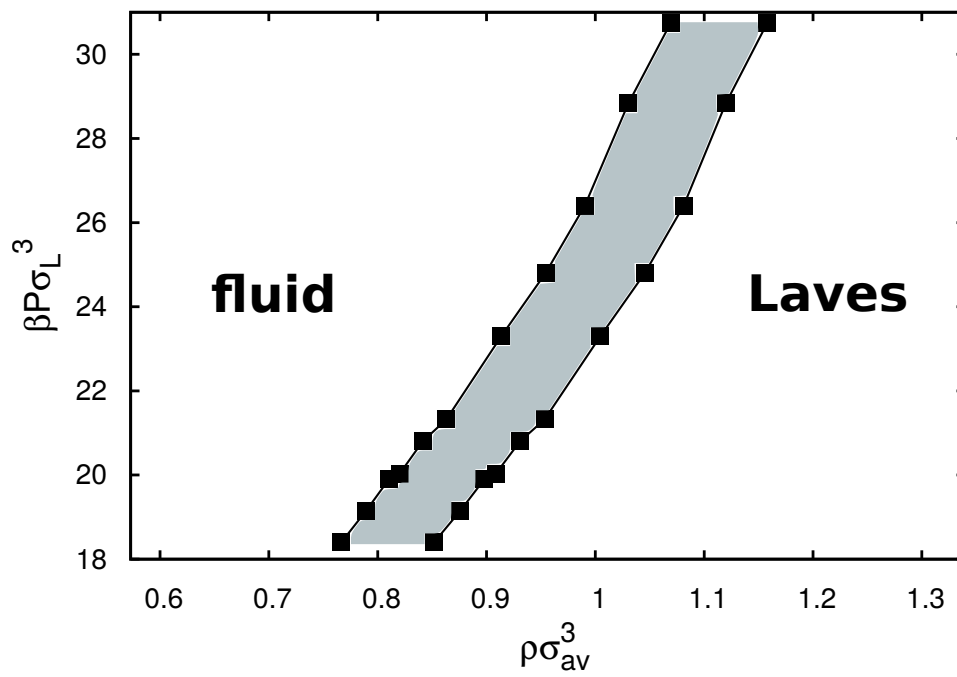


**Figure 6.10:** Fluid-Laves phase coexistence of a binary mixture of WCA spheres with a diameter ratio  $q = 0.78$  at a fixed composition  $x_L = 1/3$  in the pressure  $\beta P \sigma_L^3$  - reduced density  $\rho \sigma_{av}^3$  plane.

## 6.4 Spontaneous nucleation

### 6.4.1 Order parameters

In order to study the nucleation of Laves phases, we require a criterion that distinguishes crystalline clusters with the local symmetry of the LPs from the binary fluid. To this end, we first make a distinction between particles that have a solid-like environment with a LP-like symmetry and a fluid-like environment. We use the local bond orientational order parameters  $q_{l,m}^\alpha(i)$  to determine the symmetry of the local environment of particle  $i$  with identity  $\alpha(i) \in L, S$  [116]

$$q_{l,m}^\alpha(i) = \frac{1}{N_b(i)} \sum_{j=1}^{N_b(i)} Y_{l,m}(\theta_{i,j}, \phi_{i,j}), \quad (6.8)$$

where  $N_b(i)$  represents the number of all neighbours of particle  $i$  with identity  $\beta(j)$ ,  $Y_{l,m}(\theta, \phi)$  are the spherical harmonics for  $m$  ranging from  $[-l, l]$ , and  $\theta_{i,j}$  and  $\phi_{i,j}$  are the polar and azimuthal angles of the center-of-mass distance vector  $\mathbf{r}_{ij} = \mathbf{r}_j - \mathbf{r}_i$  with  $\mathbf{r}_i$  the position of particle  $i$ . The neighbours of particle  $i$  with identity  $\alpha(i)$  include all particles  $j$  with identity  $\beta(j)$  that lie within a radial distance  $r_c$  of particle  $i$ , and we set  $r_c$  equal to the distance corresponding to the first minimum of the respective radial distribution function. Subsequently, we calculate the dot product  $d_{l,\alpha\beta}(i, j)$  for each particle pair  $i$  with identity  $\alpha(i)$  and  $j$  with identity  $\beta(j)$

$$d_{l,\alpha\beta}(i, j) = \frac{\sum_{m=-l}^l q_{l,m}^\alpha(i) q_{l,m}^\beta(j)}{\left(\sum_{m=-l}^l |q_{l,m}^\alpha(i)|^2\right)^{1/2} \left(\sum_{m=-l}^l |q_{l,m}^\beta(j)|^2\right)^{1/2}}. \quad (6.9)$$

We note that the dot product is symmetric in  $\alpha$  and  $\beta$ , i.e.,  $d_{l,\alpha\beta}(i, j) = d_{l,\beta\alpha}(i, j)$ . We choose a symmetry index  $l = 6$ . In Fig. 6.11, we show the probability distribution function of the dot-products  $d_{6,LL}$ ,  $d_{6,LS}$ , and  $d_{6,SS}$  for a fluid, and the three Laves phases MgCu<sub>2</sub>, MgZn<sub>2</sub>, and MgNi<sub>2</sub> of a binary mixture of WCA spheres with a diameter ratio  $q = 0.76$  at coexistence. For  $P(d_{6,LL})$ , a marked overlap between the fluid and the Laves phase distributions is observed. We therefore use the average bond order parameter  $\bar{q}_{l,m}^\alpha(i)$  as introduced in Ref. [181], where  $\bar{q}_{l,m}^\alpha$  includes also the bond order parameter values of all its neighbours with identity  $\alpha$

$$\bar{q}_{l,m}^\alpha(i) = \frac{1}{N_b(i) + 1} \sum_{k=0}^{N_b(i)} q_{l,m}^\alpha(k), \quad (6.10)$$

and use the average bond order parameter in the dot-product of Eq. 6.9. We present also the probability distribution function of  $\bar{d}_{6,LL}$  in Fig. 6.11, and find that we can now better distinguish the fluid phase and the Laves phases. The bond between particles  $i$  and  $j$  is classified as a *solid* bond if the dot product  $d_{l,ij}$  lies in between a lower and an upper threshold value denoted by  $d_{\alpha\beta}^\downarrow$  and  $d_{\alpha\beta}^\uparrow$ . In order to discriminate crystalline clusters with LP-like symmetries from the fluid phase, we use the following cut-off values, determined from the intersections of the dot product distributions of the fluid and Laves phases in Fig. 6.11 for the three different species correlations. For the (i) large-large correlation, we employ  $\bar{d}_{6,LL} > d_{LL}^\downarrow = 0.88$ , (ii) small-small correlation  $d_{SS}^\downarrow = -0.23 < d_{6,SS} < d_{SS}^\uparrow = -0.04$  and (iii) small-large  $d_{LS}^\downarrow = -0.46 < d_{6,LS} < d_{LS}^\uparrow = -0.1$ .

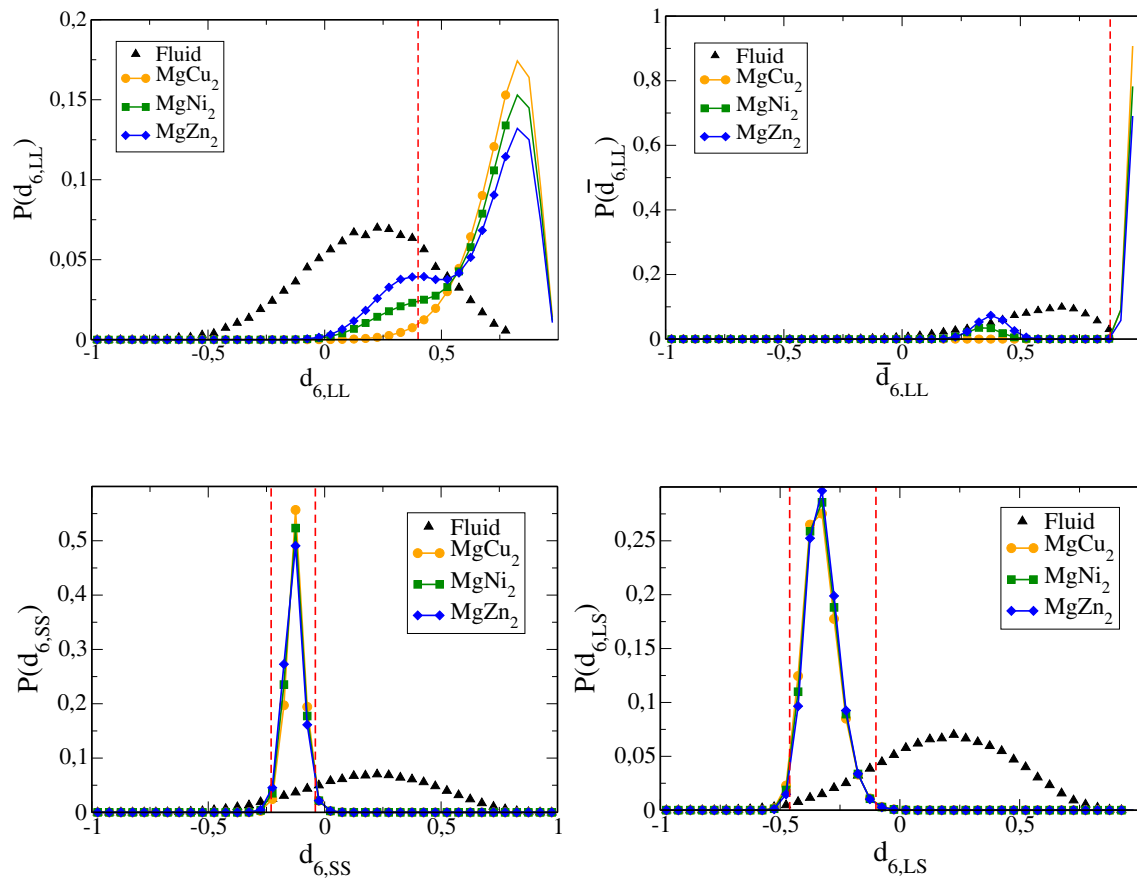


**Figure 6.11:** Probability distribution functions of the dot-product values  $d_{6,LL}$ ,  $\bar{d}_{6,LL}$ ,  $d_{6,SS}$ , and  $d_{6,LS}$  for the large-large, averaged large-large, small-small and large-small correlations, respectively, of the fluid phase and the three Laves phases of a binary mixture of WCA spheres with a diameter ratio  $q = 0.78$ , temperature  $T^* = 0.2$ , and at coexistence. The threshold values that we use in our crystal criterion are denoted by the vertical dashed lines.

We note that by using these threshold values for the large-large correlations, we miss a small distribution of particles at low  $\bar{d}_{6,LL}$  values in the  $P(\bar{d}_{6,LL})$  distribution of the Laves phases, and hence the number of particles with a LP structure is underestimated. However, we find no appreciable effect in our final crystal structure identification. Furthermore, feed-forward neural networks [182] were used to identify the LP-like clusters in the fluid on selected configurations, and we obtained a close agreement with the clusters identified by our chosen cut-offs. Using these threshold values, we define a particle  $i$  with identity  $\alpha$  as *crystalline* if the number of solid bonds satisfies  $\xi^\alpha(i) > \xi_c^\alpha$  where

$$\xi^\alpha(i) = \sum_{j=1}^{N_b(i)} H(d_{l,\alpha\beta}(i,j) - d_{\alpha\beta}^\downarrow) - H(d_{l,\alpha\beta}(i,j) - d_{\alpha\beta}^\uparrow) \quad (6.11)$$

and  $H$  is the Heaviside step function. We employ the threshold values  $\xi_c^L = 10$  and  $\xi_c^S = 9$  for the large and small species, respectively. This resulting identification criterion can be used to detect the crystalline clusters with a Laves phase symmetry from the fluid phase, but cannot be employed to distinguish between the three Laves phases.

In order to discriminate between the three Laves phases, we define the local averaged bond order parameter for particle  $i$  with identity  $\alpha(i) \in L, S$

$$\bar{q}_l^\alpha(i) = \sqrt{\frac{4\pi}{2l+1} \sum_{m=-l}^l |\bar{q}_{l,m}^\alpha(i)|^2}. \quad (6.12)$$

Subsequently, we use scatter plots of the large particles in the  $\bar{q}_4^L - \bar{q}_6^L$  to distinguish between the cubic (MgCu<sub>2</sub>) and the hexagonal (MgZn<sub>2</sub> and MgNi<sub>2</sub>) Laves phases as described in Section 6.4.3 [183].

## 6.4.2 Nucleation

We study the spontaneous crystal nucleation of Laves phases from a supersaturated fluid phase. To this end, we perform molecular dynamics simulations of a binary mixture of WCA spheres with diameter ratio  $q = 0.78$  and temperature  $T^* = 0.2, 0.1$  and  $0.025$ , and the stoichiometric composition of the Laves phase, i.e.  $x_L = 1/3$ , using HOOMD-blue (Highly Optimized Object-oriented Many-particle Dynamics) [184, 185], available under an open source license. We perform simulations in both the  $NVT$  and  $NPT$  ensemble, where we fix the number of particles  $N$ , temperature  $T$ , and the volume  $V$  or pressure  $P$ , respectively. We employ the Nosé-Hoover thermostat [186, 187] to keep the temperature constant in the  $NVT$  ensemble, and the Martyna-Tobias-Klein (MTK) barostat-thermostat [188] to fix the temperature and pressure in the  $NPT$  ensemble. We impose periodic boundary conditions in all three dimensions, and the time step is set to  $\Delta t = 0.01 \tau_{MD}$  with  $\tau_{MD}$  the MD time unit. The simulations run typically  $t \sim 10^9 \tau_{MD}$ , corresponding to weeks in real time.

## 6.4.3 Nucleation at constant density

We first investigate the spontaneous crystallization of Laves phases by performing simulations in the  $NVT$  ensemble. We fix the density in the simulations and study at which density we

observe spontaneous nucleation of the LPs from a supersaturated fluid phase with composition  $x_L = 1/3$ . We denote these densities by the red triangles in Fig. 6.9. Remarkably, we find that the density at which we find spontaneous nucleation are for all temperatures located near the melting line. We analyze the crystallization of the Laves phase in more detail for temperature  $T^* = 0.2$  and density  $\rho\sigma_{av}^3 = 0.945$ . To distinguish between the three Laves phase structures, we plot the bond order parameter values of the large particles on the  $\bar{q}_4^L$ - $\bar{q}_6^L$  plane in Fig. 6.12 for the initial fluid configuration and the final configuration at  $t = 3 \times 10^9 \tau_{MD}$ . We find that the bond order parameter values are low, i.e.  $\bar{q}_4^L \simeq 0.15$  and  $\bar{q}_6^L \simeq 0.25$  for the initial configuration as it corresponds to a disordered fluid phase, whereas we find two clear bond order parameter clouds, one at  $(\bar{q}_4^L, \bar{q}_6^L) \simeq (0.5, 0.57)$  and one at  $(\bar{q}_4^L, \bar{q}_6^L) \simeq (0.35, 0.5)$  with some scatter at low bond order parameter values in the case of the final configuration. The scatter at low bond order parameter values is to be expected as this state point lies in the fluid-Laves phase coexistence region as shown in Fig. 6.9), and thus the scatter plot shows the coexistence of fluid and Laves phases. For comparison, we also plot the bond order parameter values of the large spheres for the three Laves phases at coexistence. We clearly observe that there is a distinct cloud of order parameter values for the  $MgZn_2$  as denoted by the red box and the  $MgCu_2$  phase as shown by the blue box. The  $MgNi_2$ , which can be seen as a mixture of the  $MgCu_2$  and  $MgZn_2$  phase distributes itself between the two boxes. Comparing the bond order parameter values of the final configurations with those of the Laves phases, we clearly observe that the final structure coincides structurally with both the  $MgCu_2$  and  $MgZn_2$  LPs, and thus also the  $MgNi_2$  LP.

In addition, we also analyze the time evolution of the bond order parameters of the large and small species. In Fig. 6.13, we plot the probability distribution functions of  $\bar{q}_4^L$ ,  $\bar{q}_4^S$ ,  $\bar{q}_6^L$ , and  $\bar{q}_6^S$  at varying times. A comparison of the time evolution of  $P(\bar{q}_6^L)$  and  $P(\bar{q}_6^S)$  shows that both species order more or less simultaneously, as is revealed by the simultaneous appearance of a peak at high order parameter values at  $t = 200 \times 10^6 \tau_{MD}$ . We also observe that the structure that nucleates initially resembles that of the  $MgZn_2$  structure, but this can also be because the structure of the  $MgZn_2$  LP is closer to the disordered fluid state. When time proceeds, the crystal structure evolves into a more random stacking of Laves phases, which can be explained by the small free-energy difference between the three Laves phases, although the free energy is lowest for the  $MgZn_2$  phase. At long time scales the finite size effects become appreciable. We find that when the crystal structure ‘‘feels itself’’ through the periodic boundary conditions, the  $MgZn_2$  stacked particles start to re-orient themselves into a  $MgCu_2$  stacking. This is clearly visible from Fig. 6.13b, where the ‘ $MgZn_2$ -peak’ for the large particles goes down and the ‘ $MgCu_2$ -peak’ increases. Interestingly, Fig. 6.13d shows that the ‘ $MgZn_2$ -peak’ for the small particles remains the same and the small particles in the fluid phase order into  $MgCu_2$ -like particles, which indicates that this *reorientation* from  $MgZn_2$ -stacking to  $MgCu_2$ -stacking is dictated by the large species. The final structure that we obtain consists of  $\sim 60\%$   $MgCu_2$ -stacked particles as denoted by the blue particles and  $\sim 40\%$   $MgZn_2$ -stacked particles coloured as red in Fig. 6.12. The fluid particles are shown in purple.

#### 6.4.4 Nucleation at constant pressure

We now investigate the effect of pressure on the behaviour of the supersaturated fluid phase at  $k_B T/\varepsilon = 0.2$  via MD simulations in the  $NPT$  ensemble. We systematically sample pressures higher than the *coexistence pressure*  $\beta P \sigma_L^3 = 21.32$  (Fig. 6.10). We plot the size of the

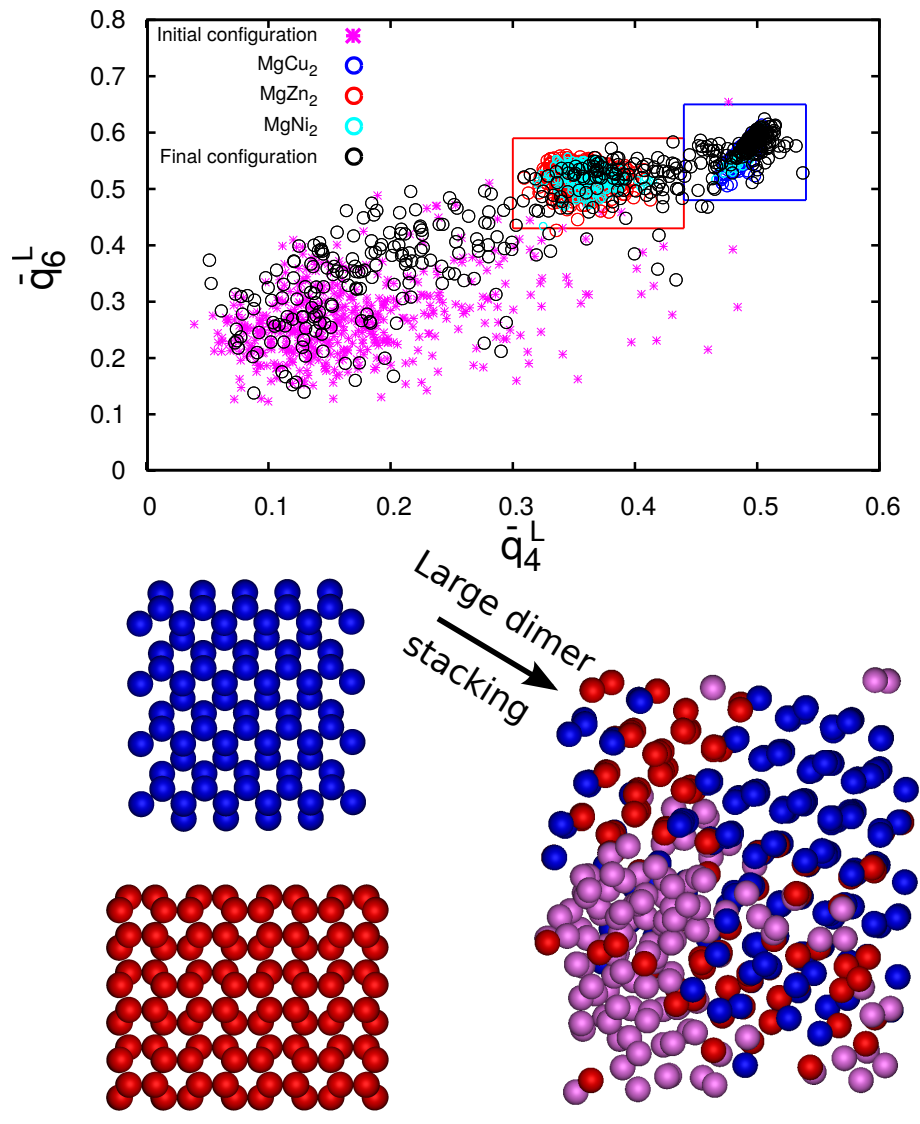


**Figure 6.12:** Scatter plot of the average bond order parameters of the large particles in the  $\bar{q}_4^L - \bar{q}_6^L$  plane of (i) the initial configuration of the disordered supersaturated fluid phase, (ii) the final configuration showing spontaneously formed crystalline clusters with signatures of the Laves phases, and (iii) the three Laves phases, MgZn<sub>2</sub>, MgCu<sub>2</sub>, and MgNi<sub>2</sub>, at bulk coexistence for comparison. The blue and red boxes signify the bond order parameter values that we used to identify the MgCu<sub>2</sub>- and MgZn<sub>2</sub>-stacking of the ordered particles in the final structure. The different stackings are also illustrated by the cartoons of the perfect MgCu<sub>2</sub> crystal (blue) and MgZn<sub>2</sub> crystal (red). The image on the right presents the final configuration in which the particles are coloured accordingly, i.e. MgZn<sub>2</sub>-stacked particles are coloured red, MgCu<sub>2</sub>-stacked particles are coloured blue. The fluid particles are shown in purple. The black arrow signifies the direction along which the stacking of large species can be identified visually as the stacking sequence described in Fig. 6.7.

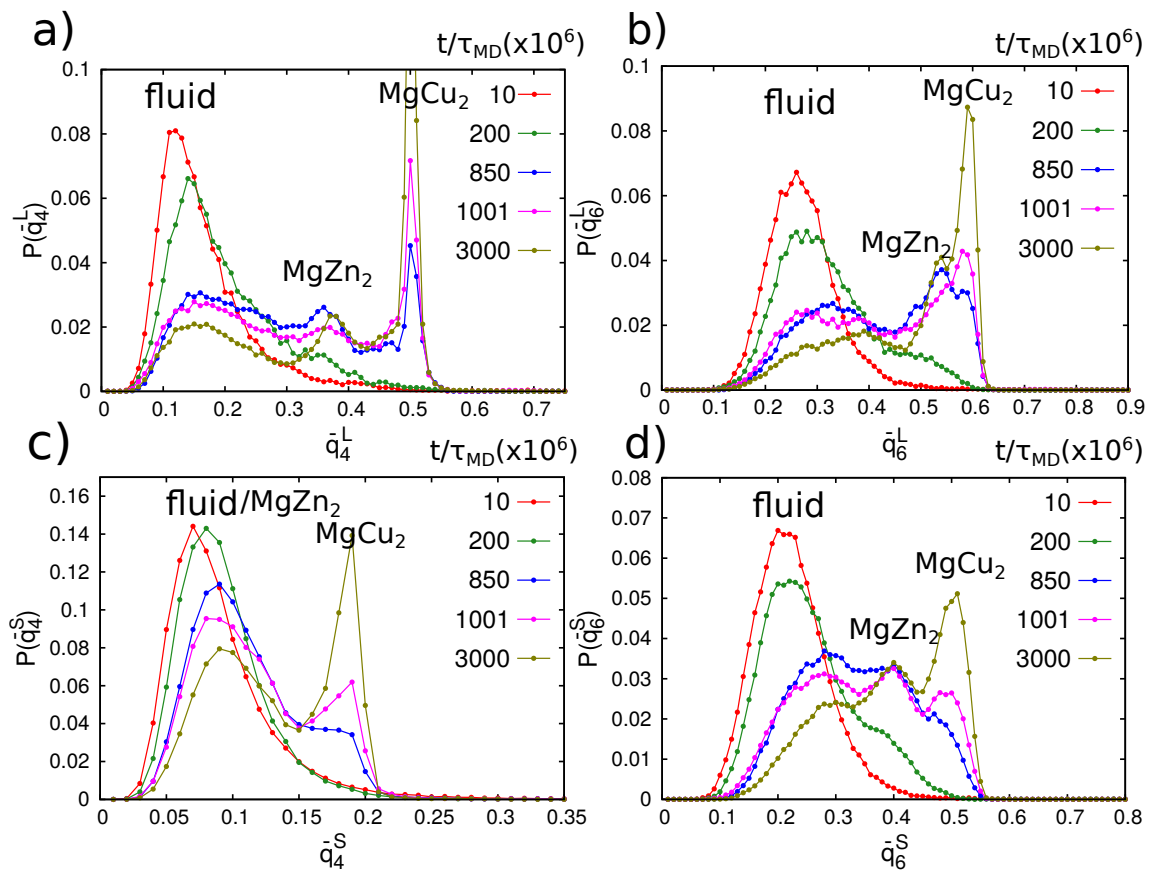


**Figure 6.13:** Time evolution of the structural order in a binary mixture of WCA particles with a diameter ratio  $q = 0.78$  and reduced temperature  $T^* = 0.2$ . Probability distribution of averaged bond order parameters for large-large and small-small species correlations, a)  $\bar{q}_4^L$ , b)  $\bar{q}_6^L$ , c)  $\bar{q}_4^S$ , and d)  $\bar{q}_6^S$ . The bond order parameters are averaged over the second shell of neighbours.

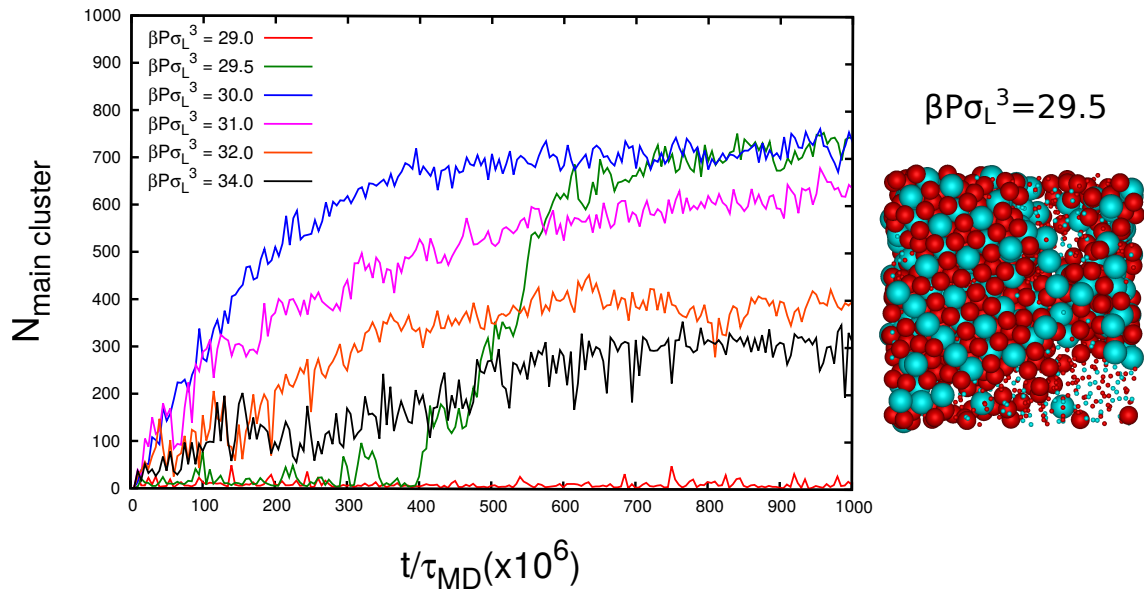


**Figure 6.14:** Size of the largest crystalline cluster for a binary mixture of WCA spheres with a diameter ratio  $q = 0.78$  and temperature  $T^* = 0.2$  as a function of time  $t/\tau_{MD}$  using MD simulations in the  $NPT$  ensemble. Profiles are averaged over three independent simulations.

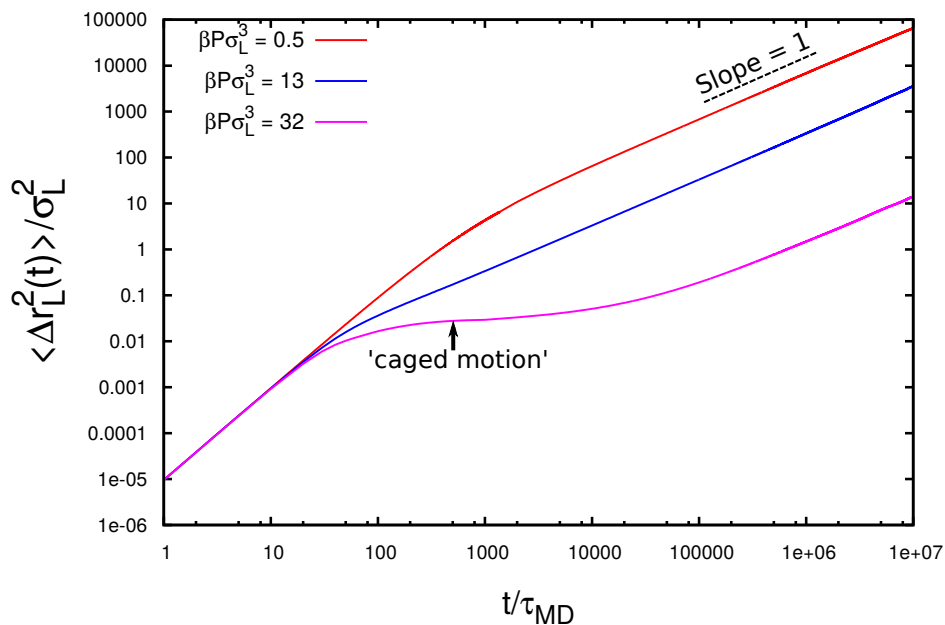


**Figure 6.15:** Mean square displacement of a binary mixture of WCA spheres with a diameter ratio  $q = 0.78$  and reduced temperature  $T^* = 0.2$  at varying pressures as labeled. At high pressure, the mean square displacement shows a cage-trapping plateau.

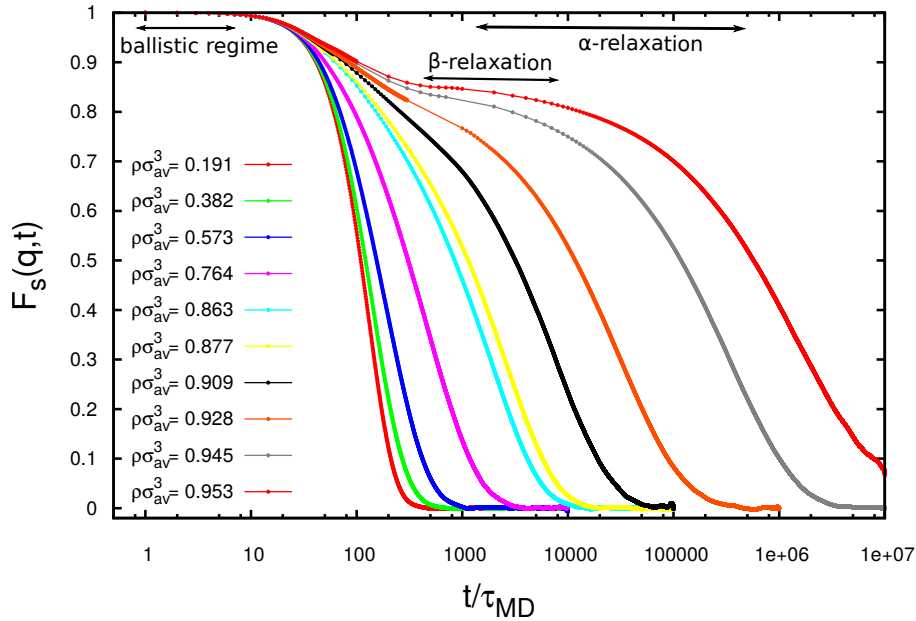


**Figure 6.16:** Self-intermediate scattering functions  $F_s(q,t)$  as a function of MD time for a binary mixture of WCA spheres with a diameter ratio  $q = 0.78$  at temperature  $T^* = 0.2$  and varying densities as labeled.

largest cluster as a function of time for varying pressures in Fig. 6.14. The Laves phase cluster that nucleates is detected using bond order parameters (BOP) for the large-large, large-small, and small-small correlations as described in Section. 6.4.1. At the lowest pressure  $\beta P \sigma_L^3 = 29$ , we find no sign of crystallization within reasonable time scales of our simulations. At a slightly higher pressure,  $\beta P \sigma_L^3 = 29.5$ , we observe that the system stays in a metastable fluid phase for some time until a nucleation event occurs where a crystalline nucleus forms in the supersaturated fluid phase, which subsequently grows out. Upon increasing the pressure further, we find that the fluid is unstable as the crystallization sets in immediately *via* spinodal decomposition indicating a *spinodal* point at  $\beta P \sigma_L^3 \simeq 30$ . For still higher pressures, we again see immediate crystallization, but the cluster grows less, which we attribute to slow dynamics. To verify this, we calculate the mean square displacement of the supersaturated fluid phase for varying pressures. We clearly observe a slowing down of the dynamics as a cage-trapping *plateau* appears in the mean square displacement at  $\beta P \sigma_L^3 = 32$ . For comparison, we also determine the mean square displacements for lower pressures. We thus conclude that the cluster growth is prohibited for  $\beta P \sigma_L^3 = 32$  in comparison with  $\beta P \sigma_L^3 = 31$  due to the onset of kinetic arrest. To investigate the kinetic arrest further, we calculate for different densities the self-intermediate scattering function  $F_s(q,t) = 1/N \sum_{j=1}^N \langle \exp \{ i \mathbf{q} \cdot [\mathbf{r}_j(0) - \mathbf{r}_j(t)] \} \rangle$  using Molecular Dynamics (MD) simulations and Monte Carlo (MC) simulations, where  $\mathbf{q}$  is the wave vector for which we use  $q = |\mathbf{q}| = 2\pi/\sigma_L$  and  $\mathbf{r}_j$  is the position vector of particle  $j$ . We plot  $F_s(q,t)$  as a function of time  $t/\tau_{MD}$  in Fig. 6.16 as obtained from MD simulations. The

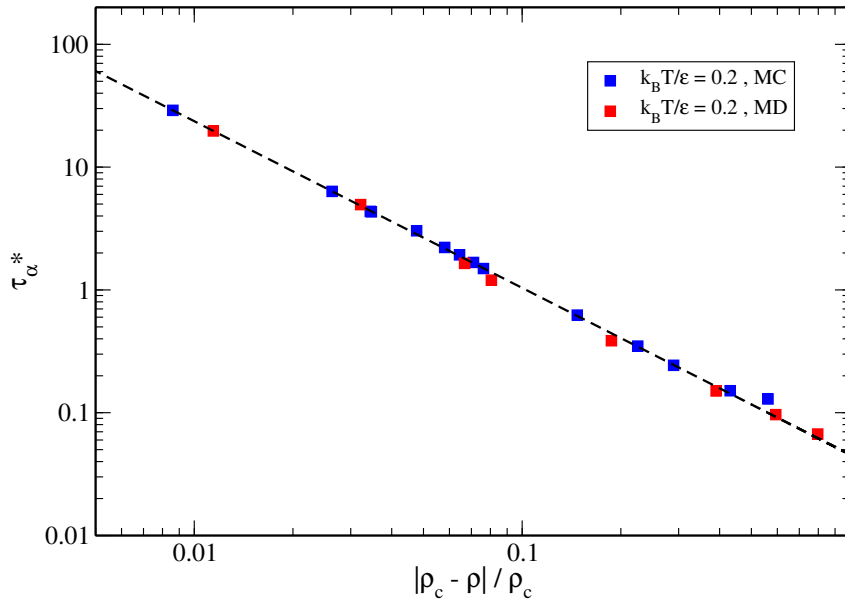


**Figure 6.17:** Structural relaxation time  $\tau_\alpha^* = \tau_{\alpha,MC} D_0 / \sigma_L^2$  as a function of density  $\rho$  with respect to the critical MCT density  $\rho_c$  for a binary mixture of WCA spheres with a diameter ratio  $q = 0.78$  at temperature  $T^* = 0.2$  as obtained from MC and MD simulations. The dashed line represents the MCT fit. Here,  $D_0$  denotes the short time diffusion coefficient of the large species.  $\tau_{\alpha,MD}^* = \tau_{\alpha,MD} \rho^{1/3} / \sqrt{m/k_B T}$  is scaled by a scaling factor  $\tau_{\alpha,MD}^* / \tau_{\alpha,MC}^* = 590$  to find the best match of the two curves. The critical MCT density is  $\rho_c \sigma_{av}^3 = 0.9396$  and the critical exponent  $\gamma = 1.3574$ .

ballistic regime is of the order of the mean collision time. For high enough supersaturations, the particles become sub-diffusive and undergo caged motion at intermediate times (the cage-trapping plateau is marked as the  $\beta$ -relaxation regime), and at long times particles become diffusive again. The dynamics slows down dramatically with increasing density. At sufficiently high densities, the structural relaxation time  $\tau_\alpha$ , defined by  $F_S(q, \tau_\alpha) = e^{-1}$  [189], diverges algebraically, *i.e.*,  $\tau_\alpha \sim |\rho_c - \rho|^{-\gamma}$  with  $\rho_c$  the critical density that represents the onset of the kinetic glass transition as described by mode coupling theory (MCT) [190]. We determine the short-time diffusion coefficient  $D_o$  of the large spheres using MC simulations, and we plot the reduced relaxation time  $\tau_{\alpha,MC}^*(\rho) = \tau_{\alpha,MC}(\rho) D_o / \sigma_L^2$  as obtained from MC simulations in Fig. 6.17. In order to compare the time scales from MC and MD simulations, we also determine  $\tau_{\alpha,MD}^*(\rho) = \tau_{\alpha,MD}(\rho) \rho^{1/3} / \sqrt{m/k_B T}$  from MD simulations, and we scale  $\tau_{\alpha,MD}^*(\rho)$  as a function of  $\rho$  by a scaling factor  $\tau_{\alpha,MD}^* / \tau_{\alpha,MC}^* = 590$  so that we obtain the best match of the two curves. Fitting the combined results obtained from both MD and MC simulations with the MCT expression, we find the critical MCT density  $\rho_c \sigma_{av}^3 = 0.9396$ .

In addition, we study the effect of temperature on the spontaneous crystallization of the Laves phase in a binary mixture of WCA spheres with a diameter ratio of  $q = 0.78$ . We recall that the pair interactions become steeper upon decreasing the temperature. We perform MD simulations in the  $NPT$  ensemble for  $T^* = 0.1$  and  $0.025$  and pressures higher than the coexistence pressures, which are  $\beta P \sigma_L^3 = 20.03$  for  $T^* = 0.1$ , and  $\beta P \sigma_L^3 = 18.35$  for  $T^* = 0.025$ , respectively. We note that  $T^* = 0.025$  has been previously used to model hard spheres [172, 173, 191]. We plot the size of the largest cluster as a function of time in Fig. 6.18 for the two temperatures, and we observe that crystallization becomes spinodal-like for  $\beta P \sigma_L^3 \simeq 27.5$  at  $T^* = 0.1$ , and  $\beta P \sigma_L^3 \simeq$

25.5 for  $T^* = 0.025$ . In addition, we also measure  $F_s(q, t)$  for varying densities for a binary mixture of WCA spheres and temperatures  $T^* = 0.1$  and  $0.025$ , and for a binary mixture of hard spheres, all at a diameter ratio of  $q = 0.78$ , using MC simulations, and plot the reduced relaxation times as a function of  $\rho$  in Fig. 6.19. We fit the relaxation times using the MCT fits, and list the critical MCT densities and critical exponents in Table 6.2 for the four systems.

Temperature	$\gamma$	$\rho_c \sigma_{av}^3$
$T^* = 0.2$	1.3574	0.9396
$T^* = 0.1$	1.3941	0.8926
$T^* = 0.025$	1.3993	0.8289
BHS	1.4314	1.0815

**Table 6.2:** Critical density  $\rho_c \sigma_{av}^3$  of the kinetic glass transition and critical exponent  $\gamma$  as obtained from MCT fits of the structural relaxation time  $\tau_\alpha^*$  as a function of density  $\rho$  for a binary mixture of WCA spheres at reduced temperature (i)  $T^* = k_B T / \varepsilon = 0.2$ , (ii) 0.1, (iii) 0.025, and (iv) a binary mixture of hard spheres (BHS), all at a diameter ratio of  $q = 0.78$ .

## 6.5 Hard sphere equivalence: Isomorphs

As already noted above, the softness of the WCA pair potential decreases upon decreasing  $T^*$ , and the WCA pair potential reduces to the pair potential of hard spheres with a diameter of  $2^{1/6} \sigma$  in the limit of  $T^* \rightarrow 0$ . In this section, we shall discuss (i) the mapping of our systems onto a binary mixture of hard spheres and (ii) the thermodynamic, structural and dynamical correlations of the fluids described by our model in comparison to those of hard-sphere fluids. In order to compare the WCA results with those of a binary hard-sphere system, we scale the WCA results in terms of an effective packing fraction as was also done in previous studies [173, 191]. To this end, we set the freezing number density of the WCA system at temperature  $T^*$  equal to the freezing density of hard spheres, which allows us to define an effective diameter  $\sigma_{\text{eff}}$  for each temperature using  $\pi \sigma_{\text{eff}}^3 / \sigma_{av}^3 (\rho \sigma_{av}^3)^{(f)} (x_L + (1 - x_L) q^3) / 6 = \eta_{\text{BHS}}^{(f)}$  with  $\eta_{\text{BHS}}^{(f)}$  the binary hard-sphere freezing packing fraction and  $(\rho \sigma_{av}^3)^{(f)}$  the reduced freezing density of the WCA system. For a binary mixture of hard spheres with a diameter ratio  $q = 0.78$ , the freezing packing fraction is  $\eta_{\text{BHS}}^{(f)} = 0.5356$ . Using the effective diameter  $\sigma_{\text{eff}}$ , the phase diagram in Fig. 6.9 may be rescaled to the  $k_B T / \varepsilon$  - packing fraction  $\eta_{\text{eff}}$  plane by mapping the WCA systems at each temperature  $T^*$  to the binary hard-sphere freezing packing fraction. In this representation, the freezing line becomes a vertical line as the freezing density for all temperatures of the WCA system is scaled to the freezing density of hard spheres. In addition, this phase diagram, where the density is scaled with respect to that at freezing, shows the effect of softness of the interactions on the melting line and the width of the coexistence region. We find that the melting line shifts slightly to lower packing fraction and that the width of the coexistence region decreases upon increasing the softness of the potential, i.e. increasing the reduced temperature  $T^*$ .

In another approach, the effective diameter may be scaled to the hard-core limit  $\sigma_{HS,L} = 2^{1/6} \sigma_L$ , in view of the limiting case of ‘infinite hardness’ of the WCA potential (Fig. 6.2) at  $T \rightarrow 0$ .

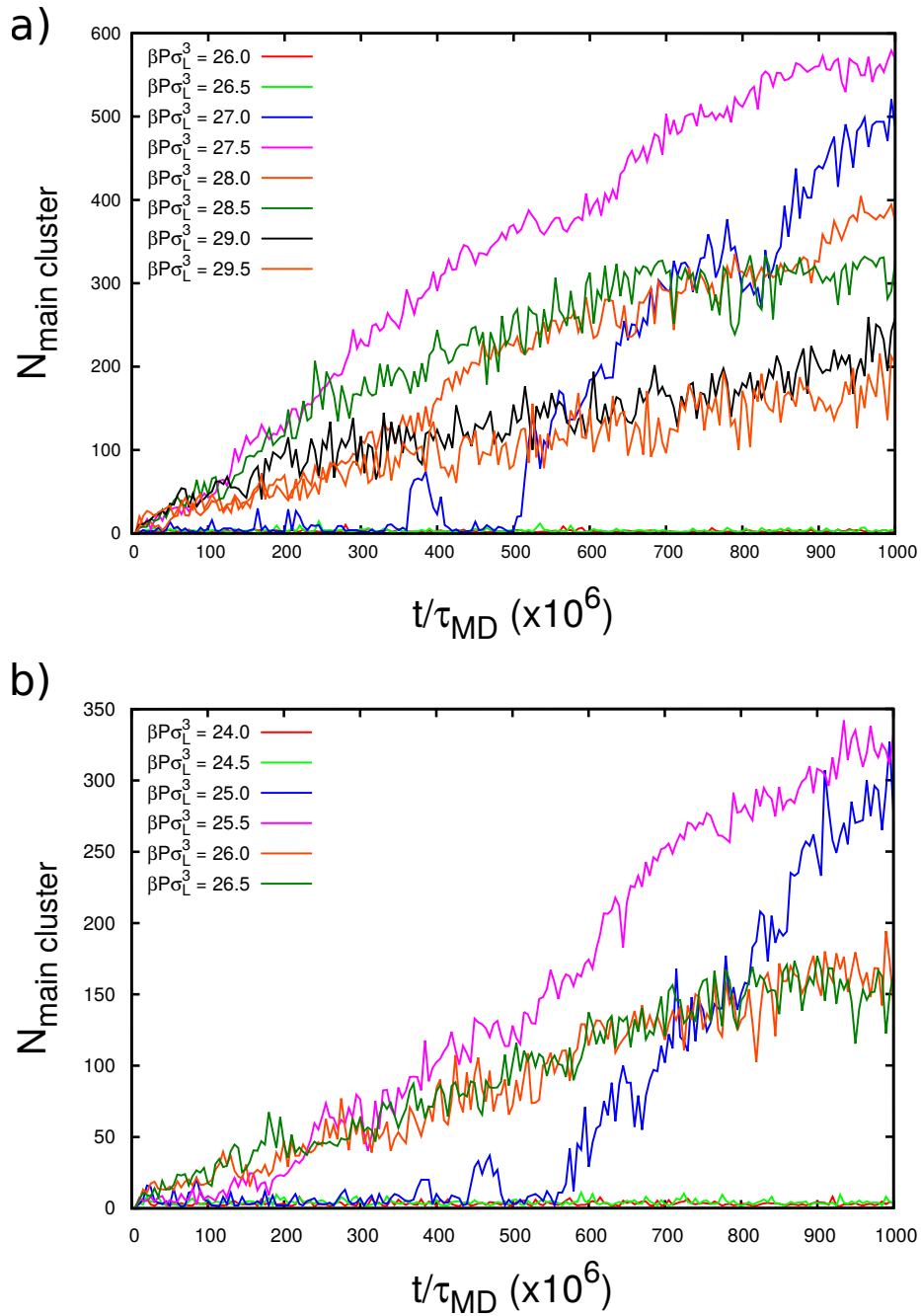


**Figure 6.18:** Size of the largest crystalline cluster for a binary mixture of WCA spheres with a diameter ratio  $q = 0.78$  at temperature a)  $T^* = 0.1$  and b)  $T^* = 0.025$ , as a function of time  $t/\tau_{\text{MD}}$  using MD simulations in the  $NPT$  ensemble. Profiles are averaged over three independent simulations.

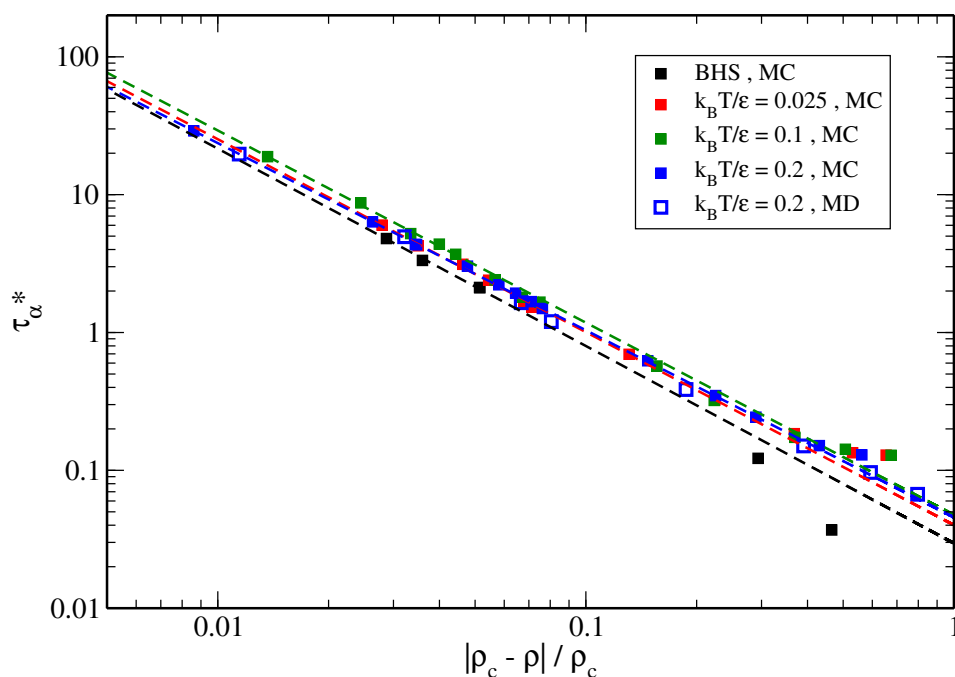


**Figure 6.19:** Structural relaxation time  $\tau_\alpha^* = \tau_{\alpha,MC} D_0 / \sigma_L^2$  as a function of density  $\rho$  with respect to the critical MCT density  $\rho_c$  for a binary mixture of WCA spheres with a diameter ratio  $q = 0.78$  at temperature  $T^* = 0.025, 0.1$  and  $0.2$ , and for a binary mixture of hard spheres, all at a diameter ratio of  $q = 0.78$ , as obtained from MC (and also MD for  $T^* = 0.2$ ) simulations. The dashed lines represent the MCT fit. Here,  $D_0$  denotes the short time diffusion coefficient of the large species.  $\tau_{\alpha,MD}^* = \tau_{\alpha,MD} \rho^{1/3} / \sqrt{m/k_B T}$  is scaled by a scaling factor  $\tau_{\alpha,MD}^* / \tau_{\alpha,MC}^* = 590$ . The critical MCT densities and critical exponents are listed in Table 6.2 for the four cases.

With this scaling, we plot the chemical potential difference  $\beta\Delta\mu = \beta\mu_{\text{Laves}}(P) - \beta\mu_{\text{fluid}}(P)$  between the Laves phases and the fluid phase as a function of supersaturation pressure  $\beta P\sigma_{HS,L}^3$  in Fig. 6.20a. The chemical potential difference between the Laves phases and the fluid phase at various supersaturations is calculated from the Gibbs-Duhem relation

$\beta \int_{\mu(P_{\text{coex}})}^{\mu(P)} d\mu' = \int_{P_{\text{coex}}}^P \frac{1}{\rho(P')} dP'$  [166]. If we now compare the values of  $\beta\Delta\mu$  corresponding to the pressures at which spinodal decomposition was observed in Section 6.4.4 (Fig. 6.25), we find an intriguing “universality” in the thermodynamic driving force for nucleation of the Laves phase for  $k_B T/\varepsilon = 0.025$  ( $\beta\Delta\mu = -0.53$ ), 0.1 ( $\beta\Delta\mu = -0.52$ ) and 0.2 ( $\beta\Delta\mu = -0.53$ ). More surprisingly, if we plot  $\beta\mu$  as a function of  $\beta P\sigma^*$ , where  $\sigma^*$  is defined in such a way that the coexistence pressure of the WCA systems at temperatures  $T^*$  equals the coexistence pressure of a binary hard-sphere mixture  $\beta P\sigma_{HS,L}^3 = 25.4$  with  $\sigma_{HS,L}$  the hard-core diameter of the large spheres, we find a collapse of the equations of state upto  $\beta P\sigma^{*3} \approx 40$  (Fig. 6.20b).

These observations immediately raise the exciting possibility of an equivalence between the thermodynamics, structure, and dynamics of our WCA mixtures and that of binary hard-sphere mixtures under the hidden scale invariance [192] of simple liquids, which may enable us to make predictions on the nucleation of the Laves phase in a purely hard-sphere system.

The development of perturbation and integral equation theories for simple liquids in the 1970s was based on the basic premise that the structure of a monoatomic fluid at high density is close to that of a hard-sphere system [171, 193, 194]. Hard spheres, as is generally known, have a single thermodynamic state variable, the packing fraction, which yields a one-dimensional phase diagram and consequently a unique freezing/melting transition. On this basis one can reasonably expect invariance of the structure along the melting/freezing line for simple fluids, and in thermodynamic properties such as the relative density change upon freezing/melting [195, 196]. In order to ascertain whether the thermodynamic driving force for nucleation is an invariant property, we open the discussion on “isomorphs”, which are curves in the thermodynamic phase diagram along which the structure and dynamics in appropriately reduced units are invariant. These reduced units are defined in terms of the length unit  $l_0 = \rho^{-1/3}$ , and energy unit  $e_0 = k_B T$  for the state-point properties, and time unit  $t_0 = \rho^{-1/3} \sqrt{m/k_B T}$  for dynamic properties using Newtonian dynamics. For instance, the particle coordinates of a microscopic configuration  $\mathbf{R} \equiv (\mathbf{r}_1, \dots, \mathbf{r}_N)$  at density  $\rho$  is defined in reduced units as  $\rho^{1/3}\mathbf{R}$ , which corresponds to the coordinates of a scaled coordinate system with unit density. We can now define two thermodynamic state points at density and temperature  $(\rho_1, k_B T_1/\varepsilon)$  and  $(\rho_2, k_B T_2/\varepsilon)$  to be *isomorphic*, when the two microscopic configurations  $\mathbf{R}^{(1)} \equiv (\mathbf{r}_1^{(1)}, \dots, \mathbf{r}_N^{(1)})$  and  $\mathbf{R}^{(2)} \equiv (\mathbf{r}_1^{(2)}, \dots, \mathbf{r}_N^{(2)})$  have the same reduced coordinates, i.e.  $\rho_1^{1/3}\tilde{\mathbf{R}}^{(1)} = \rho_2^{1/3}\tilde{\mathbf{R}}^{(2)}$ , and have proportional Boltzmann factors [197] (Eq. 6.13)

$$e^{-U(\mathbf{r}_1^{(1)}, \dots, \mathbf{r}_N^{(1)})/k_B T_1} = C_{12} e^{-U(\mathbf{r}_1^{(2)}, \dots, \mathbf{r}_N^{(2)})/k_B T_2}, \quad (6.13)$$

with  $C_{12}$  a proportionality constant that depends on the two state points. Isomorphic curves in the phase diagrams are defined as curves on which any two state points are isomorphic. Only inverse power law (IPL) liquids (for which the interactions scale with distance as  $\propto r^{-n}$ ) have exact isomorphs for state points  $\rho_1^{n/3}/T_1 = \rho_2^{n/3}/T_2$  with  $C_{12} = 1$ . Any other system, including the WCA system, which is a combination of two IPLs, cannot have exact isomorphs, but we will assume that isomorphic curves may exist to a good approximation in the thermodynamic

phase diagram in the case the fluid is strongly correlating as in the supersaturated fluid state as considered here. In view of this, we shall now check the proportionality between Boltzmann factors, which defines an isomorph. This direct isomorph check can be phrased in the form of a question: for a given change in density (for the two thermodynamic state points we wish to compare), does a temperature exist for which the new density state point is isomorphic to the initial one? From computer simulations, we can check this condition by plotting the potential energy of each generated microscopic configuration against the potential energy of the same configuration but scaled to the new density. If the potential energies are highly correlated, this would assert the proportionality condition as Eq. 6.13 implies  $U(\mathbf{R}^{(1)})/k_B T_1 = U(\mathbf{R}^{(2)})/k_B T_2 + C_{12}$ . We thus correlate thermodynamic state points along the fluid freezing line, crystal melting line, and the spinodal line in the phase diagram. To this end, we perform Monte Carlo simulations at the density state point on the freezing line at  $T^* = 0.2$ , and plot in Fig. 6.21 the potential energy of the simulation configurations against the potential energy of the same configurations but rescaled to the freezing density at  $T^* = 0.14$ . We find strong correlations between the potential energies for the two state points as shown by the stretched oval cloud of points. The interpretation of the slope of the straight line fit through the stretched oval cloud is that two state points are isomorphic if the temperature of the new density is the slope times the old temperature, i.e.,  $0.779898 \cdot 0.2 = 0.156$ , which is slightly higher than the temperature  $T^* = 0.14$  corresponding to this freezing density. By rescaling the potential energy of these configurations to the freezing densities at other temperatures  $T^*$ , enables us to trace out the freezing line isomorph on the thermodynamic phase diagram. We find that even if the actual freezing line itself is not an exact isomorph, it lies close to the resulting freezing line isomorph. Similarly, we find strong potential energy correlations between the *spinodal* state points for  $k_B T/\epsilon = 0.025, 0.1$  and  $0.2$  (although we only show the quantitative correlation between the state points of the last two temperatures in Fig. 6.21). However, we find that the correlation between thermodynamic state points along the crystal melting line is not very strong. In spite of this, we also trace out the melting line isomorph on the thermodynamic phase diagram. As the direct isomorph check as described above depends on the reference state point for which we take the state points at  $T^* = 0.2$  here, we will assume in the remainder of this Chapter the actual freezing line, melting line, and spinodal to be approximately isomorphic.

In the case two state points  $(\rho_1, k_B T_1/\epsilon)$  and  $(\rho_2, k_B T_2/\epsilon)$  are isomorphic, they are characterised by the same structure and dynamics in reduced units. In order to verify the structural invariance of state points on our freezing line and spinodal line, we plot the radial distribution function for the large spheres as a function of reduced radial distance for (i) three state points on the freezing line and (ii) three state points on the spinodal line in Fig. 6.22. There is good data collapse for both sets of  $g(r)$ 's as the peak positions coincide. In addition, one also observes that with lowering temperature, the  $g(r)$  becomes more and more hard-sphere-like. Upon lowering the temperature, we find from the first peak of the  $g(r)$  that the penetrability of the particles decreases, and as the number of particles in the first shell should remain the same for all three temperatures, the height of the first peak increases with lowering the temperature. To verify the dynamic invariance [197, 198], we investigate the structural relaxation by comparing their self-intermediate scattering functions  $F_s(\tilde{q}, \tilde{t})$  at the reduced wave vector  $\tilde{q} = ql_0$  as a function of the reduced time  $\tilde{t} = t/t_0$  with  $l_0 = \rho^{-1/3}$  and  $t_0 = \rho^{-1/3} \sqrt{m/k_B T}$ . We compare  $F_s(\tilde{q}, \tilde{t})$  for state points on the freezing line for  $k_B T/\epsilon = 0.025, 0.1$  and  $0.2$  and on the spinodal line ( $\beta \Delta \mu =$

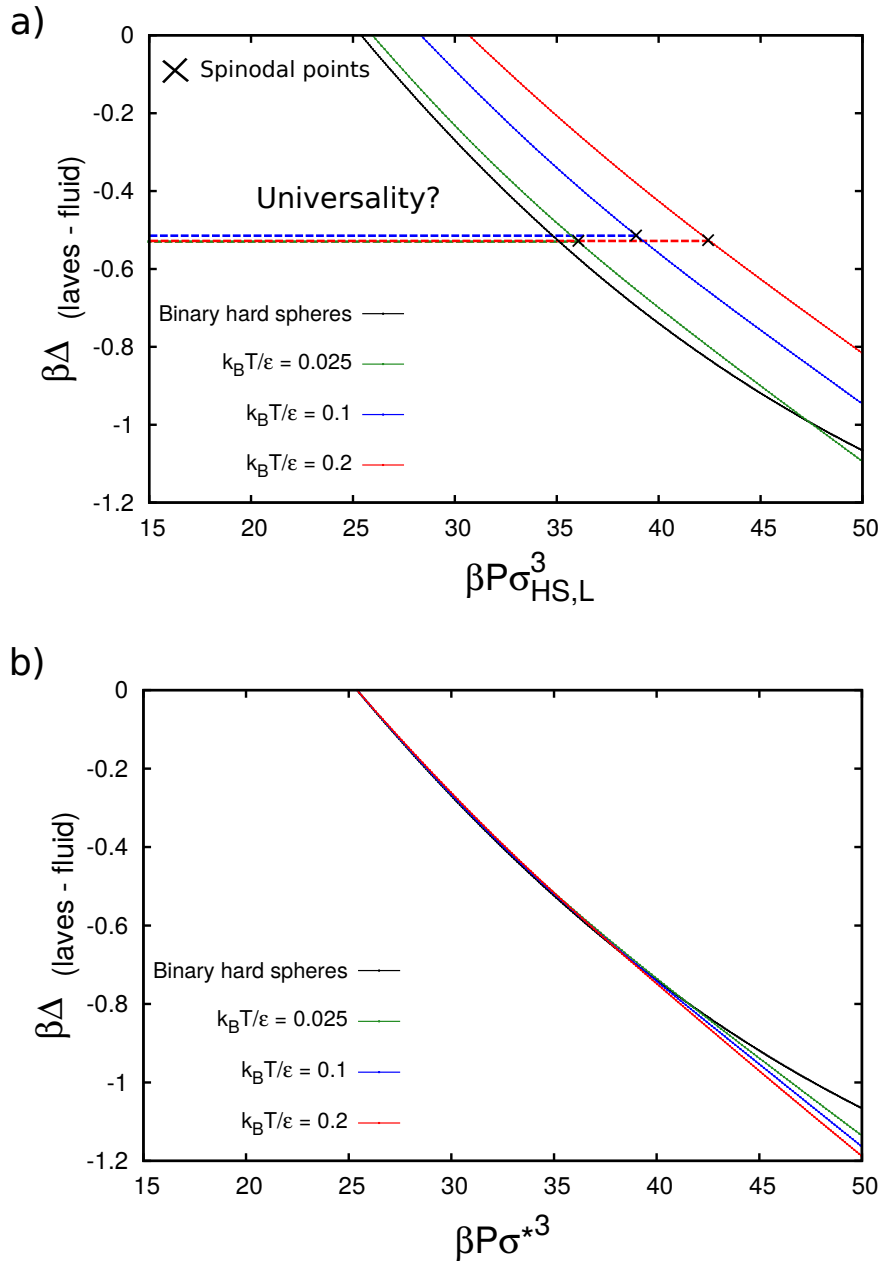


**Figure 6.20:** a) Chemical potential difference  $\beta\Delta\mu = \beta\mu_{\text{Laves}}(P) - \beta\mu_{\text{fluid}}(P)$  between the Laves phases and the fluid phase as a function of supersaturation pressure  $\beta P \sigma_{HS,L}^3$  for  $k_B T/\epsilon = 0.2, 0.1, 0.025$  and binary hard spheres. Here,  $\sigma_{HS,L}$  denotes the large sphere hard-core diameter, which for the WCA potentials corresponds to  $2^{1/6}\sigma_L$  in the zero temperature limit. b) Chemical potential difference  $\beta\Delta\mu$  as a function of  $\beta P \sigma^{*3}$ , where  $\sigma^*$  is defined in such a way that the coexistence pressures of the WCA systems at temperatures  $T^*$  equal the coexistence pressure of the binary hard-sphere mixture for  $q = 0.78$ , i.e.,  $\beta P \sigma_{HS,L}^3|_{\text{coex}} = 25.4$ .

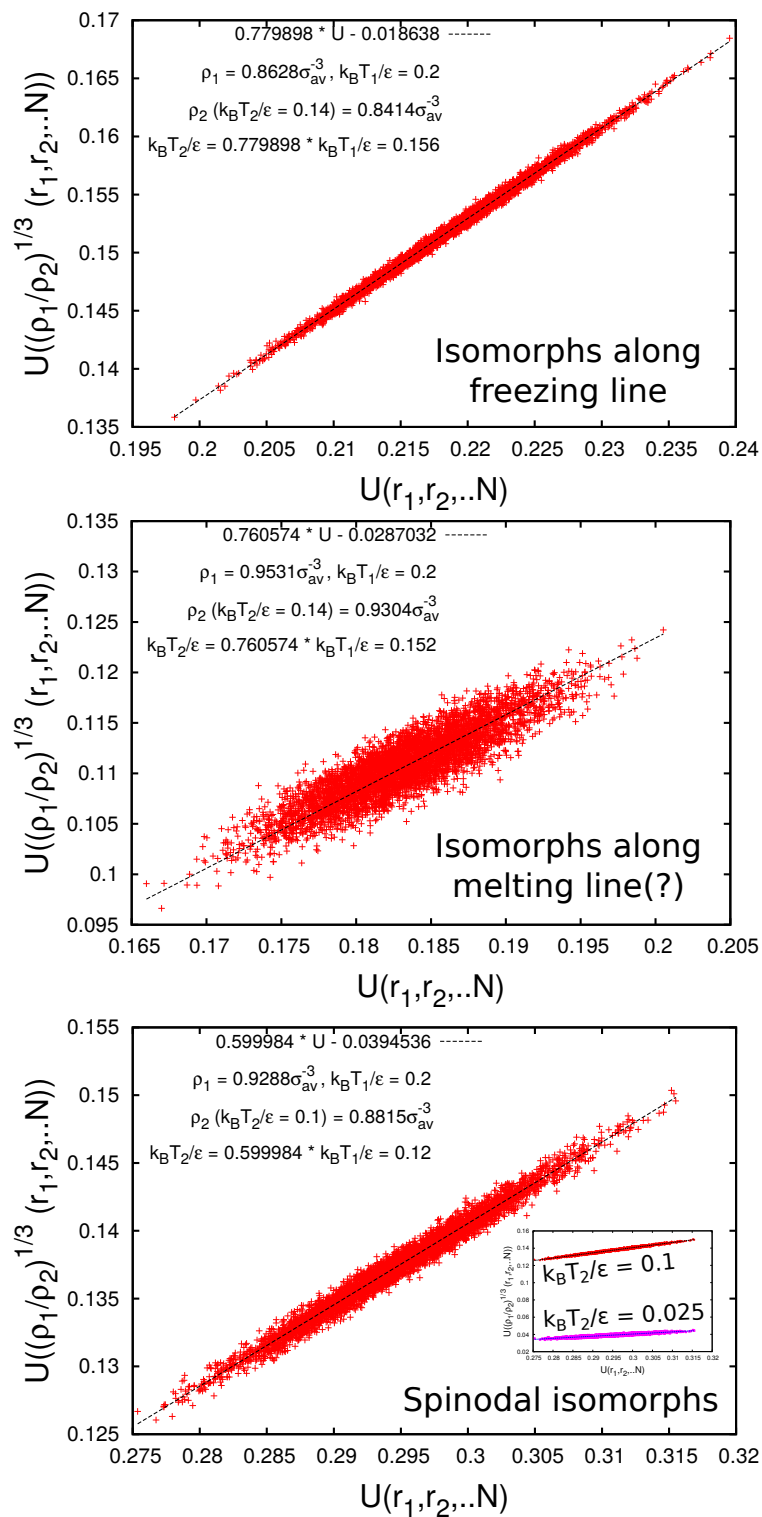


**Figure 6.21:** Direct check of the isomorph condition Eq. 6.13 for thermodynamic state points along the freezing line, melting line and spinodal line. For all the cases,  $k_B T/\epsilon = 0.2$  was used as the reference potential.

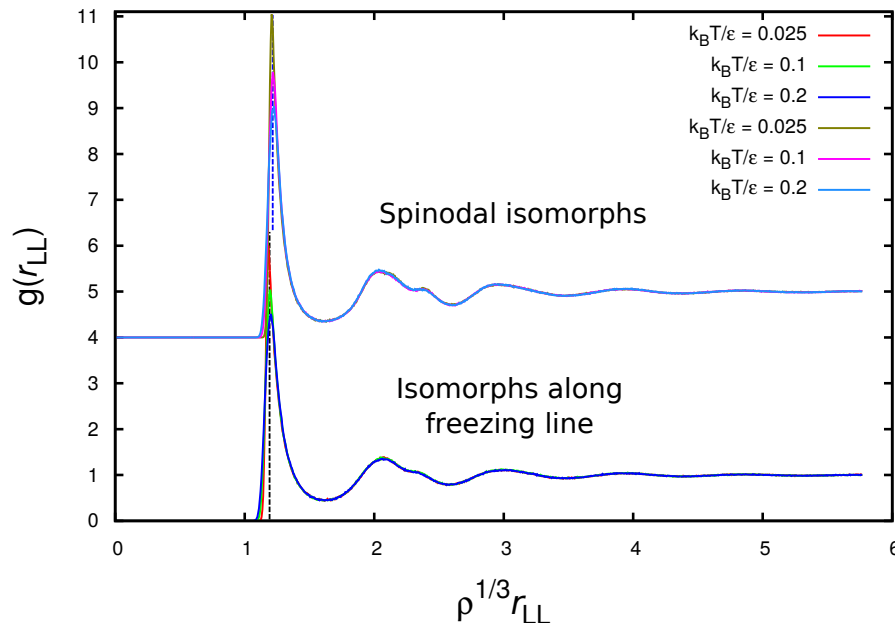


**Figure 6.22:** The radial distribution function  $g(r_{LL})$  of the large spheres as a function of the reduced radial distance  $\rho^{1/3} r_{LL}$  for three state points on the freezing line and for three state points on the spinodal line.

-0.53) corresponding to  $k_B T / \epsilon = 0.025$  and  $0.1$  in Fig. 6.23. We observe an excellent collapse for the state points on the freezing line as well as on the spinodal line.

We summarise our results in this section in a *revised* phase diagram in the reduced temperature  $k_B T / \epsilon$  - effective packing fraction  $\eta_{\text{eff}}$  plane. As we now discuss our systems in relation to binary mixtures of hard spheres, we have converted the density to packing fraction, which is commonly used for hard-particle systems. To this end, the reduced densities from Fig. 6.9 have been scaled to an effective packing fraction  $\eta_{\text{eff}} = \pi \sigma_{\text{av}}^3 2^{1/2} \rho / 6$ , and the resulting fluid-Laves phase coexistence is denoted by the blue region in Fig. 6.24. The scaling factor  $2^{1/2}$  enters here as the WCA system reduces to hard spheres with a diameter  $2^{1/6} \sigma$  in the limit  $T \rightarrow 0$ , see Fig. 6.2. The binary hard-sphere freezing and melting volume fractions are denoted by the blue crosses for comparison. An alternative mapping of the coexistence region is also shown in shaded grey, where the freezing densities of the WCA systems at different temperatures  $T^*$  are scaled to that of a binary hard-sphere mixture by defining an effective diameter  $\sigma_{\text{eff}}$  for the WCA systems at each temperature. In this representation, the freezing line becomes a vertical line as the freezing packing fraction for all temperatures of the WCA system is scaled to that of hard spheres. We clearly find that the width of the coexistence region decreases upon increasing the softness of the potential, i.e. increasing the reduced temperature  $T^*$ , which is consistent with previous studies [199, 200]. For instance, in the case of a binary mixture of hard spheres, the change in packing fraction between melting and freezing is  $\Delta \eta_{\text{coex}} = 0.0584$ , whereas this change in packing fraction for the softest system at  $T^* = 0.2$  is  $\Delta \eta_{\text{coex}} < 0.04$ . In addition, we plot the freezing/melting line isomorphs, denoted by the dashed lines, as obtained from the direct isomorph check (Eq. 6.13) with the WCA system at  $T^* = k_B T / \epsilon = 0.2$  as a reference

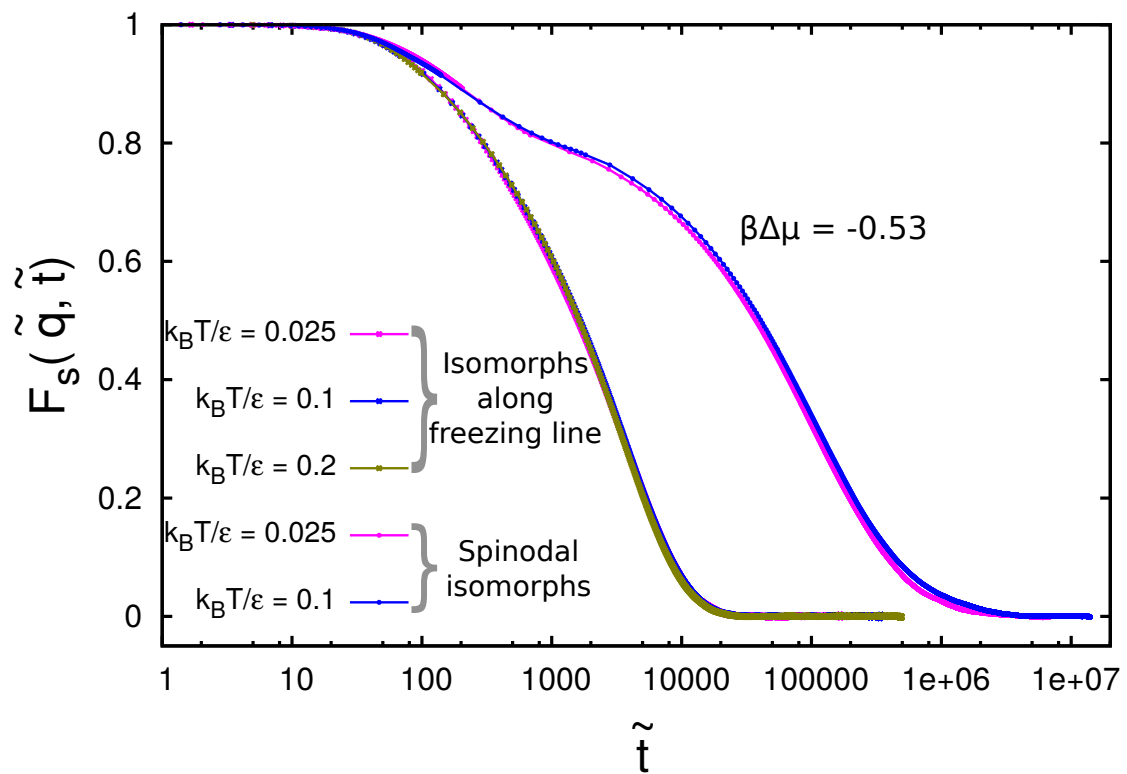


**Figure 6.23:** The self-intermediate scattering functions at the reduced wave vector  $\tilde{q} = ql_0$  as a function of the reduced time  $\tilde{t} = t/t_0$  with  $l_0 = \rho^{-1/3}$  and  $t_0 = \rho^{-1/3} \sqrt{m/k_B T}$  for three state points on the freezing line and two state points on the spinodal line.

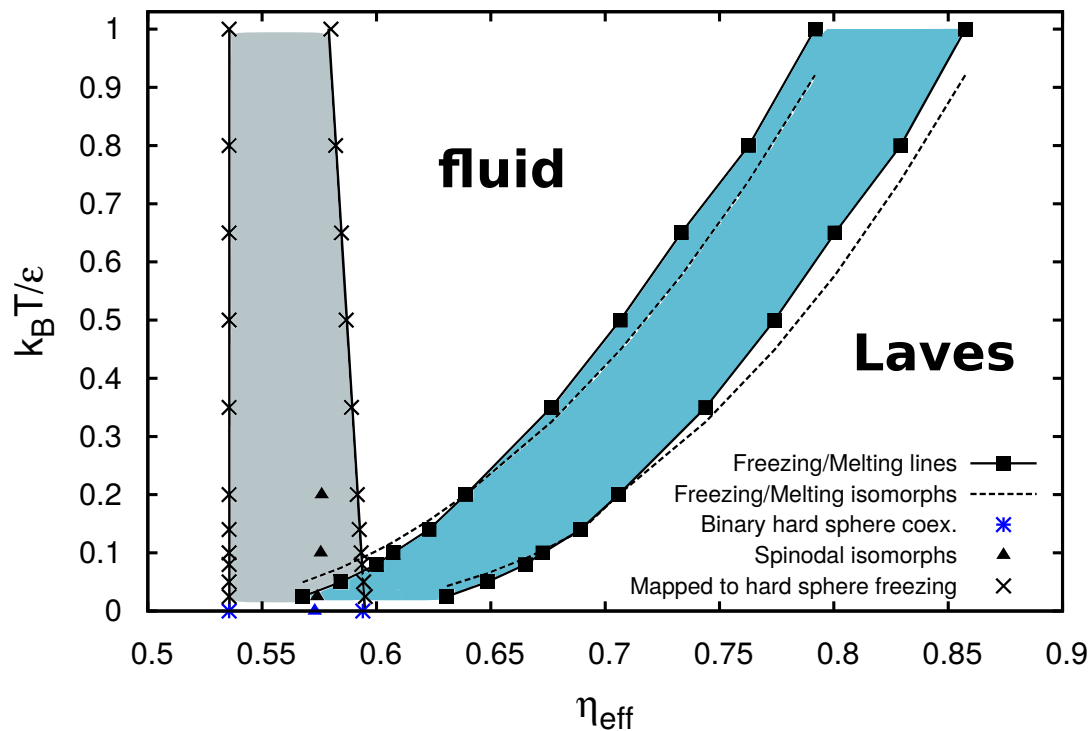


**Figure 6.24:** Fluid-Laves phase coexistence of a binary mixture of WCA spheres with a diameter ratio  $q = 0.78$  at a fixed composition  $x_L = 1/3$  in the reduced temperature  $k_B T / \epsilon$  - effective packing fraction  $\eta_{\text{eff}}$  plane. There are two kinds of scalings that have been used for the WCA densities, for a comparison with a binary hard-sphere mixture of  $q = 0.78$ . (i) The reduced densities from Fig. 6.9 have been scaled to an effective packing fraction  $\eta_{\text{eff}} = \pi \sigma_{\text{av}}^3 2^{1/2} \rho / 6$ , and the resulting fluid-Laves phase coexistence is denoted by the blue region. The scaling factor  $2^{1/2}$  enters here as the WCA system reduces to hard spheres with a diameter  $2^{1/6} \sigma$  in the limit  $T \rightarrow 0$ , see Fig. 6.2. The freezing/melting line isomorphs, obtained from the direct isomorph method using the WCA system at  $T^* = k_B T / \epsilon = 0.2$  as a reference state, are marked as dashed lines in the figure. The binary hard-sphere freezing and melting volume fractions are denoted by the blue crosses for comparison. (ii) An alternative mapping of the coexistence region is also shown in shaded grey, where the freezing densities of the WCA systems at temperature  $T^*$  are scaled to that of the binary hard-sphere mixture. Additionally, the *spinodal isomorphs* are marked as black triangles.

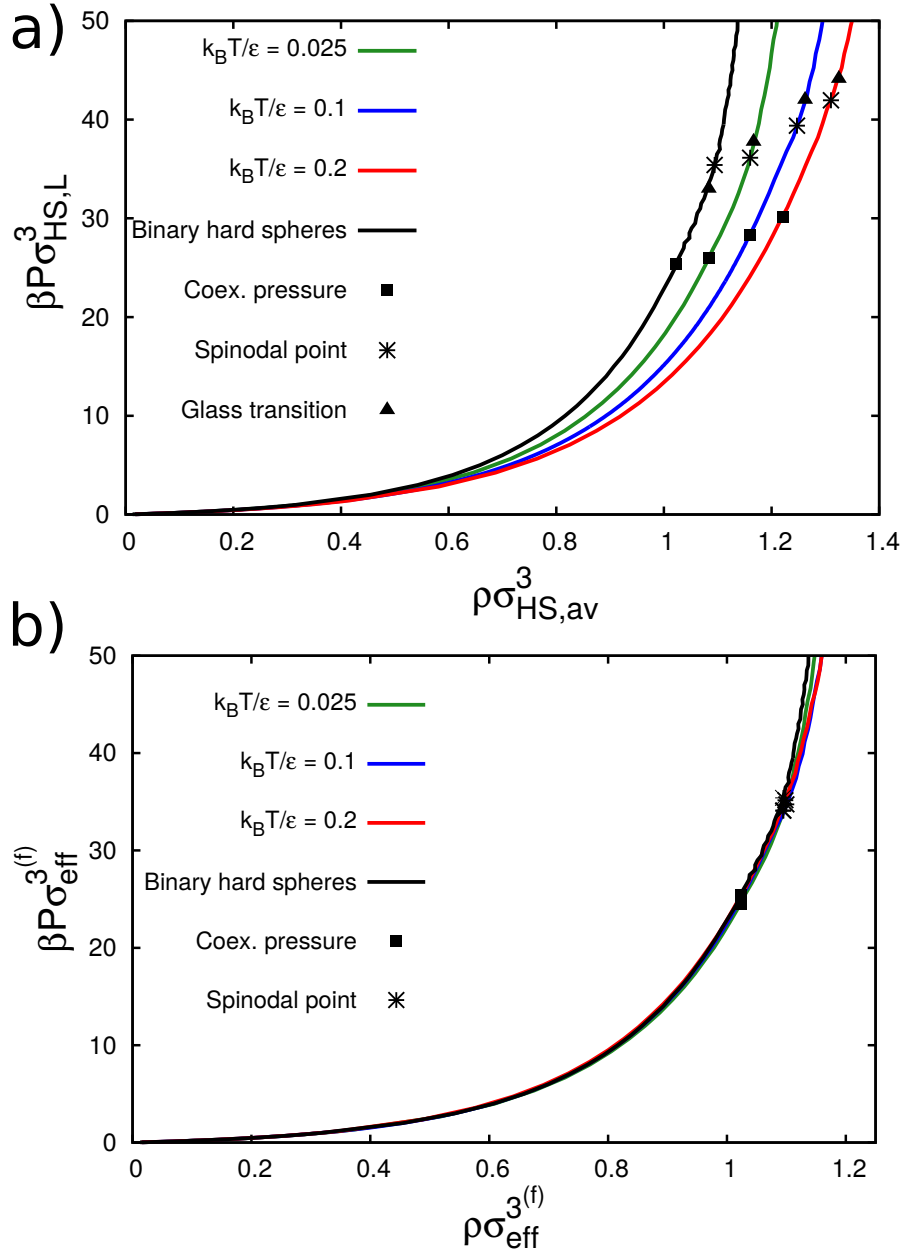


**Figure 6.25:** a) Equations of state, reduced pressure  $\beta P \sigma_{HS,L}^3$  versus reduced density  $\rho \sigma_{HS,av}^3$  for binary WCA mixtures at reduced temperature  $T^* = k_B T/\epsilon = 0.2, 0.1,$  and  $0.025,$  and a binary hard-sphere mixture. For the WCA systems,  $\beta P \sigma_{HS,L}^3 = 2^{1/2} \beta P \sigma_L^3$  and  $\rho \sigma_{HS,av}^3 = 2^{1/2} \rho \sigma_{av}^3$ . The scaling factor  $2^{1/2}$  enters here as the WCA system reduces to hard spheres with a diameter  $2^{1/2} \sigma$  in the limit  $T \rightarrow 0,$  see Fig. 6.2. The coexistence pressure, spinodal pressure, and kinetic glass transition are marked for a comparison of the four systems. For the WCA systems, the spinodal point is at lower pressures (densities) than the MCT glass transition. However, glass transition pre-empts the spinodal point for binary hard spheres. b) A collapse of the equations of state, and the coexistence and spinodal points, of the four systems. Here, the effective diameter used to scale the pressure and density of the WCA systems is obtained by mapping their freezing densities to the binary hard-sphere freezing density.

state. As these isomorphs lie close to our actual freezing and melting lines, we assume that these lines can be considered to be isomorphs to a good approximation. Additionally, the *spinodal isomorphs* are marked as triangles. We observe that the spinodal points for  $k_B T/\varepsilon = 0.025, 0.1, 0.025$  and binary hard spheres are approximately at the same effective packing fraction. A direct consequence of the existence of isomorphs is the structural and dynamic invariance of state points, such as the density change on freezing/melting (discussed above), and the entropy of fusion[196]. We find an invariance in the thermodynamic driving force for spontaneous crystallization  $\beta\Delta\mu \sim -0.53$  for our mixtures (related to the fusion entropy plus an enthalpic term). In addition, we prove the structural and dynamic invariance of the spinodal line by comparing the  $g(r)$ 's and the reduced self-intermediate scattering functions, and show a good data collapse of both (Fig. 6.22 and Fig. 6.23). Assuming that a similar driving force of  $\beta\Delta\mu = -0.53 \pm 0.03$  is required for the spontaneous nucleation of the Laves phase in a binary mixture of hard spheres, we find that the respective supersaturated binary fluid phase has a packing fraction of  $\eta = 0.573 \pm 0.002$ , which is above the MCT kinetic glass transition at  $\eta = 0.5663$  (Table 6.2) of this system as determined in Section 6.4.4.

We summarise our findings in Fig. 6.25a), where we have shown the equations of state of the four systems, namely the three WCA mixtures for  $T^* = k_B T/\varepsilon = 0.2, 0.1,$  and  $0.025$  and the binary hard-sphere mixture. We mark here, for a direct comparison, the coexistence pressure, spinodal pressure, and MCT glass transition for all four systems. In order to compare the WCA systems with binary hard spheres, the reduced pressure and reduced density of the WCA systems have been scaled to an effective pressure  $\beta P \sigma_{\text{HS,L}}^3 = 2^{1/2} \beta P \sigma_L^3$  and effective density  $\rho \sigma_{\text{HS,av}}^3 = 2^{1/2} \rho \sigma_{\text{av}}^3$  respectively. The scaling factor  $2^{1/2}$  enters here as the WCA system reduces to hard spheres with a diameter  $2^{1/6} \sigma$  in the limit  $T \rightarrow 0$ , see Fig. 6.2. As observable in Fig. 6.25a), for all three WCA systems, the spinodal point is at lower pressures (densities) than that of the MCT glass transition. In contrast, the spinodal point for spontaneous crystallization of the Laves phases in a binary mixture of hard spheres is *pre-empted* by the kinetic glass transition. We surmise that this may be the reason why the spontaneous nucleation of Laves phases has never been observed within reasonable time scales in computer simulations of binary hard spheres, as the structural relaxation is extremely slow for packing fractions above the kinetic glass transition.

Additionally, we further emphasize the thermodynamic invariance between the WCA mixtures and binary hard spheres in Fig. 6.25b), where we scaled the reduced pressure and reduced density of the WCA systems using an effective diameter obtained, as described above, from mapping the WCA freezing densities to the freezing density of the BHS mixture. We observe an excellent collapse of the equations of state of the four systems, along with the coexistence pressures and spinodal points, thus further justifying our use of the phraseology *hard-sphere-like* for our WCA systems.

## 6.6 Nucleation barrier, $k_B T/\varepsilon = 0.2$

A nucleation event occurs when a crystalline nucleus forms in the supersaturated liquid phase due to thermal fluctuations. In the case that the size of such a cluster exceeds the critical cluster size, the nucleus will grow out into the surrounding fluid. In order to understand the crystal nucleation process, it is crucial to have information on the size, structure and the rate

at which a crystalline nucleus appears. The physical observables of interest within the context of nucleation are often computed by sampling rare events using biasing techniques such as Umbrella Sampling or Forward Flux Sampling, which are computationally demanding. More recently, the *seeding approach* has been introduced in order to overcome this problem [201–203]. This technique involves inserting a crystalline seed of a pre-determined shape and size into a metastable fluid. The configuration is subjected to a two-step equilibration process in the  $NPT$  ensemble where (i) the interface between the crystalline cluster and surrounding fluid is equilibrated by keeping the cluster fixed and then (ii) the constraint on the cluster is relaxed and the system is equilibrated until the number of crystalline particles stabilise. Subsequently, the equilibrated configuration is simulated for a range of pressures in order to determine the critical pressure  $\beta P_c \sigma_L^3 (k_B T_c / \epsilon)$  at which the critical cluster size  $N_c$  stabilises. The equilibration steps were performed using MC simulations in the  $NPT$  ensemble, and subsequent sampling of the pressures to determine the critical pressures were done *via* MD simulations in the  $NPT$  ensemble. An illustration is shown in Fig. 6.26, where a  $\text{MgZn}_2$  LP seed melts, stabilises and grows out (as seen from the profile of the cluster size with MD time) at  $\beta P \sigma_L^3 = 22.6, 23$  and  $25$ , respectively. The crystalline clusters are detected using the bond order parameter criteria described and used in Section 6.4.1.

Combining the seeding approach with classical nucleation theory, we can estimate the height (maxima) of the Gibbs free energy nucleation barrier

$$\beta \Delta G_c(\beta P_c \sigma_L^3) = N_c |\beta \Delta \mu| / 2 \quad (6.14)$$

where  $|\beta \Delta \mu|$  is the chemical potential difference between the two phases at the critical pressure  $\beta P_c \sigma_L^3$ . The height of the Gibbs free energy barrier for different critical pressures (different critical seed sizes) is plotted in Fig. 6.27 as a function of chemical potential difference between the Laves phases and the fluid phase at the critical pressure. As anticipated, the profile approaches  $\infty$  at the coexistence pressure which corresponds to  $\beta \Delta \mu = 0$ , and goes asymptotically towards 0 at the spinodal point  $\beta \Delta \mu \simeq -0.53$ . Assuming a spherical shape for the cluster, we can also write the critical cluster size  $N_c$  as a function of the interfacial free energy  $\gamma$  as

$$N_c = \frac{32\pi\gamma^3}{3\rho_s^2 |\Delta\mu|^3} \quad (6.15)$$

where  $\rho_s$  is the density of the crystalline cluster. We plot the interfacial tension similarly to above as a function of the chemical potential difference between phases in Fig. 6.27. At high supersaturations, the differences in the interfacial free energies for the three Laves phases are minute enough to be well within the error margin, and at low supersaturations the error bars are too large to make a conclusive comparison. Finally, we come to the advantages of using a crystalline seed to direct crystal growth as opposed to spontaneous nucleation. As discussed in Section 6.3, due to the very small free-energy difference between the three Laves phases, one expects to obtain a randomised stacking of Laves phases in the crystal phase. This was indeed the case in our spontaneous nucleation simulations as shown in Figs. 6.12 (final structure was 60%  $\text{MgCu}_2$ -stacked and 40%  $\text{MgZn}_2$ -stacked) and 6.13 (showed the appearance of peaks in both the  $\text{MgCu}_2$  and  $\text{MgZn}_2$  order parameter regions during the course of the nucleation). However, as observable in Fig. 6.28, if one were to seed the supersaturated fluid phase with a nucleus of the desired Laves phase structure, the seeds would direct the growth of the crystalline

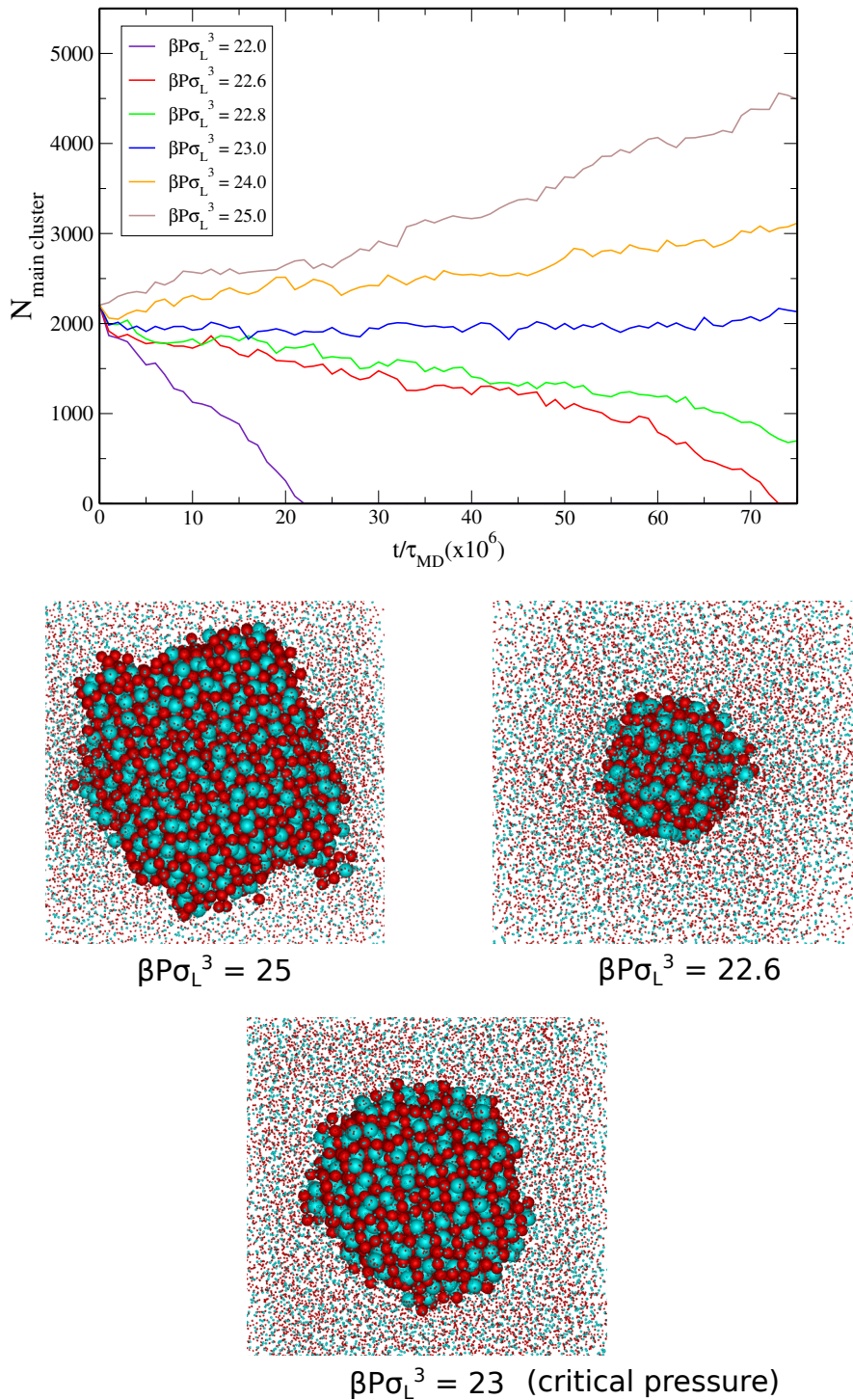


**Figure 6.26:** The largest cluster size as a function of time using the seeding approach in Molecular Dynamics simulations in the  $NPT$  ensemble in order to estimate the critical pressure  $\beta P_c \sigma_L^3$ . The initial seed size is 2688 particles of the  $\text{MgZn}_2$  Laves phase. The snapshots show the melting of the seed, growth of the seed, and the seed size more or less stabilised at the critical pressure. Fluid particles are reduced in size for visual clarity.

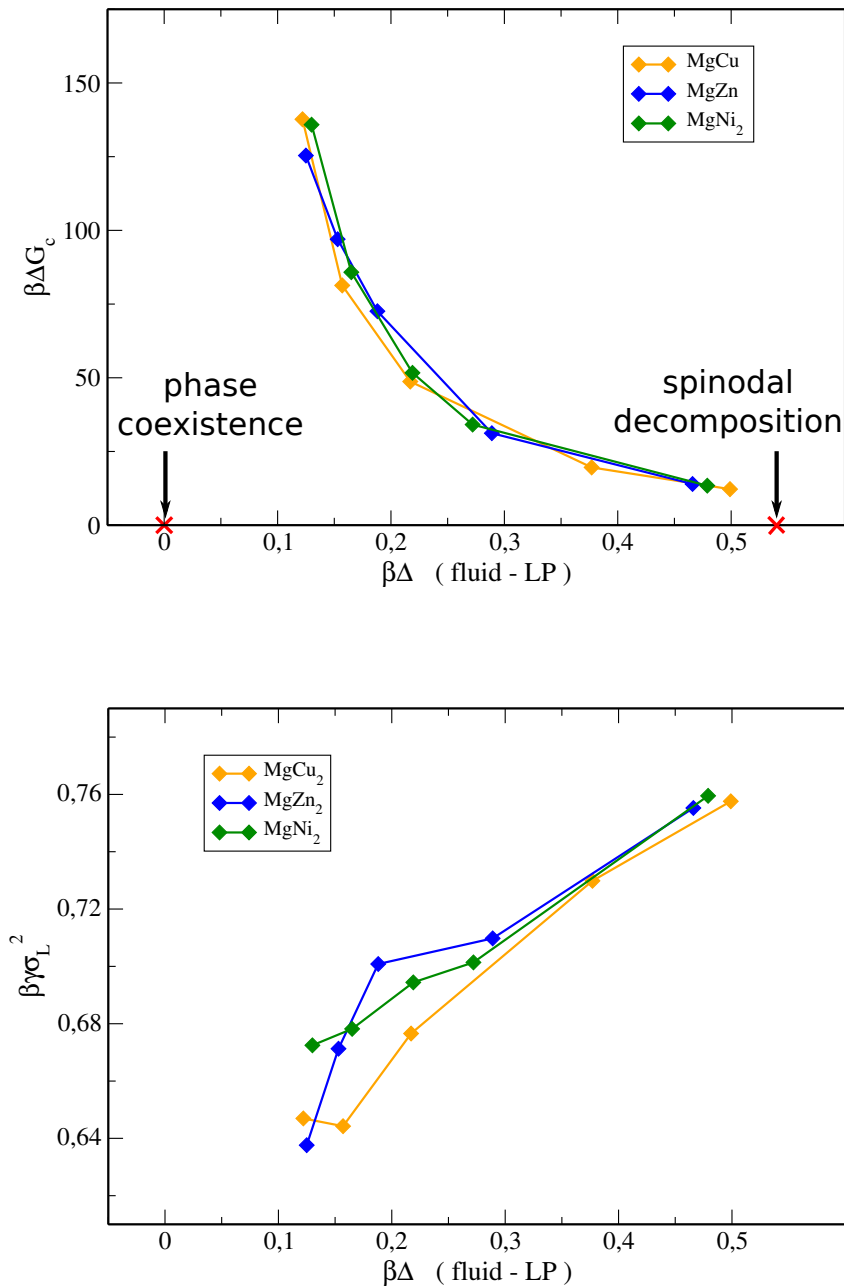


**Figure 6.27:** (i) The height of the Gibbs free energy barrier  $\beta\Delta G_c$  plotted as a function of the chemical potential difference  $\beta\Delta\mu$  between the LP and fluid phase, which corresponds to the respective critical pressures. The profile shows the anticipated trend in that the barrier height asymptotically increases  $\rightarrow \infty$  at the coexistence pressure ( $\beta\Delta\mu = 0$ ) and  $\rightarrow 0$  as it approaches the spinodal point ( $\beta\Delta\mu \simeq -0.53$ ). (ii) The interfacial free energy  $\beta\gamma\sigma_L^2$  plotted as a function of the chemical potential difference between the LP and fluid phase, which corresponds to the respective critical pressures.

cluster which would then mimic the structure of the seed. The final structures for the three different types of seeds used are shown in Fig. 6.28, and one can *visually* ascertain the nature of the Laves phase structure formed, by referring to Fig. 6.7, from simply the stacking of the “large dimers”. Therefore, by using a seeding approach one can circumvent to a large extent the formation of a randomised stacking of Laves phases [203].

## 6.7 Summary and conclusions

In conclusion, we used free-energy calculations and a thermodynamic integration technique to calculate the binary phase diagrams of WCA mixtures describing the phase coexistence between four stable phases - fluid phase, two single-component fcc phases and the  $\text{MgZn}_2$  Laves phase (the most thermodynamically stable LP), for three different softnesses of the WCA potentials by changing the temperatures  $k_B T / \varepsilon = 0.025, 0.1$  and  $0.2$ . We then calculated the melting and freezing densities of the stable Laves phase and a fluid phase at stoichiometric composition for a range of temperatures. At selected thermodynamic state points on this phase diagram, we observed the spontaneous nucleation of binary Laves phases from a supersaturated fluid phase with the same composition from MD simulations both in the  $NVT$  and  $NPT$  ensembles, in accordance with the thermodynamic phase diagram(s). We identified bond order parameters to (i) detect Laves phase crystalline clusters forming in the supersaturated fluid and (ii) distinguish the different stackings observed in the resulting Laves phases. We then used a combination of Monte Carlo and Molecular Dynamics simulations to estimate the pressures characterising (i) spinodal decomposition and (ii) the MCT glass transition, and found that for all three WCA mixtures, spinodal decomposition precedes the kinetic glass transition. When comparing the spinodal pressures for the three different pair potentials, we noticed an intriguing invariance in the thermodynamic driving force for spontaneous crystallization, which led us to study the hidden scale invariance of these systems. We identified the isomorphic curves on the thermodynamic phase diagram, along which the structure and dynamics of thermodynamic state points are invariant. In addition, we find an invariance in the thermodynamic driving force for spontaneous crystallization  $\beta \Delta \mu \sim -0.53$  for our WCA mixtures, and by showing that the spinodal line can be considered to be an isomorph, we can predict the spinodal point for a binary hard-sphere mixture. Comparing the packing fraction corresponding to the spinodal point with the critical packing fraction of the MCT glass transition in binary hard spheres, we found that the kinetic glass transition pre-emptes the spontaneous crystallization of Laves phases in a binary mixture of hard spheres with a diameter ratio  $q = 0.78$ . This may be reason why the spontaneous nucleation of Laves phases have never been reported in computer simulations of binary hard-sphere mixtures. Next, we computed the Gibbs free energy nucleation barrier height using the seeding approach, and found that it shows the anticipated behaviour in accordance with the freezing and spinodal pressures discussed thus far. Finally, we showed how the crystalline seed can direct the growth of the desired Laves phase and can prevent the formation of a randomly stacked LP structure.

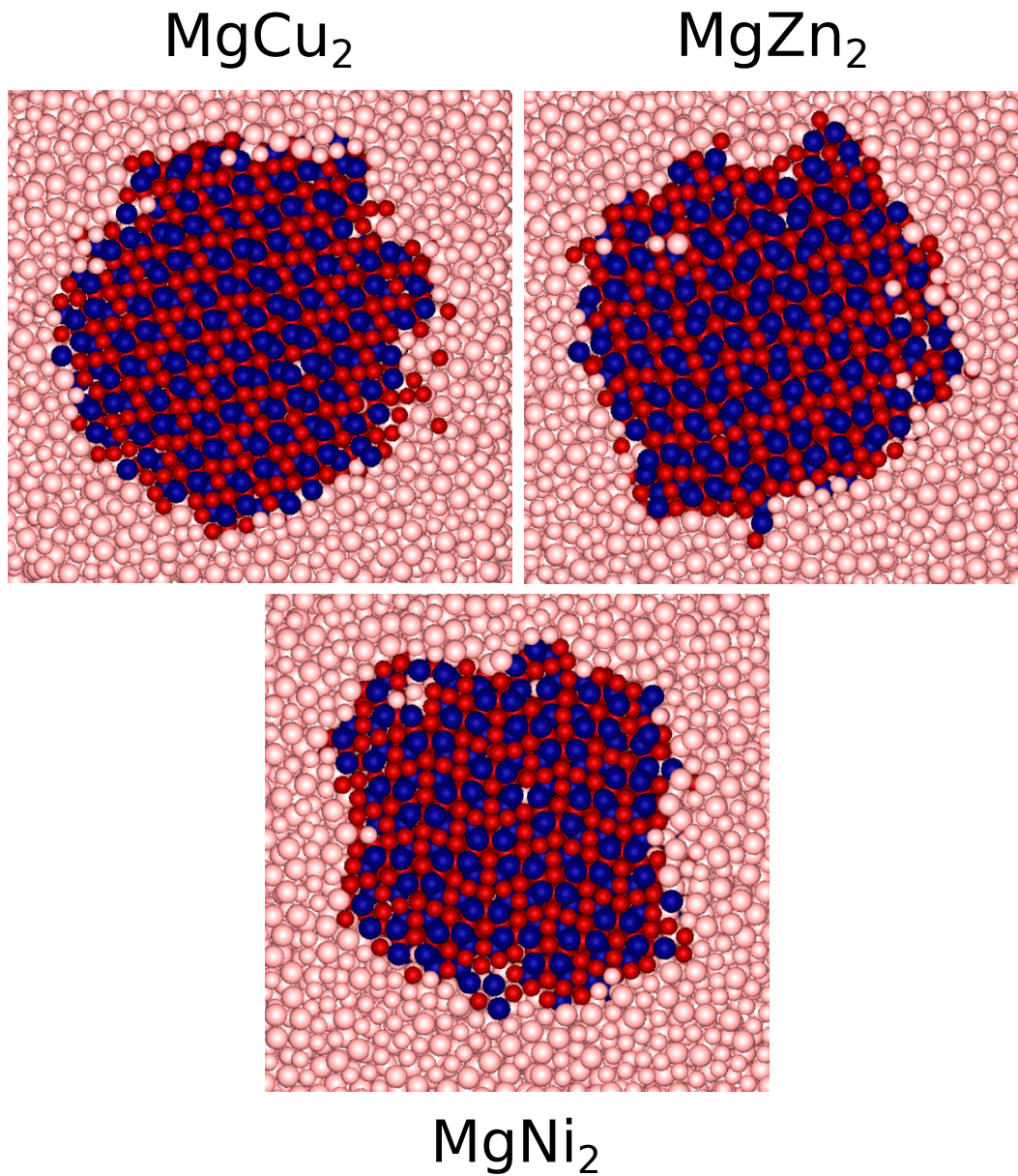


**Figure 6.28:** Directing the crystal growth using a crystalline seed. Snapshots of a cross-section of the crystalline cluster shows that the growing crystal follows the structure of the initial seed. The large dimer stacking shown in Fig. 6.7 is observable from the images. Fluid particles are coloured lilac. Large species are coloured in dark blue. Small species are coloured red.

## 6.8 Acknowledgements

I would like to thank Gabriele Coli for an excellent collaboration on this project, in particular for investigating the nucleation behaviour of this system using the seeding approach, estimating the kinetic glass transition from Monte Carlo simulations, and identifying bond order parameters that can be used to detect the formation of Laves phase crystalline clusters in the supersaturated fluid. I gratefully acknowledge Siddharth Paliwal for answering many HOOMD-blue related questions during the course of this project. I sincerely thank Emanuele Boattini for performing a neural network analysis, to detect LP-like clusters, on some of my configurations. I would like to thank Da Wang for discussions on experimental models, Giulia Fiorucci for useful discussions, and all the simulators in the group for their kind consideration in accommodating my heavy computational needs for the seeding simulations.

---

## Binary icosahedral quasicrystals of hard-sphere-like colloids in spherical confinement

---

The influence of geometry on the local and global packing of particles is important to many fundamental and applied research themes such as the structure and stability of liquids, crystals and glasses. Here, we show by experiments and simulations that a binary mixture of hard sphere-like particles crystallizing into the  $\text{MgZn}_2$  Laves phase in bulk, spontaneously forms 3D icosahedral quasicrystals in slowly drying droplets. Moreover, the local symmetry of 70-80% of the particles changes to that of the  $\text{MgCu}_2$  Laves phase. Both of these findings are significant for photonic applications. Our simulations show that the quasicrystals form *via* homogeneous nucleation and grow along five-fold symmetric structures. Our findings not only open the way for particle-level studies of nucleation and growth of 3D quasicrystals, but also of binary crystallization.

## 7.1 Introduction

Crystallization experiments in which droplets were used have contributed significantly to our current understanding of structural aspects and the kinetics of phase transformations in condensed matter physics. Over half a century ago, David Turnbull *et al.* showed in seminal experiments that liquids could be undercooled by as much as hundreds degrees below the freezing temperature if they were dispersed as small droplets [204]. The small size of the droplets ensured the absence of heterogeneous nucleation sites, and as a consequence nucleation could only occur homogeneously. The large undercoolings demonstrated that the local structure of liquids differs substantially from that of crystals. These findings inspired Charles Frank to hypothesise that the short-range order in liquids has icosahedral symmetry, which is incompatible with the perfect long-range translational order of crystals [205]. The icosahedral order arises locally when one maximises the density, using the convex hull, of a packing of 12 identical spheres on the surface of a central sphere with the same size [206]. The densest packing is obtained by arranging the outer spheres on the vertices of an icosahedron, rather than by using 13-sphere subunits of face-centered cubic (FCC) and hexagonal close-packed (HCP) bulk crystals, which are known to pack 3D space closest at  $\sim 74\%$  [116, 207, 208].

Long-range icosahedral order is found in icosahedral quasicrystals (iQCs), one class of quasicrystals which shows quasiperiodicity in three dimensions [209, 210]. Due to their higher point group symmetry than ordinary crystals, iQCs have been demonstrated to be an ideal candidate for complete bandgap photonic crystals [211]. IQCs have been abundantly discovered in binary, ternary and multinary intermetallic compounds [210]. Polygonal quasicrystals have been found in non-atomic or soft matter systems, such as assemblies of NCs and star polymers, whereas iQCs have not yet been found in such systems [212]. Recently Engel *et al.* showed by computer simulations that iQCs can be obtained by the self-assembly of one-component particles interacting *via* an oscillating isotropic pair potential. Although the realisation of such a potential is non-trivial, their research suggests routes for designing iQCs in precisely tailored systems in the future [213].

Colloidal suspensions are widely used as model systems to study fundamental processes such as crystallization, melting, nucleation, and the glass transition [51, 214–217]. This is because they have a well-defined thermodynamic temperature, and consequently they display the same phase behaviour as atoms and molecules. Additionally, they can be investigated on a single-particle level, even in concentrated systems [51, 214–217]. This has led to a wealth of new insights, ranging from the nucleation and growth of hard-sphere (HS) crystals [214], to the observation of dynamical heterogeneities close to the glass transition [215]. The use of droplets has also been of interest in the soft matter field, not only because it is a powerful method to study protein crystallization, topological defects in liquid crystal droplets, and the crystallization kinetics of colloids [216, 217], but also to fabricate clusters of particles composed of smaller particles, also termed ‘supraparticles (SPs)’, upon drying the droplets [140, 218]. An unexpected and recent finding in both experiments and simulations is that when up to 90,000 HSs are compressed under the spherical confinement of a slowly drying emulsion droplet, the system spontaneously crystallizes into icosahedral clusters and not into the thermodynamically stable FCC bulk crystal [132]. Using crystallization in spherical confinement, icosahedral clusters were obtained for a range of particle systems [219–221], including rounded cubes [222].

Free-energy calculations on monodisperse HSs confined in a spherical confinement showed that clusters with an icosahedral symmetry are thermodynamically more stable than FCC clusters at packing fractions just above freezing [132]. This raises the question whether spherical confinement is also able to change the equilibrium structures that form in the case of binary mixtures of spheres, possibly also inducing icosahedral symmetry. Here we demonstrate, by computer simulations (and occasional descriptions of similar experimental findings), that a binary mixture of hard sphere-like (HS-like) colloids with a diameter ratio  $q = 0.78$ , which crystallizes into a structure analogous to the binary metallic  $\text{MgZn}_2$  Laves phase in bulk, forms an *iQC* induced by a spherical confinement.

The Laves phases ( $\text{LS}_2$ ) are three closely related structures composed of small (S) and large (L) spheres: the hexagonal C14  $\text{MgZn}_2$  structure, the cubic C15  $\text{MgCu}_2$  structure and the hexagonal C36  $\text{MgNi}_2$  structure as shown in Fig. 6.7. The three structures can also be identified by the stacking sequence of the L spheres as viewed in Fig. 6.7 along the  $[11\bar{2}0]$  or  $[110]$  projections of the hexagonal or cubic structures, respectively. Specifically, the stacking of the L sphere-dimers in the C14, C15, and C36 structures is ...aa-bb..., ...aa-bb-cc..., and ...aa-bb-cc-bb..., respectively. The  $\text{MgZn}_2$  Laves phase was found to be the thermodynamically stable structure for a binary mixture of large and small hard spheres with a diameter ratio in the range of 0.76–0.84, although the free-energy difference between the three Laves phases is small ( $\sim 10^{-3}k_B T$  per particle at freezing) [27, 28].

In this Chapter, we discuss the results of a collaboration with Wang *et al.* who studied the behaviour of binary hard-sphere-like nanoparticles (NPs) in spherical confinement. They synthesised large lead selenide (PbSe) nanoparticles with a core diameter of 7.6 nm (9.9 nm total diameter including the ligands; 1.3% polydispersity) and small cadmium selenide (CdSe) NCs with a core diameter of 5.1 nm (7.6 nm total diameter; 2.1% polydispersity), and let the binary mixture of PbSe/CdSe NPs with a 1:2 (PbSe:CdSe number density) composition self-assemble in slowly drying emulsion droplets, and investigated the structure of the self-assembled SPs composed of PbSe/CdSe NCs using electron microscopy. Surprisingly, they found that about 80% of all their transmission electron microscopy (TEM) images of SPs with sizes from a few hundreds to tens of thousands of particles showed five-fold symmetry. To corroborate this intriguing finding, we performed molecular dynamics (MD) simulations, with HOOMD-blue [184, 185], of a binary mixture of spheres interacting with a short-range repulsive Weeks-Chandler-Anderson (WCA) potential, inside a spherical confinement. The WCA potential has been used in literature to mimic the hard-sphere potential [172–175] and as such, reduces to the hard-sphere potential at  $k_B T / \epsilon \rightarrow 0$ . Historically, a soft-core WCA system has been related to a reference hard-sphere system as a perturbation of the latter, and is mapped to the hard-sphere system through the determination of an *effective diameter* which can be obtained by performing an expansion of its reduced free-energy density about that of hard spheres. We have further explored this connection explicitly in Section 6.5, and found that a WCA mixture is thermodynamically invariant, in appropriately reduced units, to a binary hard-sphere (BHS) mixture of the same diameter ratio. Therefore, we refer to our system as ‘hard-sphere-like’ as we expect the physics of crystallization to be similar to that of a BHS mixture. Remarkably, we observed that the binary fluid crystallizes into a cluster with five-fold symmetry under a spherical confinement, revealing a striking agreement with the experimentally observed SPs. Furthermore, from our simulations, we were able to observe how these quasicrystals nucleate and grow.

## 7.2 Results and Discussion

### 7.2.1 Recap: Laves phases in Bulk

In Chapter 6, we discussed how Laves phases (LPs) spontaneously nucleate in bulk from a binary mixture of repulsive particles interacting *via* the Weeks-Chandler-Andersen (WCA) potential [171] which has the form described by Eq.6.1. The WCA potential is repulsive and short-range and reduces to a hard-sphere potential at  $k_B T/\epsilon \rightarrow 0$  (see Fig. 6.2) with a hard-core diameter of  $2^{\frac{1}{6}}\sigma$ , where  $\sigma$  is the interaction range of the WCA pair potential (see Eq. 6.1). We showed by free-energy calculations in Chapter 6 that the thermodynamically stable crystal phase in bulk among the three LPs is the  $\text{MgZn}_2$  LP, although the difference in the free energies of the 3 LPs ( $\text{MgZn}_2$ ,  $\text{MgCu}_2$  and  $\text{MgNi}_2$  LPs) is very small (of the order of  $\sim 10^{-3}k_B T$  per particle, at melting), resulting in a randomised stacking of the LPs on spontaneous crystallization. We used bond order parameters for the structural correlation between the large species to distinguish  $\text{MgCu}_2$ -like and  $\text{MgZn}_2$ -like stacking ( $\text{MgNi}_2$ -stacking is a combination of  $\text{MgCu}_2$ -stacking and  $\text{MgZn}_2$ -stacking) and identified this random stacking in the crystal structure spontaneously crystallizing from a highly supersaturated binary fluid phase (See Fig. 6.12) in bulk.

### 7.2.2 Effect of spherical confinement

We now study the same binary mixture of particles in spherical confinement to study the effect, if any, of the spherical geometry of the confinement on the crystal structure obtained. We perform molecular dynamics (MD) simulations on a binary mixture of repulsive particles interacting *via* a pairwise WCA potential (Eq. 6.1),  $\alpha, \beta$  denote the particle type (*i.e.*  $L, S$ ). For our binary mixture,  $\epsilon_{LL} = \epsilon_{SS} = \epsilon_{LS} = \epsilon$ ,  $\sigma_{LL} \equiv \sigma_L$ ,  $\sigma_{SS} \equiv \sigma_S$ , diameter ratio  $q = \sigma_S/\sigma_L = 0.78$  with  $\sigma_{LS} = (\sigma_L + \sigma_S)/2$ , and reduced temperature  $T^* = k_B T/\epsilon = 0.2$ . The WCA potential is hard-sphere-like (see Section 6.5) and can be mapped onto hard spheres by means of an *effective diameter* which is obtained by mapping the freezing density of the WCA mixture to the freezing density of a binary hard-sphere mixture of diameter ratio  $q = 0.78$  [173, 191]. The interaction potential of the particles with the wall is also a repulsive WCA potential with  $\epsilon_w = \epsilon$  and  $\sigma_w = \sigma_L$ . The simulations are performed using HOOMD-blue [184, 185] in the canonical  $NVT$  ensemble, where the number of particles  $N$ , temperature  $T$ , and the volume  $V$  are fixed. The temperature is kept constant *via* the MTK [188] integration of the equations of motion based on the Nosé – Hoover thermostat [186, 187], with coupling constant  $\tau_T = 1.0$ . The time step is set to  $\Delta t = 0.01\tau_{MD}$  where  $\tau_{MD} = \sigma_L\sqrt{m/\epsilon}$  is the MD time unit. In order to ensure sufficient time for equilibration, the simulations are performed on a constant spherical volume. The system crystallizes after a long time (onset of crystallization is at  $t/\tau_{MD} \sim 10^8$ ), and subsequently, the crystallized SPs are subjected to a fast compression up to very high densities so as to arrest the positions of the spheres in the SP (for analysis of the final structures). For a close comparison with the experiments, where five-fold SPs were only observed for compositions close to  $LS_2$ , we modulate the composition of our binary mixtures such that the number fraction of  $L$  particles  $x_L = \frac{N_L}{N_L+N_S}$  is  $\sim 0.3$  in the ‘core’. The *core* comprises of the SP *excluding* those particles positioned at a radial distance  $> R_{SC} - 2\sigma_L$  from the center of the SP, where  $R_{SC}$  denotes the radius of the spherical confinement. The effective number of particles in the core is denoted by  $N$  while the total number of particles in the SP is denoted by  $N_{tot}$ . We

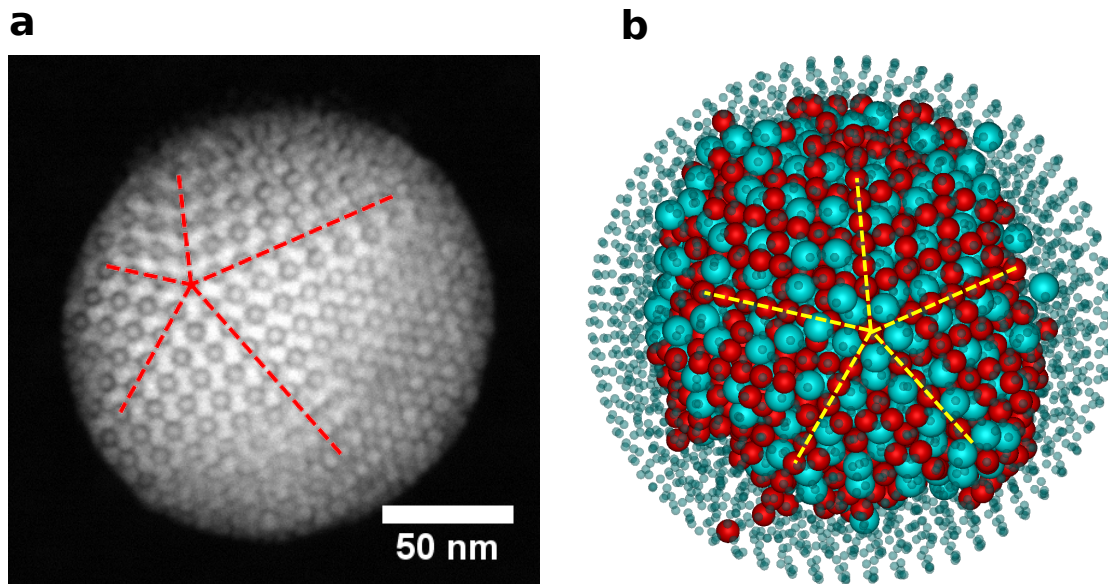


**Figure 7.1:** Binary supraparticles as obtained from experiments and computer simulations. a) High Angle Annular Dark-Field (HAADF) - Scanning Transmission Electron Microscopy (STEM) image of a typical supraparticle of diameter 170 nm, containing lead selenide PbSe and cadmium selenide CdSe nanoparticles. Five-fold symmetry is observed, as indicated by the red dashed lines. b) Simulated supraparticle composed of a binary mixture of 5,000 HS-like particles (interacting *via* a pairwise WCA,  $T^* = k_B T / \epsilon = 0.2$ ). The simulated SP also exhibits five-fold symmetry, similar to the experimental SP in a), as indicated by the dashed yellow lines. The particles in the outermost layer are reduced in size and made transparent in order to visualize the core crystal structure.

simulated  $N_{tot} = 3,500, 5,000$  and  $10,000$  spheres, which correspond to an effective number of  $N = 1,990, 3,060$  and  $6,870$  particles in the core respectively. The supersaturated core densities  $\rho \sigma_{av, core}^3 (= \frac{3N\sigma_L^3}{4\pi(R_{SC}-2\sigma_L)^3} (x_L + (1-x_L)q^3))$  for which crystallization is observed in our constant volume simulations lie between 0.883–0.946<sup>a</sup>. These densities are equivalent to an *effective density* range 1.046–1.121 for a binary hard-sphere mixture of diameter ratio  $q = 0.78$ . Here, the effective density for the BHS mixture is calculated using an effective diameter, which is obtained from equating the freezing number density of a bulk WCA mixture at  $k_B T / \epsilon = 0.2$  to the freezing density of the bulk BHS mixture.

We observe that the fluid undergoes crystallization and the ordered structure shows five-fold symmetry. This five-fold symmetry is observed in both the experimental supraparticles and the simulated supraparticles (Fig. 7.1), and the center of symmetries in both cases are off-center, signifying that the simulation model captures the crystallization physics of the experimental HS-like nanoparticles inside the oil-water emulsion droplet.

<sup>a</sup>The compressed configurations have core densities in the range 1.016–1.090.

### 7.2.2.1 Diffraction pattern of 3D icosahedral quasicrystals

We now explore the implications of the five-fold symmetry exhibited by our SPs. Inspired by the beautiful work of Shechtman *et al.* [209] that led to the discovery of icosahedral quasicrystals in 1984, we analysed Fast Fourier Transforms (FFTs) of the particle coordinates in our simulated supraparticles. IQCs have 3D long-range order, and therefore display sharp peaks in their 3D spatial FFT, but they exhibit orientational symmetries which are not compatible with having a periodic repeating unit, such as a *five-fold* rotational symmetry (Fig. 7.2). In Fig. 7.2, we present the diffraction pattern of the SP structure that spontaneously self-assembled from a 5,000 particle simulation. The diffraction pattern of the simulated SP is calculated on the coordinates of particles belonging to the iQC cluster after the following treatment: (1) the compressed SP is subjected to a short equilibration cycle ( $t/\tau_{MD} = 10^6$ ,  $\Delta t = 10^{-3}\tau_{MD}$ ) and the particle coordinates are averaged over 10,000 configurations, and (2) the time-averaged coordinates are subsequently run through a cluster criterion based on bond-orientational order parameters (BOPs), which distinguishes the particles belonging to the iQC cluster from particles with a different local symmetry, as determined by  $d_{6,\alpha\beta}(i,j)$  correlations of the particles with their neighbours. Here,  $\alpha,\beta$  denotes the type of species (*i.e.*  $L,S$ ) and  $i,j$  represents the index of the particle and its neighbour respectively. In order to suppress noise, the intensity profile has been filtered with a 1 pixel Gaussian blur. Further details on the BOP criteria used to identify particles belonging to an iQC cluster are provided in Section 7.2.3. The sharp Bragg peaks exhibit five-fold (Fig. 7.2) as well as two-fold and three-fold orientational symmetries (Fig. 7.3), which was also observed for simulated one-component IQCs [213].

The diffraction pattern in Fig. 7.2 shows *inflated* pentagons following a  $\tau^n$  sequence, where  $\tau = (1 + \sqrt{5})/2$  is the golden mean and is irrational. This so-called  $\tau^n$  sequence is a direct consequence of the non-crystallographic pentagonal symmetry and is characteristic of IQCs [210]. The perfect agreement of the positions of the Bragg peaks in our data along a projection vector as shown in Fig. 7.2, with the  $\tau^n$  sequence, signifies that our SP structure is indeed an iQC. This also ties in with the concept of IQCs being ‘irrational’ projections in 3D space of regular periodic crystals in hyper-dimensional space [223, 224]. We also remark that our structure are different from multiple-twinned crystals, as the latter would show diffraction patterns similar to those of IQCs but the Bragg peaks would display a twinned substructure in the diffraction pattern, which we do not see. We therefore conclude that our supraparticle corresponds to a binary icosahedral quasicrystalline cluster.

### 7.2.2.2 Real space analysis of icosahedral quasicrystals

Fundamental clusters that are often used in the classification of IQCs are the Mackay cluster [225, 226], the Bergman cluster [227, 228], and the Tsai cluster [229, 230], comprising of concentric shells (with vertices on polygons) of particles. Upon inspecting our iQC clusters in more detail, we observe that the SPs indeed contain such regular concentric shells of either  $S$  or  $L$  particles around the center of symmetry (Figs. 7.4a,b). From the center out, these shells are: an icosahedron of 12  $S$  spheres, dodecahedron of 20  $L$  spheres, icosahedron of 12  $S$  spheres, truncated icosahedron of 60  $S$  spheres, dodecahedron of 20  $L$  spheres, icosahedron of 12  $S$  spheres, icosidodecahedron of 30  $S$  spheres, rhombicosidodecahedron of 60  $L$  spheres. The Archimedean and Platonic solids corresponding to the concentric shells are shown in Fig. 7.4a). Interestingly, the first 3 shells constitute the 44-atom Bergman cluster [227, 228] (shown by

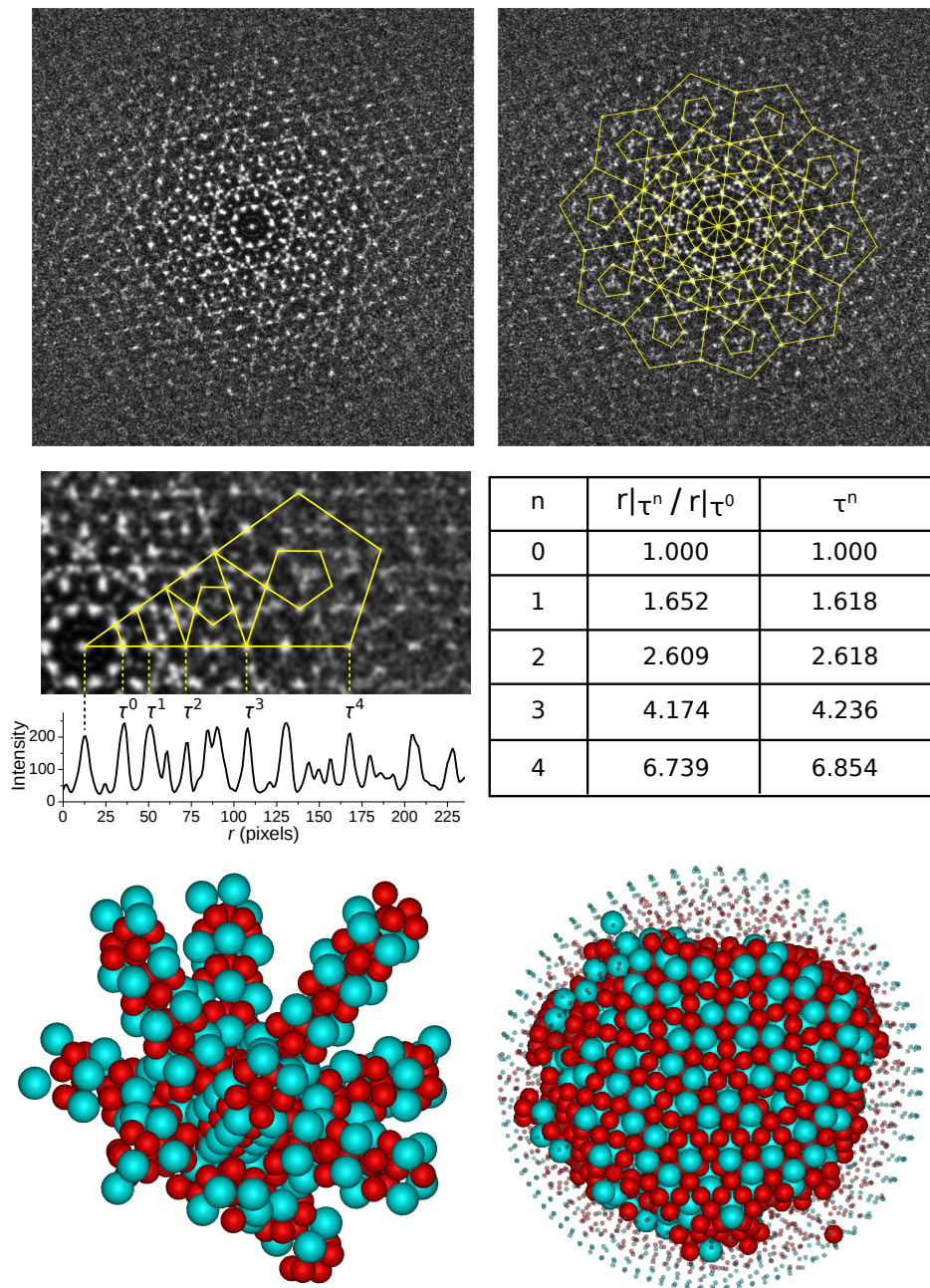


**Figure 7.2:** **Top panel:** The diffraction pattern of the simulated binary icosahedral cluster, showing five-fold rotational symmetry, on the left panel. The yellow lines highlight the presence of inflating pentagons in the diffraction pattern, which is a direct consequence of the non-crystallographic five-fold symmetry, depicting quasiperiodicity. **Middle panel:** One of the ten domains in the diffraction pattern showing the inflating pentagon sequence. The intensity profile along the horizontal yellow line features peaks whose positions follow the  $\tau^n$  sequence, where  $\tau$  is the golden ratio, as listed in the table. **Bottom panel:** Pictorial representations of the five-fold in real space of the SP. The left figure shows the ‘pentagonal tubes’ that run through the whole SP and the right figure shows the five-fold symmetry of the SP as observed in a cross-section. The particles belonging to the iQC cluster are identified using bond order parameters. The particles not belonging to the iQC cluster are reduced in size for visual clarity.

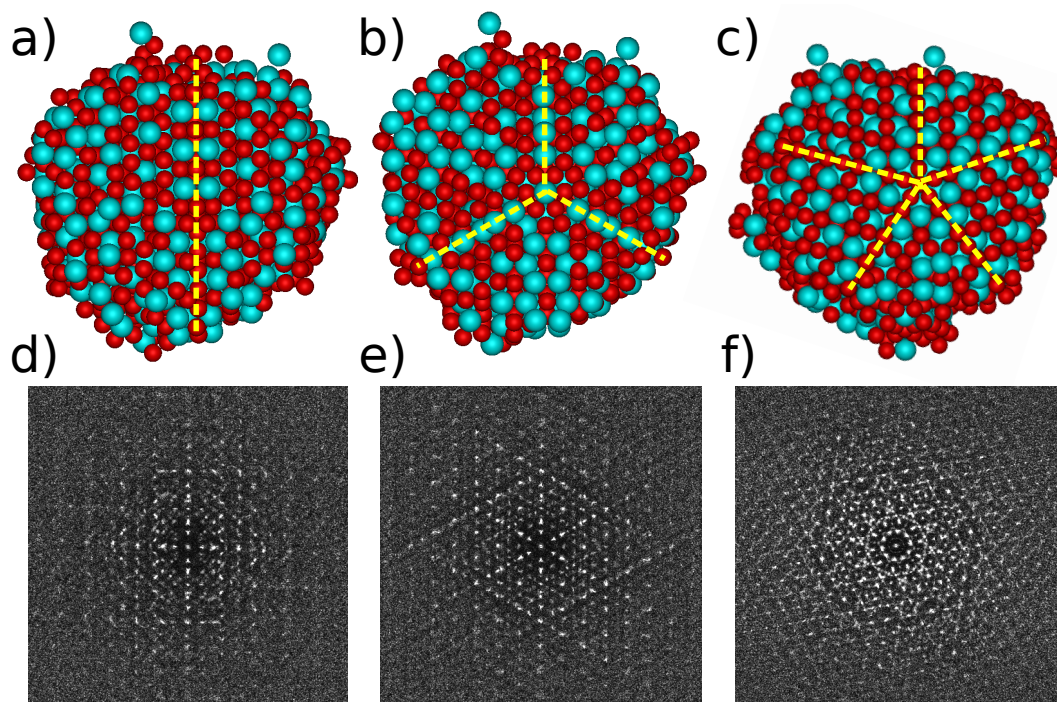


**Figure 7.3:** Cross-section views of computer rendered representations of a simulated SP exhibiting two-, three- and five-fold symmetries. a,b,c) Configurations of the simulated SP composed of  $N_{tot} = 5,000$  spheres and d,e,f) corresponding diffraction patterns of a,c and e, viewed along two-, three- and five-fold axes. The FFT is calculated on time-averaged coordinates of particles belonging to the iQC cluster identified using BOPs described in Section 7.2.3.

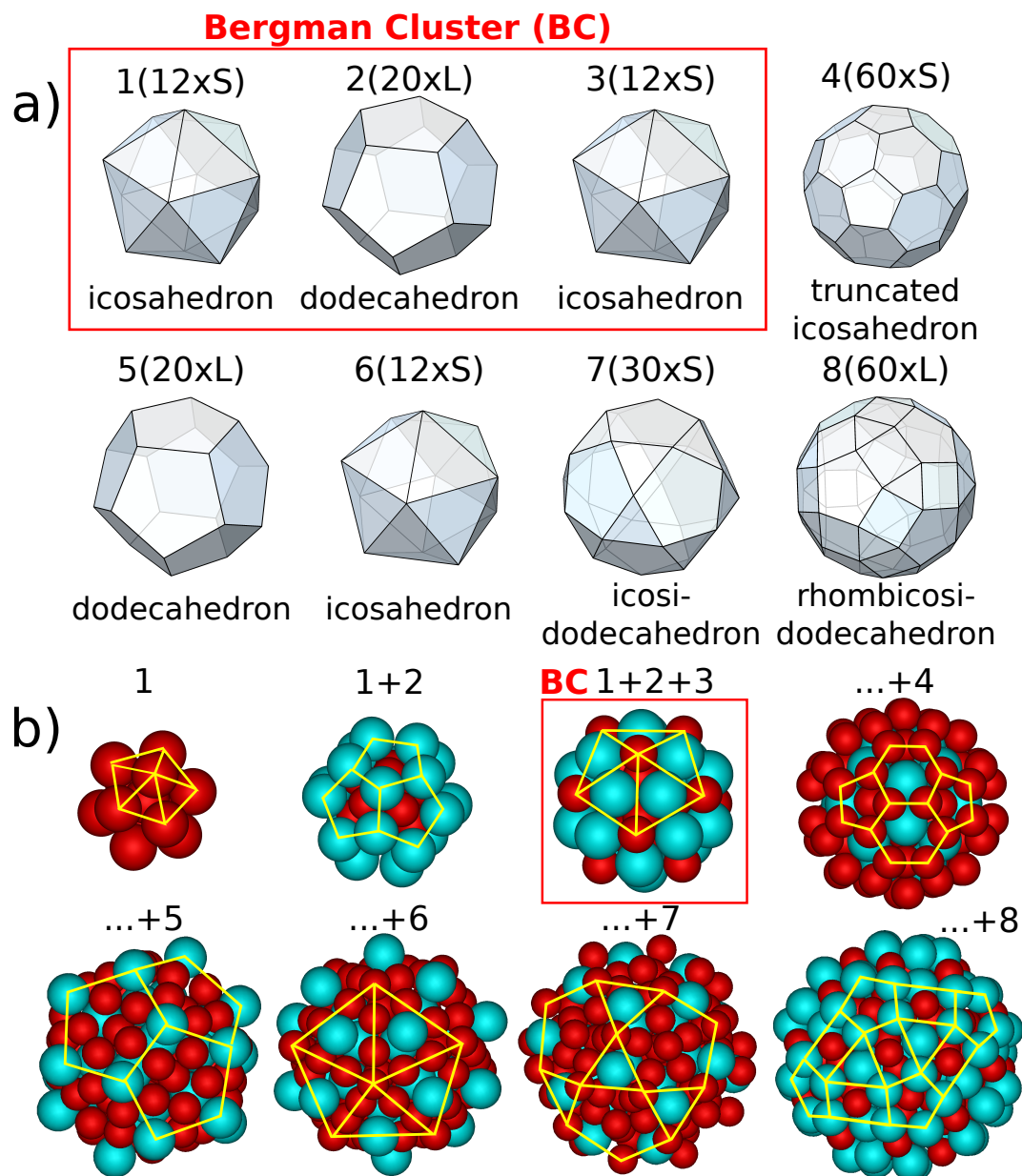


**Figure 7.4: Structure of the iQC.** iQC clusters were found to contain concentric shells around the center of symmetry with geometries corresponding to Platonic and Archimedean solids. a) The regular polygons describing the shells up to the 8<sup>th</sup> shell and the number of particles (of *L* or *S* species) forming them. b) Corresponding regular shells as found in simulations, where *L* and *S* spheres are coloured in cyan and red, respectively. The yellow lines denote the regular polygons corresponding to the surface tiling of the geometric solids. The 44-particle cluster up to the 3<sup>rd</sup> shell, as delineated by the red boxes, corresponds to the Bergman cluster.

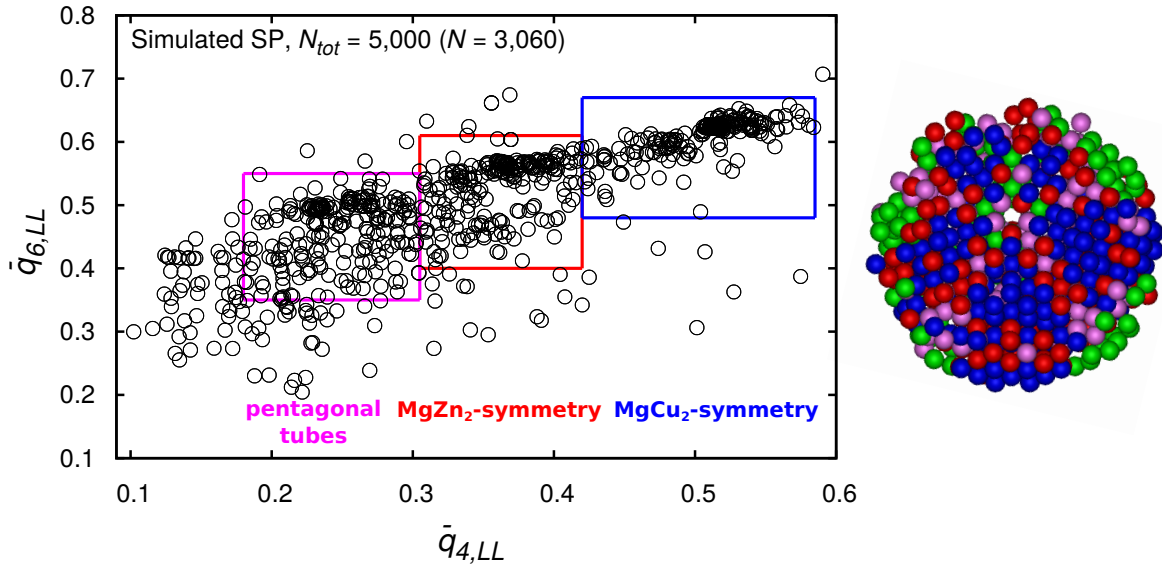


**Figure 7.5: Local structural symmetries of  $L$  species in a supraparticle.** Scatter plot of the average BOPs of the  $L$  particles in the  $\bar{q}_{4,LL} - \bar{q}_{6,LL}$  plane of the crystal structure of a simulated supraparticle. Only the BOP values of the  $N$  particles in the core are plotted. The blue and red boxes signify the BOP values that we used to identify the  $\text{MgCu}_2$ -like and  $\text{MgZn}_2$ -like local symmetry, respectively, of the particles in the final structure. The purple box represents the symmetry of the pentagonal tubes (or icosahedral chains) that run through the SP. These pentagonal tubes are formed by the edges of five neighbouring tetrahedral domains. A cross-section view of the corresponding configuration of the SP is shown in which the particles are coloured accordingly, *i.e.*,  $\text{MgZn}_2$ -stacked,  $\text{MgCu}_2$ -stacked particles, and pentagonal tubes are coloured in red, blue and purple, respectively. All other particles (not belonging to either of the three boxes) are coloured green. It is observed that the tetrahedral domains in the icosahedral SP are composed of particles with  $\text{MgCu}_2$ -like symmetry (blue). The faces of the tetrahedral  $\text{MgCu}_2$  domains show  $\text{MgZn}_2$ -like symmetry (red).

red boxes in Fig. 7.4-a,b). We found that the center of symmetries of these clusters are at off-centered positions in the spherical confinement. iQCs have been found in many binary and ternary intermetallic compounds [210, 228]. To the best of our knowledge, it is not yet known that equilibrium iQCs can form from HS-like particles induced by a spherical confinement, nor have binary iQCs been observed which contain Bergman clusters.

In addition, we analysed the local structural environment of the particles in the SP using a BOP analysis [181] on the  $L$  particles only. In particular, the  $\bar{q}_4$  and  $\bar{q}_6$  order parameters were used.  $\bar{q}_l$  of a particle  $i$  is defined as  $\bar{q}_l(i) = \sqrt{\frac{4\pi}{2l+1} \sum_{m=-l}^l |\bar{q}_{l,m}(i)|^2}$  where  $\bar{q}_{l,m}(i) = \frac{1}{N_b(i)+1} \sum_{k=0}^{N_b(i)} q_{l,m}(k)$  with  $N_b(i)$  denoting the number of ( $L$ ) neighbours of ( $L$ ) particle  $i$  and  $k=0$  represents the particle  $i$  itself.  $q_{l,m}(i)$  is the traditionally defined normalised 3D bond order parameter for ( $L$ ) particle  $i$  [116]. Nearest neighbours were determined by locating all particles within a cut-off distance  $r_c$  from particle  $i$ , where  $r_c$  corresponded to the first minimum of the radial distribution function  $g_{LL}(r)$ . As particles close to the SP surface have a lower number of nearest neighbours and therefore have a lower BOP value, particles closer than  $2\sigma_L$  to the spherical

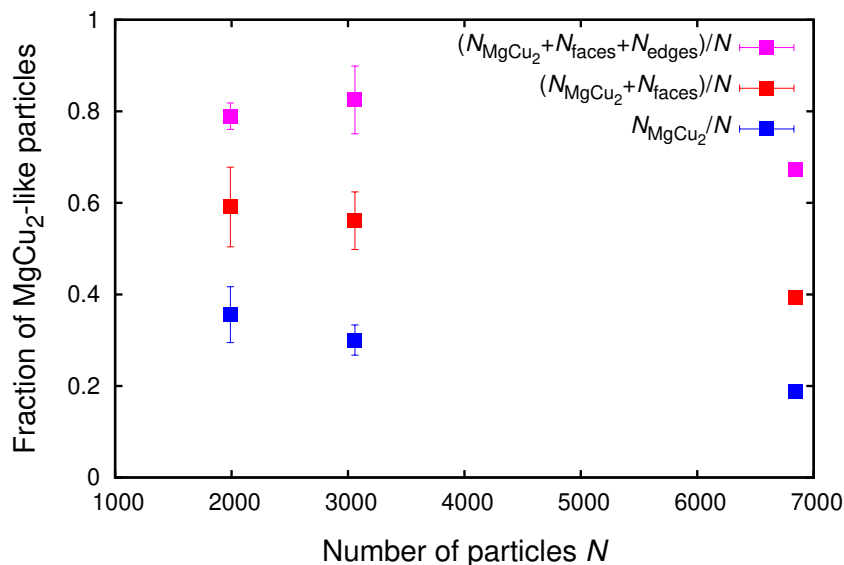


**Figure 7.6:** Fraction of  $\text{MgCu}_2$ -like particles in the SP, calculated numerically from the BOP cutoffs shown in Fig. 7.5, for SP system sizes  $N = 660, 1990, 3060$  and  $6840$  particles. The different estimates of the  $\text{MgCu}_2$ -like fraction are based on the different grouping of particle symmetries as described in the legend. The errorbars are obtained from three independent simulations.

confinement in simulations were not presented in the scatter plot and ignored in the estimation of the threshold BOP values used to characterise the local structural environment. The fraction of  $\text{MgCu}_2$ -like particles (see Fig. 7.6) is calculated without accounting for these ‘surface’ particles. Interestingly, the BOPs of the  $L$  particles in the iQC cluster coincide with the BOP signatures of the  $L$  particles in both equilibrated  $\text{MgZn}_2$  and  $\text{MgCu}_2$  Laves phases in bulk (see Fig. 6.12). By subsequent colouring of the particles in relation to their position in the  $\bar{q}_{6,LL}$ – $\bar{q}_{4,LL}$  scatter plot, their local symmetry was identified. The colour of the particles correspond to the colour of the bounding boxes delineating different symmetries in the BOP scatterplot of Fig. 7.5. To distinguish the local environment corresponding to the  $\text{MgZn}_2$ -like and  $\text{MgCu}_2$ -like symmetries, the following regions in the scatter plot were defined as  $0.305 < \bar{q}_{4,LL} < 0.42$  and  $0.4 < \bar{q}_{6,LL} < 0.61$  ( $\text{MgZn}_2$ -like), and  $0.42 < \bar{q}_{4,LL} < 0.585$  and  $0.48 < \bar{q}_{6,LL} < 0.67$  ( $\text{MgCu}_2$ -like). The  $\text{MgCu}_2$ -like particles are coloured in blue, and  $\text{MgZn}_2$ -like particles are denoted in red. We observe that the iQC cluster consists of twenty tetrahedral domains that predominantly consist of particles with a  $\text{MgCu}_2$ -like symmetry, whereas the *faces* of these tetrahedral domains are  $\text{MgZn}_2$ -like. When we say that the faces are  $\text{MgZn}_2$ -like, we are referring to the local environment of these particles. If we follow the stacking of large dimers (see Fig. 6.7), where the tetrahedral wedges meet, the stacking of the large dimers (which follow the  $\dots aa-bb-cc-aa\dots$  stacking in the  $\text{MgCu}_2$ -stacked tetrahedral domains) changes, because the two large particles making up a dimer at the shared face are individually part of two differently oriented tetrahedral domains, and show a local flip consistent with a  $\text{MgZn}_2$  large-dimer stacking  $\dots aa-bb-aa\dots$ . Numerically, this is reflected in the order parameters from large species correlations which coincide with a  $\text{MgZn}_2$ -like symmetry. Based on single particle systems, where the tetrahedral domains of the icosahedral clusters were found to be (cubic) FCC-like [132], it is not surprising that the wedges of our icosahedral SP structures follow a cubic  $\text{MgCu}_2$ -like symmetry. Therefore,

effectively, the hexagonal  $\text{MgZn}_2$  Laves phase which is obtained in bulk has been transformed into a structure that is locally close to that of the cubic  $\text{MgCu}_2$  Laves phase in these domains. In Fig. 7.5, we used an additional criterion to colour, in purple, the  $L$  particles that are part of the pentagonal tubes:  $0.18 < \bar{q}_{4,LL} < 0.305$  and  $0.35 < \bar{q}_{6,LL} < 0.55$ . The *edges* of five neighbouring tetrahedral domains form a pentagonal tube (or icosahedral chain [231]), that originates from the Bergman cluster, runs through the whole SP, and ends at one of twelve vertices with five-fold symmetry on the surface of the SP. In the bottom panel of Fig. 7.2, we show the twelve pentagonal tubes originating from the Bergman cluster. We remark that the pentagonal tubes differ in length as the Bergman cluster is eccentric with respect to the spherical confinement. Using the BOP criteria detailed above, we estimated the fraction of  $\text{MgCu}_2$ -like particles in our simulated SPs, for different SP sizes. We observe that the spherical confinement forces the local symmetry of 70-80% of the particles in the SP to change to resemble the  $\text{MgCu}_2$  Laves phase (Fig. 7.6). We therefore find that a binary mixture of HS-like particles, that crystallizes into the  $\text{MgZn}_2$  Laves phase in bulk, spontaneously forms an iQC cluster composed of tetrahedral domains with  $\text{MgCu}_2$ -like symmetry induced by a spherical confinement.

### 7.2.3 Nucleation and growth

Now that we have established that the structure of our SPs corresponds to a binary iQC cluster, we investigated one of the many open questions on iQCs [232], namely, how do iQCs grow? Does our binary iQC nucleate from a Bergman cluster and grow shell-by-shell? Or does crystallization start at the spherical interface similar to the formation of icosahedral clusters from HSs in spherical confinement [132]? In order to study the nucleation and growth of iQCs from a supersaturated binary fluid phase, we used a BOP-based criterion to identify and track the crystal nucleation in our simulations inside a spherical confinement of fixed volume.

**BOP criterion for tracking iQC crystalline clusters:** We use a dot product  $d_{l,\alpha\beta}(i, j) = \sum_{m=-l}^l q_{l,m}^\alpha(i) q_{l,m}^{\beta*}(j)$  correlation between particle  $i$  and its neighbour  $j$  for all three species combinations, with  $\alpha, \beta$  denoting the type of species, to identify particles belonging to the iQC crystalline cluster. Nearest neighbours  $j$  were determined by locating all particles within a cut-off distance  $r_c$  from particle  $i$ , where  $r_c$  corresponds to the first minimum of the radial distribution function  $g_{\alpha\beta}(r)$ . For the (i)  $L$ - $L$  species correlation, we used  $d_{6,LL} > 0.4$ , (ii)  $S$ - $S$  species correlation,  $-0.23 < d_{6,SS} < -0.04$  and (iii)  $S$ - $L$  species correlation  $-0.46 < d_{6,LS} < -0.1$ . If the dot product  $d_{l,\alpha\beta}(i, j)$  between the BOPs of two particles was greater than the relevant cut-off values (based on the species type), they share a “solid-like” bond. If the total number of solid-like bonds of a particle  $i$  with its neighbours was greater than a threshold value  $\xi_c$ , then particle  $i$  was crystalline. For a  $L$  particle,  $\xi_c^L = 10$  and for a  $S$  particle,  $\xi_c^S = 9$ . The above criteria were sufficient to distinguish the crystalline particles from the surrounding fluid. Additionally, to distinguish the tetrahedral domains from each other, we employed a dot product  $\bar{d}_{6,\alpha\beta}^d(i, j)$  correlation between two neighbouring  $L$  crystalline particles  $i$  and  $j$ , and identified  $i$  and  $j$  as belonging to the same crystalline domain if  $\bar{d}_{6,LL}^d(i, j) > 0.8$ . Here  $\bar{d}_{l,\alpha\beta}^d(i, j)$  has the same form as defined above, but is calculated with the average BOPs [181].  $\bar{q}_{l,m}(i)$  is defined similarly as in Section 7.2.2.2. The small particles were assigned domain IDs corresponding to their closest crystalline  $L$  particle neighbour.

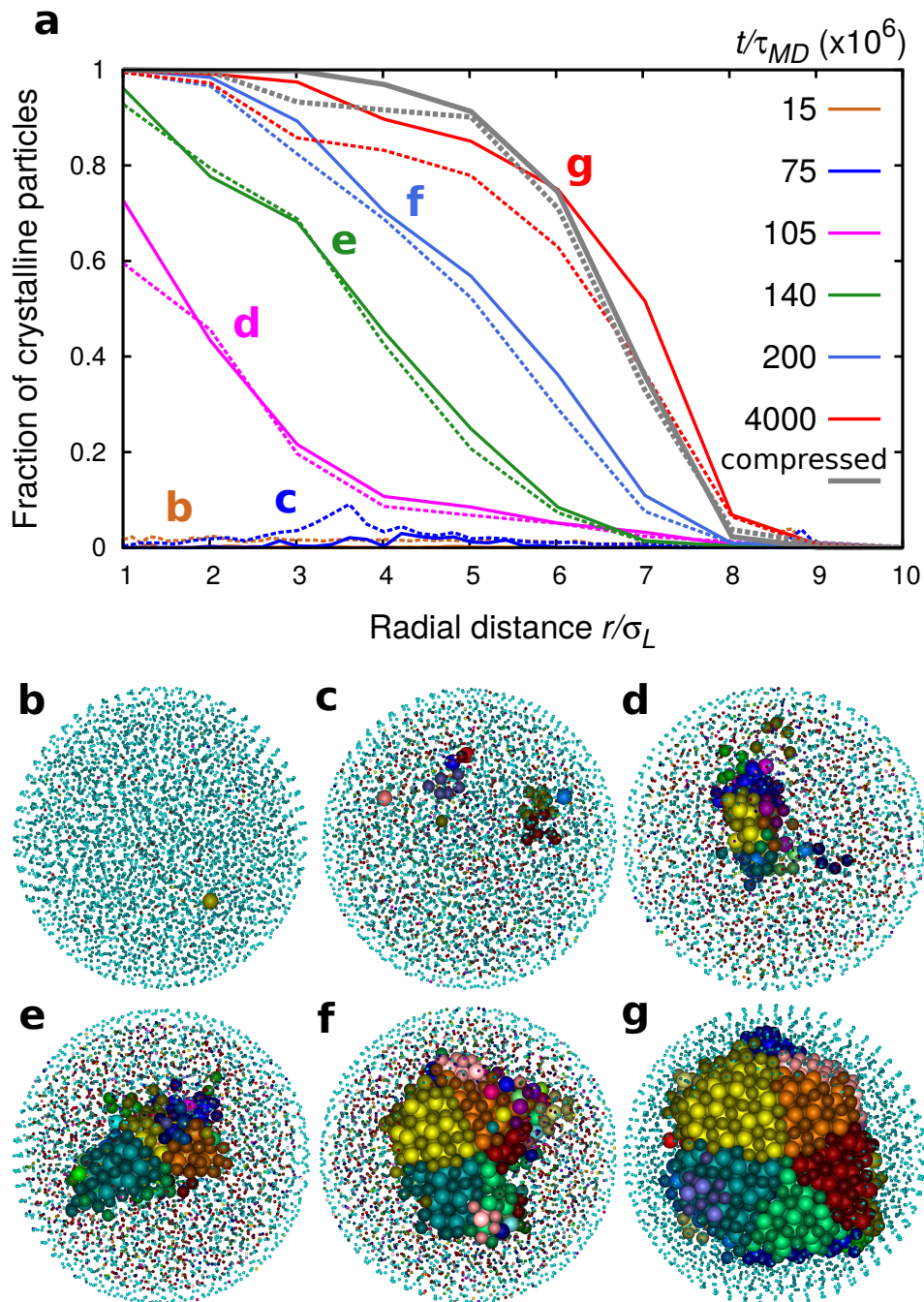


**Figure 7.7: Nucleation and growth of iQC.** a) The fraction of crystalline particles as a function of the radial distance from the center of the SP at different MD times. Crystalline particles belonging to the iQC cluster are identified using BOPs. The solid lines denote the crystalline fraction of  $L$  spheres and the dashed lines represent that of the  $S$  species. The crystalline fraction is calculated over the total number of particles of the same species and averaged over 1000 configurations. The profile shows that the crystal nucleates homogeneously at an off-centered position and grows radially outward with time. b-g): Typical configurations corresponding to the crystallization profiles shown in a), the labels (b-g) are shown in a) next to and in the same colour as the corresponding crystallization profile, for clarity. The different crystalline domains are shown in different colors. For crystalline and domain classification, see Section 7.2.3. The  $S$  spheres are coloured in a darker shade of the same color as the  $L$  spheres. Particles not belonging to the iQC cluster are reduced in size for visual clarity.

Using the above BOP criteria, in Fig. 7.7a, we plot the fraction of crystalline particles as a function of the radial distance from the center of a SP consisting of 5,000 particles at different times along with corresponding typical configurations (Figs. 7.7b-g). The solid lines denote the crystalline fraction of  $L$  spheres while the dashed lines represent the crystalline fraction of the  $S$  spheres. The crystalline fraction is calculated over the total number of particles of the same species and averaged over 1000 configurations. The evolution of the structure within the SP shows all the characteristics of nucleation and growth (Figs. 7.7b-g). We find that the system remains for a long time in the supersaturated fluid phase, in which small crystalline clusters form and melt in subsequent frames in the spherical confinement (Fig. 7.7c). At long times (onset of crystallization is at  $t/\tau_{MD} \sim 10^8$ ), a single primary cluster nucleates at an off-centered position and starts to grow (Fig. 7.7d). The nucleus diffuses slightly towards the center of the spherical confinement and grows into the surrounding fluid with time (Figs. 7.7e-g). This can also be appreciated from Fig. 7.7a that shows that the crystallization front has grown radially outward with time. The long period that the system stayed in a supersaturated fluid phase and the induction time before a single cluster starts to grow are typical for *homogeneous* nucleation. We therefore conclude that the iQC forms *via* homogeneous nucleation. In addition, we find that first a pentagonal tube is formed from which the structure grows out. The growth is therefore not initiated by the Bergman cluster.

An intriguing question is why a binary mixture that crystallizes into the  $\text{MgZn}_2$  Laves phase in bulk spontaneously forms an iQC cluster under spherical confinement. As the iQC cluster forms *via* homogeneous nucleation away from the spherical interface, the curvature can only be communicated *via* the supersaturated fluid phase. We measured the radial density profiles of the SP at different times in our simulations and found that the density profiles display pronounced layering of particles in concentric shells at the spherical interface, which lends strong support to the formation of the iQC being driven by the structural correlations and frustrations induced by the spherical curvature in the highly structured fluid phase (Fig. 7.8a). From the pair correlation functions of an equilibrated supersaturated bulk fluid, it can be seen that structural correlations in the fluid phase persist over long length scales (Fig. 7.8b).

## 7.2.4 Implications for photonic crystal research

Our finding that iQCs can self-assemble from a binary mixture of colloidal HS-like particles in spherical confinement is also interesting for photonic applications. Experiments on 3D printed structures in plastic using microwave radiation have already demonstrated that iQCs possess strong photonic band gaps that do not allow the propagation of light [211]. Moreover, our results show that the local symmetry of 70-80% of the particles has been changed to  $\text{MgCu}_2$ -like, where the  $\text{MgCu}_2$  is composed of a cubic diamond lattice of the  $L$  spheres and a pyrochlore lattice of the  $S$  spheres, both of which have a photonic band gap for low refractive index contrasts [27, 28]. Although it still has to be determined theoretically which structure, either the iQC cluster or the wedges with  $\text{MgCu}_2$ -like symmetry, is best suited for opening up a photonic band gap at low refractive index contrast [211], it is almost certain that if hard particles with a large index contrast such as titania are used, for which the optical properties on the single particle level can be tuned in great detail [233], a photonic band gap can be realised for visible wavelengths. Although it has recently become possible to grow photonic crystals with diamond sub-structures using DNA interactions [106, 234], the procedures are complicated and the crystals and index

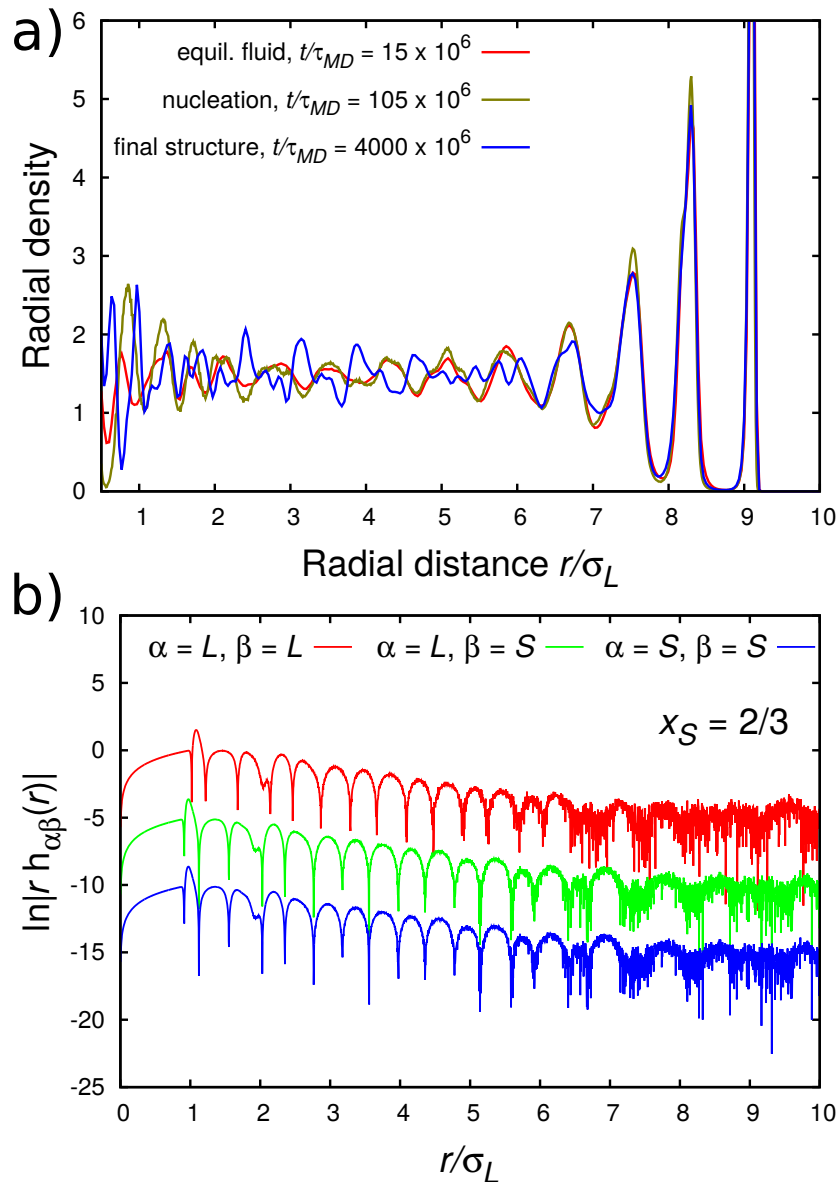


**Figure 7.8: Density profile and structural correlations of the fluid phase.** a) Radial density profile of a binary mixture of  $N_{tot} = 5,000$  HS-like simulated particles in the (i) equilibrated fluid phase (Fig. 7.7a), (ii) at the onset of nucleation (Fig. 7.7c), and (iii) the final SP structure (Fig. 7.7g). Strong layering in the outermost shells is observed early in the simulation. The radial density profiles are averaged over 1000 configurations. b) The logarithm of the total correlation function  $\ln|r h_{\alpha\beta}(r)|$  of an equilibrated bulk fluid at a composition  $x_S = N_S/(N_S + N_L) = 2/3$  and density  $\rho\sigma_{av}^3 = 0.945$ , as a function of radial distance  $r/\sigma_L$ , where  $\alpha, \beta$  denotes the particle type (L/S). All three species correlations L-L, L-S and S-S are shown, indicating a highly-structured fluid with structural correlations persisting over long length scales, with a common decay length.

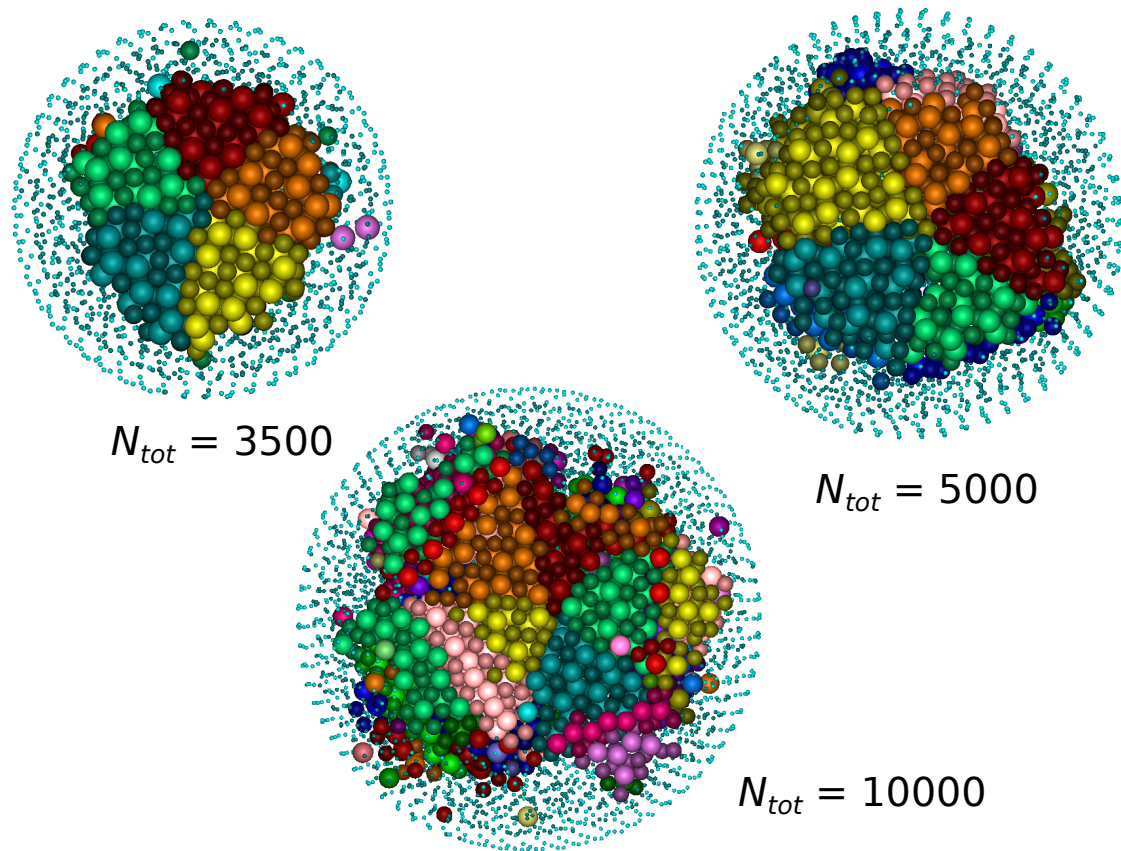


**Figure 7.9: SPs of different system sizes as obtained from MD simulations.** The simulations are performed on system sizes of  $N_{tot} = 3,500$ ,  $5,000$  and  $10,000$  spheres and binary iQCs are observed to spontaneously crystallize for all of them. Crystalline particles belonging to the iQC cluster are identified using BOPs. The different crystalline domains are shown in different colors. For crystalline and domain classification, see Supplementary Section 5. The  $S$  particles in each domain are coloured in a darker shade of the same color as the  $L$  particles. Particles not belonging to the iQC cluster are reduced in size for visual clarity.

contrasts are not yet good enough to open up photonic band gaps. Crystallization of HS-like particles with a large refractive index contrast provides a much easier route to obtain a band gap for visible light. Moreover, as our results have been obtained for HS-like particles, it will be fairly straightforward to extend these results to particles with a size closer to the wavelengths of visible light.

### 7.3 Conclusions and outlook

Our findings in this Chapter have strengthened the connection already made in previous work between icosahedral order and frustration brought about by curved space [132, 235, 236]. Even though the work in its complete form involves a collaboration with experiments, we mostly discuss the spontaneous nucleation of binary iQCs from computer simulations in this Chapter, with a remark that the simulated SPs closely resemble in structure the experimentally obtained

SPs. The iQCs were found to consist of Bergman clusters with additional concentric shells of particles. In addition, we found that the local symmetry of the particles in the tetrahedral domains of the icosahedral cluster transformed to a  $\text{MgCu}_2$ -like symmetry which is, next to an iQC itself, an important and much sought after structure in photonic crystal research. Furthermore, we studied the evolution of the iQC in computer simulations, and tracked the nucleation and growth mechanism by identifying the particles belonging to the iQC cluster using BOPs. We observed that the iQC clusters form *via* homogeneous nucleation and that the iQC growth is induced by the pronounced layering of the highly-structured fluid at the spherical surface. We simulated  $N_{tot} = 3,500, 5,000$  and  $10,000$  spheres under spherical confinement (Fig. 7.9) and observed iQCs for all these system sizes, thus indicating that a crossover to the  $\text{MgZn}_2$  crystal phase requires a bigger system size. This expectation is in line with the observed structural crossover found for monodisperse HSs from icosahedral clusters or larger surface-reconstructed icosahedral clusters to FCC ordering (which is the stable crystal phase in bulk) for bigger system sizes with  $> 90,000$  HSs [132]. As recently HS-like  $\text{MgZn}_2$  colloidal crystals have been realised [24] with spheres on the submicron lengthscale, it is likely that by having such systems self-assemble inside a spherical confinement interesting colloidal photonic iQCs can now be realised as well. This means that the droplet platform as explored here, but using larger colloidal particles that can be imaged in 3D by light nanoscopy, can also be used to obtain the first experimental single particle level information on binary nucleation and growth.

## 7.4 Acknowledgements

The work discussed in this Chapter was done in close collaboration with Da Wang, Ernest van der Wee, Thomas Atlantzis, Daniele Zanaga, Yaoting Wu under the supervision of Marjolein Dijkstra, Alfons van Blaaderen, Sara Bals (Antwerp) and Chris Murray (Philadelphia). I thank everyone for an extremely rewarding collaboration. Da Wang synthesised the supraparticles which exhibited five-fold symmetry and kickstarted this whole collaboration. Yaoting Wu synthesised the  $\text{PbSe/CdSe}$  nanoparticles. Da Wang along with Thomas Atlantzis obtained the real space coordinates of the experimental SPs using electron tomography and Sparse Sphere Reconstruction (SSR) techniques. Daniele Zanaga implemented the SSR technique. Ernest van der Wee was invaluable in identifying and describing the quasicrystal structure, and also performed BOP calculations on the real space 3D coordinates of the experimental SPs, for comparison with my simulated SPs. I thank Da Wang for providing the beautiful HAADF-STEM image of an experimental SP showing five-fold symmetry shown in Fig. 7.1, for comparison with a simulated SP. I sincerely thank Gerhard Blab for the 3D-printing of numerous truncated tetrahedra which not only helped us better understand the structure of the iQC and the Laves phases but will undoubtedly serve as excellent presentation aides on this topic. Nick Tasios and Siddharth Paliwal are sincerely thanked for their contribution towards calculating the Fast Fourier Transform of the SPs. Gabriele Coli is thanked for the BOP cut-off criterion that he developed for detecting LP clusters in bulk, which were also used in this work to detect the nucleation of the iQC clusters. Michiel Hermes is thanked for developing reader-interactive views of our structures. Ernest and Da are also thanked for many useful discussions, and for co-writing the manuscript on this work.



## References

- [1] J. G. Kirkwood, *Phase transformations in solids*. Edited by R. Smoluchowski, J. E. Mayer, and W. A. Weyl, pages 67–73, 1951.
- [2] B. J. Alder and T. E. Wainwright, *Phase transition for a hard sphere system*. *The Journal of Chemical Physics*, 27(5):1208–1209, 1957.
- [3] W. W. Wood and J. D. Jacobson, *Preliminary results from a recalculation of the Monte Carlo equation of state of hard spheres*. *The Journal of Chemical Physics*, 27(5):1207–1208, 1957.
- [4] J. K. Percus. *The Many-Body Problem*. 1963.
- [5] E. G. Noya and N. G. Almarza, *Entropy of hard spheres in the close-packing limit*. *Molecular Physics*, 113(9-10):1061–1068, 2015.
- [6] B. J. Alder, D. A. Young, M. R. Mansigh, and Z. W. Salsburg, *Hard sphere equation of state in the close-packed limit*. *Journal of Computational Physics*, 7(3):361–366, 1971.
- [7] W. M. Visscher and M. Bolsterli, *Random packing of equal and unequal spheres in two and three dimensions*. *Nature*, 239(5374):504, 1972.
- [8] J. Tobochnik and P. M. Chapin, *Monte Carlo simulation of hard spheres near random closest packing using spherical boundary conditions*. *The Journal of Chemical Physics*, 88(9):5824–5830, 1988.
- [9] L. F. Töth. *Lagerungen in der Ebene auf der Kugel und im Raum*. Springer-Verlag, 1953.
- [10] T. C. Hales and S. P. Ferguson, *A formulation of the Kepler conjecture*. *Discrete & Computational Geometry*, 36(1):21–69, 2006.
- [11] T. Hales, M. Adams, G. Bauer, T. D. Dang, J. Harrison, H. Le Truong, C. Kaliszyk, V. Magron, S. McLaughlin, T. T. Nguyen, et al. *A formal proof of the Kepler conjecture*. In *Forum of Mathematics, Pi*, volume 5. Cambridge University Press, 2017.
- [12] P. N. Pusey and W. van Megen, *Phase behaviour of concentrated suspensions of nearly hard colloidal spheres*. *Nature*, 320(6060):340–342, 1986.
- [13] A. Vrij, J. W. Jansen, J. K. G. Dhont, C. Pathmamanoharan, M. M. Kops-Werkhoven, and H. M. Fijnaut, *Light scattering of colloidal dispersions in non-polar solvents at finite concentrations. Silic spheres as model particles for hard-sphere interactions*. *Faraday Discussions of the Chemical Society*, 76:19–35, 1983.
- [14] W. C. K. Poon, *Colloids as big atoms*. *Science*, 304(5672):830–831, 2004.
- [15] P. Bartlett, R. H. Ottewill, and P. N. Pusey, *Freezing of binary mixtures of colloidal hard spheres*. *The Journal of Chemical Physics*, 93(2):1299–1312, 1990.
- [16] P. Bartlett, R. Ottewill, and P. Pusey, *Superlattice formation in binary mixtures of hard-sphere colloids*. *Physical Review Letters*, 68(25):3801, 1992.

- [17] M. D. Eldridge, P. A. Madden, P. N. Pusey, and P. Bartlett, *Binary hard-sphere mixtures: A comparison between computer simulation and experiment*. *Molecular Physics*, 84(2):395–420, 1995.
- [18] P. N. Pusey, W. C. K. Poon, S. M. Ilett, and P. Bartlett, *Phase behaviour and structure of colloidal suspensions*. *Journal of Physics: Condensed Matter*, 6(23A):A29, 1994.
- [19] F. X. Redl, K.-S. Cho, C. B. Murray, and S. O'Brien, *Three-dimensional binary superlattices of magnetic nanocrystals and semiconductor quantum dots*. *Nature*, 423(6943):968, 2003.
- [20] A. B. Schofield, P. N. Pusey, and P. Radcliffe, *Stability of the binary colloidal crystals  $AB_2$  and  $AB_{13}$* . *Physical Review E*, 72(3):031407, 2005.
- [21] E. C. M. Vermolen, A. Kuijk, L. C. Filion, M. Hermes, J. H. J. Thijssen, M. Dijkstra, and A. van Blaaderen, *Fabrication of large binary colloidal crystals with a NaCl structure*. *Proceedings of the National Academy of Sciences*, 106(38):16063–16067, 2009.
- [22] E. V. Shevchenko, D. V. Talapin, N. A. Kotov, S. O'Brien, and C. B. Murray, *Structural diversity in binary nanoparticle superlattices*. *Nature*, 439(7072):55, 2006.
- [23] W. H. Evers, B. de Nijs, L. Filion, S. Castillo, M. Dijkstra, and D. Vanmaekelbergh, *Entropy-driven formation of binary semiconductor-nanocrystal superlattices*. *Nano Letters*, 10(10):4235–4241, 2010.
- [24] N. Schaertl, D. Botin, T. Palberg, and E. Bartsch, *Formation of Laves phases in buoyancy matched hard sphere suspensions*. *Soft Matter*, 14:5130–5139, 2018.
- [25] E. Trizac, M. D. Eldridge, and P. A. Madden, *Stability of the AB crystal for asymmetric binary hard sphere mixtures*. *Molecular Physics*, 90(4):675–678, 1997.
- [26] M. D. Eldridge, P. A. Madden, and D. Frenkel, *Entropy-driven formation of a superlattice in a hard-sphere binary mixture*. *Nature*, 365(6441):35, 1993.
- [27] A.-P. Hynninen, J. H. J. Thijssen, E. C. M. Vermolen, M. Dijkstra, and A. van Blaaderen, *Self-assembly route for photonic crystals with a bandgap in the visible region*. *Nature Materials*, 6(3):202, 2007.
- [28] A.-P. Hynninen, L. Filion, and M. Dijkstra, *Stability of LS and  $LS_2$  crystal structures in binary mixtures of hard and charged spheres*. *The Journal of Chemical Physics*, 131(6):064902, 2009.
- [29] J. L. Lebowitz and J. S. Rowlinson, *Thermodynamic properties of mixtures of hard spheres*. *The Journal of Chemical Physics*, 41(1):133–138, 1964.
- [30] J. L. Lebowitz, *Exact solution of generalized Percus-Yevick equation for a mixture of hard spheres*. *Physical Review*, 133(4A):A895, 1964.
- [31] T. Biben and J.-P. Hansen, *Phase separation of asymmetric binary hard-sphere fluids*. *Physical Review Letters*, 66(17):2215, 1991.
- [32] M. Dijkstra, R. van Roij, and R. Evans, *Phase diagram of highly asymmetric binary hard-sphere mixtures*. *Physical Review E*, 59(5):5744, 1999.
- [33] E. Yablonoitch, *Inhibited spontaneous emission in solid-state physics and electronics*. *Physical Review Letters*, 58(20):2059, 1987.

- [34] S. John, *Strong localization of photons in certain disordered dielectric superlattices*. Physical Review Letters, 58(23):2486, 1987.
- [35] E. Yablonovitch, T. J. Gmitter, and K. M. Leung, *Photonic band structure: The face-centered-cubic case employing nonspherical atoms*. Physical Review Letters, 67(17):2295, 1991.
- [36] Y. A. Vlasov, X.-Z. Bo, J. C. Sturm, and D. J. Norris, *On-chip natural assembly of silicon photonic bandgap crystals*. Nature, 414(6861):289, 2001.
- [37] T. T. Ngo, C. M. Liddell, M. Ghebrebrhan, and J. D. Joannopoulos, *Tetrastack: Colloidal diamond-inspired structure with omnidirectional photonic band gap for low refractive index contrast*. Applied Physics Letters, 88(24):241920, 2006.
- [38] A. Garcia-Adeva, *Band gap atlas for photonic crystals having the symmetry of the kagome and pyrochlore lattices*. New Journal of Physics, 8(6):86, 2006.
- [39] M. F. Chisholm, S. Kumar, and P. Hazzledine, *Dislocations in complex materials*. Science, 307(5710):701–703, 2005.
- [40] J. G. Kirkwood and E. Monroe, *Statistical mechanics of fusion*. The Journal of Chemical Physics, 9(7):514–526, 1941.
- [41] N. Metropolis, A. W. Rosenbluth, M. N. Rosenbluth, A. H. Teller, and E. Teller, *Equation of state calculations by fast computing machines*. The Journal of Chemical Physics, 21(6):1087–1092, 1953.
- [42] M. N. Rosenbluth and A. W. Rosenbluth, *Further results on Monte Carlo equations of state*. The Journal of Chemical Physics, 22(5):881–884, 1954.
- [43] G. Battimelli and G. Ciccotti, *Berni Alder and the pioneering times of molecular simulation*. The European Physical Journal H, 43(3):303–335, 2018.
- [44] M.-A. M. Karlsen. *Interview (August 20, 2015), by Daan Frenkel, unpublished*.
- [45] V. I. Manousiouthakis and M. W. Deem, *Strict detailed balance is unnecessary in Monte Carlo simulation*. The Journal of Chemical Physics, 110(6):2753–2756, 1999.
- [46] M. Dijkstra. *Modelling and Simulation, Lecture notes, unpublished*. 2018.
- [47] M. Newman and G. Barkema. *Monte Carlo methods in statistical physics, Chapter 1-4*. Oxford University Press: New York, USA, 1999.
- [48] D. P. Landau and K. Binder. *A guide to Monte Carlo simulations in statistical physics*. Cambridge university press, 2014.
- [49] K. E. Jensen, D. Pennachio, D. Recht, D. A. Weitz, and F. Spaepen, *Rapid growth of large, defect-free colloidal crystals*. Soft Matter, 9(1):320–328, 2013.
- [50] E. C. Nelson, N. L. Dias, K. P. Bassett, S. N. Dunham, V. Verma, M. Miyake, P. Wiltzius, J. A. Rogers, J. J. Coleman, X. Li, et al., *Epitaxial growth of three-dimensionally architected optoelectronic devices*. Nature Materials, 10(9):676–681, 2011.
- [51] A. van Blaaderen and P. Wiltzius, *Real-space structure of colloidal hard-sphere glasses*. Science, 270(5239):1177–1179, 1995.

- [52] P. Schall, I. Cohen, D. A. Weitz, and F. Spaepen, *Visualization of dislocation dynamics in colloidal crystals*. *Science*, 305(5692):1944–1948, 2004.
- [53] P. Schall, I. Cohen, D. A. Weitz, and F. Spaepen, *Visualizing dislocation nucleation by indenting colloidal crystals*. *Nature*, 440(7082):319–323, 2006.
- [54] P. G. Bolhuis, D. Frenkel, S.-C. Mau, and D. A. Huse, *Entropy difference between crystal phases*. *Nature*, 388(6639):235–236, 1997.
- [55] P. N. Pusey, W. van Megen, P. Bartlett, B. J. Ackerson, J. G. Rarity, and S. M. Underwood, *Structure of crystals of hard colloidal spheres*. *Physical Review Letters*, 63(25):2753, 1989.
- [56] L. Filion, M. Hermes, R. Ni, and M. Dijkstra, *Crystal nucleation of hard spheres using molecular dynamics, umbrella sampling, and forward flux sampling: A comparison of simulation techniques*. *The Journal of Chemical Physics*, 133(24):244115, 2010.
- [57] S. Pronk and D. Frenkel, *Can stacking faults in hard-sphere crystals anneal out spontaneously?* *The Journal of Chemical Physics*, 110(9):4589–4592, 1999.
- [58] W. K. Kegel and J. K. Dhont, *Aging of the structure of crystals of hard colloidal spheres*. *The Journal of Chemical Physics*, 112(7):3431–3436, 2000.
- [59] V. C. Martelozzo, A. B. Schofield, W. C. K. Poon, and P. N. Pusey, *Structural aging of crystals of hard-sphere colloids*. *Physical Review E*, 66(2):021408, 2002.
- [60] A. Yethiraj and A. van Blaaderen, *A colloidal model system with an interaction tunable from hard sphere to soft and dipolar*. *Nature*, 421(6922):513–517, 2003.
- [61] J. P. Hoogenboom, D. Derks, P. Vergeer, and A. van Blaaderen, *Stacking faults in colloidal crystals grown by sedimentation*. *The Journal of Chemical Physics*, 117(24):11320–11328, 2002.
- [62] J. P. Hoogenboom, P. Vergeer, and A. van Blaaderen, *A real-space analysis of colloidal crystallization in a gravitational field at a flat bottom wall*. *The Journal of Chemical Physics*, 119(6):3371–3383, 2003.
- [63] N. V. Dziomkina and G. J. Vancso, *Colloidal crystal assembly on topologically patterned templates*. *Soft Matter*, 1(4):265–279, 2005.
- [64] I. Ramsteiner, K. E. Jensen, D. A. Weitz, and F. Spaepen, *Experimental observation of the crystallization of hard-sphere colloidal particles by sedimentation onto flat and patterned surfaces*. *Physical Review E*, 79(1):011403, 2009.
- [65] J. Zhu, M. Li, R. Rogers, W. Meyer, R. Ottewill, W. Russel, P. Chaikin, et al., *Crystallization of hard-sphere colloids in microgravity*. *Nature*, 387(6636):883–885, 1997.
- [66] Z. Cheng, P. M. Chaikin, J. Zhu, W. B. Russel, and W. V. Meyer, *Crystallization kinetics of hard spheres in microgravity in the coexistence regime: Interactions between growing crystallites*. *Physical Review Letters*, 88(1):015501, 2001.
- [67] J. Hilhorst, J. R. Wolters, and A. V. Petukhov, *Slanted stacking faults and persistent face centered cubic crystal growth in sedimentary colloidal hard sphere crystals*. *CrystEngComm*, 12(11):3820–3826, 2010.

- [68] M. Marechal, M. Hermes, and M. Dijkstra, *Stacking in sediments of colloidal hard spheres*. The Journal of Chemical Physics, 135(3):034510, 2011.
- [69] A. van Blaaderen, R. Ruel, and P. Wiltzius, *Template-directed colloidal crystallization*. Nature, 385(6614):321–324, 1997.
- [70] M. Heni and H. Löwen, *Precrystallization of fluids induced by patterned substrates*. Journal of Physics: Condensed Matter, 13(21):4675, 2001.
- [71] Y. Yin, Y. Lu, B. Gates, and Y. Xia, *Template-assisted self-assembly: a practical route to complex aggregates of monodispersed colloids with well-defined sizes, shapes, and structures*. Journal of the American Chemical Society, 123(36):8718–8729, 2001.
- [72] J. P. Hoogenboom, A. K. van Langen-Suurling, J. Romijn, and A. van Blaaderen, *Hard-sphere crystals with hcp and non-close-packed structure grown by colloidal epitaxy*. Physical Review Letters, 90(13):138301, 2003.
- [73] J. P. Hoogenboom, A. K. van Langen-Suurling, J. Romijn, and A. van Blaaderen, *Epitaxial growth of a colloidal hard-sphere hcp crystal and the effects of epitaxial mismatch on crystal structure*. Physical Review E, 69(5):051602, 2004.
- [74] W.-S. Xu, Z.-Y. Sun, and L.-J. An, *Heterogeneous crystallization of hard spheres on patterned substrates*. The Journal of Chemical Physics, 132(14):144506, 2010.
- [75] K. E. Davis, W. B. Russel, and W. J. Glantschnig, *Disorder-to-order transition in settling suspensions of colloidal silica: X-ray measurements*. Science, 245(4917):507–510, 1989.
- [76] P. Strating, *Brownian dynamics simulation of a hard-sphere suspension*. Physical Review E, 59(2):2175, 1999.
- [77] A. Scala, T. Voigtmann, and C. De Michele, *Event-driven brownian dynamics for hard spheres*. The Journal of Chemical Physics, 126(13):134109, 2007.
- [78] R. Piazza, *Settled and unsettled issues in particle settling*. Reports on Progress in Physics, 77(5):056602, 2014.
- [79] P. R. Ten Wolde, M. J. Ruiz-Montero, and D. Frenkel, *Numerical evidence for bcc ordering at the surface of a critical fcc nucleus*. Physical Review Letters, 75(14):2714, 1995.
- [80] M. Heni and H. Löwen, *Surface freezing on patterned substrates*. Physical Review Letters, 85(17):3668, 2000.
- [81] I. Volkov, M. Cieplak, J. Koplik, and J. R. Banavar, *Molecular dynamics simulations of crystallization of hard spheres*. Physical Review E, 66(6):061401, 2002.
- [82] S. Auer and D. Frenkel, *Line tension controls wall-induced crystal nucleation in hard-sphere colloids*. Physical Review Letters, 91(1):015703, 2003.
- [83] S. Dorosz and T. Schilling, *On the influence of a patterned substrate on crystallization in suspensions of hard spheres*. The Journal of Chemical Physics, 136(4):044702, 2012.
- [84] T. Biben, R. Ohnesorge, and H. Löwen, *Crystallization in sedimentation profiles of hard spheres*. Europhysics Letters, 28(9):665, 1994.

- [85] J.-M. Meijer, V. W. A. de Villeneuve, and A. V. Petukhov, *In-plane stacking disorder in polydisperse hard sphere crystals*. *Langmuir*, 23(7):3554–3560, 2007.
- [86] M. Heni and H. Löwen, *Interfacial free energy of hard-sphere fluids and solids near a hard wall*. *Physical Review E*, 60(6):7057, 1999.
- [87] M. Marechal and M. Dijkstra, *Crystallization of colloidal hard spheres under gravity*. *Physical Review E*, 75(6):061404, 2007.
- [88] V. J. Anderson and H. N. W. Lekkerkerker, *Insights into phase transition kinetics from colloid science*. *Nature*, 416(6883):811–815, 2002.
- [89] B. Li, D. Zhou, and Y. Han, *Assembly and phase transitions of colloidal crystals*. *Nature Reviews Materials*, 1:15011, 2016.
- [90] S.-Y. Lin, E. Chow, V. Hietala, P. R. Villeneuve, and J. D. Joannopoulos, *Experimental demonstration of guiding and bending of electromagnetic waves in a photonic crystal*. *Science*, 282(5387):274–276, 1998.
- [91] J. Ge and Y. Yin, *Responsive photonic crystals*. *Angewandte Chemie International Edition*, 50(7):1492–1522, 2011.
- [92] M. Wang and X. Wang, *Electrodeposition zinc-oxide inverse opal and its application in hybrid photovoltaics*. *Solar Energy Materials and Solar Cells*, 92(3):357–362, 2008.
- [93] E. Haugan, H. Granlund, J. Gjessing, and E. S. Marstein, *Colloidal crystals as templates for light harvesting structures in solar cells*. *Energy Procedia*, 10:292–296, 2011.
- [94] K. Busch and S. John, *Photonic band gap formation in certain self-organizing systems*. *Physical Review E*, 58(3):3896, 1998.
- [95] K. Ho, C. T. Chan, and C. M. Soukoulis, *Existence of a photonic gap in periodic dielectric structures*. *Physical Review Letters*, 65(25):3152, 1990.
- [96] F. Laves and H. Witte, *Der Einfluß von Valenzelektronen auf die Kristallstruktur ternärer Magnesiumlegierungen*. *Metallwirtsch*, 15(36):840–842, 1936.
- [97] E. H. A. De Hoog, W. K. Kegel, A. van Blaaderen, and H. N. W. Lekkerkerker, *Direct observation of crystallization and aggregation in a phase-separating colloid-polymer suspension*. *Physical Review E*, 64(2):021407, 2001.
- [98] J. Perrin, *Mouvement brownien et molécules*. *Journal de Physique Théorique et Appliquée*, 9(1):5–39, 1910.
- [99] D. de las Heras and M. Schmidt, *The phase stacking diagram of colloidal mixtures under gravity*. *Soft Matter*, 9(36):8636–8641, 2013.
- [100] D. de las Heras and M. Schmidt, *Sedimentation stacking diagram of binary colloidal mixtures and bulk phases in the plane of chemical potentials*. *Journal of Physics: Condensed Matter*, 27(19):194115, 2015.
- [101] M. Schmidt, M. Dijkstra, and J.-P. Hansen, *Floating liquid phase in sedimenting colloid-polymer mixtures*. *Physical Review Letters*, 93(8):088303, 2004.
- [102] H. Pattabhiraman and M. Dijkstra, *Periodic layers of a dodecagonal quasicrystal and a floating hexagonal crystal in sedimentation-diffusion equilibria of colloids*. *The Journal of Chemical Physics*, 147(10):104902, 2017.

- [103] D. de las Heras, L. L. Treffenstädt, and M. Schmidt, *Reentrant network formation in patchy colloidal mixtures under gravity*. *Physical Review E*, 93(3):030601, 2016.
- [104] D. De Las Heras, N. Doshi, T. Cosgrove, J. Phipps, D. I. Gittins, J. S. Van Duijneveldt, and M. Schmidt, *Floating nematic phase in colloidal platelet-sphere mixtures*. *Scientific reports*, 2:789, 2012.
- [105] G. Avvisati, T. Dasgupta, and M. Dijkstra, *Fabrication of colloidal Laves phases via hard tetramers and hard spheres: Bulk phase diagram and sedimentation behavior*. *ACS Nano*, 11(8):7702–7709, 2017.
- [106] É. Ducrot, M. He, G.-R. Yi, and D. J. Pine, *Colloidal alloys with preassembled clusters and spheres*. *Nature Materials*, 16(6):652, 2017.
- [107] G. A. Mansoori, N. F. Carnahan, K. E. Starling, and T. W. Leland Jr, *Equilibrium thermodynamic properties of the mixture of hard spheres*. *The Journal of Chemical Physics*, 54(4):1523–1525, 1971.
- [108] R. J. Speedy, *Pressure of the metastable hard-sphere fluid*. *Journal of Physics: Condensed Matter*, 9(41):8591, 1997.
- [109] J. M. Polson, E. Trizac, S. Pronk, and D. Frenkel, *Finite-size corrections to the free energies of crystalline solids*. *The Journal of Chemical Physics*, 112(12):5339, 2000.
- [110] C. Vega, E. Sanz, J. L. F. Abascal, and E. G. Noya, *Determination of phase diagrams via computer simulation: methodology and applications to water, electrolytes and proteins*. *Journal of Physics: Condensed Matter*, 20(15):153101, 2008.
- [111] T. Drwenski, P. Hooijer, and R. van Roij, *Sedimentation stacking diagrams of binary mixtures of thick and thin hard rods*. *Soft matter*, 12(26):5684–5692, 2016.
- [112] T. Dasgupta, J. R. Edison, and M. Dijkstra, *Growth of defect-free colloidal hard-sphere crystals using colloidal epitaxy*. *The Journal of Chemical Physics*, 146(7):074903, 2017.
- [113] T. Geigenfeind and D. de las Heras, *The role of sample height in the stacking diagram of colloidal mixtures under gravity*. *Journal of Physics: Condensed Matter*, 29(6):064006, 2016.
- [114] L. Fillion and M. Dijkstra, *Prediction of binary hard-sphere crystal structures*. *Physical Review E*, 79(4):046714, 2009.
- [115] D. Frenkel and B. Smit. *Understanding molecular simulation: from algorithms to applications*, volume 1. Elsevier, 2001.
- [116] P. J. Steinhardt, D. R. Nelson, and M. Ronchetti, *Bond-orientational order in liquids and glasses*. *Physical Review B*, 28(2):784, 1983.
- [117] N. A. Mahynski, A. Z. Panagiotopoulos, D. Meng, and S. K. Kumar, *Stabilizing colloidal crystals by leveraging void distributions*. *Nature Communications*, 5, 2014.
- [118] S.-C. Mau and D. A. Huse, *Stacking entropy of hard-sphere crystals*. *Physical Review E*, 59(4):4396, 1999.
- [119] H. N. W. Lekkerkerker and R. Tuinier. *Colloids and the depletion interaction*, volume 833. Springer, 2011.

- [120] M. Dijkstra, R. van Roij, and R. Evans, *Direct simulation of the phase behavior of binary hard-sphere mixtures: test of the depletion potential description*. Physical Review Letters, 82(1):117, 1999.
- [121] B. Smit, *Grand canonical Monte Carlo simulations of chain molecules: adsorption isotherms of alkanes in zeolites*. Mol. Phys., 85(1):153–172, 1995.
- [122] E. P. Bernard, W. Krauth, and D. B. Wilson, *Event-chain Monte Carlo algorithms for hard-sphere systems*. Physical Review E, 80:056704, Nov 2009.
- [123] J. R. Errington, *Evaluating surface tension using grand canonical Transition Matrix Monte Carlo simulation and finite size scaling*. Physical Review E, 67:012102, 2003.
- [124] M. Fitzgerald, R. R. Picard, and R. N. Silver, *Canonical transition probabilities for adaptive metropolis simulation*. EPL (Europhysics Letters), 46(3):282, 1999.
- [125] J. R. Errington, *Direct calculation of liquid–vapor phase equilibria from Transition Matrix Monte Carlo simulation*. The Journal of Chemical Physics, 118(22):9915–9925, 2003.
- [126] A. Z. Panagiotopoulos, *Monte Carlo methods for phase equilibria of fluids*. Journal of Physics: Condensed Matter, 12(3):R25, 2000.
- [127] L. Filion, M. Hermes, R. Ni, E. C. M. Vermolen, A. Kuijk, C. G. Christova, J. C. P. Stiefelhagen, T. Vissers, A. van Blaaderen, and M. Dijkstra, *Self-assembly of a colloidal interstitial solid with tunable sublattice doping*. Physical Review Letters, 107(16):168302, 2011.
- [128] Pusey, P. N., *The effect of polydispersity on the crystallization of hard spherical colloids*. Journal de Physique, 48(5):709–712, 1987.
- [129] N. A. Mahynski, S. K. Kumar, and A. Z. Panagiotopoulos, *Relative stability of the fcc and hcp polymorphs with interacting polymers*. Soft Matter, 11(2):280–289, 2015.
- [130] N. A. Mahynski, S. K. Kumar, and A. Z. Panagiotopoulos, *Tuning polymer architecture to manipulate the relative stability of different colloid crystal morphologies*. Soft Matter, 11(25):5146–5153, 2015.
- [131] N. A. Mahynski, L. Rovigatti, C. N. Likos, and A. Z. Panagiotopoulos, *Bottom-up colloidal crystal assembly with a twist*. ACS Nano, 10(5):5459–5467, 2016.
- [132] B. de Nijs, S. Dussi, F. Smalenburg, J. D. Meeldijk, D. J. Groenendijk, L. Filion, A. Imhof, A. van Blaaderen, and M. Dijkstra, *Entropy-driven formation of large icosahedral colloidal clusters by spherical confinement*. Nature Materials, 14(1):56, 2015.
- [133] F. Montanarella, J. J. Geuchies, T. Dasgupta, P. T. Prins, C. van Overbeek, R. Dattani, P. Baesjou, M. Dijkstra, A. V. Petukhov, A. van Blaaderen, and D. Vanmaekelbergh, *Crystallization of nanocrystals in spherical confinement probed by in situ X-ray scattering*. Nano Letters, 2018.
- [134] M. Grzelczak, J. Vermant, E. M. Furst, and L. M. Liz-Marzán, *Directed self-assembly of nanoparticles*. ACS Nano, 4(7):3591–3605, 2010.
- [135] M. A. Boles, M. Engel, and D. V. Talapin, *Self-assembly of colloidal nanocrystals: From intricate structures to functional materials*. Chemical Reviews, 116(18):11220–11289, 2016.

- [136] V. N. Manoharan, *Colloidal matter: Packing, geometry, and entropy*. Science, 349(6251):1253751, 2015.
- [137] F. Li, D. P. Josephson, and A. Stein, *Colloidal assembly: the road from particles to colloidal molecules and crystals*. Angewandte Chemie International Edition, 50(2):360–388, 2011.
- [138] M. Cargnello, A. C. Johnston-Peck, B. T. Diroll, E. Wong, B. Datta, D. Damodhar, V. V. Doan-Nguyen, A. A. Herzing, C. R. Kagan, and C. B. Murray, *Substitutional doping in nanocrystal superlattices*. Nature, 524(7566):450, 2015.
- [139] Y. Xia and Z. Tang, *Monodisperse inorganic supraparticles: formation mechanism, properties and applications*. Chemical Communications, 48(51):6320–6336, 2012.
- [140] S. Wintzheimer, T. Granath, M. Oppmann, T. Kister, T. Thai, T. Kraus, N. Vogel, and K. Mandel, *Supraparticles: functionality from uniform structural motifs*. ACS Nano, 12:5093–5120, 2018.
- [141] D. Vanmaekelbergh, L. K. van Vugt, H. E. Bakker, F. T. Rabouw, B. d. Nijs, R. J. van Dijk-Moes, M. A. van Huis, P. J. Baesjou, and A. van Blaaderen, *Shape-dependent multiexciton emission and whispering gallery modes in supraparticles of cdse/multishell quantum dots*. ACS Nano, 9(4):3942–3950, 2015.
- [142] H. Friedrich, C. J. Gommers, K. Overgaag, J. D. Meeldijk, W. H. Evers, B. d. Nijs, M. P. Boneschanscher, P. E. de Jongh, A. J. Verkleij, K. P. de Jong, et al., *Quantitative structural analysis of binary nanocrystal superlattices by electron tomography*. Nano Letters, 9(7):2719–2724, 2009.
- [143] S. Bals, B. Goris, L. M. Liz-Marzán, and G. Van Tendeloo, *Three-dimensional characterization of noble-metal nanoparticles and their assemblies by electron tomography*. Angewandte Chemie International Edition, 53(40):10600–10610, 2014.
- [144] T. Udayabhaskararao, T. Altantzis, L. Houben, M. Coronado-Puchau, J. Langer, R. Popovitz-Biro, L. M. Liz-Marzán, L. Vuković, P. Král, S. Bals, et al., *Tunable porous nanoallotropes prepared by post-assembly etching of binary nanoparticle superlattices*. Science, 358(6362):514–518, 2017.
- [145] P.-W. Yang, S. Thoka, P.-C. Lin, C.-J. Su, H.-S. Sheu, M. H. Huang, and U.-S. Jeng, *Tracing the surfactant-mediated nucleation, growth, and superpacking of gold supercrystals using time and spatially resolved X-ray scattering*. Langmuir, 33(13):3253–3261, 2017.
- [146] M. C. Weidman, D.-M. Smilgies, and W. A. Tisdale, *Kinetics of the self-assembly of nanocrystal superlattices measured by real-time in situ X-ray scattering*. Nature Materials, 15(7):775, 2016.
- [147] J. J. Geuchies, C. Van Overbeek, W. H. Evers, B. Goris, A. De Backer, A. P. Gantapara, F. T. Rabouw, J. Hilhorst, J. L. Peters, O. Konovalov, et al., *In situ study of the formation mechanism of two-dimensional superlattices from pbse nanocrystals*. Nature Materials, 15(12):1248, 2016.
- [148] K. N. Pham, A. M. Puertas, J. Bergenholtz, S. U. Egelhaaf, A. Moussaid, P. N. Pusey, A. B. Schofield, M. E. Cates, M. Fuchs, and W. C. Poon, *Multiple glassy states in a simple model system*. Science, 296(5565):104–106, 2002.

- [149] P. J. Lu, E. Zaccarelli, F. Ciulla, A. B. Schofield, F. Sciortino, and D. A. Weitz, *Gelation of particles with short-range attraction*. *Nature*, 453(7194):499, 2008.
- [150] E. Sanz, M. E. Leunissen, A. Fortini, A. van Blaaderen, and M. Dijkstra, *Gel formation in suspensions of oppositely charged colloids: Mechanism and relation to the equilibrium phase diagram*. *The Journal of Physical Chemistry B*, 112(35):10861–10872, 2008.
- [151] P. C. Ohara, D. V. Leff, J. R. Heath, and W. M. Gelbart, *Crystallization of opals from polydisperse nanoparticles*. *Physical Review Letters*, 75(19):3466, 1995.
- [152] J. N. Israelachvili. *Intermolecular and surface forces*. Academic press, 2011.
- [153] B. Faure, G. Salazar-Alvarez, and L. Bergström, *Hamaker constants of iron oxide nanoparticles*. *Langmuir*, 27(14):8659–8664, 2011.
- [154] R. Van Santen, *The ostwald step rule*. *The Journal of Physical Chemistry*, 88(24):5768–5769, 1984.
- [155] A. Fortini, E. Sanz, and M. Dijkstra, *Crystallization and gelation in colloidal systems with short-ranged attractive interactions*. *Physical Review E*, 78(4):041402, 2008.
- [156] A. M. Kalsin, M. Fialkowski, M. Paszewski, S. K. Smoukov, K. J. Bishop, and B. A. Grzybowski, *Electrostatic self-assembly of binary nanoparticle crystals with a diamond-like lattice*. *Science*, 312(5772):420–424, 2006.
- [157] K. J. Bishop, N. R. Chevalier, and B. A. Grzybowski, *When and why like-sized, oppositely charged particles assemble into diamond-like crystals*. *The Journal of Physical Chemistry Letters*, 4(9):1507–1511, 2013.
- [158] Y. Wang, Y. Wang, D. R. Breed, V. N. Manoharan, L. Feng, A. D. Hollingsworth, M. Weck, and D. J. Pine, *Colloids with valence and specific directional bonding*. *Nature*, 491(7422):51, 2012.
- [159] W. Liu, M. Tagawa, H. L. Xin, T. Wang, H. Emamy, H. Li, K. G. Yager, F. W. Starr, A. V. Tkachenko, and O. Gang, *Diamond family of nanoparticle superlattices*. *Science*, 351(6273):582–586, 2016.
- [160] B. A. Lindquist, R. B. Jadrich, and T. M. Truskett, *Communication: From close-packed to topologically close-packed: Formation of Laves phases in moderately polydisperse hard-sphere mixtures*. *The Journal of Chemical Physics*, 148(19):191101, 2018.
- [161] D. Coslovich, M. Ozawa, and L. Berthier, *Local order and crystallization of dense polydisperse hard spheres*. *Journal of Physics: Condensed Matter*, 30(14):144004, 2018.
- [162] P. K. Bommineni, N. R. Varela-Rosales, M. Klement, and M. Engel, *Complex crystals from size-disperse spheres*. arXiv preprint arXiv:1811.00061, 2018.
- [163] S. Jungblut and C. Dellago, *Crystallization of a binary Lennard-Jones mixture*. *The Journal of Chemical Physics*, 134(10):104501, 2011.
- [164] S. Punnathanam and P. A. Monson, *Crystal nucleation in binary hard sphere mixtures: A Monte Carlo simulation study*. *The Journal of Chemical Physics*, 125(2):024508, 2006.
- [165] S. R. Ganagalla and S. N. Punnathanam, *Free energy barriers for homogeneous crystal nucleation in a eutectic system of binary hard spheres*. *The Journal of Chemical Physics*, 138(17):174503, 2013.

- [166] P. K. Bommineni and S. N. Punnathanam, *Molecular simulation of homogeneous crystal nucleation of  $AB_2$  solid phase from a binary hard sphere mixture*. The Journal of Chemical Physics, 147(6):064504, 2017.
- [167] I. N. Stranski and D. Totomanow, *Keimbildungsgeschwindigkeit und ostwaldsche stufenregel*. Zeitschrift für Physikalische Chemie, 163(1):399–408, 1933.
- [168] E. Sanz, C. Valeriani, D. Frenkel, and M. Dijkstra, *Evidence for out-of-equilibrium crystal nucleation in suspensions of oppositely charged colloids*. Physical Review Letters, 99(5):055501, 2007.
- [169] O. Peters, J. D. Neelin, and S. W. Nesbitt, *Mesoscale convective systems and critical clusters*. Journal of the Atmospheric Sciences, 66(9):2913–2924, 2009.
- [170] R. Ni, F. Smallenburg, L. Filion, and M. Dijkstra, *Crystal nucleation in binary hard-sphere mixtures: the effect of order parameter on the cluster composition*. Molecular Physics, 109(7-10):1213–1227, 2011.
- [171] J. D. Weeks, D. Chandler, and H. C. Andersen, *Role of repulsive forces in determining the equilibrium structure of simple liquids*. The Journal of Chemical Physics, 54(12):5237–5247, 1971.
- [172] T. Kawasaki and H. Tanaka, *Formation of a crystal nucleus from liquid*. Proceedings of the National Academy of Sciences, 107(32):14036–14041, 2010.
- [173] L. Filion, R. Ni, D. Frenkel, and M. Dijkstra, *Simulation of nucleation in almost hard-sphere colloids: The discrepancy between experiment and simulation persists*. The Journal of Chemical Physics, 134(13):134901, 2011.
- [174] D. Richard and T. Speck, *Crystallization of hard spheres revisited. i. extracting kinetics and free energy landscape from forward flux sampling*. The Journal of Chemical Physics, 148(12):124110, 2018.
- [175] D. Richard and T. Speck, *Crystallization of hard spheres revisited. ii. thermodynamic modeling, nucleation work, and the surface of tension*. The Journal of Chemical Physics, 148(22):224102, 2018.
- [176] T. Kister, M. Mravlak, T. Schilling, and T. Kraus, *Pressure-controlled formation of crystalline, janus, and core-shell supraparticles*. Nanoscale, 8(27):13377–13384, 2016.
- [177] M. Hasaka, H. Nakashima, and K. Oki, *Structure of the Laves phase observed in polystyrene latexes*. Transactions of the Japan Institute of Metals, 25(2):65–72, 1984.
- [178] S. Auer and D. Frenkel, *Crystallization of weakly charged colloidal spheres: a numerical study*. Journal of Physics: Condensed Matter, 14(33):7667, 2002.
- [179] S. Auer, W. C. K. Poon, and D. Frenkel, *Phase behavior and crystallization kinetics of poly-12-hydroxystearic-coated polymethylmethacrylate colloids*. Physical Review E, 67(2):020401, 2003.
- [180] D. Frenkel and B. Smit. *Understanding molecular simulations: from algorithms to applications*. Technical report, Academic press, 2002.
- [181] W. Lechner and C. Dellago, *Accurate determination of crystal structures based on averaged local bond order parameters*. The Journal of Chemical Physics, 129(11):114707, 2008.

- [182] E. Boattini, M. Ram, F. Smallenburg, and L. Filion, *Neural-network-based order parameters for classification of binary hard-sphere crystal structures*. *Molecular Physics*, 116(21-22):3066–3075, 2018.
- [183] D. Moroni, P. R. Ten Wolde, and P. G. Bolhuis, *Interplay between structure and size in a critical crystal nucleus*. *Physical Review Letters*, 94(23):235703, 2005.
- [184] J. A. Anderson, C. D. Lorenz, and A. Travesset, *General purpose molecular dynamics simulations fully implemented on graphics processing units*. *Journal of Computational Physics*, 227(10):5342–5359, 2008.
- [185] J. Glaser, T. D. Nguyen, J. A. Anderson, P. Lui, F. Spiga, J. A. Millan, D. C. Morse, and S. C. Glotzer, *Strong scaling of general-purpose molecular dynamics simulations on gpus*. *Computer Physics Communications*, 192:97–107, 2015.
- [186] S. Nosé, *A unified formulation of the constant temperature molecular dynamics methods*. *The Journal of Chemical Physics*, 81(1):511–519, 1984.
- [187] W. G. Hoover, *Canonical dynamics: equilibrium phase-space distributions*. *Physical Review A*, 31(3):1695, 1985.
- [188] G. J. Martyna, D. J. Tobias, and M. L. Klein, *Constant pressure molecular dynamics algorithms*. *The Journal of Chemical Physics*, 101(5):4177–4189, 1994.
- [189] R. Ni, M. A. C. Stuart, and M. Dijkstra, *Pushing the glass transition towards random close packing using self-propelled hard spheres*. *Nature communications*, 4:2704, 2013.
- [190] W. Götze, *Recent tests of the mode-coupling theory for glassy dynamics*. *Journal of Physics: Condensed Matter*, 11(10A):A1, 1999.
- [191] D. Richard and T. Speck, *The role of shear in crystallization kinetics: From suppression to enhancement*. *Scientific reports*, 5:14610, 2015.
- [192] J. C. Dyre, *Hidden scale invariance in condensed matter*. *The Journal of Physical Chemistry B*, 118(34):10007–10024, 2014.
- [193] J.-P. Hansen and I. R. McDonald. *Theory of simple liquids*. Elsevier, 1990.
- [194] Y. Rosenfeld and N. Ashcroft, *Theory of simple classical fluids: Universality in the short-range structure*. *Physical Review A*, 20(3):1208, 1979.
- [195] M. Ross, *Generalized Lindemann melting law*. *Physical Review*, 184(1):233, 1969.
- [196] U. R. Pedersen, L. Costigliola, N. P. Bailey, T. B. Schröder, and J. C. Dyre, *Thermodynamics of freezing and melting*. *Nature Communications*, 7:12386, 2016.
- [197] N. Gnan, T. B. Schröder, U. R. Pedersen, N. P. Bailey, and J. C. Dyre, *Pressure-energy correlations in liquids. iv. “isomorphs” in liquid phase diagrams*. *The Journal of Chemical Physics*, 131(23):234504, 2009.
- [198] L. A. Roed, D. Gundermann, J. C. Dyre, and K. Niss. *Communication: Two measures of isochronal superposition*, 2013.
- [199] W. G. Hoover, S. G. Gray, and K. W. Johnson, *Thermodynamic properties of the fluid and solid phases for inverse power potentials*. *The Journal of Chemical Physics*, 55(3):1128–1136, 1971.

- [200] R. Agrawal and D. A. Kofke, *Solid-fluid coexistence for inverse-power potentials*. Physical Review Letters, 74(1):122, 1995.
- [201] J. R. Espinosa, C. Vega, C. Valeriani, and E. Sanz, *Seeding approach to crystal nucleation*. The Journal of Chemical Physics, 144(3):034501, 2016.
- [202] J. R. Espinosa, P. Sampedro, C. Valeriani, C. Vega, and E. Sanz, *Lattice mold technique for the calculation of crystal nucleation rates*. Faraday Discussions, 195:569–582, 2017.
- [203] M. Hermes, E. C. M. Vermolen, M. E. Leunissen, D. L. J. Vossen, P. D. J. van Oostrum, M. Dijkstra, and A. van Blaaderen, *Nucleation of colloidal crystals on configurable seed structures*. Soft Matter, 7(10):4623–4628, 2011.
- [204] D. Turnbull. *Phase changes*. volume 3 of *Solid State Physics*, pages 225–306. 1956.
- [205] F. C. Frank, *Supercooling of liquids*. Proc. R. Soc. Lond. A, 215(1120):43–46, 1952.
- [206] J. Taffs and C. P. Royall, *The role of fivefold symmetry in suppressing crystallization*. Nature Communications, 7:13225, 2016.
- [207] D. R. Nelson and F. Spaepen. *Polytetrahedral order in condensed matter*. In *Solid State Physics*, volume 42, pages 1–90. Elsevier, 1989.
- [208] F. Spaepen, *Condensed-matter science: Five-fold symmetry in liquids*. Nature, 408(6814):781, 2000.
- [209] D. Shechtman, I. Blech, D. Gratias, and J. W. Cahn, *Metallic phase with long-range orientational order and no translational symmetry*. Physical Review Letters, 53(20):1951, 1984.
- [210] A.-P. Tsai, “*Back to the future*”- an account discovery of stable quasicrystals. Accounts of Chemical Research, 36:31–38, 2003.
- [211] W. Man, M. Megens, P. J. Steinhardt, and P. M. Chaikin, *Experimental measurement of the photonic properties of icosahedral quasicrystals*. Nature, 436(7053):993, 2005.
- [212] T. Dotera, *Quasicrystals in soft matter*. Israel Journal of Chemistry, 51(11-12):1197–1205, 2011.
- [213] M. Engel, P. F. Damasceno, C. L. Phillips, and S. C. Glotzer, *Computational self-assembly of a one-component icosahedral quasicrystal*. Nature Materials, 14:109, 2014.
- [214] U. Gasser, E. R. Weeks, A. Schofield, P. N. Pusey, and D. A. Weitz, *Real-space imaging of nucleation and growth in colloidal crystallization*. Science, 292(5515):258–262, 2001.
- [215] W. K. Kegel and A. van Blaaderen, *Direct observation of dynamical heterogeneities in colloidal hard-sphere suspensions*. Science, 287(5451):290–293, 2000.
- [216] Z. Cheng. *Colloidal Crystallization*, chapter 12, pages 203–248. Wiley-Blackwell, 2016.
- [217] A. Fernandez-Nieves and A. M. Puertas. *Fluids, Colloids and Soft Materials: An Introduction to Soft Matter Physics*, volume 7. John Wiley & Sons, 2016.
- [218] T. Wang, D. LaMontagne, J. Lynch, J. Zhuang, and Y. C. Cao, *Colloidal superparticles from nanoparticle assembly*. Chemical Society Reviews, 42(7):2804–2823, 2013.
- [219] J. Lacava, P. Born, and T. Kraus, *Nanoparticle clusters with Lennard-Jones geometries*. Nano Letters, 12(6):3279–3282, 2012.

- [220] Y. Yang, B. Wang, X. Shen, L. Yao, L. Wang, X. Chen, S. Xie, T. Li, J. Hu, D. Yang, and A. Dong, *Scalable assembly of crystalline binary nanocrystal superparticles and their enhanced magnetic and electrochemical properties*. *Journal of the American Chemical Society*, 140:15038–15047, 2018.
- [221] J. Wang, C. F. Mbah, T. Przybilla, B. Apeleo Zubiri, E. Spiecker, M. Engel, and N. Vogel, *Magic number colloidal clusters as minimum free energy structures*. *Nature Communications*, 9(6):5259, 2018.
- [222] D. Wang, M. Hermes, R. Kotni, Y. Wu, N. Tasios, Y. Liu, B. de Nijs, E. B. van der Wee, C. B. Murray, M. Dijkstra, et al., *Interplay between spherical confinement and particle shape on the self-assembly of rounded cubes*. *Nature Communications*, 9(1):2228, 2018.
- [223] C. Hermann, *Kristallographie in räumen beliebiger dimensionszahl. i. die symmetrieoperationen*. *Acta Crystallographica*, 2(3):139–145, 1949.
- [224] A. P. Tsai, *Icosahedral clusters, icosahedral order and stability of quasicrystals – a view of metallurgy*. *Science and Technology of Advanced Materials*, 9(1):013008, 2008.
- [225] A. L. Mackay, *A dense non-crystallographic packing of equal spheres*. *Acta Crystallographica*, 15(9):916–918, 1962.
- [226] K. H. Kuo, *Mackay, anti-mackay, double-mackay, pseudo-mackay, and related icosahedral shell clusters*. *Structural Chemistry*, 13(3-4):221–230, 2002.
- [227] G. Bergman, J. L. T. Waugh, and L. Pauling, *The crystal structure of the metallic phase Mg<sub>32</sub> (Al, Zn) 49*. *Acta Crystallographica*, 10(4):254–259, 1957.
- [228] W. Steurer and S. Deloudi, *Fascinating quasicrystals*. *Acta Crystallographica Section A: Foundations of Crystallography*, 64(1):1–11, 2008.
- [229] A. P. Tsai, J. Q. Guo, E. Abe, H. Takakura, and T. J. Sato, *A stable binary quasicrystal*. *Nature*, 408:537, 2000.
- [230] R. Maezawa, S. Kashimoto, and T. Ishimasa, *Icosahedral quasicrystals in Zn–T–Sc (T = Mn, Fe, Co or Ni) alloys*. *Philosophical Magazine Letters*, 84(4):215–223, 2004.
- [231] Z. Yang, L. Zhang, M. F. Chisholm, X. Zhou, H. Ye, and S. J. Pennycook, *Precipitation of binary quasicrystals along dislocations*. *Nature Communications*, 9(1):809, 2018.
- [232] W. Steurer, *Quasicrystals: What do we know? What do we want to know? What can we know?* *Acta Crystallographica Section A: Foundations and Advances*, 74(1):1–11, 2018.
- [233] A. Jannasch, A. F. Demirörs, P. D. J. Van Oostrum, A. van Blaaderen, and E. Schäffer, *Nanonewton optical force trap employing anti-reflection coated, high-refractive-index titania microspheres*. *Nature Photonics*, 6(7):469, 2012.
- [234] Y. Wang, I. C. Jenkins, J. T. McGinley, T. Sinno, and J. C. Crocker, *Colloidal crystals with diamond symmetry at optical lengthscales*. *Nature Communications*, 8:14173, 2017.
- [235] R. E. Guerra, C. P. Kelleher, A. D. Hollingsworth, and P. M. Chaikin, *Freezing on a sphere*. *Nature*, 554(7692):346, 2018.
- [236] J. F. Sadoc, *Use of regular polytopes for the mathematical description of the order in amorphous structures*. *Journal of Non-Crystalline Solids*, 44(1):1–16, 1981.

# Summary

The work presented in this thesis is based on the crystallization and phase behaviour of colloidal systems. In a colloidal system, one insoluble phase (such as fluid droplets, particulate solid) is dispersed in a continuous phase or medium. The main feature of colloidal particles, as explained by Einstein beginning with his doctoral thesis, is that they show a constant ‘fidgeting’ movement known as *Brownian* motion due to collisions with molecules of the solvent phase (medium). The length scale of the colloidal particle, such that they exhibit Brownian motion, is such that at least one dimension should be between 1 nm and 1  $\mu\text{m}$ . The slow Brownian motion of colloidal particles in the continuous medium allows for the system to explore thermodynamically favourable microscopic configurations, and under certain conditions, arrange themselves into ordered structures such as a *crystal* phase. This phenomenon is known as *self-assembly*, and this thesis discusses spontaneous or directed self-assembly in colloidal systems, with a particular focus on colloidal *photonic crystals*.

Photonic crystals are structures which exhibit a photonic band gap (analogous to an electronic band gap in semiconductors) as a consequence of alternating regions of high and low dielectric constants in the material. In this thesis, we are interested in self-assembling *colloidal* photonic crystals which, due to the size of the colloidal building blocks, display a photonic band gap in the visible range of the electromagnetic spectrum. Colloidal photonic crystals have a number of applications such as optical wave guides, optical sensors, energy storage and conversion.

A well known photonic crystal is the inverted face-centered-cubic (FCC) structure. From the colloidal perspective, this structure is significant because it is known to spontaneously self-assemble from monodisperse hard spheres, in experiments and computer simulations. The hard sphere model is a well-established model for studying crystallization in certain colloidal systems such as polymethyl-methacrylate (PMMA) or silica particles coated with polymer. However the FCC structure displays a photonic bandgap which is narrow and therefore susceptible to defects. Therefore, there is a strong motivation for self-assembling defect-free FCC single crystals. This is particularly challenging as, apart from natural defects arising from spontaneous self-assembly, the FCC crystal has a thermodynamically competing crystal phase in the hard-sphere phase diagram known as the hexagonal-close-packed (HCP) structure wherein the free-energy difference between the two structures is only  $\sim 10^{-3}k_B T$  per particle at melting, and therefore one would more often than not obtain a random stacking of these two structures in the crystal phase.

In **Chapter 2**, we studied the formation of large FCC crystals formed by pure hard spheres under an applied gravitational field. In order to circumvent random stacking, we templated the bottom of the sedimentation column to direct the self-assembly. The template patterns correspond to the three densest cross-sectional planes of the FCC crystal. We then investigated the optimal sedimentation conditions under which large nearly defect-free FCC single crystals may be formed, such as the (i) gravitational Péclet number ( $Pe$ ) (ii) lattice spacing of the template and (iii) particle volume fraction before switching on the gravity field. We found that the best FCC single crystals (fraction of similarly oriented FCC particles  $\simeq 90\%$ ) were obtained at high  $Pe$  (high sedimentation velocities) on a FCC (100) template with a lattice constant correspond-

ing to a close-packed FCC crystal. Furthermore, the initial particle concentration did not have an effect on the quality of the sediment formed for  $Pe > 1$ .

In **Chapter 3**, we studied sedimenting *binary* hard-sphere mixtures with the objective of forming the *binary* MgCu<sub>2</sub> Laves Phase (LP). The Laves phases, which are crystal structures with a LS<sub>2</sub> stoichiometry (L = large species, S = small species), were first found in intermetallic compounds: MgCu<sub>2</sub>, MgZn<sub>2</sub> and MgNi<sub>2</sub>. The three LPs have a very small free-energy difference,  $\sim 10^{-3}k_B T$  per particle around the freezing point, with the MgZn<sub>2</sub> LP being the most stable one. However, from a photonic standpoint, we are more interested in the MgCu<sub>2</sub> LP, whose L and S species sublattices correspond to the diamond and pyrochlore structures respectively. Both the diamond and pyrochlore crystal structures are photonic champions in that even for low refractive index contrasts they display wide photonic band gaps. For an optical bandgap, the spheres must be on a colloidal length scale in which regime the thermal and gravitational energies are comparable. We studied the thermodynamics of such a system in sedimentation-diffusion equilibrium using a theory propounded by de las Heras and Schmidt which correlates the thermodynamic bulk phase diagram of a colloidal mixture to the phenomenology of the stacking of phases in a sedimentation column. The resultant phase space that is constructed includes gravity in the description and is known as a *phase stacking diagram*. With the *a priori* knowledge that binary hard-sphere mixtures show stable LPs for a diameter ratio  $q$  between 0.76–0.84, where the most optimal packing is obtained for  $q = 0.82$ , we constructed the bulk phase diagram and corresponding stacking diagram for  $q = 0.82$  (and for  $q = 0.85$  for which the Laves phase drops out as a stable phase from the bulk phase diagram). We then simulated the sedimentation dynamics for selected state points (which correspond to unique phase stacking sequences) in our stacking diagram. While our simulations formed the one-component phases in accordance with our phase stacking predictions, we found it challenging to obtain the binary MgCu<sub>2</sub> LP in spite of using a MgCu<sub>2</sub> (110) template to assist the self-assembly. This depicts that binary crystallization in entropic systems is more complex and challenging than for one-component systems.

In **Chapter 4**, we discuss an approach to avoid a random stacking of the FCC and HCP crystals upon crystallization, as they are free-energetically degenerate crystal phases with respect to the thermodynamic phase diagram of monodisperse hard spheres. Specifically, the FCC and HCP crystal structures have the same close-packed volume fraction and the same kind of voids in the crystal structure but differ in the way that the voids are connected with each other throughout the structure. The idea of leveraging this difference in void distributions using a polymer chain inside the colloidal polymorph was elucidated in a paper by Mahynski *et al.* We carried this idea forward to study the relative stability of the FCC and HCP crystal polymorphs in colloid-polymer mixtures, where the colloids are modelled as hard spheres and the polymers are modelled as freely-jointed chains of significantly smaller hard-sphere monomer beads. For the shortest polymer chain length (1 monomer bead), the system reduces to a highly asymmetric binary hard sphere mixture with  $q = 1/7$ . We calculated thermodynamic phase diagrams for two different chain lengths of 10 and 14 monomer beads and obtained a stability region for the HCP polymorph for the latter case. The polymer-induced depletion attraction between the colloids yielded a gas-liquid phase separation in both the thermodynamic phase diagrams, but in both cases this region was metastable with respect to a broad fluid-crystal phase coexistence. Additionally, we also studied the chain dynamics inside the colloidal structures for three different polymer chain lengths, which led to some intriguing observations.

In **Chapter 5**, we explicitly employed attractions between colloidal spheres to follow their crystallization inside a slowly shrinking spherical confinement in order to study the crystallization mechanism of nanocrystals inside a slowly evaporating oil-in-water emulsion droplet. We observed four completely different kinetic pathways on tuning the strength of attraction between the spheres from  $-3 k_B T$  to 0 (hard spheres), thus demonstrating the sensitivity of the self-assembly to this parameter. Our findings therefore emphasize the importance of accounting for attractions in nanoparticle self-assembly. In the last part of this thesis, we focus on binary crystal nucleation in entropic systems. In repulsive systems, the freezing transition lies at high densities in which regime nucleation may be significantly hampered by slow or even glassy dynamics. Additionally, crystallization in binary mixtures is much more challenging with respect to one-component systems due to fractionation effects.

In **Chapter 6**, we proceeded with the objective of realising the spontaneous crystallization of the binary Laves phases in a purely repulsive binary mixture. As discussed in Chapter 3, even though the LPs has been proven to be thermodynamically stable in a binary hard-sphere mixture for certain diameter ratios, LPs have never been observed to spontaneously crystallize from such a fluid mixture in ‘brute force’ computer simulations. We therefore introduce some softness into the interaction potential while still simulating a purely repulsive binary mixture, in order to see if it stimulates crystal nucleation. Here, the particles interact via a pairwise Weeks-Chandler-Andersen (WCA) potential, which has been previously used to mimic the hard-sphere potential and as such reduces to the hard-sphere potential at  $k_B T / \epsilon \rightarrow 0$ . Historically, the *soft-core* WCA potential has been employed as a perturbation to a reference hard-sphere system, and is mapped to the hard-sphere system through the determination of an *effective diameter* which can be obtained through performing an expansion of its reduced free-energy density about that of hard spheres. We calculated the binary phase diagrams (for three different temperatures) for our WCA mixtures for  $q = 0.78$ , which (similar to the binary hard-sphere phase diagram for the same diameter ratio) showed a stable Laves phase in coexistence with the binary fluid and pure FCC phases in various regions of the phase diagram(s). Our phase diagrams showed congruent freezing/melting lines at the composition equal to the stoichiometry of the LP (*i.e.*  $LS_2$ ) meaning that the Laves solid melts into a fluid of the same composition with reducing pressure, therefore avoiding fractionation effects. Encouraged by these observations, we performed molecular dynamics simulations on a supersaturated binary fluid of this composition at selected state points in the relevant phase diagram, and observed the spontaneous nucleation of the Laves phase in both the  $NVT$  and  $NPT$  ensembles. We identified bond order parameters to detect the LP crystalline clusters nucleating in the supersaturated fluid. We then estimated the pressures that corresponded to the spinodal decomposition and the MCT glass transition, and during the estimation of the spinodal point we noticed an intriguing invariance in the thermodynamic driving force for nucleation. A further investigation into this thermodynamic invariance established the presence of *isomorphic curves* on the thermodynamic phase diagram, along which the structure and dynamics, in reduced units, of thermodynamic state points are invariant, effectively signifying a one-dimensional phase diagram which is a unique feature of hard spheres. Assuming therefore that the thermodynamic driving force for nucleation is the same for the corresponding binary hard sphere system (*i.e.*  $q = 0.78$ ), we estimated the pressures corresponding to the spinodal decomposition and glass transition in hard spheres. A comparison of the pressures for all four systems (three WCA mixtures and binary hard spheres) presented an interesting observation. We observed that whereas for our WCA mixtures spinodal decomposition invariably

precedes the MCT glass transition, contrarily, the kinetic glass transition interrupts spontaneous nucleation in binary hard spheres.

In **Chapter 7**, we simulated the same binary mixture (at  $k_B T/\varepsilon = 0.2$ ) inside a spherical confinement in order to observe the effect, if any, of the spherical geometry of the confinement on the crystal structure obtained. Instead of the Laves phase which crystallizes in bulk, binary *icosahedral quasicrystal* clusters were observed to nucleate *homogenously* in what we believe to be the first report of 3D icosahedral quasicrystals (iQCs) forming from purely repulsive (nearly hard sphere) colloids in spherical confinement. We characterized the quasicrystal through its trademark  $\tau$ -inflation observable in the diffraction diagram along the five-fold axes, and identified a known quasicrystalline subunit (known as the Bergman cluster) making up the core of the iQC. The iQC cluster is made up of twenty tetrahedral domains meeting at twelve points, which show five-fold symmetry, on the surface of a circumscribing sphere. We used bond order parameters to track the nucleation process, and used an additional order parameter to distinguish the tetrahedral domains. A different kind of order parameter analysis applied to only the large particles showed the structure of the tetrahedral domains to be similar to that of the photonic  $\text{MgCu}_2$  LP. We performed this study in close collaboration with experiments on binary hard-sphere-like nanocrystals inside a slowly evaporating emulsion droplet, and found iQCs with the same structure in both experiments and our simulations. Our findings not only illustrate how curved space affects the structure of matter and how quasicrystals nucleate and grow but are also important to the field of photonics as icosahedral quasicrystals are known to exhibit a large and robust photonic bandgap.

The work presented in this thesis represents a step towards fabricating colloidal photonic crystals in bulk, in a gravitational field and inside a spherical confinement, using computer simulations. In a large section of this thesis, we focus on self-assembling the binary Laves phase, and in the process, address the significant challenges associated with binary crystal nucleation in repulsive systems. We hope that our findings not only provide fabrication routes for photonic crystals but also enhance the understanding of the physics of crystal nucleation and self-assembly in colloidal systems.

# Samenvatting

Het werk gepresenteerd in dit proefschrift is gebaseerd op de kristallisatie en het gedrag van colloïdale systemen. In een colloïdaal systeem, een onoplosbare fase (bijvoorbeeld druppels vloeistof of vastestofdeeltjes) is verspreid in een andere fase. Het hoofdkenmerk van colloïdale deeltjes, uitgelegd door Einstein in zijn proefschrift, is dat ze continu ‘wiebelen’, een fenomeen wat beter bekend is als Brownse beweging, doordat moleculen van de oplosmiddel tegen de deeltjes aan botsen. Een colloïdaal deeltje vertoont Brownse beweging, wanneer tenminste één dimensie van het deeltje tussen de 1 nanometer en 1 micrometer is. De langzame Brownse beweging van colloïdale deeltjes in een oplosmiddel betekent dat het systeem thermodynamisch gunstige configuraties kan ontdekken, en in bepaalde condities, zichzelf kan arrangeren in geordende structuren zoals een kristalfase. Dit fenomeen is bekend als zelf-assemblage, en dit proefschrift bediscussieert de spontane of gerichte zelf-assemblage in colloïdale systemen, met een focus op colloïdale fotonische kristallen.

Fotonische kristallen zijn structuren die een fotonische bandkloof hebben (analoog aan elektronische bandkloven in halfgeleiders) als gevolg van afwisselende gebieden met een hoge en lage diëlectrische constante in het materiaal. In dit proefschrift, zijn wij geïnteresseerd in zelf-assemblerende fotonische kristallen die, als gevolg van de grootte van de bouwblokken, een fotonische bandkloof laten zien in het zichtbare gebied van licht. Colloïdale fotonische kristallen hebben een aantal toepassingen zoals optische golfgeleiders, optische sensoren, en de opslag en conversie van energie.

Eén bekend fotonisch kristal is de inverse vlakgecentreerde kubische (FCC) structuur. Vanuit het colloïdale perspectief is deze structuur belangrijk omdat het mogelijk is om deze spontaan te zelf-assembleren met harde bollen, in zowel experimenten als computer simulaties. Het harde-bollenmodel is een gevestigd model voor het bestuderen van kristallisatie in bepaalde colloïdale systemen zoals deeltjes van polymethylmethacrylaat (PMMA) of silica bedekt met polymeer. De FCC structuur vertoont echter een smalle fotonische bandkloof die gevoelig is voor defecten. Daardoor is er een sterke motivatie voor de zelf-assemblage van defectvrije FCC kristallen. Dit is nogal een uitdaging doordat, naast de natuurlijke defecten van spontane zelf-assemblage, het FCC kristal een thermodynamisch concurrerende kristalfase heeft in het harde bollen fase-diagram, de hexagonale dichtste stapeling (HCP), waarin het verschil in de vrije energie tussen de twee structuren slechts  $\sim 10^{-3} k_B T$  per deeltje is rond het smeltpunt, en daardoor een willekeurige stapel van beide structuren normaal gesproken wordt verkregen in de kristalfase.

In **Hoofdstuk 2** hebben we de formatie in een zwaartekrachtveld van grote FCC kristallen van zuiver harde bollen bestudeerd. Om een willekeurige stapeling te voorkomen hebben we op de bodem van een sedimentatiekolom een regelmatig patroon aangebracht om de zelf-assemblage aan te sturen. De patronen corresponderen met de drie doorsneden van het FCC kristal met de dichtste pakkingen. Daarna hebben we de optimale sedimentatiecondities onderzocht waaronder grote bijna defectvrije FCC kristallen kunnen worden gevormd, zoals (i) het zwaartekrachtsgetal van Peclet ( $Pe$ ), (ii) de roosterafstand van het patroon, en (iii) de deeltjes-volumefractie voordat het zwaartekrachtveld in werking is. We hebben gevonden dat de beste FCC kristallen (fractie van vergelijkbaar geordeneerde FCC deeltjes 90%) werden verkregen bij een hoge  $Pe$  (hoge sedimentatiesnelheden) op een FCC (100) patroon met een roostercon-

stante die correspondeert met die van een dichtste-bolstapeling FCC kristaal. De concentratie van deeltjes had geen invloed op de kwaliteit van het sediment die gemaakt was voor  $Pe > 1$ .

In **Hoofdstuk 3** hebben we de sedimentatie van binaire mengsels van harde bollen bestudeerd met het doel om de binaire  $MgCu_2$  Laves fase (LP) te maken. De Laves fases, wat kristal structuren zijn met een  $LS_2$  stoichiometrie of verhouding (L= groot deeltje, S=klein deeltje), zijn als eerste in intermetallische verbindingen gevonden:  $MgCu_2$ ,  $MgZn_2$ , en  $MgNi_2$ . Deze drie LPs hebben een klein vrije-energieverschil,  $\sim 10^{-3}k_B T$  per deeltje rond het vriespunt, alwaar de  $MgZn_2$  LP het meest stabiel is. Maar vanuit een fotonisch perspectief zijn wij meer geïnteresseerd in de  $MgCu_2$  LP, wiens subroosters van L en S deeltjes corresponderen aan respectievelijk de diamant en pyrochloor structuren. Beide structuren zijn fotonische kampioenen – ze hebben een grote bandkloof zelfs voor lage brekingsindex contrasten. Voor het vormen van een kristal met een optische bandkloof, moeten de bollen een colloïdale lengteschaal hebben waar de thermische en zwaartekrachtsenergieën vergelijkbaar zijn met elkaar. We hebben de thermodynamica van zo'n systeem in sedimentatie-diffusieevenwicht bestudeerd door middel van een theorie voorgesteld door de las Heras en Schmidt, die het thermodynamische bulk fase-diagram van een colloïdaal mengsel correleert met de stapeling van bollen in een sedimentatiekolom. De resulterende faseruimte waar zwaartekracht in mee is genomen staat bekend als een fase-stapelingsdiagram. Met de voorkennis dat binaire mengsels van harde bollen stabiele LPs vormen bij een diameter verhouding  $q$  tussen 0.76-0.84, waarin de meest optimale stapeling gevonden wordt bij  $q = 0.82$ , hebben we het bulk fase-diagram opgesteld, alsmede het corresponderende stapelingsdiagram voor  $q = 0.82$  (en voor  $q = 0.85$  waar de LP wegvalt als een stabiel fase). We hebben vervolgens de sedimentatie dynamica gesimuleerd voor geselecteerde staatpunten (die corresponderen aan unieke fase stapeling sequenties) in onze stapelingsdiagram. Ook al vormden onze simulaties de verwachte één-component fases, het was een uitdaging om de binaire  $MgCu_2$  LP te verkrijgen, ondanks het feit dat we een  $MgCu_2$  (110) patroon gebruikt hadden om de zelf-assemblage te assisteren. Dit laat zien dat binaire kristallisatie in entropische systemen ingewikkelder en uitdagender is dan voor één-component systemen.

In **Hoofdstuk 4** hebben we geprobeerd om de aanwezigheid van een willekeurige stapeling van vrije-energie gedegenereerde kristalstructuren (FCC en HCP) te voorkomen in het fase-diagram van één-component harde bollen. We hebben specifiek naar de FCC en HCP kristalstructuren gekeken die dezelfde dichtste-bolstapeling volumefractie en type holtes in de kristalstructuur hebben, maar verschillen in de manier waarop de holtes verbonden met elkaar zijn in de structuur. Het idee om gebruik te maken van het verschil in de verbindingen tussen de holtes door middel van het introduceren van een polymeer is beschreven in een artikel van Mahynski *et al.* We hebben dit idee gebruikt om de stabiliteit van FCC en HCP kristal polymorfen te bestuderen in colloïden-polymeermengsels, waarin de colloïden zijn gemodelleerd als harde bollen en de polymeren als vrij-verbonden ketens opgebouwd uit veel kleinere harde bollen. Voor de kortste ketenlengte (1 bolletje), wordt het systeem een zeer asymmetrisch binair harde-bollenmengsel op  $q = 1/7$ . We hebben de thermodynamische fase-diagrammen berekend voor twee verschillende ketenlengtes van 10 en 14 bolletjes en hebben voor het laatste geval een stabiel gebied verkregen voor de HCP polymorf. De polymeer geïnduceerde depletie interactie tussen de colloïden leverde een gas-vloeistof fasescheiding op in beide thermodynamische fase-diagrammen, maar in beide gevallen was dit gebied meta-stabiel in verhouding tot een brede vloeistof-kristalfase overgang. Aanvullend hebben we ook de ketendynamica bestudeerd binnen de colloïdale structuren voor drie verschillende polymeer ketenlengtes.

In **Hoofdstuk 5** hebben wij attracties tussen colloïdale bollen geïntroduceerd om de kristallisatie te volgen binnen een langzaam krimpende sferische begrenzing om het kristallisatiemechanisme van nanokristallen in langzaam verdampende olie-in-water druppels te bestuderen. We namen 4 verschillende kinetische routes waar wanneer wij de sterkte van de attractie varieerden van  $-3 k_B T$  naar 0 (harde bollen), wat de gevoeligheid van de zelf-assemblage voor deze parameter demonstreert. Onze bevindingen benadrukken daarom het belang van deze attracties in de zelf-assemblage van nanodeeltjes. In het laatste onderdeel van dit proefschrift focussen wij ons op de nucleatie van binaire kristallen in entropische systemen. In afstotende systemen ligt de bevroeringsovergang bij hoge dichtheden, een regime waarin nucleatie mogelijk is vertraagd door glas-achtige dynamica. Bovendien is de kristallisatie in binaire mengsels veel lastiger dan in één-component systemen vanwege de effecten van fractionering.

In **Hoofdstuk 6** vervolgen wij het proefschrift met het doel om spontane kristallisatie te realiseren van de binaire LPs in een puur afstotend binaire mengsel. Zoals eerder bediscussieerd in Hoofdstuk 3, zijn LPs nog nooit spontaan gekristalliseerd uit zo'n vloeibare mengsel in 'brute kracht' computer simulaties, ook al zijn de LPs bekend als thermodynamisch stabiel in een binair mengsel van harde bollen voor bepaalde diameter verhoudingen. We introduceren daarom wat zachtheid in de interactiepotentiaal terwijl wij nog steeds een puur afstotend mengsel simuleren, om te zien of kristal nucleatie wordt gestimuleerd. Hier hebben de deeltjes een Weeks-Chandler-Anderson (WCA) interactiepotentiaal, die vroeger is gebruikt om een harde bollen systeem na te bootsen en reduceert naar de harde bollen potentiaal wanneer  $k_B T / \epsilon \rightarrow 0$ . Historisch gezien wordt de zacht-kern WCA interactiepotentiaal gebruikt als een verstoring ten opzichte van een referentie harde bollen systeem, en wordt geprojecteerd op het fase diagram van een harde-bollensysteem na bepaling van de effectieve diameter door de expansie van de gereduceerde vrije-energiedichtheid om die van harde bollen. We hebben de binaire fase diagrammen berekend (voor 3 verschillende temperaturen) voor onze WCA mengsels wanneer  $q = 0.78$ , wat (vergelijkbaar met het binaire harde bollen fase diagram voor dezelfde diameterverhouding) een stabiele LP laat zien in coëxistentie met de binaire vloeistof en zuivere FCC fases in verschillende gebieden van het fase diagram. Onze fase diagrammen vertonen overeenkomende bevroerings-/smeltingslijnen bij een compositie gelijk aan de stoichiometrie van de LP (m.a.w.  $LS_2$ ), wat betekent dat de Laves vaste stof smelt om een vloeistof te vormen met dezelfde compositie wanneer de druk afneemt, wat vervolgens dat fractionering voorkomt. Aangemoedigd door deze observaties hebben we moleculaire dynamica simulaties uitgevoerd op een oververzadigde binaire vloeistof met deze compositie op geselecteerde punten in het relevante fase diagram, en namen de spontane nucleatie van de LP waar in zowel de  $NVT$  en  $NPT$  ensembles. We hebben orde parameters geïdentificeerd om de nucleatie van de LP kristal lijne clusters te kunnen detecteren in de oververzadigde vloeistof. We hebben daarna de druk afgeschat die correspondeert met de spinodale decompositie en de MCT glasovergang. Tijdens die afchatting van het spinodale punt hadden we ook een intrigerende invariantie waargenomen in de thermodynamische drijvende kracht voor de nucleatie. Verder onderzoek resulteerde in de vondst van gelijkvormige curves in het thermodynamische fase diagram, waarlangs de structuur en de dynamica van thermodynamische toestandspunten, in gereduceerde eenheden, invariant zijn, effectief duidend op een één-dimensionaal fase diagram wat een unieke eigenschap is van harde bollen. Met de aanname dat de thermodynamische drijvende kracht achter de nucleatie hetzelfde is voor het overeenkomende binaire harde bollen systeem (m.a.w.  $q = 0.78$ ), schatten we de verschillende drukken af overeenkomend met de spinodale decompositie en glasovergang

van harde bollen. Een vergelijking van alle drukken voor alle 4 systemen (3 WCA mengsels en binaire harde bollen) resulteerde in een interessante observatie. Wij namen waar dat waar bij het WCA mengsel de spinodale decompositie consequent vooraf gaat aan de MCT glasovergang, de kinetische glasovergang de spontane nucleatie onderbreekt voor binaire harde bollen.

In **Hoofdstuk 7** hebben we hetzelfde binaire mengsel (bij  $k_B T / \varepsilon = 0.2$ ) gesimuleerd binnen een sferische begrenzing om het effect, te kunnen bekijken van de sferische geometrie van de begrenzing op de resulterende kristalstructuur, indien aanwezig. In plaats van de LP die kristalliseert in bulk, namen we binaire icosaeëdrische quasikristallijne clusters waar die vormden door middel van homogene nucleatie, wat naar ons idee de eerste beschrijving is van de vorming van driedimensionale icosaeëdrische quasikristallen (iQCs) gevormd door enkel repulsieve (bijna harde bollen) colloïdale deeltjes in sferische begrenzing. Wij karakteriseerden het quasikristal door zijn herkenbare  $\tau$ -inflatie die zichtbaar is in het diffractiepatroon langs de 5-voudige symmetrieassen, en identificeerden een bekende quasikristallijne substructuur (bekend als de Bergman cluster) die de kern van iQC vormt. De iQC cluster is opgebouwd uit 20 tetraëdrische domeinen die samen komen in twaalf punten, die 5-voudige symmetrie laten zien op het oppervlak van een omschrijvende bol. We hebben orde parameters gebruikt om het nucleatieproces te volgen, en hebben ook een extra order parameter gebruikt om de tetraëdrische domeinen te onderscheiden. Een andere soort order parameters analyse toegepast op de grote deeltjes heeft laten zien dat de kristalstructuur van de tetraëdrische domeinen vergelijkbaar is met de fotonische MgCu<sub>2</sub> LP. Deze studie is uitgevoerd in nauwe samenwerking met experimenten op binaire harde-bol-achtige nanokristallen in langzaam verdampende emulsie druppels, en de iQCs met dezelfde structuur is gevonden in zowel simulaties en experimenten. Deze bevindingen laten niet alleen zien hoe gekromde ruimte de structuur van materie beïnvloeden en hoe quasikristallen vormen en groeien, maar zijn ook belangrijk voor het onderzoeksveld van de fotonica, aangezien het bekend is dat icosaeëdrische quasikristallen grote en robuuste bandkloven hebben.

Het werk gepresenteerd in dit proefschrift geeft een stap weer naar het ontwikkelen van colloïdale fotonische kristallen in bulk, in een zwaartekracht veld en ook binnen sferische begrenzing, met gebruik van computersimulaties. In een groot deel van dit proefschrift focussen we ons op de zelf-assemblage van de binaire LP, en terwijl we dat doen, benoemen we de flinke uitdagingen die komen kijken bij de nucleatie van binaire kristallen in repulsieve systemen. Wij hopen dat onze bevindingen niet alleen routes verstrekken voor het maken van fotonische kristallen, maar ook het kennis vergroten van de natuurkunde van de nucleatie en zelf-assemblage van kristallen in colloïdale systemen.

# Acknowledgements

I stepped outside the borders of the Indian subcontinent for the very first time in 2014 to pursue a doctorate degree in the Netherlands, a period which has proven, simply put, remarkable. In these years, I have had the good fortune to interact, in both a professional and personal capacity, with some wonderful people. I am glad to have this opportunity to thank some of them in writing.

It is difficult to express only in a few words all that I have learnt in terms of scientific knowledge and work ethics from my supervisor Marjolein Dijkstra. In short, I feel a deep sense of admiration and gratitude towards her. Marjolein, thank you for giving me an opportunity to do a PhD in your group, your impeccable scientific supervision over these years, always making yourself available for discussions even at a moment's notice, reviewing papers (and thesis chapters) with incredible promptness, immensely stimulating scientific discussions, and all in all for bringing new meaning to the 'super' in supervisor. It has been an honour working in your group. On a more personal note, thank you for your constant enthusiasm and encouragement, and for looking out for me when I would occasionally tend to work late.

In my final year, I was fortunate enough to be able to work quite closely with Alfons van Blaaderen, and it has been an extremely rewarding experience. Alfons, thank you for your inspiring ideas, extremely interesting scientific discussions from which I have always emerged with more knowledge and ideas than I had going in, and all your questions and comments over various presentations which have always improved my research. In particular, thank you very much for reading my thesis so carefully and painstakingly.

I sincerely thank the scientific staff of the SCM&B and ITF groups, and visitors to our group: Laura Fillion, René van Roij, Joost de Graaf, Michiel Hermes, Frank Smalenburg, Gerhard Blab, Bob Evans, Kate Jensen, Arnout Imhof, Patrick Baesjou, Freddy Rabouw, Marijn van Huis, Krassimir Velikov, Hans Gerritsen, and Henk van Beijeren. Thank you for all the valuable comments and suggestions that you have given me at various points of time, which have enormously improved both my scientific research and presentations. Thank you Gerhard, for 3D printing so many truncated tetrahedra (and even making  $n$ -stacks of the polyhedra) so graciously. These were invaluable in our understanding of the Laves phase and quasicrystal structures, and would undoubtedly serve as extremely useful aides in future presentations on the subject. I really enjoyed going to pub quizzes after work, where your in-depth knowledge of really niche things never failed to amaze me. Thank you Laura, for always being available for discussions, answering numerous questions, and your insightful advice on various things in general. Along with all of the simulators, I thank you and Carel for your efficient management of the clusters. Thank you, René and Laura, for your excellent lectures on the Advanced Statistical Physics course. René, I immensely enjoyed our conversation at Cafe Le Journal in December and look forward to more such evenings in the future with you and Marjolein.

Hester van der Putte and Dianne Ickenroth are heartily thanked for all their help with the administrative tasks. Thank you for humouring my incessant queries about forms and protocol. I gratefully acknowledge Marion Wijburg for her kind assistance with administrative matters at the beginning of my PhD. Peter Helfferich is sincerely thanked for his assistance over technical difficulties and promptly providing external hard drives when needed. Dave van den Heuvel

is sincerely thanked for creating a very pleasant atmosphere and fun discussions at the coffee corner, as are Relinde Moes-van Dijk, Elleke van Harten and Mijke Heldens.

I sincerely thank all my colleagues, both the current and former members of the SCM&B, ITF groups whom I have crossed paths with, for being available to one another and making the atmosphere in the group really nice. Whether we had a scientific discussion or a non scientific one, our shared goal was always to learn and have fun together. For this, thank you very much to Wiebke, Giulia, Harini, Anna, Jessi, Nina, Henriëtte, Relinde, Xiaodan, Jantina, Frankje, Douglas, Chris, John, Siddarth, Somil, Sandeep, Naveed, Rama, Da, Ernest, Pepijn, Rik, Bernd, Gabriele, Carmine, Emanuele, Massi, Srivatssan, Robin (van Damme), Maarten, Albert, Tom, Sina, Stijn, Erik, Federico, Dyaneshwar, Robin (Geitenbeek), Xiaobin, Guido, Anjan, Nick, Simone, Zdenek, Vassilis, Fabian, Wessel, Peter (Elroy), Sajjad, Ravi, Yang, Ajoy, Tara, Sela, Bram, Mathijs, Jeffery, Ben, Jeroen, Peter (Cats), Giuseppe, Jasper and all the Master and Bachelor students in the group. Thank you Harini and Robin, for keeping us up-to-date about work discussions. Thank you Fabian, Nina and Anna, for organising Sweets & Cookies Monday. Thank you Wessel, for baking delicious cakes for the group. Thank you Chris, Doug, Hester, Massi, Anna, Albert, Frankje and others for organising fantastic Christmas dinners and games for us all to enjoy. To all the simulators in the SCM group, my heartfelt thanks to all of you for accommodating my heavy computational needs while running the seeding simulations. I am thankful to my fellow Teaching Assistants for the *Structuur van de Materie* and *Modelling and Simulation* courses. Guido and Jasper (SvM), Nick and Sid (M&S), thank you all for making the processes not only smooth but also enjoyable.

I am unaccountably grateful to John Edison for being nothing less than a mentor to me in my first year, for helping me set up my first project, many useful discussions on many other projects, always being available for any advice or assistance, the late night burgers, long walks through the center of Utrecht, and overseas chats about everything ranging from music to comedy shows. John, you are, and always will be, extremely special.

Dear Peter, you and Alex were among my first friends here. Thank you both so much for making me feel welcome in the entirely new cultural backdrop, all the movie outings and board game nights. Pete, Lex and little Brinn, my best wishes to you on your very own happily ever after.

I am immeasurably grateful to Doug, Ernest and Robin for painstakingly translating, correcting and proofreading my ‘Samenvatting’ respectively. Thank you all so much for your efforts!

Dear Anjan, we had too short an overlap for my liking but thank you so much for the lovely moments that we shared. My first proper social interaction in the Netherlands was with you and John in Botanische Tuinen on my first day here (I don’t know if you remember :)), where you bought me a piece of pie and gave me a short account of work life in Ornstein! My best wishes to you, Raji and little Akshara, always. Dear Anna, in the short time that I have known you, you have never ceased to amaze me. Not only do you have an incredible flair for making beautiful presentations, you are constantly brimming with fun new ideas for parties, gatherings and defenses! Contrary to what you believe, I enjoyed your late night ‘interruptions’ (as you termed it) :). I look forward to future meet-ups and kitten-sitting! Dear Naveed, I will always remember the fun conversations, UMC lunches, movie nights, concerts, chance meet-ups at Schiphol and evening teas. Thank you for creating such a nice atmosphere wherever you go. Rama, you never fail to make me laugh with your quick comments, often accompanied by darting winks. I particularly enjoy chatting with you and Sid in Hindi, brings back a flavour of

home! Carmine, thanks for the engaging chats about football, here's hoping that Inter Milan and Arsenal fulfill our hopes and dreams in times to come.

Dear Maria and Paulo, you made Holland home for me in my first few years. Maria, your big heart, will always endear you to those of us who have had the good fortune of living with you. Paulo, your good humour and great spirit is wonderful to be around. I wish you both good health and great happiness going ahead, lots of love. Emma, Li, you guys were the best housemates, I will never forget those times, especially our trip to Afsluitdijk!

The India-gang, Chapter I: Chris, Wiebke and Doug. This was quite easily the most brilliant trip of my PhD. It would have been sufficiently remarkable to spot a tiger *and* a bull elephant up close in the wild, or scale the 11500 feet-high Khaliya peak in Munsyari, but your company is what made it the best experience ever. I look forward to many more such chapters in our lives.

The India-gang, Chapter II, Rama's wedding: Naveed, Samaneh, Massi, Gabriele, Chris, Doug (and the groom himself!) - thank you guys for such a memorable trip! From experiencing the *Kathakali*, among the tea-gardens of Munnar, over the waters of Alleppey, through the streets of Kochi, all the way to Rama's wedding *mandap* in Visakhapatnam, it was an unforgettable trip for me. Massi, I must say I am in awe of your organisational skills, in spite of being *from* the country I didn't have to arrange anything, you handled it all with aplomb! Rama, I wish you and Sarita a wonderful life together, thank you for inviting us to your wedding!

My trips to England have been quite wonderful owing to the hospitality and warmth shown to me by Doug's family. Kim, thank you and Paul for making me feel so welcome in your lovely home, that lovely day out in Bristol, hilly walks through Weston-super-Mare, and 'Scrabbled' evenings. The time we spent together was indeed 'as good as it gets'! Catherine, thank you and Darren for being so gracious and welcoming to me. I loved that memorable trip to the fish-cake joint ;), playing Jaipur, strolling through Bedford Park with little Bella. Love to you both and your absolutely gorgeous kids! Thom and Kate, thank you both for welcoming us to your place in London, I look forward to watching North London Derbies together!

I am grateful to all the people I have collaborated with: Da, Ernest, Gabriele, Michiel, Thomas, Guido and Federico. Thank you all for great collaborations!

Da, on top of finding that elusive five-fold symmetry in your supraparticles which spawned such a nice collaboration, thank you for being such a good friend, for all the hard work you put in, the various scientific and non-scientific chats, and all the thesis related advice which has helped me so much! Ernest, my thesis-buddy, you spot symmetry like no other, thank you for this nice collaboration, your meticulousness, great discussions over late overseas Skype calls, the long "figure-specific" email chains (which I assure you and Da that I am going to archive for posterity), and all round general fun times! Thank you Michiel, for setting up reader-interactive views which would enable the readers of our article (when published) to visualise these interesting structures. Gabriele, thanks for a wonderful collaboration and your hard work, I really enjoyed working with you and your spirit in doing whatever it takes! I really look forward to writing these paper(s) with you. All the best for your PhD! Guido, thanks for such a fun collaboration. I have always enjoyed our scientific discussions immensely, and the speed with which we work together. Federico, thank you for a rewarding collaboration. I really admire how well and speedily you write scientific articles, it is an enviable trait. All the best for Zürich!

Dear Harini, thank you for all the talks and advice, I think if it had not been for you telling me what forms to fill out in my first year, there is a strong chance that I may have been deported! I loved sharing rooms with you at all those conferences! ;)

Dear Guido, our perpetual *saboteur*, thanks for the ridiculously fun board game evenings, foosball sessions, walks, talks and collaborations. Well, collaboration, singular, but perhaps there are more to come in the future, who knows!

A big, big thank you to the best office mates anyone can ask for, Giulia and Siddharth. I count myself extremely lucky that they are also among my closest friends here. Dear Giulia, I have loved our long walks and chats over these years, around Ornstein, at Pickles, at random coffee bars, and various conferences. I look forward to many more wonderful years of hangouts, board games and Woody Allen movies! Dear Sid, thank you firstly for moving into our office, which has led to so many enjoyable coffee-chats, lunches, and after work, Bollywood movie nights and board game evenings. Thank you for always being so helpful with scientific discussions, you are indeed a great person to have for an office mate! Berend, my office-mate from another date, I really enjoyed sharing offices with you, and working in perfect harmony with our chairs back to back. Congratulations on a remarkable PhD thesis! Simone, thank you for being so inspiring, and in fact, portions of my thesis are quite literally inspired by your work!

Somil, *yaar*, I thank my stars that we met, and hold those same stars responsible for making us meet in the future, in whichever part of the world it happens. See you in Bangalore!

Dear Anirvan, thank you so much for encouraging me to return to academia and do a Master's degree. All this would not have been possible without you. My best wishes are always with you. Also, I am very grateful to your parents for always being so kind to me.

Here's a shout out to my best friends from university, Rithika, Megha, Teesta and Shilpa! A timeless support system of one's old friends is that rarest of jewels. I love you all more than I can describe in words, but you know that already.

Dear Wiebke, I love our Yoghurt Barn breakfast rituals, it makes me happy to think of the many more that are yet to come. Thanks for being such a good friend, even from across the border now that you are in Antwerp. I miss 'Paper Club' with you and Doug!

Christmas-Tree Kennedy/Chissers/Chis, what can I say to you. You're my best mate. I'm falling woefully short of words due to an inexplicable surge of emotion, but I just want to say that I'm thankful that we met. Here's to a glorious future dipped in friendship, laughter and travel!

This part goes out to my family, without whom I would be lost. Dinu, your *shobuj kantha* is always connected with you in thought. Mamu, TC, you are the lighthouse to my lost ship...Love, Benny. Pips, my little *bhai*, you are my heart, I am so very proud of you. My superMami, you're so so special! Dear BM, your words, steeped in wisdom, shall always resonate in my heart and mind, lots of love to you and my 'powerhouse' MM. Manin, my brave heart, you have my eternal admiration and love...MK.

I thank my parents, for *everything*. All that I am is because of your unwavering, unconditional love and support. Home is where you are. I am well aware that every kid would say this, but I feel as though I have the best parents in the world. Thank you, Mamma and Babu. I love you.

And finally, dearest Doug, thank you for everything. I look forward to a fulfilling, laughter-filled and incredibly happy future with you.

# List of publications

This thesis is based on the following publications:

- T. Dasgupta, J. R. Edison, and M. Dijkstra, *Growth of defect-free colloidal hard-sphere crystals using colloidal epitaxy*, The Journal of Chemical Physics **146**, 074903 (2017). † (Chapter 2) † 2017 Editors' Choice, The Journal of Chemical Physics
- T. Dasgupta and M. Dijkstra, *Towards the colloidal Laves phase from binary hard-sphere mixtures via sedimentation*, Soft Matter **14**, 2465 (2018). (Chapter 3)
- J. R. Edison, T. Dasgupta, and M. Dijkstra, *Stabilizing the hexagonal close packed structure of hard spheres with polymers: Phase diagram, structure, and dynamics*, The Journal of Chemical Physics. **145**, 054902 (2016). (Chapter 4)
- F. Montanarella, J. J. Geuchies, T. Dasgupta, P. T. Prins, C. van Overbeek, R. Dattani, P. Baesjou, M. Dijkstra, A. V. Petukhov, A. van Blaaderen, and D. Vanmaekelbergh, *Crystallization of nanocrystals in spherical confinement probed by in-situ X-ray scattering*, Nanoletters **18**, 3675 (2018). (Chapter 5)
- T. Dasgupta/G. M. Coli, and M. Dijkstra, *Spontaneous nucleation of binary Laves phases in nearly hard spheres*, manuscript in preparation. (Chapter 6)
- D. Wang/T. Dasgupta/E. B. van der Wee, D. Zanaga, T. Atlantzis, Y. Wu, G. M. Coli, C. B. Murray, S. Bals, M. Dijkstra, and A. van Blaaderen, *Binary icosahedral quasicrystals of hard spheres in spherical confinement*, to be submitted. (Chapter 7)

Other publications by the author:

- G. Avvisati, T. Dasgupta, and M. Dijkstra, *Fabrication of colloidal Laves phases via hard tetramers and hard spheres: Bulk phase diagram and sedimentation behavior*, ACS Nano **11**, 7702 (2017).
- D. Wang/E. B. van der Wee/Y. Wu, D. Zanaga, T. Atlantzis, T. Dasgupta, S. Bals, M. Dijkstra, C. B. Murray, and A. van Blaaderen *Real space analysis of Laves phase supraparticles*, to be submitted.
- D. Wang, M. Hermes, Y. Wu, E. B. van der Wee, Y. Liu, S. Najmr, T. Dasgupta, E. A. Gaulding, M. Dijkstra, C. B. Murray, and A. van Blaaderen *Morphological diversity in binary supraparticles obtained by drying oil in water distersions*, to be submitted.
- T. Dasgupta, S. N. Punnathanam, and K. G. Ayappa, *Effect of functional groups on separating carbon dioxide from CO<sub>2</sub>/N<sub>2</sub> gas mixtures using edge functionalized graphene nanoribbons*, Chemical Engineering Science **121**, 279 (2015).

# Oral and poster presentations

The contents of this thesis were presented at the following conferences:

- Physics@FOM 2015, Veldhoven (NL) (poster)
- Physics@FOM 2016, Veldhoven (NL) (poster)
- 4th International Soft Matter Conference 2016, Grenoble (FR) (poster)
- Physics@FOM 2017, Veldhoven (NL) (poster)
- Computational Sciences for Future Energy Conference 2017, Eindhoven (NL) (oral)
- International Association of Colloid and Interface Scientists 2018, Rotterdam (NL) (oral)
- Physics@Veldhoven 2019, Veldhoven (NL) (oral)

## About the author

Tonnishtha Dasgupta was born on 25th September, 1988 in Kolkata, West Bengal, India. She completed high school in Kolkata, and was awarded the *Medhavi Chhatra Puraskar* for academic excellence 2003-2004 by the Governor of West Bengal. She then moved to the west coast of India to pursue a Bachelor's degree in Chemical Engineering. She graduated with a B.E. (Honors) from Birla Institute of Technology and Science Pilani, Goa campus, following which she worked briefly in the Information Technology sector in Bangalore, India. Soon after, she returned to academia by joining a Master's programme at the Indian Institute of Science, Bangalore, from where she graduated with an M.Sc. (Engg.) degree in Chemical Engineering while holding a department rank 1 in course work. During her Master's programme, she worked on a research project under the joint supervision of Prof. K. Ganapathy Ayappa and Prof. Sudeep N. Punnathanam, and the resultant thesis was entitled "Effect of functional groups on separating carbon dioxide from CO<sub>2</sub>/N<sub>2</sub> gas mixtures using edge-functionalized graphene nanoribbons & Carbon dioxide adsorption in a flexible Metal-Organic Framework". Shortly after this, she was accepted into a Ph.D. programme offered jointly by the Netherlands Organisation for Scientific Research (NWO) and Shell Global B.V., and under the same, has been a Ph.D. candidate at the Soft Condensed Matter Group in the Debye Institute for Nanomaterials Science of Utrecht University, under the supervision of Prof. dr. ir. Marjolein Dijkstra, since 18th July 2014. Some of the results presented in this thesis have been presented at national and international conferences, and published in peer-reviewed scientific journals.

Other than scientific research, she loves to read, travel, write the occasional short story, and is particularly fond of whodunnits, comedic panel shows and ballroom dance. She enjoys watching football and tennis, and is an unabashed supporter of Arsenal FC.

